Magnetic Resonance Imaging to Improve Structural Localisation in Radiotherapy Planning

Scott Lewis Hanvey, M.Sci., M.Phil., M.Sc.

Thesis submitted in fulfilment of the requirements for the degree of Doctor of Philosophy

University of Glasgow

UNIVERSITY
of
GLASGOW

School of Medicine

Department of Clinical Physics

October 2013

Abstract

The purpose of this thesis is to develop the role of magnetic resonance imaging (MRI) in the radiotherapy (RT) planning process. This began by assessing a prototype inline three-dimensional distortion correction algorithm. A number of quality assurance tests were conducted using different test objects and the 3D distortion correction algorithm was compared with the standard two-dimensional version available for clinical use on the MRI system.

Scanning patients using MRI in the RT position within an immobilisation mask can be problematic, since the multi-channel head coils typically used in diagnostic imaging, are not compatible with the immobilisation mask. To assess the image quality which can be obtained with MR imaging in the RT position, various MRI quality assurance phantoms were positioned within an immobilisation mask and a series of image quality tests were performed on four imaging coils compatible with the immobilisation mask. It was shown that only the 4-channel cardiac coil delivered comparable image quality to a multi-channel head coil.

An investigation was performed to demonstrate how MRI patient position protocols influence registration quality in patients with prostate cancer undergoing radical RT. The consequences for target volume definition and dose coverage with RT planning were also assessed. Twenty patients with prostate cancer underwent a computed tomography (CT) scan in the RT position, a diagnostic MRI scan and an MRI scan in the RT position. The CT datasets were independently registered with the two MRI set-ups and the quality of registration was compared. This study demonstrated that registering CT and MR images in the RT position provides a statistically significant improvement in registration quality, target definition and target volume dose coverage for patients with prostate cancer.

A similar study was performed on twenty-two patients with oropharyngeal cancer undergoing radical RT. It was shown that when patients with oropharyngeal cancer undergo an MRI in the RT position there are significant improvements in CT-MR image registration, target definition and target volume dose coverage.

Table of contents

Chapter 2

The principles of radiotherapy planning and magnetic resonance imaging

Chapter 6

The influence of MRI scan position on patients with oropharyngeal cancer undergoing radiotherapy

Chapter 7

Final Conclusions

List of tables

List of figures

Acknowledgements

I would like to express my deep gratitude to the following people:

- To my supervisors Dr John Foster and Dr Mark McJury for their support and advice throughout the PhD.

- To the diagnostic radiographers at the Beatson MRI scanner who were always helpful and cheerful.

- To Martin Glegg for his sound radiotherapy advice and guidance.

- To the Beatson radiotherapy radiographers, especially Maureen Thomson, for their helpful participation in the clinical studies.

- To the Oncologists who took part in the clinical studies, namely: Dr Azmat Sadoyze, Dr Claire Paterson, Dr Lye Mun Tho, Dr Mohammed Rizwanullah, Dr Allan James and Dr Derek Grose.

- To my colleagues in Radiotherapy Physics for their help and support.

- To the NHS Greater Glasgow and Clyde Learning and Education Fund and to the Beatson Oncology Fund who provided financial support.

- To my parents and family for their love and support throughout.

- To my children Ben and Lucy for their smiles and for helping me to maintain perspective on everything.

- Finally, and most importantly, to my wife Fiona for her support, encouragement and love over the years, helping me to reach the finish line.

Author’s declaration

I declare that, except where explicit reference is made to the contribution of others, that this thesis is the result of my own work and has not been submitted for any other degree at the University of Glasgow or any other institution.

Signature:

Printed name: Scott Lewis Hanvey

Abbreviations

1D – one-dimensional

^{1}H-MRS – proton MR spectroscopy

2D – two-dimensional

3D – three-dimensional

4-ch – 4-channel

AAA - anisotropic analytical algorithm

AAPM - American Association of Physicists in Medicine

ADC - apparent diffusion coefficient

AIF – arterial input function

B_0 – static magnetic field

B_1 – oscillating magnetic field

BDS – beam directional shell

Beatson - Beatson West of Scotland Cancer Centre

CHHiP - Conventional or Hypofractionated High Dose Intensity Modulated Radiotherapy for Prostate Cancer

Cho - choline

Cho/W – choline relative to water ratio in MR spectroscopy

CI – confidence interval

CN – conformation number

CNR – contrast-to-noise ratio

CT – computed tomography

CT-MRI – MRI registered to CT dataset

CTV – clinical target volume

CTV LR – lower risk clinical target volume

$CuSO_4$ – copper sulphate

DCE – dynamic contrast enhanced

DL – differential linearity

DRR - digitally reconstructed radiograph

DVH – dose volume histogram

DWI – diffusion weighted imaging

EES - extravascular extracellular space

EPID – electronic portal imaging device

ESMRMB – European Society for Magnetic Resonance in Medicine and Biology

ESTRO – European Society for Radiotherapy and Oncology

FDG-PET - ^{18}F-labelled fluorodeoxyglucose positron emission tomography

FLAIR - fluid attenuated inversion recovery

FOV – field of view

FRFSE - fast recovery fast spin echo

FSE – fast spin echo

FSPGR – Fast SPoiled GRadient echo

FWHM - full width at half maximum

GE – General Electric

GTV – gross tumour volume

GTV_C – gross tumour volume delineated using PP_C

GTV_D – gross tumour volume delineated using PP_D

GTV_{RT} – gross tumour volume delineated using PP_{RT}

HU – Hounsfield units

ICRU – International Commission on Radiation Units and Measurements

IMAT - intensity modulated arc therapy

IMRT - intensity modulated radiotherapy

IPEM – Institute of Physics in Engineering and Medicine

ISMRM – International Society for Magnetic Resonance in Medicine

k_{ep} – wash-out rate in dynamic contrast enhanced imaging

K^{trans} - the forward leakage rate of the contrast medium

Linac - linear accelerator

M_0 - net magnetisation vector

MAVRIC - multi-acquisition variable-resonance image combination

MLC – multi-leaf collimator

MRI - magnetic resonance imaging

MRI_D – MRI scan in the standard diagnostic position

MRI_{RT} - MRI scan in the radiotherapy position

MRS – magnetic resonance spectroscopy

MU – monitor unit

M_{xy} – transverse magnetisation

M_z – longitudinal magnetisation

NAA - N-acetyl aspartate

NbTi - niobium-titanium

NHS – National Health Service

NSNR – normalized signal-to-noise ratio

OAR – organ at risk

PASA – Purchasing and Supply Agency

PDD – percentage depth dose

PET – positron emission tomography

PMMA - polymethyl methacrylate

PNS – peripheral nerve stimulation

PP_C – patient position protocol whereby a patient's CT scan and

MRI_D scan are viewed on separate computer consoles

PP_D – patient position protocol whereby a patient's CT scan and MRI_D scan are registered

PP_{RT} - patient position protocol whereby a patient's CT scan and MRI_{RT} scan are registered

PTV – planning target volume

PTV_C – planning target volume expanded from GTV_C

PTV_D – planning target volume expanded from GTV_D

PTV LR – lower risk planning target volume

PTV_{RT} – planning target volume expanded from GTV_{RT}

PURE - Phased array Uniformity correction

QA – quality assurance

Q-factor – quality-factor

RF – radiofrequency

RL – relative linearity

ROC - receiver operating characteristic

ROI – region of interest

RT – radiotherapy

SD – standard deviation

SE – spin echo

SNR – signal-to-noise ratio

STIR – short TI recovery

TE - echo time

TE_{eff} – effective echo time

TI – inversion time

TLD - thermoluminescent dosimeter

TMR – tissue maximum ratio

TR – repetition time

TSE – turbo spin echo

v_e - fractional extravascular extracellular space

v_p – plasma volume fraction

VMAT - volumetric modulated arc therapy

Publications

Hanvey S, Glegg M, Foster J. 2009. Magnetic resonance imaging for radiotherapy planning of brain cancer patients using immobilization and surface coils. *Physics in Medicine and Biology*, 54, 5381-5394

Hanvey S, Sadoyze AH, McJury M, Glegg M, Foster J. 2012. The influence of MRI scan position on image registration accuracy, target delineation and calculated dose in prostatic radiotherapy. *The British Journal of Radiology*, 85, e1256-e1262

Nyholm T, Jonsson J, Söderström K, Bergström P, Carlberg A, Frykholm G, Behrens CF, Geertsen PF, Trepiakas R, **Hanvey S**, Sadoyze A, Ansari, J, McCallum H, Frew J, McMenemin R, Zackrisson B. 2013. Variability in prostate and seminal vesicle delineations defined on magnetic resonance images, a multi-observer, -center and -sequence study. *Radiation Oncology*, 8, (1) 126

Hanvey S, McJury M, Tho LM, Glegg M, Thomson M, Grose D, James A, Rizwanullah M, Paterson C, Foster J. 2013. The influence of MRI scan position on patients with oropharyngeal cancer undergoing radical radiotherapy. *Radiation Oncology*, 8, (1) 129

Robertson EV, Derakhshan MH, Wirz AA, Lee YY, Seenan JP, Ballantyne SA, **Hanvey S**, Kelmanm AW, Going JJ, McColl KEL. 2013. Central obesity in asymptomatic volunteers is associated with increased intrasphincteric acid reflux and lengthening of the cardiac mucosa. *Gastroenterology*, Epub. ahead of print.

1 The integration of MRI into the radiotherapy planning process

1.1 Motivation and Aims

The motivation for this thesis was to evaluate and develop the use of magnetic resonance imaging (MRI) in radiotherapy (RT). Analysis of a three-dimensional (3D) distortion correction algorithm was assessed since geometric distortion is an important consideration when implementing MRI into the RT planning process. The primary aim of the thesis was to develop a technique to enable patients to be scanned in the RT position when undergoing an MRI which would be used for RT planning. The secondary aim was to evaluate the clinical impact of positioning patients in the RT position and whether it affected the planning process.

These studies help to improve the integration of MRI into RT and improve the accuracy of the volume and location of target structures and organs at risk. There are no other studies in the literature which compare the effects of patient set-up on dose received by the gross tumour volume during RT. Using the results of this work, this thesis should inform on the optimal patient set-up for future clinical trials involving MRI for RT.

The following chapter investigates current publications via a systematic literature review to explain how MRI is used in the field of RT. This literature review begins by exploring geometric distortion and the two main types of geometric distortion are explained, namely object induced and system related distortion. Distortion correction algorithms are considered and a quality assurance program explained. CT-MR image registration in RT is then discussed, including manual, automated and deformable registration. The effect of the differences in patient positioning is also explored since this is one of the main themes of this thesis. Finally, the role of MRI in RT is placed in the context of the current ongoing work in this field. This begins with a review of the publications showing that MRI offers an improved tumour definition over CT. The subject of MRI only RT planning is reviewed, followed by a discussion on an integrated MRI and linear accelerator (linac). This chapter closes by investigating

the use of functional MRI in RT, including diffusion-weighted imaging, dynamic contrast enhanced MRI and proton MR spectroscopy.

In this literature review special emphasis was placed on studies related to the areas of research relevant to the anatomical sites examined via experimentation in this thesis, namely, the brain; prostate and head and neck. Greater importance was also given to the studies related to the field of RT.

1.2 Geometric Distortion

1.2.1 Search strategy used and sources of information

Databases PubMed and SciVerse ScienceDirect were searched with no restrictions set on date range, document type or subject areas. English only articles were assessed. The following search terms were used ‘magnetic resonance imaging’ (or ‘magnetic’ and ‘resonance’ and imaging’ or ‘MRI’) and ‘radiotherapy’ and ‘geometric’ and ‘distortion’; ‘magnetic resonance imaging’ (or ‘magnetic’ and ‘resonance’ and imaging’ or ‘MRI’) and ‘radiotherapy’ and ‘distortion’; ‘magnetic resonance imaging’ (or ‘magnetic’ and ‘resonance’ and imaging’ or ‘MRI’) and distortion. The objectives of this literature review were to determine what are the essential components of geometric distortion in MRI; to establish which distortion correction algorithms are available and how is geometric distortion measured by means of a quality assurance program.

1.2.2 Introduction

Image distortion has always been an inherent challenge of MRI (Fransson et al. 2001). The production of geometrically accurate images in MRI depends on the precisely specified linear variation in the magnetic field across the sample being imaged and throughout the imaging process. It is not always possible to achieve this in practice because of differing material susceptibility, shim imperfections of the static field or tissue dependent chemical shift artefacts. Inhomogeneities in the static magnetic field lead to geometric distortion, since accurate image reconstruction on the resonance frequency of a spin depends on a homogeneous external field and a spatially linear gradient. If a spin experiences a magnetic field that is different from the value expected by the reconstruction algorithm, this results in its spatial position being incorrectly located in the image

(Reinsberg et al. 2005). The geometric distortions can appear both as in-plane distortions in the MR image and as slice position errors.

Geometric distortions may be acceptable for purely diagnostic purposes, however, if MRI is to be used in RT for the delineation of the planning target volume and organs at risk the image distortion in these images must be reduced to a minimum to maintain geometric accuracy.

MRI distortion correction becomes increasingly relevant with modern MRI scanners, since higher field MRI scanners results in larger susceptibility effects and shorter bore magnets compromises gradient linearity. Current wide bore MRI scanners have gradient rise times of less than 200 μs. To achieve such short rise times, manufacturers have restricted the length of the gradient coils and used fewer turns, since it takes longer to turn on a large coil than a small coil. The quality of the gradient amplifier must also be considered for gradient rise times as a large voltage is required to overcome the inductance of the coil. This increased use of stronger gradient coils with fast slew rates (short gradient rise times), has led to an increase in gradient field nonlinearity, which results in increased geometric distortion. As well as image distortion, gradient field nonlinearity has an effect on MRI applications such as diffusion-weighted MRI (Bammer et al. 2003) and phase contrast MRI (Markl et al. 2003).

1.2.3 Types of geometric distortion in MRI

There are two major types of geometric distortion in MRI: those related to the magnetic properties of the imaged object and those related to the imaging hardware. The impact of these types of distortion varies with magnetic field strength and with imaging protocol.

It is possible to subdivide the hardware related errors leading to geometric distortion into two categories: inhomogeneities in the static magnetic field B_0 and errors in the field provided by the magnetic field gradient coils. Hardware related distortions increase with distance from the magnet isocentre (Wang et al. 2004b).

The homogeneity of the static magnetic field B_0 can be optimised by active and/or passive shimming. Active shimming is achieved using special shim coils inserted in the magnet system. Passive shimming is performed by positioning pieces of ferromagnetic metal around the magnet bore. Shimming technologies in recent magnets enable the field homogeneity inside the diameter spherical volume to be within a few hertz at 1.5T, which is likely to result in a geometric error of less than 0.2 mm. In today's superconducting MRI systems with sophisticated shimming coils, geometric distortion from the inhomogeneity of the static field is small when compared to the gradient field nonlinearity (Wang et al. 2004b).

Chemical shift is an object-induced distortion. This shift is generated because protons bound in carbon-hydrogen chains in fatty tissue have a slightly different resonance frequency than tissue with water protons. Since the spatial encoding cannot distinguish between the signal from fat and water and because the water frequency is the reference frequency, the signal from fat will be incorrectly positioned. The higher the magnetic field the more pronounced the chemical shift effect. While increasing the readout bandwidth can help reduce the effect of chemical shift this leads to a decrease in the signal to noise. In RT treatment planning the effects of chemical shift is most pronounced in anatomical regions with extensive fatty tissue, such as the patient outline.

Another common object-induced distortion is susceptibility. This is the measure of the ability of a material to become magnetised in an external magnetic field. Local field changes occur at the interface between tissues with different susceptibility as a result of the magnetisation of the tissue. This causes geometric distortions, since the magnetic field strength at a given location has a different from expected field strength at this location. Distortion of the signal intensity can also occur at regions of differing susceptibility. These intensity distortions are pronounced when using a gradient-echo protocol.

Susceptibility artefacts are most prominent at tissue-air interfaces, such as the nasal cavities or the patient outline or for example at air pockets in the rectal cavity. These susceptibility artefacts can result in field changes in the order of 9 ppm which can create position errors in the mm range (Schenck 1996). As with chemical shift effects, susceptibility-induced distortions are more prominent at

higher field strength and can be reduced by increasing the bandwidth of the readout gradient.

1.2.4 Distortion correction

A method for correcting B_0 inhomogeneities by acquiring two images of the same slice with forward and reverse frequency-encoding gradients has been documented, as shown in Figure 1.1 (Chang et al. 1990). This post-processing technique involves a two step process. Firstly, corresponding features in the forward and reverse read gradient images are identified. Secondly, the corrected intensity at the average position of the identified corresponding features is calculated. Mapping the forward gradient image onto the reverse gradient image is essential for good image quality. This method corrects for the inhomogeneity of the main field and corrects these distortions to a maximum error of 1.2 mm after correction. Edge ringing artefacts are introduced by this approach in regions of chemical shift, since the pixels containing fat are shifted onto the pixels containing water. The pixel intensities are thus added or void pixels occur when encoded by forward or reverse read gradients. A disadvantage with this technique is the imaging time is doubled because of the requirement for two image sets to perform the correction.

Another group presented an automatic tool for correcting the effects of B_0 inhomogeneities based on the gradient-reversal technique of Chang and Fitzpatrick (Reinsberg et al. 2005). This uses the mutual information maximisation for the mapping of the pixel locations in the forward and reverse frequency-encoding gradient polarity images. This technique performed better with chemical shift artefacts than using the Chang and Fitzpatrick method. However, the chemical shift artefact observed in echo planar imaging is still too large to be corrected by this process.

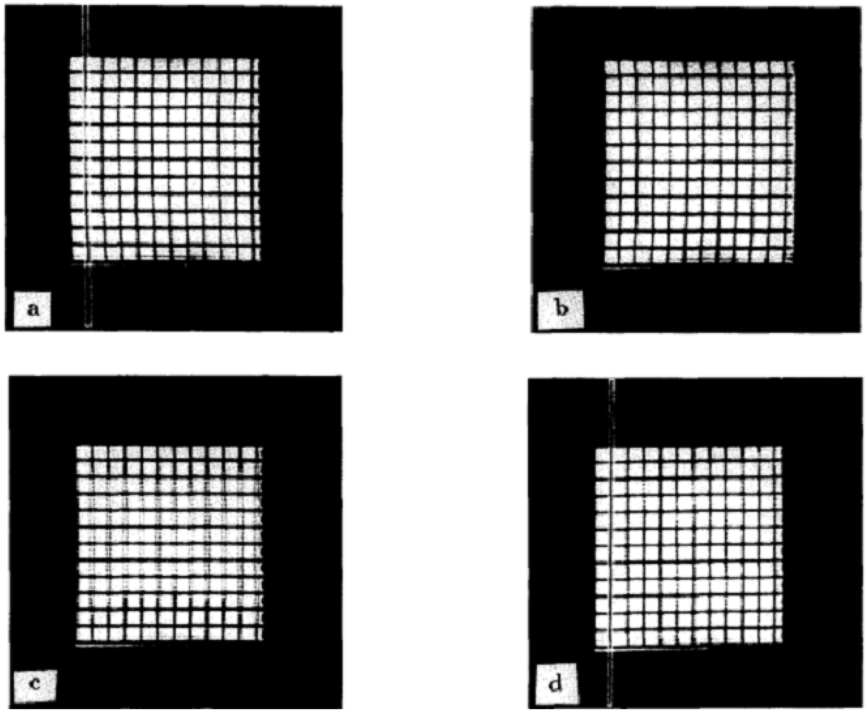

Figure 1.1 Grid phantom showing (a) image acquired with the readout gradient in the right to left direction; (b) image acquired with the readout gradient acquired left to right ; (c) the superimposition of the first two images and (d) the rectified image. Reproduced from (Chang et al. 1992).

Other publications describe the correction of gradient induced distortions using specially constructed phantoms (Doran et al. 2005; Schad et al. 1992). In the publication by Doran the methodology involves acquiring a distorted MR and undistorted CT images of a linearity test object of volume 440 × 270 × 360 mm^3. The corresponding marker positions are then identified in the two image sets. Using a finite number of discrete markers, distortion maps are produced giving distortion values at each voxel. Finally, these maps are used to perform a 3D correction of the MR datasets. The advantage of this technique is that through plane distortion can be quantified and corrected. At the edges of the phantom, however, where the through plane distortion is extreme, this method provided only partial correction, since some markers were distorted completely out of the image. Doran argues that this could be rectified by acquiring the data using a larger field of view. Actively shielded gradient designs are often employed in modern MRI systems to reduce gradient nonlinearity (Fransson et al. 2001).

Schad (Schad et al. 1992) used a water filled cylindrical phantom 17 cm in radius 10 cm in depth to measure two-dimensional (2D) geometric distortion. This phantom consisted of plastic rods spaced 2 cm apart. This 2D distortion was

corrected by modelling the distortion as a fourth order 2D polynomial. After performing 2D correction, a 3D distortion correction was performed using a 3D phantom. This phantom comprised of a grid of regular water filled boreholes, with oblique water filled boreholes in between. This produced datasets containing reference points (regular boreholes) and measurement points (oblique boreholes) from which the 3D position of the imaging plane was reconstructed. Through plane distortion was corrected by adjusting the gradient shimming current. While this technique corrected the image distortion to around 1 mm, it is a time consuming process requiring the manufacture and imaging of two phantoms. It also relies on a manual adjustment of the shimming gradients which would introduce subjective errors. Additionally, the shim correction required is likely to be different when imaging a phantom than when imaging a subject.

The use of 3D phantoms to measure and correct for geometric distortions has also been developed (Breeuwer et al. 2001; Wang et al. 2004a). Breeuwer's phantom contained 427 reference structures for the head phantom and 793 for the body phantom. The reference structures are automatically detected in the scanned images and a higher-order 3D polynomial distortion correction transformation is calculated. This transformation is then applied to the images to correct for the measured distortion. Using this phantom the distortion was corrected from a mean error of 2.08 mm and maximum error of 4.31 mm to a mean of 0.28 mm and a maximum of 1.05 mm. Wang's phantom contained 10,830 control points (see Figure 1.2). This phantom was an improvement on Breeuwer's phantom since instead of using point like objects for control points, which has limitations on the numbers that can be introduced, a set of three orthogonal points were employed. The positions of the control points are determined automatically using edge detection software of the interfacial boundaries formed between the surface of the grid sheet and the water. A trilinear interpolation was used to map the uncorrected pixels to their correct position. After correction this resulted in a mean error in the order of 0.1 mm and a maximum error of ~0.6 mm.

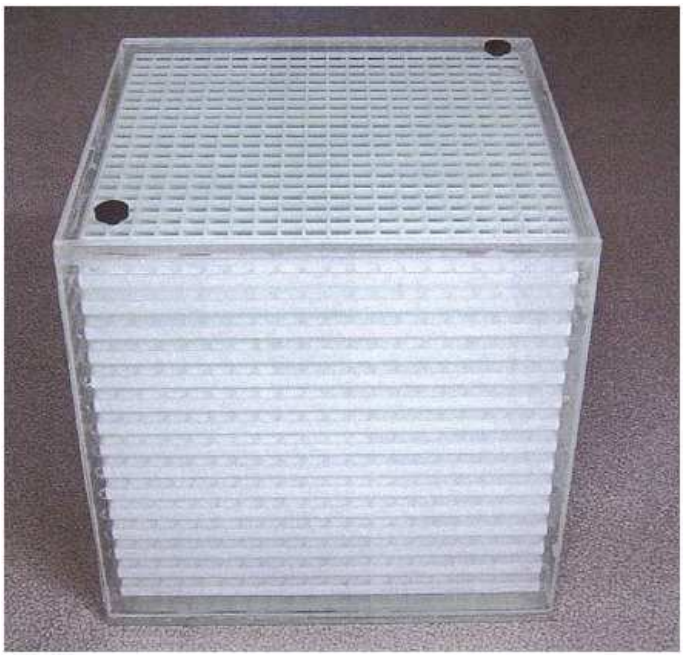

Figure 1.2 Image of a 3D phantom consisting of grid sheets aligned in parallel filled with water. Reproduced from (Wang et al. 2004a).

Patients with implanted metal objects (such as hip prostheses, dental amalgam, surgical pins etc.) demonstrate enhanced susceptibility distortions close to these objects. Imaging near metal with MRI results in image artefacts largely due to the inhomogeneous static magnetic field generated. This can result in signal loss due to dephasing, failure of fat suppression and displacement artefacts (Hargreaves et al. 2011). Close to metal objects the magnetic field variation can be very rapid. This leads to dephasing which manifests as signal loss. However, dephasing effects can be almost completely avoided by using spin-echo protocols. Advanced imaging techniques such as multi-acquisition variable-resonance image combination (MAVRIC) can correct in-plane and through-plane displacement artefacts from metal (Koch et al. 2009). MAVRIC limits the range of frequency offsets imaged at one time by using a frequency-selective excitation. By limiting the range of frequencies the in-plane displacement is also limited.

One publication has recorded a correction method taking into account both machine and object-related distortions for applications in RT planning (Moerland et al. 1995). The first step was to correct for machine related distortions which arise from gradient non-linearity and static magnetic field inhomogeneity. Error maps of a grid phantom of known dimensions were determined by varying the direction of the read-out gradient. 3D error maps were inferred by bicubic

interpolation and the required correction was applied to patient data. Correcting for chemical shift and susceptibility induced distortions was achieved by the Chang and Fitzpatrick technique (Chang et al. 1990). Using this method both machine and object related distortions can be corrected. A disadvantage of this technique is that it requires the additional step of generating field maps and applying a correction. This would make it more time consuming than the Chang and Fitzpatrick process, which already involves acquiring two image sets.

There are several publications which have investigated measuring distortion in MRI, using test objects of known geometry, (Wang et al. 2004a; Wang et al. 2004b) and have applied corrections as a result of these measurements (Doran et al. 2005; Reinsberg et al. 2005; Wang et al. 2004c). As well as in-house distortion corrections, manufacturers have developed 2D and 3D correction algorithms as part of their acquisition and evaluation software to improve the geometrical accuracy of MR images (Karger et al. 2006). Another approach is to correct for hardware related geometric distortions by acquiring a magnetic field map (Irarrazabal et al. 1996). This method involves acquiring a local field map, finding the best fit to a linear map and using it to correct the image distortions due to local frequency variations. The linear field map is calculated using a maximum likelihood estimator with weights proportional to pixel intensity.

Object-induced distortions are not accounted for by these procedures. Correction of susceptibility effects have been successfully applied using field mapping techniques (Weis et al. 1998). In this paper techniques that enable a correction of chemical shift effects have also been presented. Static magnetic field distributions are measured by a spectroscopic imaging technique based on a radiofrequency (RF) spoiled gradient echo sequence. Spectroscopic imaging is inherently robust against many artefacts because the magnetic field deviations are determined from the shift of voxel water or fat spectral lines. Therefore, effects that influence the amplitude but not the position of the spectral lines are not considered. These effects include spatial RF inhomogeneity, steady state effects, movement artefacts and flow artefacts. An automated geometrical interpolation corrects the distorted images. Since this technique is fully automated, it is not user dependent. However, while it is feasible that the magnetic field distribution measurement could be extended to 3D, this was not demonstrated in this paper.

Table 1.1 illustrates the results from publications in MRI geometric distortion correction. These results mainly demonstrate distortion correction for machine related errors such as magnetic field inhomogeneities and gradient nonlinearities. One of the publications in this table attempted to correct for both machine-related distortions (gradient non-linearity and static magnetic field inhomogeneities) and object-induced distortions (chemical shift and susceptibility distortions) (Moerland et al. 1995).

The two publication which demonstrated the greatest distortion correction (Doran et al. 2005; Wang et al. 2004a) recorded uncorrected distortion error value of 25 mm and greater than 9 mm being corrected to a mean error of 0.6 mm and an approximate error of 0.6 mm respectively. Both authors used large phantoms (for example Figure 1.2) to map the distortion errors and then interpolated the uncorrected pixel locations to the known corrected positions.

Table 1.1 Summary of results from MRI distortion correction publications

Paper	Field strength (T)	Study medium	Max error prior to correction (mm)	Max error post correction (mm)	Distortion correction technique
(Chang et al. 1990)	1.5	2-D grid immersed in water. Water filled centrifuge tube structure. Computer simulations.	Computer simulation : 20 pixels	Computer simulation: 1 pixel	Acquire two images with reversed slice selection & read-out gradients.
(Chang et al. 1992)	1.5	Grid in $CuSO_4$. Figure 1.1	5.8	1.2	Acquire two identical pulse sequences images with altered gradients.
(Sumanaweera et al. 1994)	1.5	Tissue phantom (hen in acrylic plastic box with $CuS0_4$ capillary tubes).	1.88	0.25	Magnetic field inhomogeneities were corrected using B_0 maps.

Paper	Field strength (T)	Study medium	Max error prior to correction (mm)	Max error post correction (mm)	Distortion correction technique
(Moerland et al. 1995)	1.5	Grid phantom. Fluid filled tubes on a localisation frame and cast for 10 patients with brain cancer	2 (chemical shift); 4 (static magnetic field); 3.5 (gradient non-linearities)	1.3	Grid phantom corrected machine errors by varying read-out gradient. Object errors were corrected using anatomical landmarks
(Irarrazabal et al. 1996)	Not stated	T2-weighted breath held spiral image of patient with liver metastases.	320 x 320 field of view	Visually inspected reduction in blurring	Acquire local field map to find best fit to linear map and use it to correct blurring due to frequency variation
(Breeuwer et al. 2001)	1.5	Spheres and rod spaces filled with $CuSO_4$ in a 260 mm diameter cylinder.	4.31	1.05	Interpolation of pixel values from distorted position to known values in 3D

Paper	Field strength (T)	Study medium	Max error prior to correction (mm)	Max error post correction (mm)	Distortion correction technique
(Wang et al. 2004a)	1.5	310 x 310 x 310 mm^3 phantom containing 10,830 control points Figure 1.2.	> 9.0	~ 0.6	Trilinear piecewise interpolation of pixel values from distorted control points to known corrected points in 3D
(Doran et al. 2005)	1.5	440 x 270 x 360 mm^3 phantom of 132 crossed fluid filled tubes.	25	Mean error 0.6 mm	Distortion maps were generated in 3D using 2 scans with opposing read gradient to allow for gradient nonlinearity and inhomogeneities in the main magnetic field. Interpolation corrected the image set.

Paper	Field strength (T)	Study medium	Max error prior to correction (mm)	Max error post correction (mm)	Distortion correction technique
(Karger et al. 2006)	3 and 1.5	A phantom of length 230 mm and diameter 230mm containing 5 cylindrical target points and 4 linear tubes.	5.8 (3T) 2.8 (1.5T)	1.2 (3T) 2.3 (1.5T)	Gradient nonlinearities are corrected in 3D using a manufacturer supplied correction algorithm.

1.2.5 Quality assurance program

Since the geometric properties of MR data are closely connected with the performance of hardware components, such as the magnet, gradient and RF systems, a QA program should be established to monitor the long-term system functionality. In this regard, the reproducibility of the MR data can be evaluated and deviations from acceptable limits can be identified early. Geometric distortion should be periodically tested as part of the regular QA program that is conducted on an MRI scanner (Firbank et al. 2000). As well as recommendations for image quality tests such as SNR, and image uniformity, Firbank's group proposes monthly geometric distortion measurements. The suggested method involves comparing the known diameter of a phantom with that measured using the distance measurement on the scanner console. The Eurospin TO2 phantom can also be used to measure plates of known dimensions. The mean length and coefficient of variation can then be calculated. At our centre we complete the QA tests recommended in IPEM Report 81 (IPEM 1999) which stipulates that geometric distortion checks should be performed on a weekly basis. The geometric distortion and linearity tests performed measure known distances of spaced Perspex rods in a phantom (see section 4.5.4 of Chapter 4).

1.3 Image Registration

1.3.1 Search strategy used and sources of information

Databases PubMed and SciVerse ScienceDirect were searched with no restrictions set on date range, document type or subject areas. The following search terms were used 'registration' and 'MR*' and 'radiotherapy'; 'registration' and 'MR*' and 'radiation'; 'image' and 'registration' and 'quality assurance'; 'fusion' and 'MRI' and radiation'; 'magnetic resonance' and 'treatment planning'; 'image' and 'registration' and 'radiation'.

1.3.2 Introduction

MRI and CT are being increasingly employed in the RT planning process. There are a number of advantages to incorporating MRI into RT. MRI offers superior soft-tissue contrast over CT allowing tumour and normal tissue to be distinguished more accurately. MRI has the ability to provide a range of image contrast specific to the anatomy and pathology being imaged, by varying the weighting of the sequence from T1-weighted and T2-weighted to proton density scans. Unlike CT, MR can image in any plane enabling a better assessment of tissue boundaries. Despite this, a large variability in delineations of the prostate, and in particular the seminal vesicles, was observed in a multi-centre trial with which this author participated (Nyholm et al. 2013). Metal artefacts such as dental amalgam or hip prostheses are localised in MRI often allowing accurate tumour delineation where it would not be possible using CT alone (Charnley et al. 2005). Better target delineation with MRI could lead to improved tumour control rates and reduced normal tissue complications (Tanaka et al. 2011). It may be possible to reduce the dose received by healthy tissue since margins will be more conformed to the "true" target volume. MRI can also provide physiological and biochemical information which may lead to improved treatment.

Image registration is the method of determining the geometric transformation required to relate the spatial coordinates of two imaging datasets. Registration of MRI to CT is an effective method of gaining both the improved target definition of MRI and the geometric accuracy and electron density of CT. However, although MRI provides improved soft tissue contrast, there are several

challenges with integrating MRI into the RT planning process. MRI is known to suffer from geometric distortion due to the non-linearity of the imaging gradients over large fields of view (Doran et al. 2005). This has largely been managed through the provision of in-plane distortion correction by most MRI vendors (Khoo et al. 2006). Due to the lengthy scan times of MRI, motion artefacts can diminish the image quality and alter the accuracy of target localisation. Today, advanced MR sequences can minimise motion related artefacts. Magnetic susceptibility can affect the main magnetic field homogeneity resulting in further localised distortion (Fransson et al. 2001; Schenck 1996) and so should be considered when outlining tumours close to, for example, the nasal cavities. Patient preparation must also be considered, since, for example, changes in bowel and bladder filling can adversely affect CT-MR registration (Brunt 2010).

When registering an MR scan to CT it can be expected that the MR will possess some degree of geometric distortion, will vary in slice angulation and coordinate origin position, that there are likely to be differences in slice number, thickness and spacing and that the image matrix size and pixel dimensions will not be the same. While it may not be possible to correspond all of these factors with a planning CT scan, it would be feasible to match the slice angulation, thickness and spacing of an MRI scan to that of a planning CT scan, if the MRI scan was undertaken as part of a RT planning protocol.

Various review articles exist on medical image registration (Balter et al. 2007; Brunt 2010; Crum et al. 2004; Hill et al. 2001; Maintz et al. 1998). Many of the papers in these review articles discuss the application of image registration to RT and most are concerned with rigid body transformations. Rigid body transformations shift the MR slices by rotation and translation to match the CT.

The following studies published investigate rigid registration accuracy (Li et al. 2008; Moore et al. 2004; Mutic et al. 2001; Veninga et al. 2004). In the study by Mutic, a QA method is presented to determine the accuracy of multimodality image registration. They used an anthropomorphic head phantom filled with water and containing CT, MR and PET visible targets. This phantom enabled the verification of the accuracy of the registration software by the correlation of anatomic landmarks. Moore et al. assessed the registration accuracy of their

treatment planning system by outlining structures on a registered phantom. Veninga's group validated a 3D fully automated registration procedure for RT planning of brain tumours. The normalised mutual information method was used for image registration. Registration accuracy was estimated by measuring the differences between CT and MRI anatomical landmarks. Finally, Li et al. examined a 3D volumetric image registration method. This technique aligns the images using anatomic structure volumes and surfaces.

A multi-centre study found that a registration accuracy of approximately 2 mm is achievable for cranial CT-MR image registration (Ulin et al. 2010). This study also showed that manual registration performed significantly better than automatic registration.

1.3.3 Patient Positioning

The feasibility of achieving accurate image registration is strongly reliant on the similarity of patient positioning across the modalities. Many publications detail the importance of patient positioning in MRI because of the effect it has on image registration (Ahmed et al. 2010; Brunt 2010; McJury et al. 2011; Prestwich et al. 2012; Webster et al. 2009).

One of the first patient positioning challenges that must be considered is the difference in the table top. CT planning scans are typically obtained using a flat table, whereas MRI scanners generally use a concave shaped table with padded patient support to maximise patient comfort because of the long scan times involved. MR scanner manufacturers are beginning to provide RT tables which are flat, contain integrated coils and are compatible with BDS base frames. It is also feasible to use flat table top inserts manufactured in-house (Brunt 2010; Hanvey et al. 2012; McJury et al. 2011).

Standard head coils are often used in the RT planning of patients with brain cancer. CT-MRI image registration is improved when the neck flexion is similar in both modalities (Brunt 2010). However, these head coils are usually not compatible with immobilisation beam directional shells (BDS) or stereotactic head frame. It has been shown that it is possible to image brain cancer patients, in the RT position within an immobilisation mask, without loss of image quality

over standard imaging methods using surface coils (Hanvey et al. 2009). An approximate image registration uncertainty of 2 mm occurs when registering CT image sets in the treatment position to a diagnostic MRI for patients with brain cancer (Kenneth et al. 2010) and this has led to RT centres routinely registering these scans for RT planning.

For patients with head and neck cancer consideration of the similarity of neck flexion between modalities becomes even more important to ensure accurate image registration. It is achievable to image this patient group within a BDS for MRI provided the BDS and base frame fit within the scanner bore (Webster et al. 2009). The base frame of some commonly used immobilisation masks can be wider than 60 cm which exceeds the bore size of many MR scanners. However, there is a trend among manufacturers towards MRI scanners with increased bore diameters, so this issue may be redundant in the near future.

While it could be anticipated that imaging patients with head and neck cancer in the treatment position would result in improved registration and target volume definition, there was no published evidence, prior to the work of this thesis, (Chapter 5 and (Hanvey et al. 2013)) to suggest that registering a planning CT scan with a diagnostic MRI provides results to the contrary. In addition, no other publications analysed the dosimetric consequences of patient positioning during MRI scan acquisition, for patients with head and neck cancer. This study contains a practical methodology for imaging head and neck patients within an immobilisation mask using laterally positioned surface coils.

Typically, pelvic patients are imaged in MRI using a diagnostic scanner. Therefore, patients would be positioned on a curved table with curved and padded imaging coils positioned posteriorly and another imaging coil positioned on the anterior surface of the patient. Pelvic patients undergoing a diagnostic MR would not be positioned in the same plane as their CT using patient positioning lasers. Bladder and bowel preparation is not regarded in the diagnostic MR process.

To improve CT-MR image registration when imaging the pelvis, the ideal patient set-up in MR is on a flat table with phased array surface coils positioned beneath the table and directly above on the anterior surface of the patient. Wall

mounted lasers must also be considered in MRI to ensure the patient is imaged in the same plane as their planning CT. Similarity of bowel and bladder filling should also be considered to aid in accurate image registration (Brunt 2010). Taking the prostate as an example, while it may be feasible to detect translations in the gland using image-guided RT, rotations are harder to detect, potentially resulting in significant underdosing when treatments with high dose gradients are employed (Litzenberg et al. 2011; Zaorsky et al. 2013).

By ensuring similarity of patient set-ups between modalities for RT, misalignments in registration, which can result in uncertainties in the location and magnitude of the GTV and thus the dose received by the patient, may be minimised (Hanvey et al. 2013; Hanvey et al. 2012). Patient positioning should also be considered when designing an MR simulator for radiotherapy planning using MR alone (section 1.4.3).

1.3.4 Manual rigid registration

Modern registration software typically provides manual registration methods. One of the earliest methods was to use fiducial markers, which are chosen to be reliable surrogates for anatomic or pathological structures. These fiducials can be externally positioned markers or implanted. Anatomical landmarks can also be chosen to perform manual image registration. While it may be possible to perform a registration with only three fiducials identified on both modalities, it is common to use at least seven to minimise the error from a misplaced point. This technique is discussed by (Hill et al. 1994) who registered 35 patients MR and CT datasets with errors of 1-2 mm. At the time of Hill's publication the most common method was to position fiducial markers to the skin surface as implanting markers is not always possible or desirable. Hill argued that the use of skin markers can lead to registration errors because of skin movement between images. MR distortions are pronounced at the patient outline due to both hardware and object related effects. This is because the static magnetic field inhomogeneity and gradient non-linearity increases with distance from isocentre and chemical shift and susceptibility artefacts are prominent at the patient outline (section 1.2.3).

Point-based registration requires the user to identify suitable points on the image sets being registered. The algorithm performs the translation by aligning the centroids of the identified points and the rotation uses a method to minimise the sum of the squares of the distance between corresponding registration points (Hill et al. 1994).

Line or surface matching techniques can also be applied. For this technique a strict one to one correspondence of specific points is not required, instead the method attempts to maximise the overlap between corresponding lines and surfaces from the two images by an iterative process (Balter et al. 2007). These structures can be obtained using automatic segmentation algorithms with minor editing. As with defining pairs of points this may be time consuming to accurately delineate corresponding lines and surfaces in both image sets.

The interactive manual registration method enables the user to apply shift and rotations to the MR to overlay this accurately with the CT. Anatomical landmarks should then be checked for accuracy of registration. This is discussed in more detail in the next section.

1.3.5 Automated rigid registration

Today, commercial software provides automatic registration, which reduces the necessity for user interaction with the registration process. All the major RT treatment planning software manufacturers provide automatic registration as standard. One such automatic technique utilises implanted fiducial markers which are identified in CT and cone-beam CT image sets for prostate patients (Koch 2008). Another group used fiducial stereotactic markers for registering MR to CT images in a phantom and patient study (Kremser et al. 1997).

Mutual information algorithms are among the most successful in use today (Veniga et al. 2004) and it was this technique that is employed in the studies described in Chapter 5 and 6 with the treatment planning system Eclipse (Varian Medical Systems, Inc. CA, USA). The mutual information procedure is based on information theory and calculates the required 3D transformation by maximising the amount of information that is common between two datasets. This technique eliminates the requirement to identify equivalent structures on

corresponding image sets, which can be manually intensive (Balter et al. 2007). When the two datasets are properly registered the mutual information of the pair of images is at a maximum. This technique is useful since it does not depend on the absolute intensity values and is robust to missing or limited data. Over the tumour volume the mutual information is low, but this does not incur a great penalty since the mutual information will be high in the surrounding tissue and so this becomes the dominant factor in the registration (Kessler 2006).

Most registration software enables the user to define the volume within which the automated method will operate. This enables regions where the registration may contain significant errors, but are irrelevant to treatment, to be disregarded (Jonsson et al. 2011).

Rigid body registration is most useful in registering anatomy which is either bone or encased in bone. The head, and in particular the brain, is the most commonly registered structure for this reason. While rigid registration is used for structures outside the head (e.g. the pelvis, neck or spine) the errors are expected to be larger (Hill et al. 2001).

While automated image registration is useful in eliminating the observer dependent interaction, manual adjustment may still be required based on visual verification using anatomical and physiological knowledge (Li et al. 2005; Sarkar et al. 2005).

1.3.6 Affine registration

When a registration includes scaling and shearing, as well as rigid body transformations, it is referred to as affine. This type of transformation can be described in matrix form and all parallel lines are preserved. A rigid registration can be considered to be a special type of affine, whereby the scaling value are unity and skews are zero.

The use of affine registration does not provide a great advantage over rigid registration since organs do not typically stretch or shear, but rather deform in a more complicated manner. However, geometric distortion can result in scaling

and skewing of the image sets which may be represented by an affine transformation (Hill et al. 2001; Maintz et al. 1998).

1.3.7 Deformable registration

Rigid body registration is only applicable when organ motion during MR and CT examinations can be disregarded. If the patient's weight changes between examinations or if there are changes in anatomy (for example, weight loss due to therapy) then rigid registration is unable to take this into account. In deformable registration correspondence between structures in two images cannot be achieved without some localised warping of the images.

Deformable registration continues to be an active area of research, but has largely been unused clinically in RT centres. One of the reasons why deformable registration has not been adopted is because it is difficult to validate its reliability, although there have been developments in this area (Brock 2010; Varadhan et al. 2013). While rigid registration generally involves 6 degrees of freedom (translation and rotation), deformable registration involves a deformation field of vectors, indicating the association between each voxel in the first image and each corresponding voxel in the second (Sarrut 2006).

Differences in images that require deformable registration can occur due to several reasons: changes in patient anatomy (intra-subject registration), images from different modalities (multimodality registration), images from different patients (inter-subject registration) and dynamic motion, such as breathing (intra-fraction motion).

Deformable registration algorithms involve the combination of several components: a feature space, a similarity measure, a transformation model (which specifies the way in which the source image can be changed to match the target) and an optimisation algorithm (Sarrut 2006). The optimisation process varies the parameters of the transformation model to maximise the matching criterion (Crum et al. 2004). Registration based on patient image content can be divided into either feature-based or intensity-based methods. Feature-based methods use landmark points (Li et al. 2003), organ contours (Schaly et al. 2004), or segmented surfaces.

Intensity-based methods match intensity patterns over the whole image and have the advantage of being almost entirely automatic; however, they are affected by image artefacts. This algorithm works by increasing the intensity similarity between the two images.

One of the most important families of transformation models used in deformable registration is the spline-based registration algorithms. This group of algorithms use control points in both image sets and a spline function to relate the correspondences outside of these points. For the B-splines algorithms a perturbation in an individual control point affects the transformation only within the vicinity of the point. B-spline deformable registrations are popular due to their computational efficiency and applicability (Crum et al. 2004).

It may be necessary with deformable registration to impose some form of regularisation to prohibit unreasonable deformations such as the warping of bones or the folding of tissue. This problem can be dealt with by including a regularisation term that penalises non-physical deformations using known or estimated tissue properties (Ruan et al. 2006).

1.3.8 Validating registration accuracy

Registration accuracy assessment is important when performing image registration for RT. It is desirable to know the expected accuracy of a technique and the registration accuracy achieved on an individual set of images. With landmark registration, the associated error is inherent in the registration process and an average registration error for the entire volume can be estimated (Fitzpatrick et al. 2001). For other registration methods, such as intensity-based methods, the algorithms do not provide a measure of accuracy as the image similarity measure is not related to error in a way which can be described simply. Validation of the quality of registration may also be completed by making additional measurements on landmarks or regions post-registration. Visual assessment by a trained user is generally the best method for ensuring acceptable accuracy prior to using registered images in RT.

The purpose of quantifying registration accuracy is to determine whether an algorithm is accurate enough for a particular clinical application or to compare

one algorithm with another. It is also useful to ascertain whether the registration accuracy of a particular subject is satisfactory prior to being used clinically.

The accuracy of a registration transformation cannot be measured by a single number since it varies spatially across the image. It is possible to use fiducial markers to determine the error in a registration. However, fiducials are not generally located at positions of interest, and so do not always give a true reflection of the registration accuracy. In most instances, the only practical means of estimating the registration accuracy is to visually assess the images. An observer investigates the registered images and using tools such as colour overlay or split views determines whether the registration is within the required accuracy. Split screen or chequerboard displays should be visualised in the axial, coronal and sagittal views to aid assessment (Kessler 2006). Visual assessment of image registration has been investigated and was found to perform well at errors of 2 mm and greater (Fitzpatrick et al. 1998).

Other groups (Hanvey et al. 2013; Hanvey et al. 2012; Veninga et al. 2004) used discrepancy in coordinate locations of anatomical landmarks in CT and MRI to determine registration accuracy. In addition the Dice coefficient has been used to determine the spatial overlap of these landmarks.

Different techniques have been suggested for validating deformable registration algorithms, such as computer modelling and a deformable phantom (Brock 2010; Kashani et al. 2008; Kaus et al. 2007; Zhong et al. 2010). Another publication (Varadhan et al. 2013) used commercial software, ImSimQA (Oncology Systems Limited, Shrewsbury, UK) to assess deformable registration quality by simulating organ deformations in image sets.

1.3.9 Image registration quality assurance

When using the fiducial point method of image registration, information on the quality of registration is inherently available. For automated registration, anatomical landmarks can be used to check for errors. Landmarks are defined for a corresponding set of anatomic points on both datasets and the distances between the location of the points on the fixed image set and the transformed

locations of the points in the second image set are computed. It may be challenging to accurately define corresponding landmarks, especially when registering multimodality data. If there has been a significant time interval between imaging morphological changes may have occurred which could result in inaccuracies in registration. The choice of landmarks should be widely spaced around the imaged anatomy.

It is possible to use test objects to determine the quality of registration, however, these do not present the same challenges to the registration software as patients. An alternative method is to use software generated DICOM image set and computationally apply known shifts, rotations or scaling. This data can be exported to the registration software and then re-imported to a software package for quantifiable analysis (OSL 2012; Varadhan et al. 2013). Pseudo-anthropomorphic and anthropomorphic physical test objects have been investigated for registration quality assurance (QA) (Kashani et al. 2007; Moore et al. 2004; Mutic et al. 2001; Shmueli et al. 2007). Serial acquisitions of 3D image series also require image registration QA (Sharpe et al. 2008).

1.4 MRI in Radiotherapy

1.4.1 Search strategy used and sources of information

Databases PubMed and SciVerse were searched with no restrictions set on date range, document type or subject areas. The following search terms were used ‘MRI’ and ‘radiotherapy’; ‘MRI’ and ‘radiotherapy’ and ‘planning’; ‘MRI’ and ‘radiation’; ‘MRI’ ‘radiotherapy’ and ‘quality assurance’; ‘magnetic resonance’ and ‘treatment planning’.

For the MRI only RT planning and integrated MRI linear accelerator sections of this chapter (sections 1.4.3 and 1.4.4) the following search terms were employed ‘magnetic resonance imaging’ (or ‘magnetic’ and ‘resonance’ and imaging’ or ‘MRI’) and ‘only’ and ‘radiotherapy’; ‘magnetic resonance imaging’ (or ‘magnetic’ and ‘resonance’ and imaging’ or ‘MRI’) and ‘radiotherapy’ and ‘linear’ and ‘accelerator’.

For the functional section of this chapter (section 1.4.5) the following search terms were included ‘magnetic resonance imaging’ (or ‘magnetic’ and ‘resonance’ and imaging’ or ‘MRI’) and ‘radiotherapy’ and ‘diffusion weighted imaging’ (or ‘DWI’); ‘magnetic resonance imaging’ (or ‘magnetic’ and ‘resonance’ and imaging’ or ‘MRI’) and ‘radiotherapy’ and ‘dynamic contrast enhanced’ (or ‘DCE’); ‘magnetic resonance imaging’ (or ‘magnetic’ and ‘resonance’ and imaging’ or ‘MRI’) and ‘radiotherapy’ and ‘spectroscopy’ (or ‘MRS’).

1.4.2 Tumour delineation with MRI

The increased use of RT planning techniques with steep dose gradients, such as intensity modulated radiotherapy (IMRT) and volumetric modulated arc therapy (VMAT), necessitates improved target volume definition. MRI offers improved soft tissue contrast and visualisation of the tumour extent enabling the delineation of more accurate target volumes (Khoo 2000). Tumours often possess similar electron densities to the surrounding soft tissue making it difficult to distinguish using CT unless there is a fat, air or bone interface between these structures. With MRI, however, there is the capacity to manipulate the imaging parameters allowing discrimination between the extent of the tumour and its boundaries of infiltration and the adjoining healthy tissue.

Another benefit to more accurate target volume delineation is the increased reliability and consistency of tumour definition. This improves both the inter-observer and intra-observer variability which is important in multi-centre trials (Khoo et al. 2006).

A further consideration to incorporating MRI into the RT planning process is that Oncologists have undergone suitable training and that there is close collaboration with MR Radiologists (Sundar et al. 2002).

MRI has been used extensively in the treatment of brain tumours with RT. Changes in the target volume have been shown at this site by including MRI into the planning process (Khoo et al. 2000; Prabhakara et al. 2007). In one publication, MRI was able to improve tumour delineation at the base of skull where X-ray attenuation at this site can obscure soft tissue using CT alone (Khoo

et al. 2000). However, CT gave additional information on the extent of bony erosion from tumour that was not available with MRI, therefore despite the many advantages of MRI over CT there are occasions when CT provides complimentary information to MRI.

Head and neck tumour delineation can also benefit from the addition of MRI in RT planning (Ahmed et al. 2010; Chung et al. 2004; Emami et al. 2003; Newbold et al. 2006). MRI has the advantage of reduced artefacts from dental amalgam, which can be particularly problematic in CT imaging, making it the imaging modality of choice for soft tissue oropharyngeal cancers (ENT UK 2011).

Changes in anatomical and tumour definition using MRI data instead of CT have also been reported in the pelvis and, in particular, the prostate (Charnley, et al. 2005; Khoo et al. 2006; Rasch et al. 1999; Sannazzari et al. 2002; Sefrova et al. 2012; Smith et al. 2007). One of the main advantages of using MRI in the pelvis is the potential to provide superior target volume delineation over CT due to the reduced interference from prosthetic hips or gold seed implants which are commonly used in image guided prostatic RT.

1.4.3 RT planning using MRI alone

MRI is the imaging modality of choice for many tumours, but the lack of electron density information and potential for geometric inaccuracy, has resulted in MRI most commonly being implemented in conjunction with CT images via image registration. Therefore, if MR images alone are to be used for RT planning any image distortion must be measured and corrected if necessary and the electron density information must be assigned to the MRI dataset. Issues related to patient set-up must also be overcome if MRI only simulation is to be a viable treatment option.

There are three main advantages with MRI only RT planning. Firstly, the image registration procedure introduces a systematic error, which can potentially compromise tumour control probability. Secondly, there is the advantage of the reduced imaging costs (Beavis et al. 1998), which will also ease patient discomfort related to multiple scans. The increased RT planning time required for organ segmentation on the MRI to assign electron density information must

be considered in this cost evaluation. It is likely that auto-segmentation tools will play a greater role in the near future and will facilitate a reduction in the time required to assign bulk density to MR data. Thirdly, by removing the CT there is a reduced dose burden on the patient. However, it could be argued that this advantage is negated by the much large doses associated with RT.

Intracranial

One of the first anatomical sites to be investigated using MRI alone for RT planning was the brain. It has been shown that the geometric distortion was less than 2 mm over a range of 24 cm and so no further distortion correction was deemed necessary (Beavis et al. 1998). One publication performed an in-house distortion correction and assigned bulk electron density values to the brain, bone and scalp to obtain good agreement in isodose distribution, dose-volume histograms and tumour-control probability based procedure. Another study found distortion errors of less than 1.5 mm within radial distances of 12 cm (Kristensen et al. 2008). This group recommended that MRI bone segmentation should be performed when using beam energies of 4 MV to avoid deviations in dose larger than 2% compared to CT.

Prostate

There have also been many publications of MRI only RT planning investigating the prostate. An absolute dose agreement of 2% was found between CT-based and MR-based prostate RT plans with bulk density assigned datasets (Chen et al. 2004; Lee et al. 2003). One publication found that MRI only RT planning of the prostate using bulk electron density for the bone and tissue resulted in an average dose error of 1.3% from CT planning (Lambert et al. 2011). If uniform density MRI based planning is performed this error increased to 2.6%. This group attributed the dose errors to the differences in the patient external contours introduced by changes in the patient set-up between modalities. Another group delineated the external patient contour, the femur, femoral heads and hipbone on the MRI only RT plans and found that the mean number of monitor units required to reach the prescribed dose was within 0.2% of CT based RT plans (Jonsson et al. 2010).

Relevant bony structures can be delineated to create MRI-derived digitally reconstructed radiographs (DRRs) for patient set-up. In one publication, deviations between CT and MRI-derived DRRs were measured across the image sets and the maximum difference observed was 3 mm (Chen et al. 2007). Another group compared the spatial uncertainties associated with an MRI-based workflow for external RT of patients with prostate cancer to a standard CT-based workflow (Nyholm et al. 2009). In this study, patients were set-up for treatment at the MRI scanner and transported to the treatment unit in the same position. The MRI-based methodology resulted in spatial uncertainties of 2-3 mm versus 3-4 mm with the CT-based workflow. The main reason for this improvement was credited to the exclusion of the CT-MR registration in the planning phase.

A recent publication demonstrated a method to convert MRI intensity values to Hounsfield units (HU) for the pelvic bones. By manually segmenting the bones of the pelvis these authors showed the mean prediction error of the conversion model was 135 HU. This method creates pseudo-CT data which can be used for dose calculation and to generate DRRs (Kapanen et al. 2012).

1.4.4 Integrated MRI and Linear Accelerator or ^{60}Co source

Currently, several groups are investigating the integration of a megavoltage radiation therapy source with MRI to allow real-time adaptive RT. Researchers have proposed merging a ^{60}Co source or a linac with an MRI system (also known as an MRI-linac).

The group at the University Medical Center Utrecht has built a prototype hybrid MRI-linac by adapting a 1.5T closed bore MRI scanner and a single energy (6MV) linac (Figure 1.3). Their design uses active magnetic shielding to create a zero magnetic field at the location of the gun of the accelerator and to minimise the magnetic field along the accelerator tube. By magnetically decoupling the linac and the MRI system they are able to minimise the accelerator induced geometric distortions in the MR images (Lagendijk et al. 2008). Two RF cages are placed at both sides of the MRI bore. Thus, the inner wall of the MRI cryostat is part of the RF cage, and the MRI is RF shielded from the rest of the room, including the accelerator (Raaymakers et al. 2009).

(a)

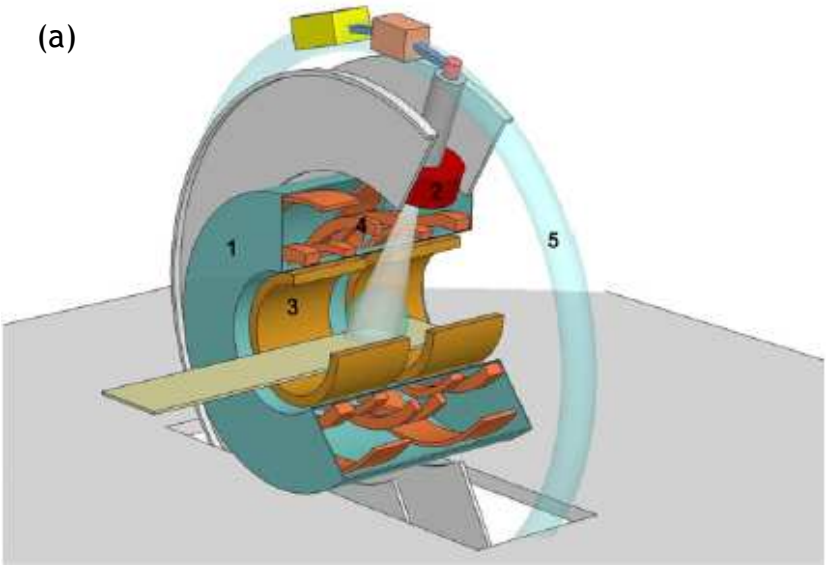

(b)

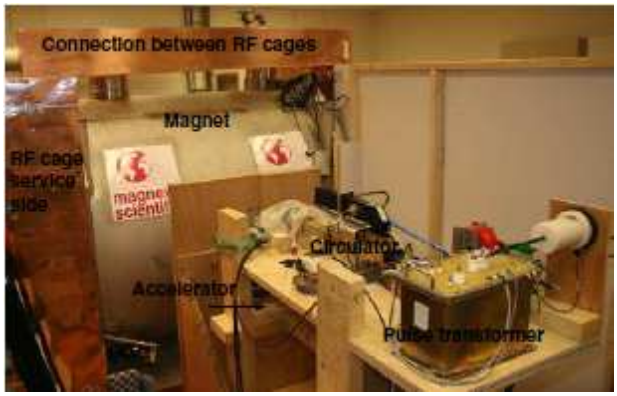

Figure 1.3 (a) Diagram of the integrated MRI linear accelerator (MRI-linac) concept, where (1) is the 1.5T MRI scanner, (2) is the 6 MV accelerator in a ring around the MRI scanner, (3) is the split gradient coil. (4) are the superconducting coils, (5) is the low magnetic field toroid in the fringe field around the MRI scanner. (b) A photograph of the prototype MRI-linac showing the accelerator on a wooden stand with the MRI situated behind it and the copper RF cage of the MRI is visible. Reproduced from (Raaymakers et al. 2009).

Since a closed bore MRI system is used this requires transmission of the radiation beam through the MRI. To accomplish this beam transmission the group have put aside the superconducting coils and have split the gradient coil to allow a non-distorted beam passage. Stripline technology is used to minimise the thickness of the RF coils thereby reducing radiation absorption. To overcome the RF interference between the linac and the MRI, the researchers synchronised the MRI RF acquisition and the accelerator pulses to give intermittent imaging and irradiation on a millisecond scale. This enables intrafraction imaging with the beam on (Lagendijk et al. 2008).

The researchers have also considered the dose distribution in the MRI-linac. The scatter induced by the beam transmitting through the MRI components has been determined by Monte Carlo simulations. The impact of the Lorentz force on secondary electrons due to the presence of the 1.5T field has also been investigated using Monte Carlo simulations. This has been shown to result in a decreased build-up distance and a shifted and asymmetrical penumbra (Raaymakers et al. 2004). In addition, at tissue-air interfaces, the Lorentz force can cause electrons to re-enter the tissue, however, this effect can be reduced by using opposing beams (Raaijmakers et al. 2005).

One of the most recent developments from this group has been gated radiation delivery where the gating signal is derived from on-line MR imaging (Crijns et al. 2011), which enables treatment where respiration induced target motion exists. This study demonstrates its capability using a phantom with a one-dimensional (1D) periodic motion. The phantom's position is established using fast 1D MR imaging and the radiation delivered is gated based on this signal.

Another prototype MRI-linac design uses a 6MV linac but directs the beam through the opening of a biplanar 0.2T permanent magnet system. The linac, magnet structure and gradient coils rotate in unison about a single axis. A conventional Faraday cage surrounds the magnet to prevent RF interferences (Fallone et al. 2009). The rotation of the magnet around a patient would introduce magnetic susceptibility related distortion. At 0.2T, this distortion was shown to be less than 0.5 mm given an encoding gradient strength of 5mT/m or higher (Wachowicz et al. 2010).

The effect of radiation induced currents in the RF coils caused by pulsed irradiation has been investigated. It was shown that by using a teflon and copper build up material radiation induced currents can be reduced by up to 60% (Burke et al. 2012). It has also been demonstrated that the RF noise from the motors of the multi-leaf collimators (MLC) can be effectively shielded to avoid signal-to-noise degradation (Lamey et al. 2010).

1.4.5 Functional MRI in RT

Diffusion-weighted imaging

Diffusion-weighted imaging (DWI) is a functional MRI technique that gives information on the microscopic motion of water molecules. The degree of restriction of water diffusion is related to the integrity of cell membranes. Cancerous tissue tends to have more restricted diffusion due to an increase in cellularity. DWI is performed by applying two opposing field gradients around the refocusing pulse. Water molecules are dephased by the first gradient and rephased by the second. If the water molecules move between the opposing gradients this will result in dephasing which is seen as signal loss. The strength and duration of the applied gradients is expressed by the b-value. By repeating the DWI sequence with different b-values the apparent diffusion coefficient (ADC) value is computed. The ADC provides an assessment of the velocity and distance a water molecule has moved during the DWI sequence.

Evaluation of tumour response during RT opens up the possibility to adaptive RT such as changing the target volume or dose escalation to nonresponding tumour subvolumes.

One study investigated the feasibility of using DWI as a measure of treatment response in patients receiving RT for prostate cancer. This study showed a significant increase in the mean ADC of tumours before treatment and after 1 week of therapy. This type of information may in the future enable changes to treatment during the course of RT (Park et al. 2011).

In head and neck cancer, a significant difference in ADC-values has been measured between responding and non-responding tumours 1 week after the start of RT (Kim et al. 2009).

Dynamic contrast enhanced MRI

Dynamic contrast-enhanced MRI (DCE-MRI) involves the acquisition of images before during and after the injection of a contrast agent. A rapid series of T1-weighted images are acquired to observe the passage of the contrast media

intravascularly and as it leaks into the extravascular extracellular space (EES). For quantitative analysis of DCE-MRI data it is necessary to know the arterial input function (AIF). The AIF is the rate of arrival of contrast medium at a tissue.

With quantitative analysis DCE-MRI can provide information related to tissue blood volume, perfusion and permeability. The most widely used method of measuring vessel permeability changes is based on the Tofts two-compartment model. In this model the contrast agent leaks into the EES and the tissue perfusion and permeability can be assessed from the wash-in and wash-out phases of the signal intensity-time curves.

Using compartmental modelling, DCE-MRI can be used to generate quantitative parameters which reflect tumour vascularity. These parameters include: K^{trans}, which describes the forward leakage rate of the contrast medium, the fractional EEP (v_e), the wash out rate (k_{ep}) and the plasma volume fraction (v_p) (Li et al. 2012).

A recent study found that a pre-treatment DCE-MRI can be used to predict the outcome in head and neck squamous cell carcinoma patients undergoing chemoradiotherapy. This study showed that the skewness of K^{trans} was a predictor of outcome in these patients (Shukla-Dave et al. 2012).

Another group showed a significant difference between the benign peripheral zone and tumour for the parameters K^{trans}, v_e and k_{ep} in patients with prostate cancer. They also demonstrated that DCE-MRI was more sensitive than T2-weighted images for prostate cancer localisation (Jackson et al. 2009).

Proton MR spectroscopy

The metabolite composition of tissue can be uncovered using in-vivo spectroscopy. This technique uses gradients to selectively excite a voxel of tissue, then record the free induction decay to produce a spectrum. Proton MR spectroscopy (^{1}H-MRS) is employed most widely in the clinical setting. Metabolites appear as peaks in the spectrum and the area under each peak is a measured of the relative number of protons in the metabolites environment.

One of the metabolites commonly used in tumour localisation is choline (Cho), since elevated levels of Cho-containing compounds in tumours is believed to reflect membrane synthesis and therefore, indirectly, elevated cell proliferation rate (Aboagye et al. 1999). In the brain, n-acetyl aspartate (NAA) indicates neuronal integrity and is reduced if neurons are being destroyed by a disease process.

In general, low-grade lesion and meningiomas show reduced NAA and elevated Cho and this becomes more prominent with increasingly malignant disease. A correlation has been shown between the NAA and Cho levels and the tumour grading (McRobbie et al. 2003).

A significant positive correlation has been shown, in patients with head and neck cancer, between Cho relative to water (Cho/W) and the total lesion glycolysis using ^{18}F-labelled fluorodeoxyglucose positron emission tomography (FDG-PET). This result implies that increased glucose metabolism is related to increased cellular proliferation.

In the same study, a significant negative correlation was observed between Cho/W and the standard deviation of K_{ep} and between Cho/W and the standard deviation of v_e. The standard deviation describes the width of the distribution and is indicative of the heterogeneity of the tumour. These results suggest that heterogeneous head and neck tumours contain regions of low proliferation and are highly necrotic which is demonstrated by significantly lower Cho concentrations.

The significance of the correlation between ^{1}H-MRS, DCE-MRI and FDG-PET to RT, is that it could be used in treatment planning, in the prediction of short-term treatment response or outcome, and in monitoring treatment (Jansen et al. 2012).

Using receiver operating characteristic (ROC) curves to assess the diagnostic performance of imaging, another group assessed the use of MRI parameters (including ^{1}H-MRS) for the detection of locally recurrent prostate cancer after external beam RT. By comparing the MRI data with a transrectal ultrasound biopsy, this study demonstrated that the area under the ROC curve for T2-

weighted imaging was 61.6% (95% confidence interval [CI] = 51.1-73.2), for DWI it was 75.5% (95% CI = 61.0-85.3) and for ^{1}H-MRS it was 83% (95% CI = 75.5-89.1). Combining ^{1}H-MRS with and DWI data resulted in significantly improved accuracy (86.3%; 95% CI = 77.5-93.3) than DWI alone. However, the area under the ROC curve for T2-weighted imaging did not change significantly from when combined with ^{1}H-MRS data. The combination of all three parameters gave the best results with the area under the ROC equal to 86.9% (95% CI = 77.6-93.4), although this was not a significant improvement over ^{1}H-MRS alone (Westphalen et al. 2012).

It has also been shown that spectroscopic imaging can offer a solution to the geometric deficiencies of MRI. The use of spectroscopy for geometric distortion correction has typically been unachievable due to the length of scan times. It is hoped that by using recent developments to reduce scan time, such as parallel imaging and compressed sensing, this may soon be a practical solution (Bakker et al. 2012).

1.5 Overview of chapters

The remaining chapters of this thesis are organised as follows:

The principles of radiotherapy planning and magnetic resonance imaging

Chapter 2 begins with an overview of the RT workflow employed at the Beatson West of Scotland Cancer Centre. The RT planning techniques IMRT and VMAT are described. Following this, the fundamental principles underlying MRI are explained. This includes the effect on spins within a magnetic field, the use of magnetic field gradients and the process of image reconstruction. Pulse sequence diagrams relevant to this thesis are also described.

Evaluation of an inline three-dimensional MRI geometric distortion correction algorithm for radiotherapy

Chapter 3 describes a study evaluating a 3D distortion correction algorithm for MRI. This study compares the 3D distortion correction algorithm with the standard 2D distortion correction algorithm. Various test object were used, including the TO3 Eurospin phantom (Diagnostic Sonar Ltd., Livingston, UK), the

MagNet (MagNET, London, UK) slice position phantom and a bespoke phantom constructed from LEGO® bricks. The purpose of this study was to investigate the accuracy of an inline 3D distortion correction algorithm and to determine a safe scanning range for RT planning.

Patient immobilisation in MRI

In Chapter 4 the benefits and problems of incorporating patient immobilisation in MRI for RT planning are discussed. Since it was known that future experiments were going to involve orientating patients in the RT position within the MRI scanner, a test object study was conducted to determine whether similar image quality could be achieved in the RT position. For the first time, quality assurance MRI phantoms were used to assess the image quality of different image coils which could be used to scan patients in the RT position within an immobilisation mask. The following tests were performed: normalised signal to noise ratio; resolution; fractional uniformity; geometric linearity and distortion; multiple slice position error; slice width and contrast to noise. Amongst the image coils tested was the 4-channel cardiac coil which was used for the clinical experiments in later chapters.

The influence of the MRI scan position on patients with prostatic cancer undergoing radiotherapy

Chapter 5 explores the effect of MRI scan position in patients with prostate cancer. In this experiment three patient position protocols are compared for twenty patients with prostate cancer: a CT scan with a diagnostic MRI scan viewed on a separate console, a CT scan registered with a diagnostic MRI scan and a CT registered with an MRI in the RT position. To scan patients in the RT position a surface coil was positioned beneath a Perspex plate to give a flat surface and an in-room laser positioning device was used to align the patients in the same way as their CT. The target volume was delineated by a Consultant Clinical Oncologist using all three patient position protocols with a week between outlining on the same patient. Delineations were made on three rigid landmarks: the femoral heads and the symphysis pubis to determine the CT-MRI registration quality. Changes in the target volume were compared for the different protocols. Finally, the effect on the quality of the RT plan for the CT

registered to the RT positioned MRI, which was the presumed gold standard, was compared with the other two patient set-ups. This was achieved by generating RT plans for the target volume of the CT registered to the MRI in the RT position while investigating the dose received by the other two target volumes. This is the first time this study had been investigated in the literature.

The influence of the MRI scan position on patients with oropharyngeal cancer undergoing radiotherapy

A similar experiment to the previous chapter was conducted for patients with oropharyngeal cancer in Chapter 6. As with the prostate study three patient position protocols were used: a CT scan with a diagnostic MRI scan viewed on a separate console, a CT scan registered with a diagnostic MRI scan and a CT registered with an MRI in the RT position within an immobilisation mask. Changes in the target volume and quality of registration were again examined. Optimising the RT plan for the presumed gold standard of the CT registered with the MRI scan in the RT position, the dose to the target volumes for the other two set-ups was investigated. This work had not been investigated prior to being described in this thesis.

Final conclusions

Chapter 7 is the final chapter and summarises the original contributions of this thesis to the field of MRI within RT as well as the limitations of the studies. Future work following on from this thesis is discussed.

2 The principles of radiotherapy planning and magnetic resonance imaging

2.1 Introduction

The following chapter describes the radiotherapy (RT) workflow for the treatment of patients with prostate and head and neck cancer at the Beatson West of Scotland Cancer Centre (Beatson). The principles of RT planning and planning algorithms are described. Intensity modulated radiotherapy (IMRT) and volumetric modulated arc therapy (VMAT) planning methods are considered, since these techniques are applied in the two clinical studies of Chapters 5 and 6 respectively. Finally, the fundamentals underlying image formation in magnetic resonance imaging (MRI) are described in this chapter, including pulse sequences employed in this thesis.

2.2 Radiotherapy workflow

The RT process workflow is the path a patient and their scan information follow when the decision to treat with RT is taken. The following workflow diagram (Figure 2.1) outlines this process from the point of booking to treatment.

From Figure 2.1 it can be seen that the patient is fitted for a custom immobilisation mask prior to receiving a computed tomography (CT) scan at the CT simulator. Immobilisation masks are made using thermoplastic sheets which, after placing in warm water, become pliable and are positioned over the patients head and shoulders (see Figure 6.2, Chapter 6). These masks are then moulded to the patient's contours and adhered to locking devices that are used daily to lock the mask in place. Immobilisation devices ensure reproducible patient positioning between simulation and subsequent treatments. It also prevents patient movement during treatment (Levitt et al. 2008). The purpose of the CT scan is to enable target volumes and critical structures to be outlined on the CT axial images within the RT planning software. The dose received by the patient can then be modelled using the RT planning software and virtual simulation can be performed three-dimensionally (3D). Additionally, the CT information can be used to display any beam's eye view on a digitally reconstructed radiograph (DRR). A DRR is a ray-line reconstruction through a 3D

volumetric CT dataset. The DRR is equivalent to a conventional radiograph using a virtual source and the geometry of the planned RT beam (Sherouse et al. 1990). The introduction of DRRs significantly improved the accuracy of field placements and enabled shielding to be designed with more accurate conformity to the target.

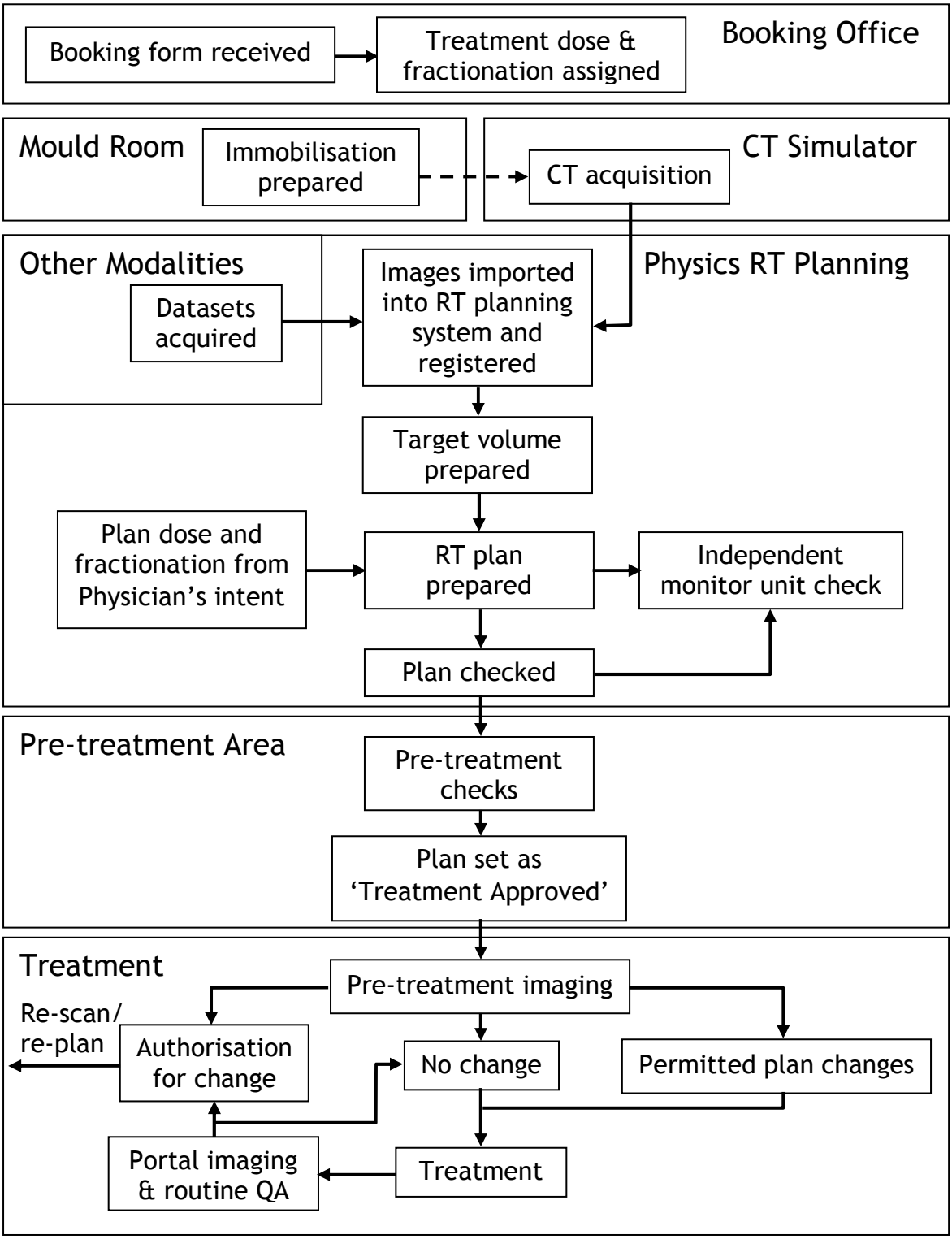

Figure 2.1 Radiotherapy workflow diagram at the Beatson.

The CT images are then imported into the RT planning system along with any other additional datasets, such as MR images. The MRI may be registered to the CT for the purposes of aiding in target definition. For more information on image registration please refer to Chapter 1, Section 1.3.

Once all target volumes and critical structures have been outlined, RT planning in accordance with the Physician's intent can begin. This planning may be conformal RT, where multiple beams are directed towards the target with static multi-leaf collimators (MLCs) positioned to provide shielding for healthy tissue. The RT planning methods used in the clinical studies of this thesis are IMRT and VMAT. These techniques are described later in Section 2.5.

Before the plan is checked by a RT planner a monitor unit (MU) check is performed by software independent to the RT planning system. This independent MU check is recommended as best practice (RCR 2008).

Pre-treatment checks ensure that the correct patient is being treated, for a given course, in accordance with the Physician's intent and that the correct anatomical site has been planned. At pre-treatment the Physician will review the plan and, provided all is correct, will approve the plan for treatment. The patient then receives pre-treatment imaging in accordance with the imaging protocol for the anatomical site being treated. The purpose of pre-treatment imaging is to ensure that the patient is correctly set-up and positioned in relation to the treatment fields to within specified tolerances. The protocol defines to what extent changes can be performed. If the patient set-up is outwith this defined range, any change may require authorisation from the Physician which may result in a re-scan and re-plan. Changes can occur when a patient loses weight during treatment or when the target volume or critical structures move. Some structures, such as the prostate, are subject to movement based on the volume of the bladder and rectum. It is generally the practice in RT centres to perform bladder preparation to maintain a reproducible prostate position. At the Beatson three gold seeds are implanted into the prostate and can be imaged prior to treatment using an electronic portal imaging device (EPID). A couch shift may then be applied to bring the target to within an acceptable tolerance.

2.3 Radiotherapy planning introduction

RT planning is the process by which the therapeutic prescribed dose of the radiation oncologist is accomplished accurately via a set of treatment instructions and a physical description of the dose to the patient is prepared. The aims of RT planning are as follows:

- To determine the tumour volume in the patient and to define the target volume for treatment.

- To define the patient data (e.g. the body outline, dimensions, tissue densities) and to locate within it the target volume and other anatomical structures which may affect the dose distribution or for which it may be necessary to apply dose constraints.

- To determine the optimum treatment configuration required to irradiate the target volume to the prescribed dose within clinical constraints (+7% and – 5% of the prescribed dose).

- To calculate the dose distribution in the patient, which is displayed in a single or multiple planar view, to allow assessment of the plan and adjustment of field parameters to achieve optimisation.

- To prepare a set of treatment instructions to allow the plan to be delivered. (Williams et al. 2000).

The International Commission on Radiation Units and Measurements (ICRU) has provided definitions related to RT planning in ICRU Report 50 (ICRU 1993). The terminology in ICRU Report 50 is summarised as follows:

- Gross Tumour Volume (GTV) – the gross palpable or visible extent and location of the malignant growth. The purpose of defining the GTV is to ensure an adequate dose is delivered to the entire GTV to achieve local control and to record the tumour response to the delivered dose.

- Clinical Target Volume (CTV) – the GTV and any subclinical microscopic spread of the disease. In external beam RT, it is necessary to treat the CTV sufficiently to achieve the aim of the therapy, whether a local cure or palliation. The CTV usually has a high tumour cell density close to the demonstrated tumour with decreasing density towards the periphery (often a margin of about 1cm).

- Planning Target Volume (PTV) – the CTV with additional margins for movement of internal organs (Internal Margin) and geometrical variations and inaccuracies in the patient set-up (Set-up Margin). The PTV is a geometrical concept and takes into account the net effect of all geometrical variations. The definition of the PTV is dependent on the precision of tools such as immobilisation devices and lasers, but does not include a margin for the dosimetric characteristics of the radiation beam (i.e. penumbral areas and build-up region), as these require an additional margin during treatment planning and shielding design. Conceptually the dose to the PTV should be considered representative of the dose to the CTV.

- Treated Volume - the volume enclosed by an isodose surface, selected and specified by the radiation oncologist as being appropriate to achieve the purpose of treatment (e.g. tumour eradication or palliation).

- Irradiated Volume - the volume of tissue that receives a dose that is considered significant in relation to normal tissue tolerance.

- Organs at Risk (OARs) – normal tissues whose radiation sensitivity may significantly influence the treatment planning and may possibly require a change in the beam arrangement or a change in the dose. Potential movement of OARs and set-up uncertainties must be considered.

OARs may be considered as serial (e.g. spinal cord), parallel (e.g. lungs) or a combination of serial and parallel (e.g. heart). If any part of a serial organ receives a dose above its threshold then there will be total loss of function, for example, in the case of the spinal cord this may result in total paralysis. With a parallel organ part of the organ may be severely damaged but the remainder of

the organ can continue to function. In a serial organ it is important to consider the volume of the organ that is receiving a dose above a threshold (Symonds et al. 2012).

Figure 2.2 is a schematic of how the ICRU terms are related to one another.

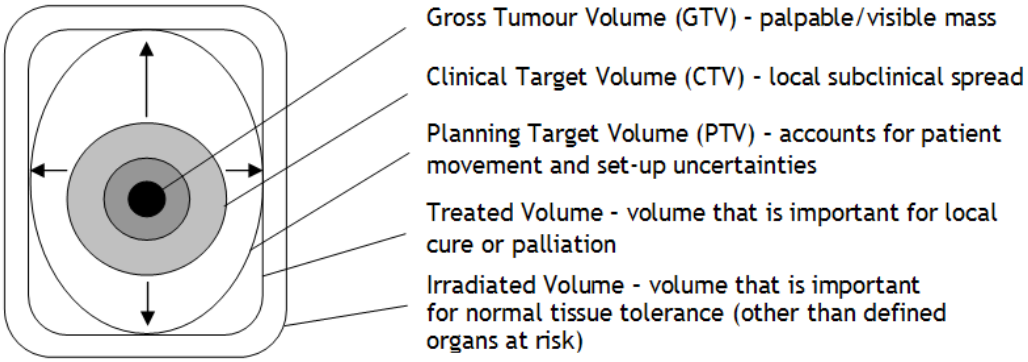

Figure 2.2 Schematic illustration of ICRU volumes.

ICRU 50 also recommends the selection of a point within the PTV, known as the ICRU Reference Point, for the purpose of dose reporting. The ICRU Reference Point is chosen according to the following criteria:

- The dose at the point should be clinically relevant and representative of the dose throughout the PTV.
- The point should be easy to define in a clear and unambiguous way.
- The point should be selected where the dose can be accurately determined.
- The point should not be selected where there is a steep dose gradient.

These criteria will be fulfilled if the ICRU Reference Point is located at the centre or central parts of the PTV and near the central axis of the beam(s). In certain circumstances the ICRU Reference Point cannot be defined at or near the centre of the PTV. In these situations it should be selected inside the tissues represented by the PTV where the dose is considered to be meaningful. This should be in a region where the tumour cell density is at a maximum.

Optimisation of a RT plan may be limited by a number of factors. Physical constraints are defined by the fundamental nature of the radiation and limitations of the RT equipment. Limited resources of a department may mean it is necessary to compromise the treatment provided. It may also be inappropriate to use a more sophisticated treatment when the patient will not gain any significant clinical benefit. Non-standard and complex plans can also increase the risk of errors.

Dose distributions are calculated using simulation software to provide the oncologist with a physical description of the prescribed treatment and to record the treatment.

Finally a prescription sheet is given to the radiographer, which is a set of instructions to enable them to deliver the treatment as described by the dose distribution. These instructions are required to be both unambiguous and accurate. Checks throughout the planning process ensure accuracy, and these checks should be included in a fully documented quality assurance (QA) system.

2.4 Radiotherapy planning algorithms

When modelling the dose distribution through a structure, the RT planning system must account for the primary and scattered components of dose. The primary dose can be calculated from experimental measurements of the dose distribution in air or by modelling the geometry of the head of the linear accelerator (linac), which includes the position and shape of the radiation source. Dose calculation is performed using the percentage depth dose (PDD) and the tissue maximum ratio (TMR) and can be applied using the inverse square law and phantom scatter corrections. The PDD is defined as the dose at depth in a phantom expressed as a percentage of the dose at a reference depth (usually the position of the peak absorbed dose) on the central axis of the beam. TMR is defined as the dose at a given depth in a phantom expressed as a ratio of the maximum dose on the central axis of the beam.

For homogeneous absorbers the scattered component of dose can be calculated using tables of scatter-air ratios which have been previously derived from depth-

dose data. The curvature of the surface of the subject being modelled must also be considered.

A further consideration in the RT planning system is secondary electrons, generated as a result of the photon beam passing through the subject. This can again be experimentally measured in a homogeneous medium and determined by deconvolving the primary distribution.

The dose in a heterogeneous medium can be modelled by calculating pencil beam kernels for the primary, singly scattered and multiply scattered components of the dose and then convolving each separately with the primary fluence. Pencil beam algorithms integrate pencil beams over the entire beam. This enables an irregularly shaped field to be irrelevant to the calculation. The effect of the heterogeneity is accounted for by scaling the kernels by the physical density of the medium at the point of interaction (Williams et al. 2000). One of the limitations of the pencil beam method is that the side scatter produced in the calculation of the dose to lung is not accurately modelled.

The Eclipse RT planning system (Varian Medical Systems, Inc. CA, USA) was employed for dose calculations in this thesis. This RT planning system uses the anisotropic analytical algorithm (AAA) which is a 3D pencil beam convolution/superposition algorithm that uses separate Monte Carlo derived modelling for primary photons, scattered extra focal photons and electrons scattered from the beam limiting devices. The AAA model provides a fast and accurate dose calculation for photon beams, even in regions of complex tissue heterogeneities. Tissue heterogeneities are accounted for anisotropically in 3D using photon scatter kernels in multiple lateral directions. This is achieved by using a radiologic scaling of the dose deposition functions and the electron density based scaling of the photon scatter kernels independently in four lateral directions. Finally, the dose distribution is acquired by the superposition of the dose calculated with the photon and electron convolutions (Varian Medical Systems 2008).

Configuration of the AAA model is based on Monte Carlo determined physical parameters that are adapted to measured clinical beam data. These are used to define the fluence and energy spectrum of the beam specific to each treatment

unit. Beam modifying accessories such as blocks, dynamic wedges and MLCs are supported in the dose calculation.

The AAA dose calculation model is comprised of two main components: the configuration algorithm and the actual dose calculation algorithm. The configuration algorithm is used to determine the basic physical parameters to characterise the fluence and energy spectra of the photons and electrons in the beam and their scattering properties in a water equivalent medium. While some of the parameters used in the dose calculation algorithms could be determined by measuring depth dose and lateral dose profiles in a water equivalent phantom, is not possible to determine all parameters experimentally. The AAA model pre-computes all the parameters using Monte Carlo simulation and then modifies these parameters to match the measured beam data. This enables a quick and highly accurate determination of all the basic physical parameters required for the AAA dose calculation.

The dose calculation is based on separate convolution models for the primary photons, scattered photons and electrons scattered from the beam limiting devices. The beam is divided into small beamlets to which the convolutions are applied. The final dose distribution is determined by the superposition of the dose calculated with photon and electron convolutions for the individual beamlets. The absorbed energy E(X,Y,Z) at an arbitrary calculation point in the patient is obtained by a superposition of the separate energy contributions from the primary photons (ph1), the extra focal photons (ph2) and the contaminating electrons from all individual beamlets denoted by index β:

Equation 2.1

$$E(X,Y,Z) = \sum_{\beta} \left(E_{ph1,\beta}(X,Y,Z) + E_{ph2,\beta}(X,Y,Z) + E_{cont,\beta}(X,Y,Z) \right)$$

Finally, the absorbed energy distribution is converted to a dose. The different homogeneities are modelled as scaled water and electron densities are used to convert the energy to dose (Varian Medical Systems 2008).

Monte Carlo techniques predict dose distribution by simulating the behaviour of a large number of photons that contribute to the beam. This algorithm encompasses the random nature of the interacting photons, the distance that

the photon will travel and the manner in which a photon is finally absorbed. The secondary electrons produced as a result of the photon interactions is also considered. Due to the complexity of this technique much simplification is required. However, Monte Carlo techniques require a very large number of random samples to achieve an acceptably accurate dose distribution (Williams et al. 2000).

The calculated dose distribution is displayed as isodose curves by the treatment planning system. Isodose curves are lines which join points of equal dose and provide a means of mapping the dose distribution as a function of depth and transverse distance from the central axis of the beam. The isodose distribution is affected by beam energy, field size, source-to-surface distance, attenuators and source/collimation geometry.

2.5 Radiotherapy planning techniques

2.5.1 Intensity modulated radiotherapy introduction

IMRT is the delivery of fields with a non-uniform fluence and provides highly conformal radiation doses to target volumes with steep dose gradients (Webb 2003). Greater conformity to the target can lead to reduced radiation toxicity and therefore fewer side-effects for the patient. It was first shown by Brahme that if the intensities can be modulated across a radiation field, the increased freedom would enable a greater ability to conform the volume of the high dose to the target than with 3D conformal RT (Brahme 1988). Inverse planning algorithms and iterative computer driven optimisation techniques are employed to generate radiation treatment fields with a varying intensity beam profile. To deliver these spatially modulated beams requires the motorised field shaping capabilities of MLCs to operate either dynamically, whereby the MLCs move while the radiation beam is on, or in a static step-and-shoot mode (Spirou et al. 1994).

IMRT is a development on the traditional practice of three-dimensional conformal RT and uses non-uniform radiation beam intensities determined using computer based optimisation techniques. IMRT is delivered using static gantry angles while the beam is on. The radiation fields in IMRT are modulated in

intensity to shape the dose distributions to the desired target. This requires additional linac capabilities to be installed, commissioned and maintained. Additional requirements are also necessary for treatment planning programs to compute the more complex intensity patterns. Commissioning to verify the dosimetric accuracy of the computer algorithms used by the treatment planning system would also be required.

2.5.2 Intensity modulated radiotherapy optimisation and calculation

Forward planning begins with a selection of field specifications, for example the beam direction, weight, shape and wedges. These beam parameters are subsequently adjusted using trial and error until a satisfactory dose distribution is achieved. Inverse planning, on the other hand, requires user-predefined criteria for dose to target volumes and surrounding healthy structures. The inverse planning algorithm then attempts to find the optimum solution based on the predefined dose-volume constraints (Chui et al. 2001).

While conformal RT planning techniques use forward planning to obtain an acceptable dose distribution, IMRT employs inverse planning. Inverse planning is the process by which the intensity distribution for each beam is determined to best meet the criteria specified by the user. These criteria include the beam directions and dose-volume objectives. The PTV is typically given a minimum and maximum dose constraint within which the entire target tissue should exist. The OARs are generally specified a maximum dose-volume constraint, with the intention of limiting the highest dose to the organ and an intermediate constraint to minimise the dose to a particular volume of the organ (Cherry et al. 2009). Priority factors are used to alter the relative weight given to different objectives. The RT planning system represents these objectives as a cost function. To change the dose calculation outcome the planner must alter the objectives and re-optimise, thereby changing the cost function. It is possible for the user to choose dose objectives which are impossible to achieve, or, conversely, that are so relaxed that they do not sufficiently guide the optimiser. Optimiser algorithms cannot guarantee a globally optimum solution or a clinically acceptable result. Generally, several attempts are required before an acceptable outcome is achieved (Leibel et al. 2002).

The dose constraints may be violated with a penalty and the penalties are specified in accordance with the relative importance of meeting each constraint, which the user defines by assigning each structure with a priority value. The computer driven optimisation algorithm divides each radiation field into a series of smaller segments with varying intensities, known as beamlets, and iteratively alters the weights until the composite 3D dose distribution corresponds to the defined objectives (Leibel et al. 2002). The treatment planning system achieves this by making an initial estimation at the required beamlet intensities and then calculating the dose distribution. An optimisation (or cost) function quantifies the difference between the calculated and the desired dose distribution. The beamlets within each field are then adjusted and the dose distribution is recalculated. If the cost function is a lower value than the initial value the new intensities are accepted, otherwise they are rejected. This iterative process continues to adjust the intensities until the constraints are met, the user interrupts the process or no further reduction in the cost function can be achieved. User interaction to adjust the constraints is possible during the inverse planning process (Cherry et al. 2009).

The result of the optimisation process is a fluence map for each beam, which is a 2D matrix of beamlet intensities for each beam (Hendee et al. 2005). The combination of each of the field's final beamlet intensities represents the fluence required to deliver the dose distribution. While the solution to the cost function from the optimisation is the ideal fluence map, physical restrictions of the linac usually require a conversion to a deliverable dose distribution (Cho et al. 2000), such as when the leaf transmission sets a lower limit on the minimum deliverable intensity. Finally, a forward dose calculation is performed to determine the dose distribution that will be delivered. A flow diagram of the IMRT optimisation and calculation process is shown in Figure 2.3.

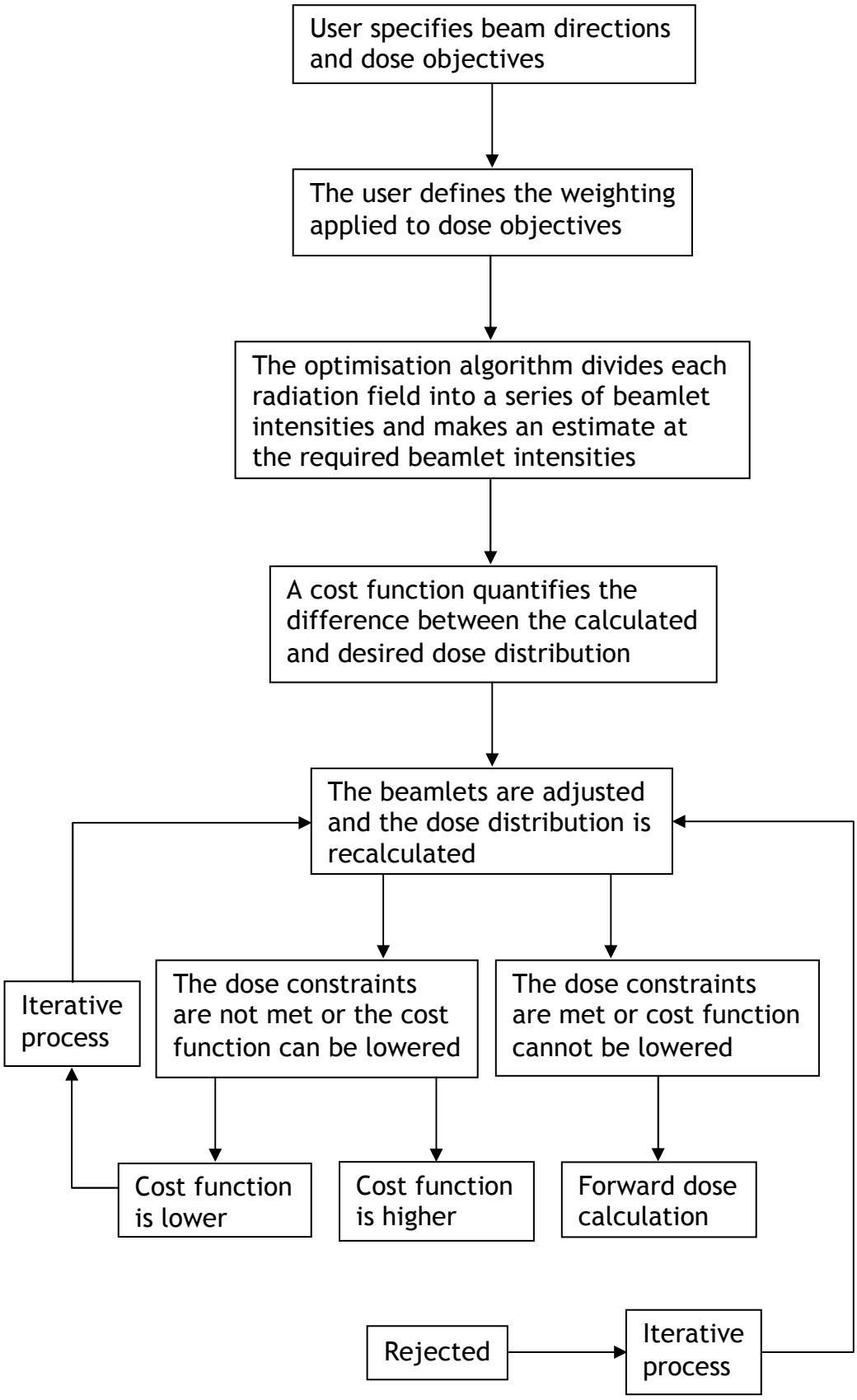

Figure 2.3 Flow diagram of the intensity modulated radiotherapy optimisation and calculation process.

A leaf-sequencing algorithm determines the MLC movements that best correspond to the desired intensity patterns. This algorithm approximates the fluence map by dividing the beam into a number of MLC patterns or segments.

In the step and shoot method, segments are delivered by the linac by setting a segment shape, turning the beam on for an appropriate number of MUs, then turning the beam off and moving the MLCs to the next segment. IMRT plans delivered at the Beatson use the MLCs in a dynamic mode. Each pair of opposing leaves travel under computer control as a sliding window during radiation delivery. The window width and leaf speed are continuously adjusted to achieve the required intensity profile. A computer program translates the intensity profiles of each intensity modulated beam into leaf sequences, and this information is subsequently transferred to the treatment machine (Spirou et al. 1994). The sliding window approach requires a more stringent MLC QA protocol, since the leaf speed must also be considered.

Different RT planning systems control the interaction between inverse planning, leaf sequencing and dose calculation differently. Some, such as the Eclipse RT planning system (Varian Medical Systems, Inc. CA, USA), used in the experiments of this thesis, employ a different algorithm for optimisation than the final dose calculation. This can help speed up the planning process. While the final dose calculation is the most important, the accuracy of the intermediate calculation can affect the optimisation results. If, for example, the optimisation calculation over- or underestimates the penumbra or scatter dose then the dose after the final calculation may be affected, generating suboptimal results (Ezzell et al. 2003). There is typically a compromise between speed and accuracy for dose calculation by the RT planning system.

As well as delineating targets, all OARs should be contoured. If a structure, required to be kept within a certain dose, is not identified and objectives set for it then the optimisation process may deposit unacceptably high doses in that region. Once delineated and optimised the dose-volume histograms (DVHs) for all structures can be evaluated.

2.5.3 Intensity modulated radiotherapy machine requirements

In conformal RT the outer aperture of the beam shape is defined by the MLC. Tolerances of around 1 to 2 mm in leaf position are acceptable, since the uncertainty is small compared to the aperture size and is likely to be inconsequential to the output and clinical outcome. In IMRT it has been shown that for beam widths of 1 cm, uncertainties of a few tenths of a millimetre can result in dose uncertainties of several percent (Ezzell et al. 2003). In addition, the beam edges are required to move to many locations to achieve the intensity profile, so high positional accuracy of the MLCs is required so that the sum of their contributions may be known. Physicists must therefore determine the MLC leaf position accuracy during IMRT commissioning and develop rigorous tests as part of the regular QA.

As well as positional accuracy the transmission characteristics of the MLC are more significant for IMRT than for conformal RT. This is because the leaves shadow the treatment area for a large proportion of the delivered MUs. A leaf transmission measurement should span a large enough area to adequately sample leaf leakage and intraleaf transmission.

Since the dimensions of the small segment beamlets may be too small, traditional calculation methods are not sufficient. Instead methods which integrate pencil beams or dose kernels may be used (Philips et al. 1999) or Monte Carlo techniques applied.

Using conformal RT techniques the transmission through collimators and the penumbra affect the edge and outside of fields and so are not as clinically important. While with IMRT beamlet intensities vary through the irradiated beam, therefore modelling of the penumbra and transmission of the MLCs is essential. For example, a five field prostate IMRT plan shields a point within the prostate for more than 60% of the MUs and leaf transmission contributes up to 4% of the entire dose (Ezzell et al. 2003)

It may be necessary to upgrade a linac to be able to provide IMRT, for example, by changing MLCs to have dynamic capability. Additionally, computer programs used for an independent MU check may need to be upgraded for IMRT

functionality. New requirements could be necessary for the computer networks to enable the required file transfers. Additional dosimetry equipment is likely to be required for the commissioning and regular QA of IMRT. The RT planning system will perhaps need upgraded to have IMRT planning capabilities and this may have consequences on the computational processing time required across the network.

2.5.4 Intensity modulated radiotherapy further considerations

Caution is required when target volumes are delineated in the build-up region. This is because the inverse planning algorithm will try to increase the intensities of the beamlets responsible for the low doses in the build-up region. Potentially, these high intensity beamlets will result in a poor overall plan quality, or cause hot spots in the target or elsewhere. The solution to this problem is to remove a margin of the PTV from the body contour. If, however, the target is required to be in the build-up region then a bolus may be required (Leibel et al. 2002).

At the plan evaluation stage, examining DVHs is a useful, but not comprehensive method, since DVHs contain no spatial information. It is possible for IMRT plans to have hot or cold spots in unexpected regions. In 3D conformal RT where beams are defined using the beam's eye view to contain the PTV on each field, it is often the case that the low dose on a DVH corresponds to the penumbra at the periphery. Using IMRT, low doses may occur within the PTV, or, conversely, high doses may exist well outside the target. For this reason, when planning with IMRT, isodoses must be inspected on every image slice to ensure erroneous dose regions do not exist.

IMRT can be used to increase the homogeneity of the dose distribution to the target volume over conventional 3D conformal RT. However, there is a greater potential for a geographical miss of the target volume using IMRT because of the increased PTV conformity of the dose distribution and delivery times can be longer than with 3D conformal RT (Staffurth 2010). The reason for the increased treatment times using IMRT is that the radiation beam is switched off after the delivery of each treatment field as the linac is moved to the next treatment angle and there are a typically a greater number of radiation beams used than with conformal RT.

The use of margins within IMRT is of the utmost importance due to the rapid dose gradients produced (Manning et al. 2001). When steep dose gradients are used, the consequence of localisation errors is of a higher significance. This highlights the need for accurate localisation in RT which can be provided by, for example, registering CT with MRI or using image guidance at treatment, such as cone-beam CT.

IMRT results in greater volumes of tissue receiving a low dose, but it is not yet fully understood the likely clinical effect of these doses. Some studies have estimated that IMRT may increase the risk of a secondary fatal cancer by a factor of around 2-5 (Hall et al. 2003; Kry et al. 2005). These studies investigated the carcinogenic implications of IMRT by considering DVHs or thermoluminescent dosimeter (TLD) measurements. Another study using both DVHs and TLD measurements concluded that the risk associated with IMRT is comparable to 3D conformal RT (Ruben et al. 2008).

IMRT requires more MUs than conformal treatment by a factor of around 2 to 10, so room shielding should be reassessed. Primary barriers are not usually affected, however the periods of use should be re-evaluated since IMRT typically uses many more gantry angles than conformal RT treatments. Greater workloads affect the leakage radiation reaching secondary barriers and so the dose through these barriers must be investigated.

In the inverse planning process, the additional dose calculations after each iteration must be performed more rapidly than with conventional algorithms. This places greater computational demands on the RT planning system. An additional processing burden on the planning system is the frequent use of very small field segments which requires the dose calculation algorithms to accurately model the penumbra.

Due to the complexity of IMRT treatments, further QA measurements are required to ensure the dose distribution is calculated accurately. Verification of the delivered dose can be achieved by comparing the calculated dose from the RT planning system with measurements using film, detector array phantoms, ionisation chambers or EPIDs (Cherry et al. 2009).

With IMRT the gantry angles are user defined and therefore the optimum treatment angles are not always considered (Palma et al. 2010). Selecting the most appropriate angles to use for IMRT can be challenging (Wang et al. 2004d). Typically, more beams are required for an IMRT plan than with conventional 3D conformal RT. For example, in the treatment of head and cancer, 3D conformal RT would commonly employ lateral fields, whereas with IMRT seven or nine beams could be utilised. This would result in dose to structures which would have been blocked with conformal RT, such as the anterior portion of the mouth and the cerebellum. While the dose to these structures will be considerably lower than the target, careful monitoring of the patient during treatment is required to detect any unexpected side effects (Hendee et al. 2005).

2.5.5 Arc therapy techniques

Arc therapy began to be used with orthovoltage energies (200-500kV) because it was difficult to achieve a high enough target to non-target ratio to treat deep-seated lesions. With the introduction of mega-voltage energies an acceptable target to non-target ratio became possible and so for many years arc therapy was not commonly used. Arc therapy then began to be utilised with megavoltage energies in the early 1990s, using dynamic MLCs (Williams et al. 2000).

Megavoltage arc therapy can be broadly classified into two types: tomotherapy and VMAT. Tomotherapy machines are very much like a CT scanner and linac combined. Radiation is delivered in a thin fan-shaped distribution which can be adjusted by the opening and closing of the binary collimator. The radiation source continuously rotates while the patient is moved through the machine. VMAT is analogous to tomotherapy, since radiation can be delivered using up to 360° beam angles (Otto 2008). However, VMAT can treat the whole tumour volume at once, rather than in slices or as a helix, and uses a standard linac. It is possible to treat a RT fraction using a single rotation, although additional arcs can sometimes be used to improve the dose distribution (Clivio et al. 2009; Verbakel et al. 2009a).

VMAT delivers radiation with the MLCs in a continuous dynamic mode while the gantry of the linac rotates through one or more arcs. This method was first proposed as intensity modulated arc therapy (IMAT) and uses rotational cone

beams of varying shapes to achieve intensity modulation (Yu 1995). IMAT converted intensity patterns into multiple segments and delivered the radiation using multiple overlapping arcs. This strategy was later developed to include a varying dose-rate and gantry rotation speed in order to deliver the radiation using a single arc algorithm, known as VMAT (Otto 2008).

Arc therapy enables highly conformal dose distributions and is an alternative form of IMRT. The three main advantages of arc therapy over IMRT are: the superior dose distributions, the improved treatment time delivery and the reduction in MU requirements due to greater treatment efficiency, which may result in a reduction in the dose to normal tissues (Palma et al. 2010). Unlike IMRT, VMAT utilises all possible treatment angles to treat the target while avoiding critical structures (Palma et al. 2010; Teoh et al. 2011).

The term VMAT in the published literature encompasses different computer algorithms developed by manufacturers. RapidArc (Varian Medical Systems, Inc, Palo Alto, CA, USA) is Varian's optimisation algorithm developed from the research by Otto (Otto 2008) and is used in the clinical study in Chapter 6. Philips (Philips Healthcare, Eindhoven, Netherlands) markets a rotational IMRT solution with the trade name SmartArc and Elekta (Elekta AB, Stockholm, Sweden) uses the trade name VMAT. Since all algorithms are variations in the principle of IMAT, the generic term VMAT will be used to describe the technique in this thesis.

2.5.6 Volumetric modulated arc therapy comparison studies

Comparison studies have shown that VMAT produces similar or improved dose distributions to IMRT (Clivio et al. 2009; Palma et al. 2008; Vanetti et al. 2009; Wu et al. 2009), while reducing the treatment time by approximately 3 minutes for a standard 2 Gy treatment and reducing the number of MUs by around 50% (Shaffer et al. 2010). Stereotactic lung RT delivers up to 20 Gy per fraction to a moving target and the treatment times can be reduced from 30-45 mins using IMRT to 4-11 mins with VMAT (Verbakel et al. 2009b). Two studies evaluating head and neck cancer treatment found that VMAT gave equivalent or improved dose distribution to IMRT while lowering the monitor units by 50-60% and

significantly reducing the treatment times (Vanetti et al. 2009; Verbakel et al. 2009a).

Monitor units give a measure of the amount of radiation produced by the linac; therefore, an increase in the number of MUs is indicative of greater scatter radiation, which in theory could increase the risk of secondary malignancies.

The reason why VMAT offers treatment time saving over IMRT is because with IMRT time is required to transfer the information to the treatment machine, reposition the gantry and to set the field to the correct shape at every field. With VMAT the radiation beam is continuously on during treatment and each arc is considered as one field so delivering the plan information to the treatment machine is only required once per arc. Furthermore, IMRT plans deliver a greater number of monitor units than with VMAT; therefore, the linac is turned on for a longer period of time.

VMAT can be delivered with either a constant dose rate or a variable dose rate during gantry rotation. A variable dose rate enables improved dose conformity and therefore greater sparing of OARs over IMRT (Palma et al. 2008).

2.5.7 Volumetric modulated arc therapy optimisation and calculation

VMAT uses an iterative inverse planning process in a similar way to IMRT. A treatment arc can be simulated by a number of equally spaced static beams. If a smaller angle is used between beams the accuracy of the calculation increases. It is believed that most VMAT planning algorithms calculate using static beams because the computational demands would be too great to trace the actual ray paths from a continuously moving source (Webb et al. 2009).

RapidArc uses a stepwise optimisation of leaf position, which is divided into 177 angles, known as control points (Verbakel et al. 2009a). Otto showed that instead of optimizing all the control points at once, which would be extremely time consuming, an optimal solution can be achieved by progressively increasing the number of control points to converge the optimisation in a short period of time (Otto 2008). The aperture shapes and weights are optimised initially for a number of coarsely spaced gantry angles, without a great consideration of

aperture connectivity. Since the connectivity of the aperture shape is ignored in the first instance, the optimiser has greater freedom to achieve an optimal dose distribution. As the solution converges, additional gantry angles are included. As the angular spacing gets smaller the optimiser considers the aperture shape connectivity both in the initialisation of the aperture shapes and during the optimisation. The shapes of the additionally inserted apertures are linearly interpolated from their neighbours. This course-to-fine sampling is known as progressive sampling and enables the optimisation to converge to a solution more quickly.

As with IMRT, after optimisation, a leaf-sequencing algorithm determines the MLC movements required to correspond with the optimised intensity profiles. Beamlets from each control point are convolved to generate a final dose distribution. The data on the leaf movement required to achieve the desired dose distribution is then transferred to the linac for treatment.

2.5.8 Volumetric modulated arc therapy further considerations

One of the main advantages of VMAT over IMRT is the improved treatment efficiency and subsequently the reduced treatment times. Longer treatment times have several negative implications. Firstly, it limits the patient throughput per treatment unit per day. Secondly, it requires patients to spend longer on the treatment couch, which can increase patient discomfort and increase the risk of intra-fraction movement of the tumour or patient. Increased treatment times also results in a rise in the machine time required for quality assurance by physics staff to measure and confirm the delivered dose distribution. Finally, in addition to the practical considerations, prolonged treatment time may have detrimental radiobiological consequences. It has been shown using radiobiological calculations that treatment times greater than 15 minutes per fraction result in decreased tumour control probability (Wang et al. 2003).

A concern with IMRT is the increased number of MUs delivered. While there is a larger volume of normal tissue receiving lower dose with VMAT than with conformal RT, there is a reduction in the number of MUs with VMAT compared to IMRT and therefore this theoretically reduces the associated risk of secondary malignancies (Hall 2006).

As with IMRT careful consideration of margins and excellent target localisation is required due to the steep dose gradients associated with VMAT. However, due to the reduced treatment time using VMAT, intrafraction motion, excluding respiratory or cardiac motion, is likely to be less of a concern than with IMRT.

Upgrades to the linac will be necessary to enable VMAT to operate, and new software will be required for dose optimisation and calculation. New capabilities will also be required for software to perform an independent MU check on VMAT plans. It is likely that upgrades will be required to computer networks due to the greater computational demands of VMAT. New dosimetry equipment will be needed to perform the pre-treatment QA to ensure the measured and calculated dose distributions correspond. While QA for VMAT is more complex and therefore more time consuming than 3D conformal RT, it is likely to require less treatment machine time than IMRT due to the reduced treatment times.

2.6 Magnetic resonance imaging

MRI is used in the management of cancer patients for diagnosis, staging, RT planning and in response to therapy. The MRI technique maps the distribution of hydrogen nuclei (protons) in water molecules throughout the subject under examination. This method is possible since the protons possess both charge and spin. The combination of charge and spin produces a nuclear magnetic dipole; therefore the nuclei can be likened to microscopic magnets. Normally, the orientation of the magnetic moments is random, but by placing a subject in a high static magnetic field, the magnetic moments align with the direction of the applied field. Not only does the applied field cause the nuclei to align in the direction of the magnetic field, but the spinning nuclei precess about the applied field, in the same way as the earth's gravitational field causes a gyroscope to precess about the vertical axis. The angular frequency, f, of the precession is governed by the Larmor equation,

Equation 2.2

$$f = \frac{\gamma B_0}{2\pi}$$

where γ is the gyromagnetic ratio (a constant for a given nucleus) and B_0 is the strength of the static magnetic field. This frequency is known as the Larmor

frequency and for a field strength of 1.5 T, the Larmor frequency is equal to 63.87 MHz.

There are two possible orientations of the spin angular momentum for protons with respect to the applied field: aligned with or against the field. These orientations correspond to different energy levels, and it requires slightly more energy for the proton to be aligned against the field. Only transitions between upper and lower energy levels are possible. At room temperature, a nucleus has a slightly greater chance of being in the lower energy state than the higher one. If you consider a large number of hydrogen nuclei (there are many millions of protons in the human body), when the field is applied, a small net magnetisation will result from the cancellation of the effects of all but a few of the precessing nuclei. At body temperature (37 °C), in a 1.5T MRI scanner, the ratio of protons aligned with the field to protons aligned against the field is about 1.000004. The vector sum of all the protons is called the net magnetisation vector, M_0, and is aligned with the applied static magnetic field, B_0, often denoted as the z direction.

The magnetisation in the body is very small in comparison to the main magnetic field, so it is virtually impossible to measure this magnetisation while it is at equilibrium and parallel with B_0. However, the net magnetisation vector can be rotated away from alignment with B_0, by applying an oscillating magnetic field of the same frequency as the rate of precession, B_1. This magnetic field is called a radiofrequency (RF) pulse, since the Larmor frequency for MRI is in the radio frequency (tens of MHz) range.

If a static, instead of an oscillating, magnetic field was applied, the resultant net magnetisation would have a complicated movement because of the precession from the two static fields. However, by temporarily applying an oscillating magnetic field at the Larmor frequency, B_1, this results in a rotation of the net magnetisation. The net magnetisation will rotate into the transverse (x-y) plane (Figure 2.4) when a "90° RF pulse" is employed. For a given magnetic field strength different nuclei precess at a different frequencies and so the effect of applying the RF pulse at the Larmor frequency of the hydrogen nuclei is to single out such nuclei to precess in the transverse plane. Using a detector

which only measures magnetic fields in the transverse plane, M_0, is now sufficiently significant that it can be measured.

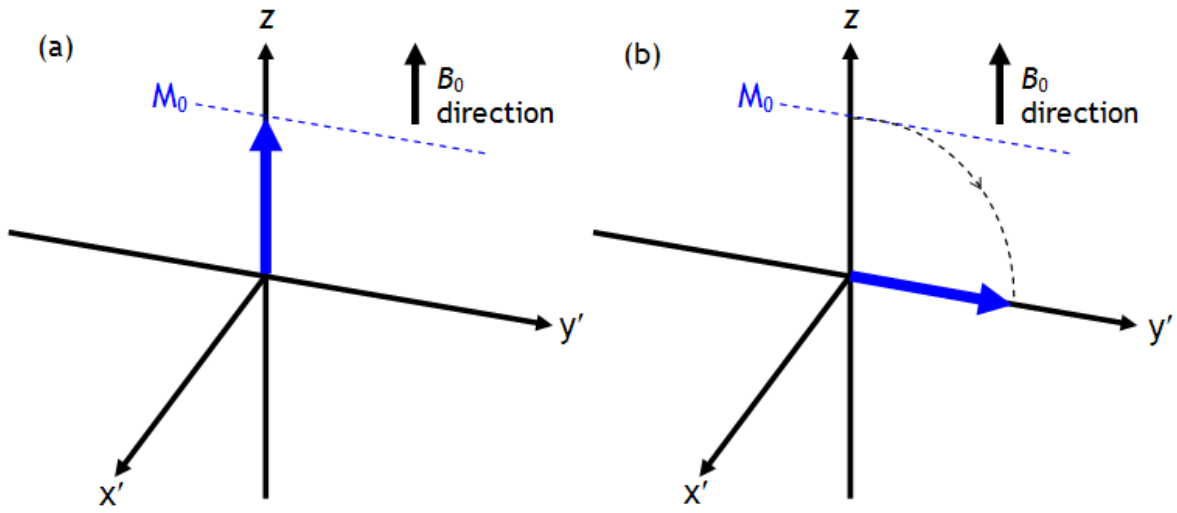

Figure 2.4 The net magnetisation vector, M_0, is orientated (a) along the direction of the applied static magnetic field, B_0, at thermal equilibrium (b) in the transverse plane following a 90° radiofrequency pulse. This diagram is in the rotating frame at the precession of the Larmor frequency. The axes x′ and y′ represents the axes rotating at the Larmor frequency.

B_1 is turned on for only a few milliseconds to achieve the rotation. By applying the oscillating magnetic field for different durations, varying amounts of rotation can be achieved. Leaving a 90° RF pulse on for twice as long, or doubling its strength, would rotate M_0 by 180° and the RF pulse would be called a 180° pulse. Since time saving is crucial in MRI, the strength of the pulse is usually changed to produce various flip angles. The RF pulse also brings the spins into phase coherence.

When the RF pulse is turned off, the magnetisation vector emits a signal at the Larmor frequency and decays as spins lose phase coherence and begin to cancel each other out. This occurs because the spins experience slightly different magnetic field strengths due to interactions with their own oscillating magnetic fields and other nuclei. The rotating magnetisation can induce an alternating current in a coil which is tuned to resonate at the Larmor frequency, which generates a sinusoidal signal in the receiver coil, which is sensitive only to magnetisation perpendicular to B_0. In a few milliseconds, the spins point in arbitrary directions and the transverse component of the net magnetisation vector is lost. Additionally, the magnetisation vector returns to being aligned

with the static field. This decaying, oscillating signal is known as the free induction decay.

2.7 MRI relaxation times

2.7.1 T2 and T1 relaxation times

After the spins have been rotated into the transverse plane, they begin to relax back to their equilibrium position when the RF pulse is switched off. The recovery of the magnetisation vector to the equilibrium state can be considered in two parts: the dephasing of the spins in the transverse plane and the re-growth of net magnetisation vector (M_0) in the z-direction, as the spins lose the energy they absorbed from the pulse to the surrounding environment (or lattice). These processes are known as T2 (spin-spin or transverse) and T1 (spin-lattice or longitudinal) respectively. Different tissues have different T1 and T2 relaxation times, which can be used to generate contrast between different tissues in an MR image.

As the spins interact with the nuclear spins of each other, they gradually dephase until there is no net magnetisation vector in the x-y plane. The T2 time relates to the monoexponential loss of phase coherence as the spins interact. After a time interval T2, 63% of the transverse magnetisation is lost. The rate of the transverse demagnetisation, following a 90° rotation of M_0, is given by,

Equation 2.3

$$M_{xy}(t) = M_{xy}(0)\exp(-t/T2)$$

The T1 time constant describes the monoexponential recovery of the magnetisation to its original value. After applying a 90° RF pulse the longitudinal component of the magnetisation vector will regrow to 63% of its maximum value in a time T1. The molecular environment of the protons will dictate the exact rate of the longitudinal remagnetisation and will follow the first-order equation,

Equation 2.4

$$M_z(t) = M_0(1 - \exp(-t/T1))$$

The T1 and T2 relaxation times are represented by Figure 2.5.

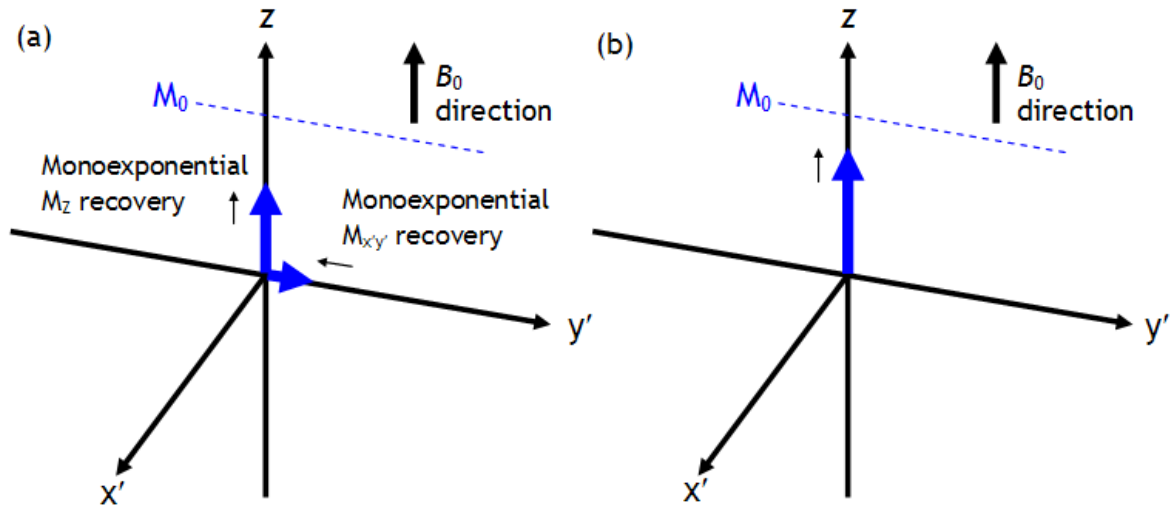

Figure 2.5 (a) Decay of the M_{xy} (time constant T2) after a given time and (b) recovery of the M_z (time constant T1) after a further time. This diagram is in the rotating frame at the precession of the Larmor frequency. The axes x′ and y′ represents the axes rotating at the Larmor frequency.

2.7.2 T2 decay*

The T2 time constant can be artificially shortened by the static magnetic field, B_0, inhomogeneities and susceptibility effects. Magnetic susceptibility is the extent to which a material becomes temporarily magnetised when it is placed in a magnetic field. Between two boundaries of different susceptibility a small magnetic field gradient will exist. Magnetic field inhomogeneities and susceptibility effects also change the magnetic field experienced by the nuclear spins, which varies the frequency of precession, causing them to move out of phase more quickly resulting in a faster loss of signal. The additional dephasing effects gives a time constant T2*. By applying a 180° refocusing RF pulse the partially dephased magnetisations reverse the direction of the dephasing (rephase) so that spins with less phase difference than others now have more and vice versa. Dephasing due to the interactions between spins (T2 time constant) will still occur resulting in signal loss. This type of signal is called a spin-echo pulse sequence (see Section 2.10.1 for more information). Multiple 180° RF pulses can be applied to repeatedly refocus the decaying transverse (M_{xy}) magnetisation and is called a multiple spin echo sequence.

2.7.3 Gadolinium contrast agent

Gadolinium has strong paramagnetic properties meaning that it becomes strongly magnetised when placed in a magnetic field. Most body tissues are diamagnetic and only become weakly magnetised. When gadolinium is injected into the body the vascular system delivers it to all perfused tissues. It has the effect of decreasing the T2 and T1 relaxation times of protons in the immediate vicinity of the molecule. This shortening of the T1 means that tissues have greater signal intensity on T1-weighted images. Gadolinium rapidly accumulates in highly vascular tumours and so become brighter on post contrast T1-weighted images. A gadolinium contrast agent was used in the clinical study of Chapter 6 to give increased signal intensity to oropharyngeal lesions.

2.8 Magnetic field gradients

To localise the area to be imaged three magnetic field gradients are applied in the three orthogonal planes. By applying combinations of gradients at once, oblique angled planes may be obtained. Field gradients are alterations to the main magnetic field and are generated by coils of wire through which current is passed. These magnetic field gradients are called the slice selection, frequency encoding and phase encoding gradients.

The slice selection gradient has the effect of changing the Larmor frequency across the subject in one direction. This enables a section to be excited by choosing the correct frequency range of RF excitation pulse. The section which contains the frequencies which match the frequencies of the oscillating magnetic field will respond and an MRI signal will be generated from that section. The position of the slice can be changed by modifying the frequency of the RF pulse, but using the same gradient strength. This changes the region which meets the resonant condition. Slice thickness can be modified by altering the slope of the gradient field or by changing the bandwidth of the RF excitation pulse. A stronger gradient will result in a thinner slice. Alternatively, using a narrower RF pulse bandwidth will equally deliver a thinner slice width.

The frequency encoding gradient is a static gradient field just like the slice selection gradient. It causes a range of Larmor frequencies to exist in the

direction that it is applied. The range of frequencies is a mix of signals from a slice and can be separated using a Fourier transform. The frequency encoding gradient is switched on when the signal is being received and is therefore often referred to as the readout gradient.

The signal must be encoded in the remaining axis of the image and this is called phase encoding. To create a single MRI signal the same signal measurement is repeated numerous times, but different phase relationships between different rows of voxels are introduced for each measurement. By comparing the rate of change of phase for each row, which is different for every row, the Fourier transform can separate out the rates of change of phase (frequencies) and signal intensity information can be discerned in the phase encoding direction.

To introduce different amounts of phase encoding for each measurement a magnetic field gradient is temporarily turned on. As with the slice selection and frequency encoding gradients this causes a range of Larmor frequencies to exist in the direction it is applied. While the gradient is on spins precess faster at one end of the gradient than at the other end. After turning off the gradient the Larmor frequencies return to their original values and are all the same frequency, but a phase difference will exist in the direction that the gradient has been applied. This concept is illustrated in Figure 2.6 where in (a) the protons are in phase following an RF pulse. When a gradient is applied along the column of protons for a short period of time, as shown in (b), the protons speed up in their precession in accordance with the strength of the magnetic field they experience. In this illustration the speed and strength of the magnetic field is greatest from top to bottom. Finally, in (c), the gradient is switched off and the protons experience the same magnetic field again. The protons therefore have the same precession frequency but are now out of phase. By varying the strength of the magnetic field gradient in the phasing encoding direction for subsequent measurements, different phase relationships are established. By determining the rates of change of phase from all measurements the location of the pixels can be deduced by a Fourier transform.

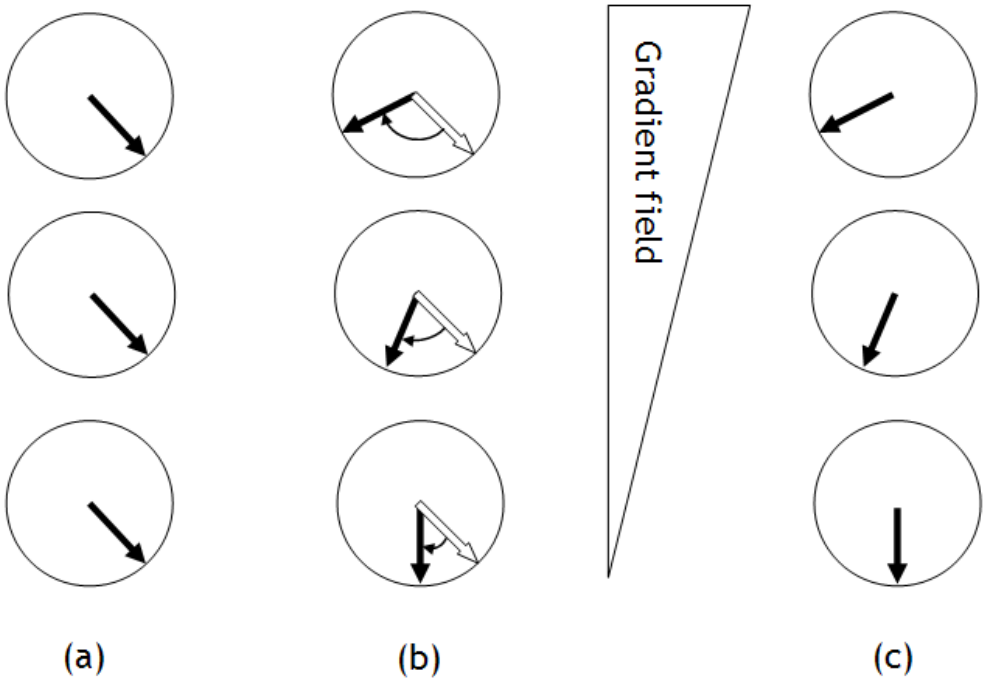

Figure 2.6 Phase encoding (a) protons are in phase, (b) a gradient field is applied changing the speed of the protons, (c) the gradient is turned off again and the protons return to precessing at the original speed but with different phase.

2.9 k-space and image reconstruction

The raw data in MRI is collected in a temporary data space, known as k-space, before reconstruction. The k-space is in two axes: the x-axis represents the frequency information and the y-axis represents the phase information. Each line of k-space is a digitised recording of the signal obtained per TR and every phase encoding gradient is a different line of k-space. The phase encoding gradient is then switched off and the frequency encoding gradient is switched on as a positive gradient which then moves the k-space coordinate horizontally across that line. For an $N \times N$ pixel image to be reconstructed, N different phase encoding steps must be applied. At the centre of the k-space, the data primarily determines the signal-to noise and contrast of an image, whereas data at the edges of the k-space contains the image resolution information.

The signal obtained during the acquisition of an image is converted using an array processor or computer. The 2D Fourier transform is applied to the data stored in k-space, with a 1D Fourier transform applied in the frequency encoding direction and another in the phase encoding direction. The 2D Fourier transformation converts the signal which has been acquired in the time domain into the frequency domain. The free induction decay is the signal acquired and

the Fourier transform separates the signal into its constituent frequency components, which contribute to the signal emitted from the image slice. While the spins in the frequency direction are shifted with respect to each other with frequency, the spins in the phase encoding direction are shifted with phase. A different rate of change of phase is applied for every line of k-space, and a rate of change of phase is equal to frequency. This enables the total signal from each pixel to be determined, which is used to generate a greyscale image.

2.10 Pulse sequences

The time interval between successive 90° pulses is known as the repetition time (TR). The TR controls the amount of T1 relaxation that has occurred. The time interval between the 90° pulse and the resulting echo is known as the echo time (TE). The TE determines the amount of T2 relaxation that has occurred. T1-weighted images have a short TE (<<50 ms) and short TR (<<500 ms), whereas T2-weighted images have a long TE (>100 ms) and a long TR (>3 s).

2.10.1 The spin echo pulse sequence

The spin echo (SE) sequence consists of a selective 90° RF pulse followed by one or more selective 180° pulses. The amplitude of the echo is a function of TE and the spin-spin relaxation time T2. The 180° pulse has the effect of flipping the spins 180° about the y axis, reversing the phase angles of the spins. Spins which were dephasing clockwise will now be dephasing anticlockwise and vice versa. Provided the spins do not move too far within the imaging volume, they will continue to experience the same magnetic field inhomogeneities and dephase in the same direction. After a period of time equal to the delay between the 90° and 180° pulse, all the spins will come back in phase about the y-axis forming the spin echo. This phase reversal technique means that the echo height depends on T2, and not on the magnetic field inhomogeneities or tissue susceptibilities.

A SE sequence acquires only a single echo from each excitation and is therefore intrinsically slow (in the order of minutes). Figure 2.7 is a schematic representation of the SE sequence. This diagram shows the 90° and 180° RF pulses and the timings of the encoding gradients.

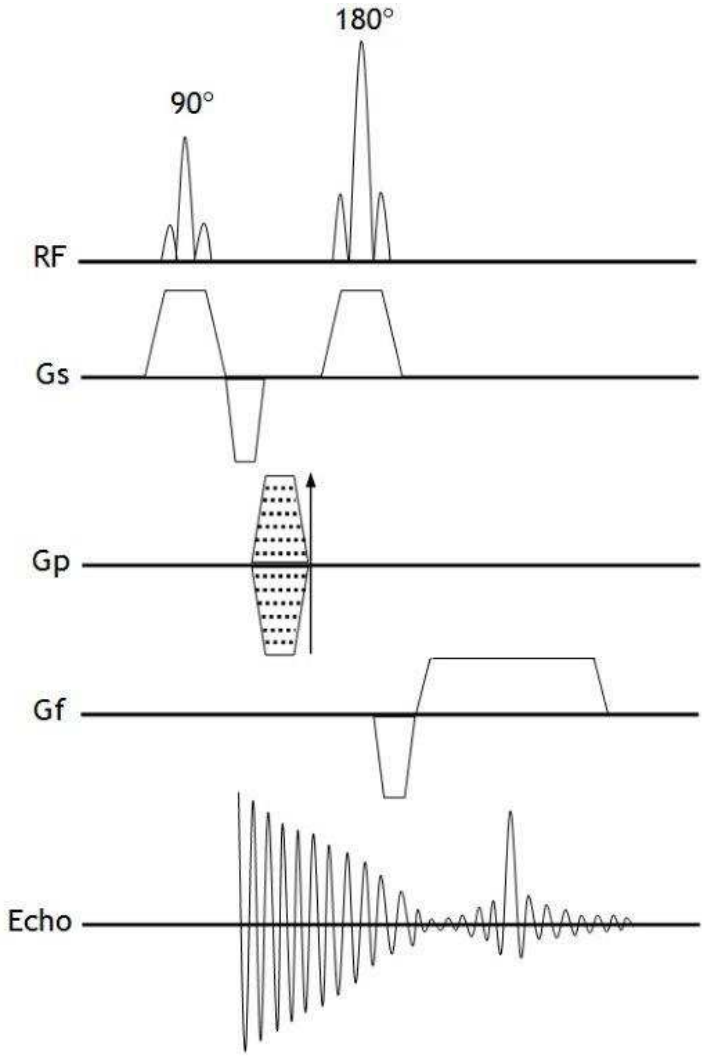

Figure 2.7 A spin-echo pulse sequence diagram, where RF are the radiofrequency pulses, Gs is the slice selection gradient, Gp is the phase encoding gradient and Gf is the frequency encoding gradient.

2.10.2 The turbo spin echo sequence

To speed up the SE sequence multiple echoes can be acquired from each single excitation pulse, as shown in Figure 2.8, and is known as a turbo spin echo (TSE) or fast spin echo sequence. In the TSE multiple 180° RF pulses are use to continually refocus the decaying transverse magnetisation to produce a train of echoes per TR interval. Each echo corresponds to one line of k-space but each successive echo in the train has increasing T2 weighting and a lower SNR. After each signal measurement the phase encoding is reset with an equal and opposite magnetic field gradient (known as a phase encoding rewinder pulse) and then a new phase encoding gradient is applied. The function of the rewinder pulse is to undo the phase change caused by the phase encoding gradient so that there is phase coherence between successive echoes. The group of signal echoes decay

with a time constant T2. The contrast and signal-to-noise ratio of an MR image are primarily determined at the position of the echo at which the phase encoding gradient has the smallest amplitude (i.e. at the centre of k-space). The time taken between the excitation pulse and this echo is known as the effective echo time (TE_{eff}). It is possible to change the TE_{eff} by changing the phase encoding pattern. The turbo factor is the number of echoes acquired per excitation. Therefore, Figure 2.8 would have a turbo factor of 4.

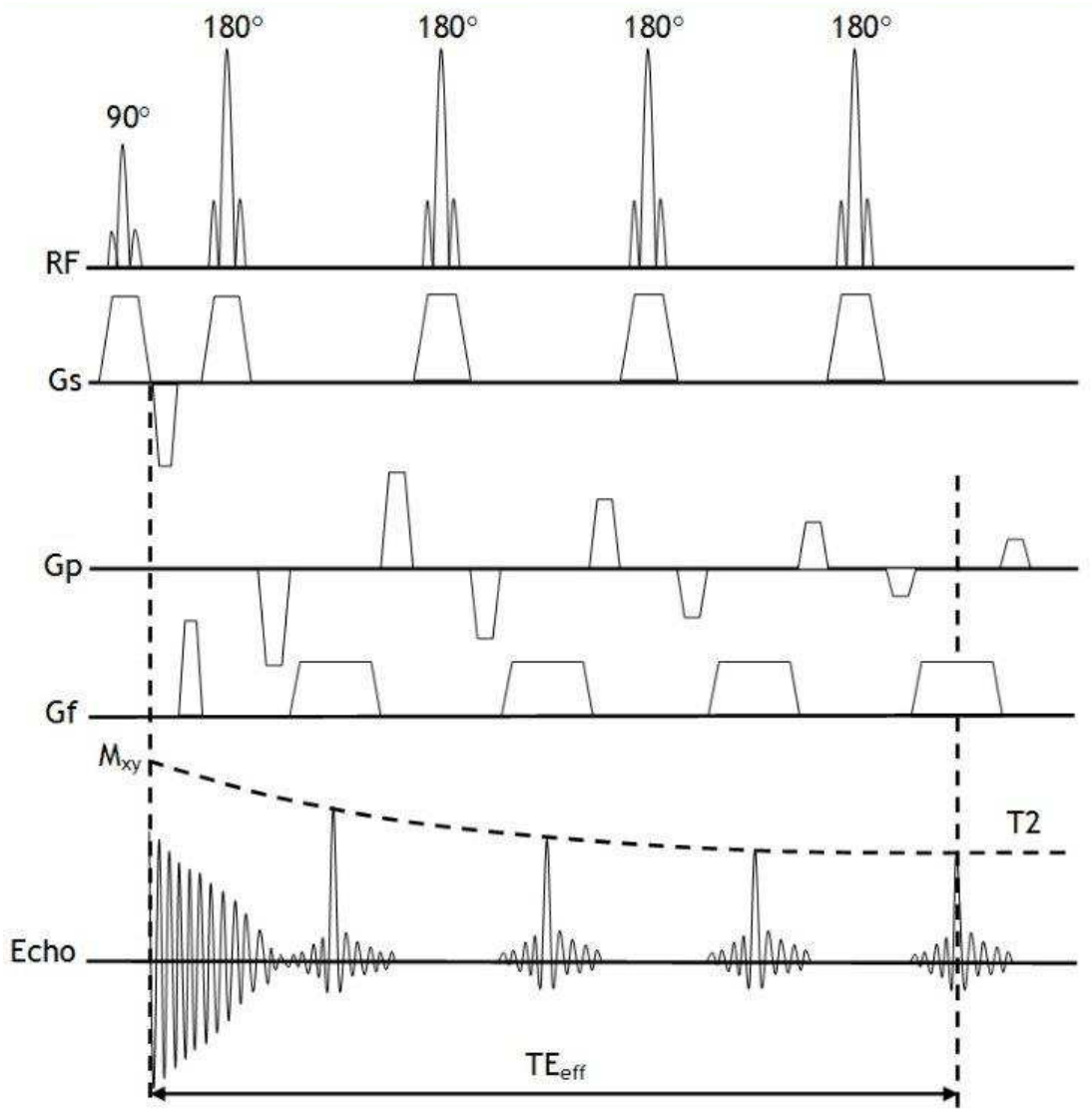

Figure 2.8 A turbo spin echo pulse sequence diagram, where RF are the radiofrequency pulses, Gs is the slice selection gradient, Gp is the phase encoding gradient, Gf is the frequency encoding gradient, M_{xy} is the decaying transverse magnetisation and TE_{eff} is the effective TE.

With a TSE a significant reduction (up to the order of 10 fold) in scan time can be achieved. The TSE sequence is usually used for T2-weighted imaging only because of the subtle contrast behaviour of this sequence type. Images produced

with these sequences can be difficult to interpret since both lipid and water appear bright.

2.10.3 The fast recovery fast spin echo sequence

The fast recovery fast spin echo (FRFSE) sequence is a spin echo sequence which quickens the return of the transverse magnetisation to equilibrium in the longitudinal direction (Figure 2.9). It achieves this by the addition of a negative 90° RF pulse after signal decay at the end of the echo train to refocus residual spins with long T2 from the transverse plane to the longitudinal axis, during the time when normal refocusing is occurring, as illustrated in Figure 2.10. This sequence results in a much faster recovery of tissues with a long T2, such as cerebrospinal fluid, to equilibrium enabling enhanced contrast resolution between tissues with long and short T2 or a shorter TR and therefore a significantly shorter scan time. This sequence can be used in conjunction with parallel imaging techniques for short breath hold imaging or with respiratory gating for free-breathing imaging.

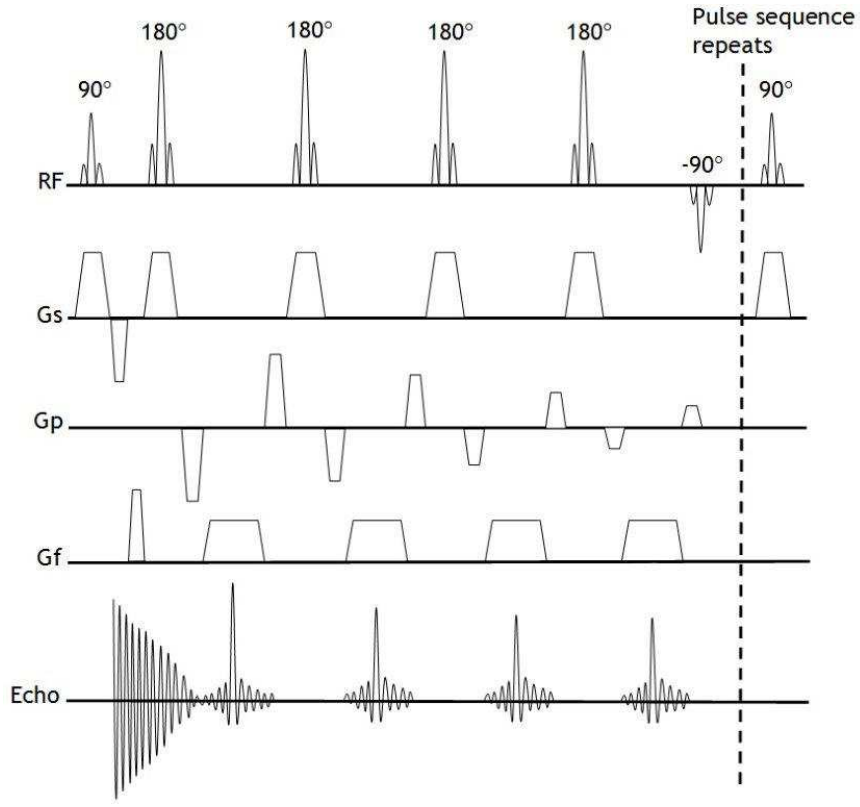

Figure 2.9 A fast recovery fast spin echo sequence, where RF are the radiofrequency pulses, Gs is the slice selection gradient, Gp is the phase encoding gradient and Gf is the frequency encoding gradient. Transverse magnetisation still present at the end of the echo train is refocused back into the longitudinal axis by applying a negative 90° pulse.

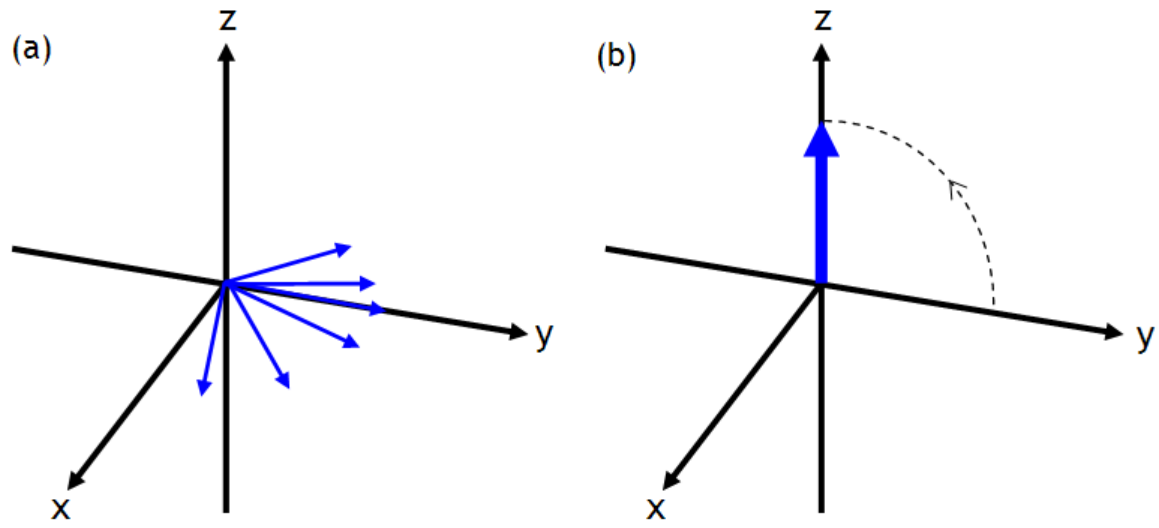

Figure 2.10 (a) Normal refocusing of the transverse magnetisation occurs at the end of the echo train prior to the negative 90° radiofrequency pulse. (b) After the application of a negative 90° radiofrequency pulse the net magnetisation vector is refocused back into the longitudinal axis.

2.10.4 The short inversion time inversion recovery sequence

The short inversion time inversion recovery (STIR) sequence is a technique with specific timing to suppress the signal from fat and is suitable for large fields of view or in regions with varying magnetic susceptibility. This sequence uses a 180° inversion preparation pulse to invert all magnetisation. Imaging begins after a delay to allow the longitudinal recovery of fat magnetisation to reach the null point so that there is no fat magnetisation which can be rotated into the x-y plane. The time between the 180° preparation pulse and the 90° excitation pulse is known as the inversion time (TI) and is chosen to be $\ln(2)T1_{fat}$, where $T1_{fat}$ is the T1 relaxation time for fat. Tissue other than fat still has signal since they have a T1 relaxation time which is different to fat and so have not yet reached the null point, or have recovered beyond it. The pulse sequence diagram for a STIR sequence is shown in Figure 2.11.

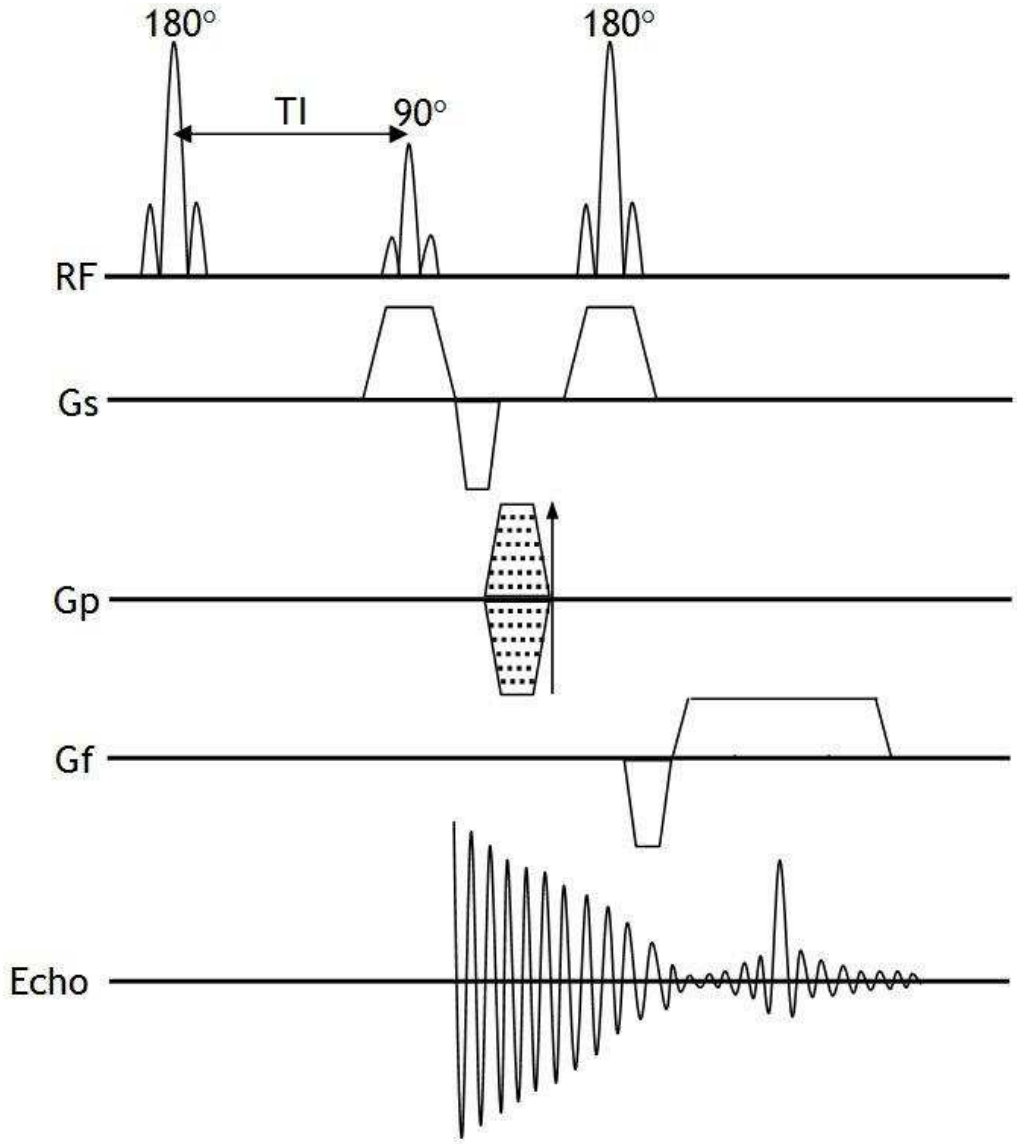

Figure 2.11 A short TI inversion recovery sequence, where RF are the radiofrequency pulses, Gs is the slice selection gradient, Gp is the phase encoding gradient, Gf is the frequency encoding gradient and TI is the inversion time.

Figure 2.12 illustrates the inversion of the net magnetisation vector by the 180° preparation pulse. After a period of time the net magnetisation vector returns to its equilibrium value in accordance with T1 relaxation.

The TI is chosen such that there is no longitudinal magnetisation to be rotated into the x-y plane from fat, which can be considered the null point of fat. Fat reaches the null point more quickly than white matter, grey matter, water or oedema, and so there will still be signal from these structures, as shown in Figure 2.13. At 1.5T an approximate TI of around 140 ms will result in the suppression of fat. A STIR sequence can be used to reduce chemical shift artefact since fat is suppressed.

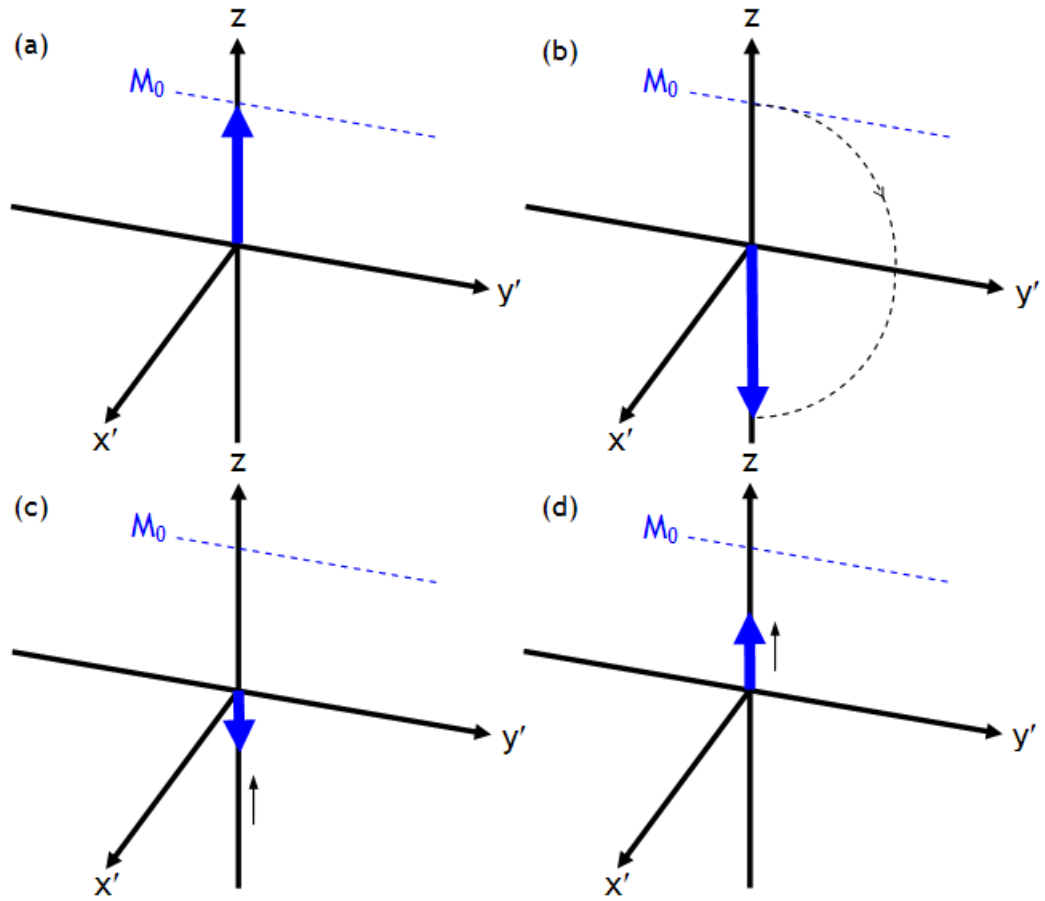

Figure 2.12 The net magnetisation vector, M_0, is orientated (a) along the direction of the applied static magnetic field, B_0, at thermal equilibrium. (b) Following a 180° radiofrequency preparation pulse the net magnetisation vector is inverted (c) After a time delay the net magnetisation returns to its equilibrium value (M_0) according to T1 relaxation. (d) After a further time delay the net magnetisation has recovered closer to M_0. This diagram is in the rotating frame at the precession of the Larmor frequency. The axes x′ and y′ represents the axes rotating at the Larmor frequency.

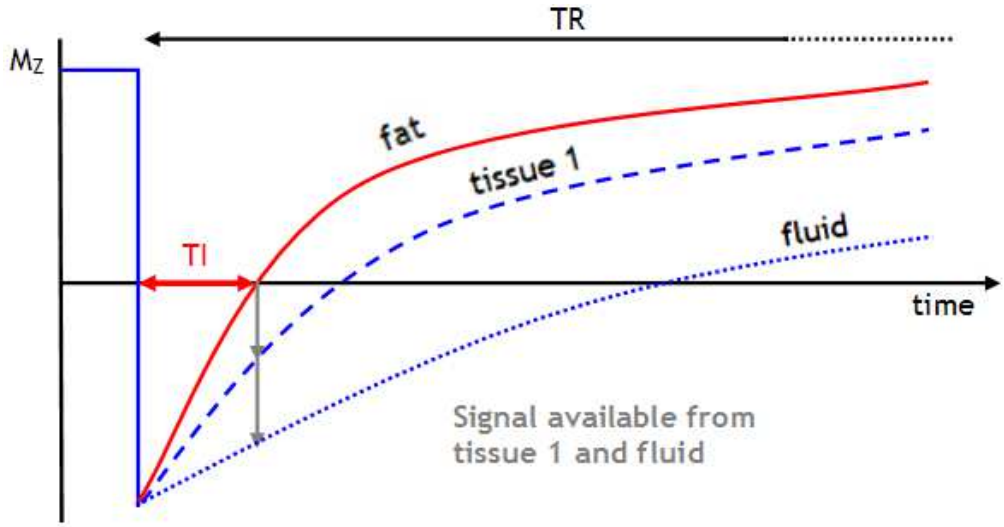

Figure 2.13 Recovery of the longitudinal magnetisation (M_z) for a short TI inversion recovery (STIR) sequence. The inversion time (TI) is chosen to null signal from fat, while signal from tissue 1 and fluid is still available. TR is the repetition time.

It is possible to suppress any tissue by selecting the appropriate TI so that the 90° RF pulse is applied at the null point of the tissue in question. The fluid attenuated inversion recovery (FLAIR) sequence is one which suppresses signal from fluid by having using a TI with a long time delay (Figure 2.14).

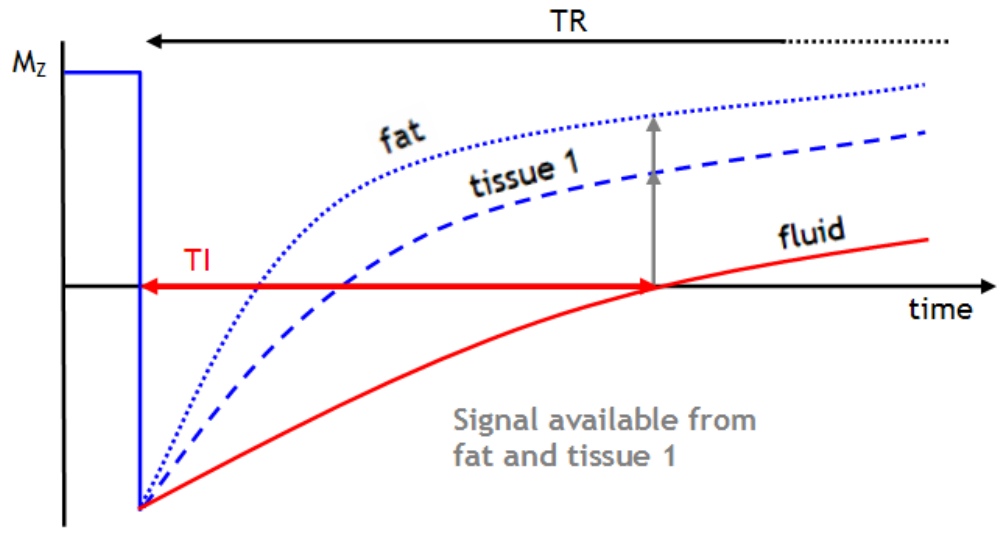

Figure 2.14 Recovery of the longitudinal magnetisation (M_z) for a fluid attenuated inversion recovery (FLAIR) sequence. The inversion time (TI) is chosen to null signal from fluid, while signal from fat and tissue 1 is still available. TR is the repetition time.

In inversion recovery sequences the MR signal from the magnetisation can be positive or negative. Typically, MR images are presented as a magnitude, without negative values, and the sign of the signal is not represented in the final image. In inversion recovery this could potentially lead to reduced contrast if different tissue types have a similar magnitude of signal, but a different sign. This can be overcome by a real-valued (true) inversion recovery sequence which reconstructs the image in a real instead of magnitude mode, presenting both positive and negative values. It achieves this by setting the background as mid-grey and ranging the image values from black to white. This achieves extremely good contrast particularly in brain tissues (McRobbie et al. 2003).

2.10.5 The gradient echo sequence

The development of fast imaging techniques has the purpose of both improving the efficiency of the clinical MRI scanner and to decrease artefacts associated with patient motion such as cardiac, respiratory and gastrointestinal. Since long

imaging times were required for the early T2 SE sequences, gradient echo sequences have been developed. Radically reduced scan times may be achieved in gradient echo sequences by using smaller excitation pulses so that TR can be reduced. Gradient echo sequences have inherently lower signal-to-noise ratio than SE sequences, but have a greater SNR per unit time. In a gradient echo sequence an RF pulse (typically of a lower flip angle than 90°) is applied and an FID is generated. As only one RF pulse is applied, the echo can be recorded more quickly, resulting in a shorter TE. If a lower flip angle is used the TR can also be shorter. The flip angle should be chosen such that a significant magnetisation is maintained in the transverse plane, while allowing a short recovery in the longitudinal plane. The optimum angle, called the Ernst angle (α_E), is given by,

Equation 2.5

$$\cos\alpha_E = \exp(-TR/T1)\,.$$

The lower flip angle has the effect that the signal is smaller and so less time is allowed to pass before the signal is recorded, as shown in Figure 2.15.

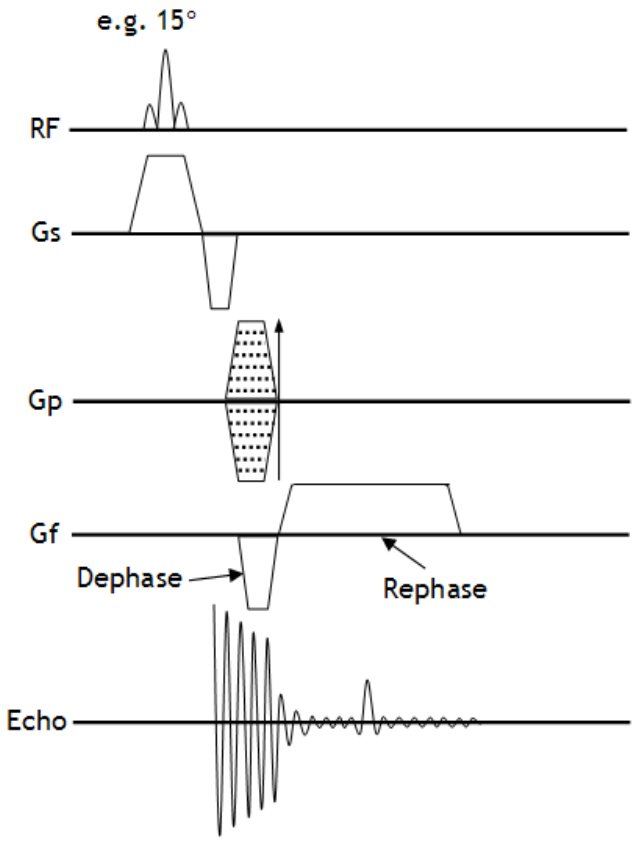

Figure 2.15 A gradient echo sequence, where RF is the radiofrequency pulse, Gs is the slice selection gradient, Gp is the phase encoding gradient and Gf is the frequency encoding gradient.

It can be seen from this figure that there is a negative portion of the slice selection gradient. The purpose of this is to rephase the MR signal to maximise the available signal. During the selective excitation process, the signal is being dephased by the gradient. A rephasing gradient of half the slice selection gradient is required to finish with all the spins in phase throughout the slice.

Most of the advanced pulse sequences are based on the gradient echo. This sequence is repeated for many different phase encoding gradients (e.g. 256 times). A low angle gradient echo sequence is fast enough to enable the acquisition of several images in a single breath hold.

Instead of applying a 180° pulse to form an echo signal, a gradient echo is formed by the reversal of the frequency encoding gradient following the 90° pulse.

When a negative magnetic field gradient is applied in a gradient echo sequence the nuclei experience different magnetic field strengths and so precess at different rates, becoming dephased in a structured manner. The nuclei are then rephased by a positive frequency encoding gradient.

Unlike the SE image contrast which is based on T2 decay, the gradient echo image contrast is dictated by T2*. The reason for this is the reversal of the polarity of the frequency encoding gradient in a gradient echo sequence, refocuses only the spins which have been dephased by the gradient itself, but does not reverse the spins dephased due to magnetic field inhomogeneities. In the SE sequence, these spins are reversed by the 180° pulse; therefore the signal-to-noise ratio is higher for SE sequence. Due to a greater dephasing of spins in gradient echo sequences than in SE techniques, gradient echo sequences possess a greater sensitivity to magnetic susceptibility effects. These susceptibility effects are most evident in the presence of metallic implants or a haemorrhage and at tissue-air interfaces. Magnetic susceptibility is discussed in more detail in Section 2.7.2.

2.10.6 The fast spoiled gradient echo sequence

When TR is shorter than T1 and T2 there is not enough time between successive RF pulses for the transverse magnetisation to fully decay. Therefore, at the time of the next RF pulse there is remnant transverse magnetisation. This can result in artefacts in gradient echo images as the transverse magnetisation in each successive TR interval contains different phase information. The fast spoiled gradient echo (FSPGR) sequence makes use of the spoiling technique, which eliminates the transverse magnetisation vector. RF spoiling is achieved by applying a phase offset to each successive RF pulse. This results in a corresponding phase shift in the transverse magnetisation vectors. A constant phase relationship between the transmitter and the receiver is possible via a phase-locked circuit and successive transverse magnetisation vectors cancel each other out. This is illustrated in the pulse sequence diagram Figure 2.16.

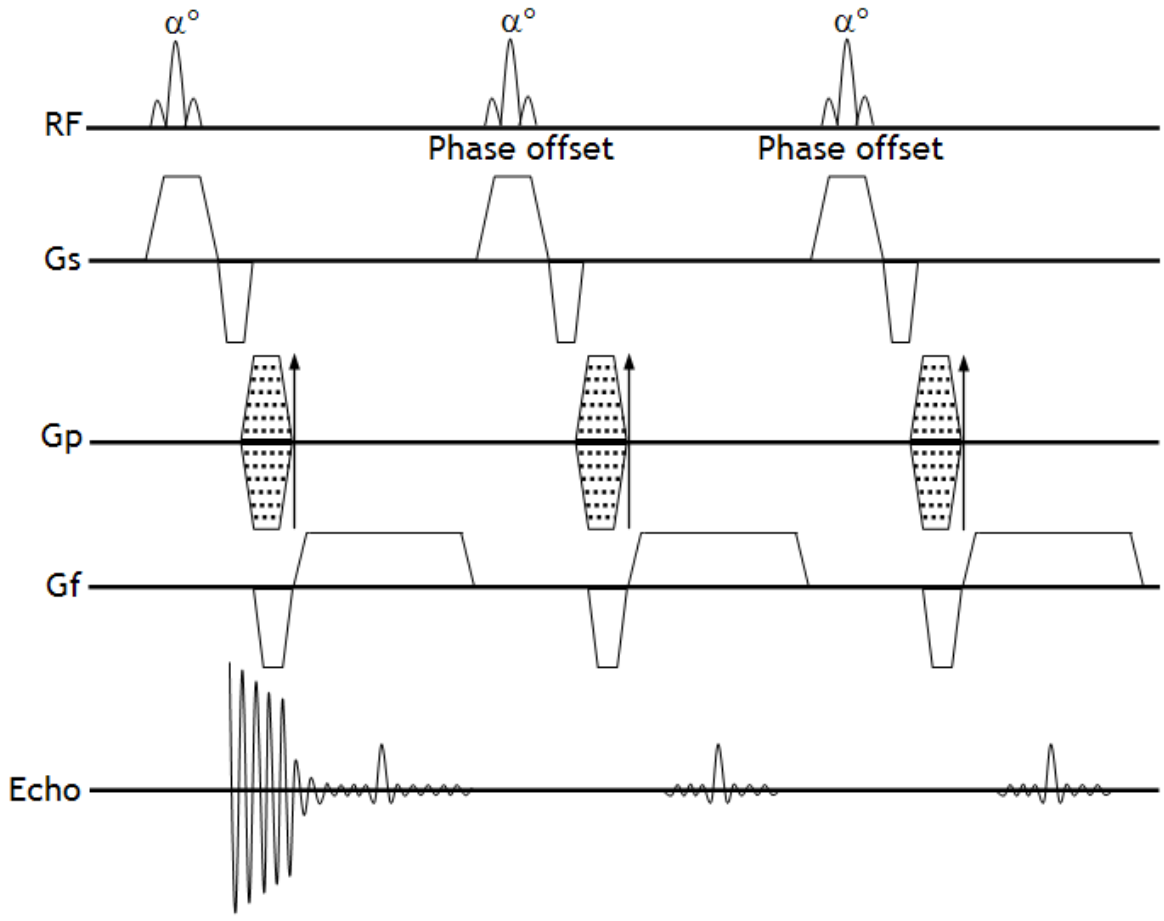

Figure 2.16 A fast spoiled gradient echo sequence, where RF are the radiofrequency pulses, Gs is the slice selection gradient, Gp is the phase encoding gradient and Gf is the frequency encoding gradient.

2.11 MRI instrumentation

A GE Signa HDxt 1.5T MRI scanner (GE Medical Systems, WI, USA) was employed for the investigations conducted in this thesis. An image of the MRI system is shown in Figure 5.2 of chapter 5. The components required for an MRI system include:

- A strong and homogeneous magnetic field to magnetise the subject
- Rapidly changing linear magnetic field gradients operating in the x, y and z axes.
- An RF system, which includes transmitting and receiving coils
- A computer system

The features of each of the components of an MRI system are discussed in the following sections.

2.11.1 Magnet and shim system

Requirements that determine the choice of magnet chosen are as follows:

- To reach the required operating field with satisfactory homogeneity over the imaging volume.
- Long and short term field stability
- Patient access (bore size)
- Cost (capital and operating)
- Physical size and weight

The basic MRI system architecture is illustrated in Figure 2.17.

An MRI system requires a static, stable and homogeneous magnetic field. The static magnetic field aligns the nuclei into low and high energy states. The magnet must provide a magnetic field of the required strength and must be uniform across the imaging volume required. The magnetic field can be produced by permanent, electromagnetic or superconducting magnets.

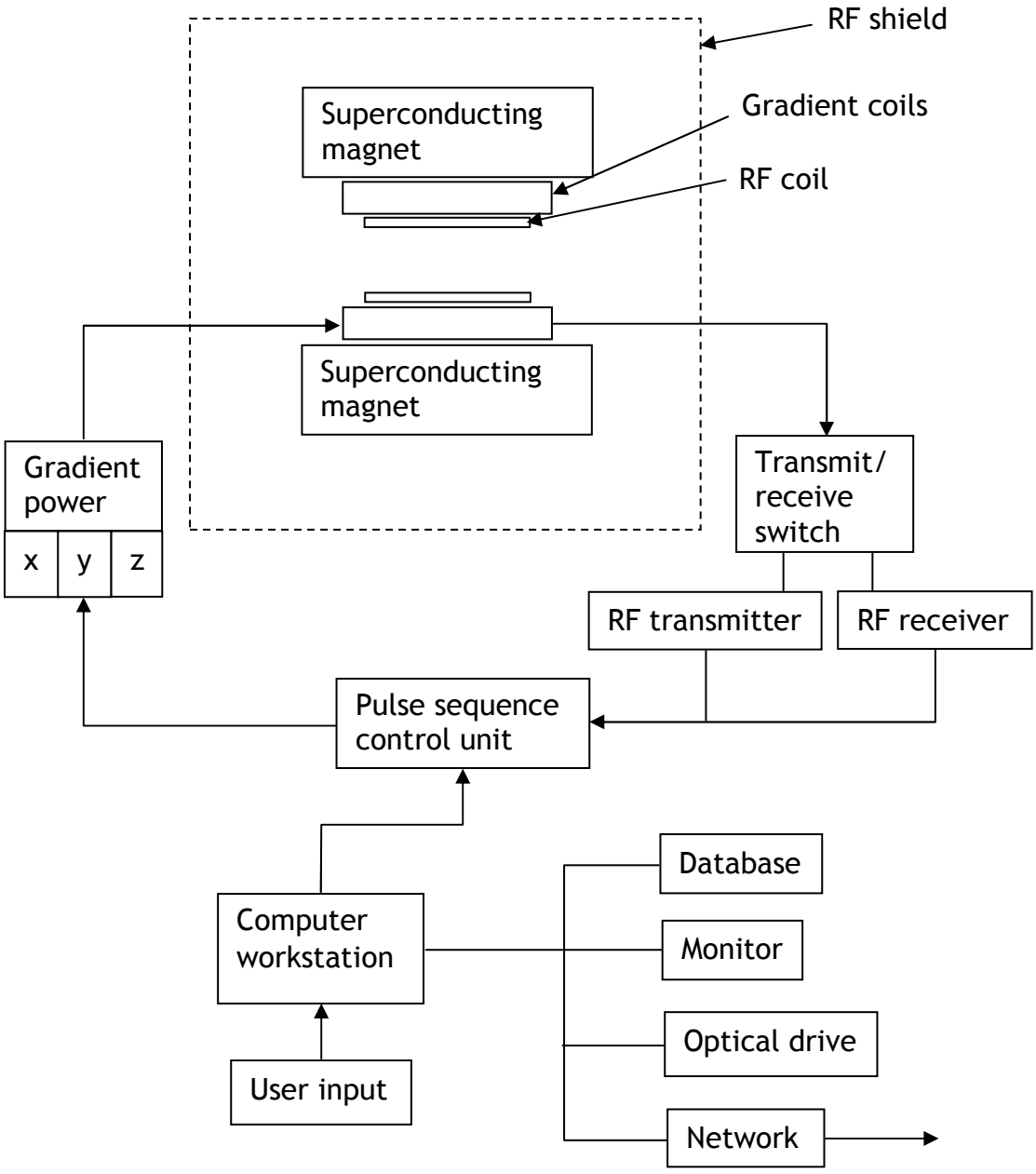

Figure 2.17 Basic components and architecture of an MRI system.

To generate the high field strength of superconducting magnets electric current passes through large coils. The components of a superconducting magnet are illustrated in Figure 2.18. The conducting wires of the coils are made from a niobium-titanium (NbTi) alloy embedded in a copper matrix. NbTi wire loses

resistance to current flow when cooled close to absolute zero, i.e. they become superconducting. An electrical current flowing in a loop of superconducting wire, maintained below its transition temperature, will continue to circulate indefinitely. A cryogen bath containing liquid helium surrounds the coils to provide cooling. The liquid helium coolant slowly boils off over time and needs refilled. Superconducting magnets are expensive to purchase, but have low electrical power requirements because of the minimal electrical resistance.

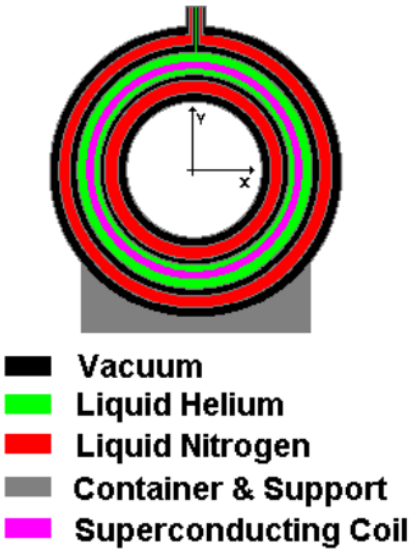

Figure 2.18 Cross sectional view of a superconducting magnet (Hornack 2000).

The fringe field is the stray magnetic field which extends outside the magnet in all three directions. Its strength depends on the magnet type and the field strength, the higher the field strength, the larger the fringe field. Two methods are available to compensate for this effect: passive and active shielding. Passive shielding can be achieved by either lining the walls of the scan room in steel or enclosing the magnet within a steel cage. With active shielding, additional superconducting coils are positioned outside of the magnet. These coils produce a magnetic field to oppose the fringe field via destructive interference.

To correct for magnetic inhomogeneities, other current carrying coils, known as shim coils, are positioned around the magnet in a process called active shimming. The shim coils can either be at room temperature or superconducting. Passive shimming is the method of mounting small ferromagnetic metal sections at appropriate positions around the magnetic bore, and a very homogenous field may be obtained.

2.11.2 Magnetic field gradients

Magnetic field gradients are discussed in more detail in Section 2.8. Gradients coils are used to provide linear gradients in all three co-ordinate axes, to spatially encode the positions of the MRI spins by changing the magnetic field across the imaging volume such that the Larmor frequency varies as a function of position. To achieve accurate spatial encoding, linear variation in the gradient field is required. Linearity decreases towards the edge of an imaging volume resulting in geometric distortion. Some manufacturers warp images after reconstruction to correct for gradient nonlinearities (see Chapter 3).

Gradient amplifiers generate the electrical currents and voltages needed to produce the pulsed gradient magnetic fields in the gradient coils. These pulses may induce eddy currents in the surrounding metallic structures of the magnet, which can introduce artefacts in the images unless they are controlled. The amplifier must be able to generate large electrical currents through the coils rapidly from zero to the maximum and then returning to zero. The pulse sequence control unit receives the scan details from the scanner software and, as well as controlling the gradients, controls the magnet, the RF transmitter and receiver and the RF coil switches.

A pulse sequence control unit co-ordinates the complex timing control of sequences including the function of the gradient amplifier and coils. This programmer is typically a separate, microprocessor controlled array of sequencers and memory. It converts the user defined sequence parameters into a digital representation of the requested gradients and RF pulses.

To achieve the switch in the direction of the linearly varying magnetic fields very quickly to implement certain pulse sequences, such as echo planar imaging, the gradients should be high power, with low inductance, to enable rapid switching, and be highly linear to minimise discrepancies in the spatial encoding of the MR image. The time taken for a field to change from zero to the peak amplitude is known as the rise time and is typically in range of 200 to 1000 μs. The gradient slew rate is calculated by dividing the peak gradient amplitude by the rise-time and is typically in the range of 20 to 150 $Tm^{-1}s^{-1}$.

2.11.3 Radiofrequency system

The RF system comprises a transmitter, coil and receiver. The transmitter generates pulses of current at the Larmor frequency. When this current is applied to the RF coil, an alternating B_1 field is generated, which rotates the net magnetisation vector. This small MRI signal needs to be boosted using a low-noise preamplifier before it is sent to the receiver. The MRI signal contains a narrow frequency range, but is contained within the Larmor frequency. The receiver digitally demodulates this signal, by removing the high frequency carrier. The design of the RF coil can range from a simple circular single turn coil, to a birdcage arrangement or a multi-element array coil which increases the uniformity and homogeneity.

The coils mainly used in the investigations of this thesis were surface coils. These RF coils are known for their improved signal reception since they are sensitive to signals close to the surface. They may, however, be optimised to image deep-body structures. These coils were multi coil array which means they contained a number of overlapping coils each with their own receiver detection circuitry. Multi-array coils increase the available imaging surface area, while maintaining the SNR obtainable equivalent to a single coil. Since acquisition occurs in each element simultaneously there is no increase in acquisition time required.

An RF signal at the resonant frequency is transmitted by the RF transmit coil to the RF amplifier and then to the RF monitor. The received RF signal is amplified before being passed to the array processor for Fast Fourier Transform. Some coils operate as both a transmit and a receive coil. If the transmit and receive coils are different then the receive coil is required to be detuned and the preamplifier switched off so that the large transmit coil does not destroy the electronics. The transmit coil is separated from the gradient coils by an RF shield.

The high power excitation of the nuclei is achieved by a short lasting RF pulse at a frequency close to or at the Larmor frequency. It should be noted that it is not the transmission and reception of radio waves which are used by the RF system, but the magnetic induction from the oscillating magnetic fields.

A Faraday cage is used to prevent interference from any external sources of RF. This consists of the room which houses the MRI scanner being lined on all sides with a copper, aluminium or steel sheeting. The electrical connections between the magnet and the electronic cabinets are connected via electrical filters through a panel in the RF shield. The windows in the MRI room are embedded with wire and the doors are required to make an electromagnetic seal with the frame. Tubes or fibre-optic cables can be passed into the MRI room via waveguides, which are metal pipes of a specific length and diameter through which RF signals below a certain frequency cannot pass.

2.11.4 Image processor and computer system

The data from the receive coils is then transmitted to an image processor which assigns a grey scale value in the image with a brightness relative to the nuclear spin density at the particular pixel location. A computer controls all the components of the MRI scanner and provides the user interface. The patient data and images are stored on the database before being stored on removable media or networked to a server for subsequent retrieval and analysis.

2.12 Clinical MRI

MRI is the imaging modality of choice for many clinical studies since it provides excellent soft tissue contrast to differentiate tissue types. In general, the more unbound water in a tissue the longer the T1 relaxation time. This is because, in fluids, the rapidly moving nuclei have fewer opportunities to interact and exchange energy. Different body tissues have different relaxation times, as shown in Table 2.1 (Atlas 1995, McRobbie et al. 2003, Reimer et al. 2010). For example, in the brain, the cerebrospinal fluid is mainly water and so has a very long T1, of the order of several seconds, whereas white matter has a great deal less water and so has a T1 of less than a second. Typically, tumours have more water than normal tissue and therefore have an intermediate T1 time constant. It is the difference in relaxation times that can be exploited to produce MR images which can be used in a clinical diagnosis.

Table 2.1 Selection of T1 and T2 values for tissues at 1.5 T, measured in vivo from human tissues (Altas 1995; McRobbie et al. 2003; Reimer et al. 2010).

Tissue	T1 (ms)	T2 (ms)
White matter	560	82
Grey matter	1100	92
Cerebrospinal fluid	2060	2200
Muscle	1075	33
Fat	200	165
Liver	570	43
Spleen	1025	62

2.13 MRI Safety

When undergoing an MRI scan there are three types of magnetic and electromagnetic fields which an individual will be exposed to: the static magnetic field, time-varying magnetic field gradients and RF magnetic fields produced by the RF coils. There is no evidence of any short or long term biological effects from MRI scanners up to field strengths of 8 T operating within safe exposure limits (MHRA 2007).

The primary hazard associated with the static magnetic field is ferromagnetic attraction. When a ferromagnetic object (one containing iron or steel) is brought within close range of a magnet it will experience a force. If the object is brought sufficiently close, this can turn an object into a dangerous projectile. Scalpels, scissors, and wheelchairs can be of particular danger and a fatality has occurred when a patient was struck by an oxygen cylinder (McRobbie et al. 2003). The larger the object the stronger the forces involved. Even small object such as paper clips and hair pins have a terminal velocity of approximately 40 mph when pulled into a 1.5 T magnet and could inflict serious injury. A twisting force known as torque occurs when the magnet attempts to align the long axis of the object with the magnetic field lines and can also result in injury.

Surgical implants such as vascular aneurysm clips can move in vivo, which can have potentially life threatening consequences, since dislocation by magnetic attraction presents the risk of haemorrhage. This risk can be minimised by careful screening of patients, staff and equipment entering the MRI unit. When RT equipment such as immobilisation is to be brought into the MRI environment this equipment must be first checked using a strong hand held magnet outside of the MRI room. If RT staff are required to assist in patient set-up in MRI they must first be assessed to ensure they are safe to enter the MR controlled area.

Certain implantable devices can be affected by the RF radiation of the MRI scanner, such as closing the reed relay of pacemakers switching it to the asynchronous mode. Magnetic attraction can also occur when implants contain ferromagnetic material.

Foreign ferromagnetic bodies may be permanently residing in the body after an accident and could be potentially dangerous if they were to become dislodged when in a strong magnetic field. X-rays can be taken prior to an MRI to confirm the presence of such materials. Some cosmetics contain ferromagnetic pigments which can distort MR images and can cause irritation if attracted to the eye. Eye cosmetics should therefore be removed before undergoing an MRI scan.

The main safety concern associated with the RF fields used in MRI is thermal heating, which can lead to heat stress induced current burns and contact burns. Induced currents can result in power dissipation within the body's tissues and therefore the accumulation of energy over time and a rise in body temperature. Absorption of energy from MRI RF fields causes an increased oscillation of molecules and the generation of heat. In human tissue this will result in an increased blood flow to remove excess heat, which is dissipated mainly through the skin. When immobilisation masks are used in MRI this can reduce the body's normal cooling mechanism and so such patients should be carefully monitored. A rise of 1°C is generally acceptable to a healthy person. Heat stress is of greater concern for patients suffering from hypertension, pregnant women, or those on certain drugs as it may impede their thermoregulatory response.

MRI systems cannot monitor RF exposure; therefore, it is necessary to measure RF absorption. The specific absorption rate (SAR) is defined as the total power in

watts per kilogram of tissue. The scanner monitors its RF transmitter output and calculates an average SAR based on the patient's weight. The exposure limits for SAR depend on the anatomy being imaged. For the whole body the SAR must be less than 0.4 Wkg^{-1}. MRI scanners limit the temperature rise experienced by subjects by limiting SAR. Heat stress can also be controlled by considering the ambient temperature, air flow, clothing and humidity.

There is also the risk that patients may receive burns through the coupling of RF energy through wires such as those used for ECG monitoring. Care must be taken to ensure cables are not formed into loops and that pads are positioned between cables and the patient prior to imaging.

The time-varying magnetic fields generated by the gradients can induce electrical currents in conducting tissues, which may exceed the nerve depolarisation threshold, resulting in peripheral nerve stimulation (PNS). While this can cause discomfort it is not harmful when the stimulation occurs in motor nerves or skeletal muscle. There is the possibility, however, that it may stimulate cardiac muscle which would present a hazard. Animal studies have shown that respiratory stimulation occurs in the order of three times the PNS threshold, while cardiac stimulation requires 80 times that required for PNS. Some modern MRI scanners have a stimulation monitor which can alert operators of the likelihood of causing PNS (McRobbie et al. 2003). While there is no evidence that the time-varying magnetic field gradients can harm the foetus or embryo, it is considered prudent to avoid exposure of pregnant women during the first trimester.

The switching of the gradient fields also results in acoustic noise. When the alternating low-frequency currents which flow through the gradient coils are immersed in the high static magnetic field, forces are exerted on the gradient coils, generating sound waves. The noise is caused by the movement of the coils against their mountings. The volume of the noise can reach uncomfortable or even dangerous levels to subjects undergoing an MRI scan (Price et al. 2001). Exposure to loud noise can result in a shift in the threshold of hearing which may be temporary or permanent if the exposure is very loud, prolonged or frequently repeated. Ear protection is required during MRI scanning to reduce the acoustic noise to acceptable levels.

The space within the magnet can be restrictive resulting in claustrophobia to the extent that it may require an examination to be terminated. This may be mitigated by optimising patient comfort and offering reassurance between scans by way of the audio equipment. RT immobilisation within MR is likely to increase the feeling of claustrophobia. It may be necessary to use light sedation or for a carer who has been appropriately screened to remain in contact with the subject during the MRI scan. Lighting and careful design of the MRI scanner can also help to reduce the effects of claustrophobia.

3 Evaluation of an inline three-dimensional MRI geometric distortion correction algorithm for radiotherapy

3.1 Introduction

This chapter comprised of a study evaluating a three-dimensional (3D) distortion correction algorithm and investigates the distortion error values in the context of defining a safe scanning range for radiotherapy (RT) planning.

One of the most important aspects of RT is accurately defining the gross tumour volume and its relationship to organs at risk. Current external beam RT planning techniques normally use computed tomography (CT) datasets to obtain axial slices of the body. Due to the superior soft-tissue contrast of magnetic resonance imaging (MRI), many tumours are better visualised and there is improved localisation of adjacent soft tissue compared to CT. MRI is therefore recognised as being a useful addition to the RT process and many publications have reported modified tumour volumes using MR compared to CT in prostate carcinomas (Charnley et al. 2005; Khoo et al. 2006; Sannazzari et al. 2002) and for brain carcinomas (Khoo et al. 2000).

A major challenge facing MRI is geometric distortion, which can have serious consequences if the images are used in therapy where geometric accuracy is very important, such as surgical guidance or RT planning. It is known that MR distortion effects are inversely proportional to the receiver bandwidth. A publication investigating the degree of bandwidth associated distortions recommends a receiver bandwidth of greater than or equal to $\pm$ 30 kHz to minimise distortion and chemical shift in MR images (Moore et al. 2004).

Geometric distortion is also dictated by the magnitude of the magnetic field and the gradient of the magnetic field. Data on the peak magnetic field, peak gradient of the magnetic field and peak force product for the GE Signa 1.5 T HDx MRI scanner, which was used in the experiments of this thesis, is contained in Table 3.1. The location of the fringe field maximum for this table is shown in Figure 3.1 (General Electric Company 2009).

Table 3.1 Maximum magnetic field (B), maximum gradient of the magnetic field and the maximum force product data and their spatial locations for the Signa 1.5 T HDx series MRI scanner. R and Z locations shown in Figure 3.1. Reproduced from (General Electric Company 2009).

Field	R(m)	Z(m)	B field (T)	Gradient (T/m)	Product (T^2/m)
Peak B	0.319	0.627	1.9	3.4	6.5
Peak gradient	0.391	0.807	1.4	7.4	10.5
Peak product (B × Gradient)	0.369	0.766	1.6	6.9	11.3

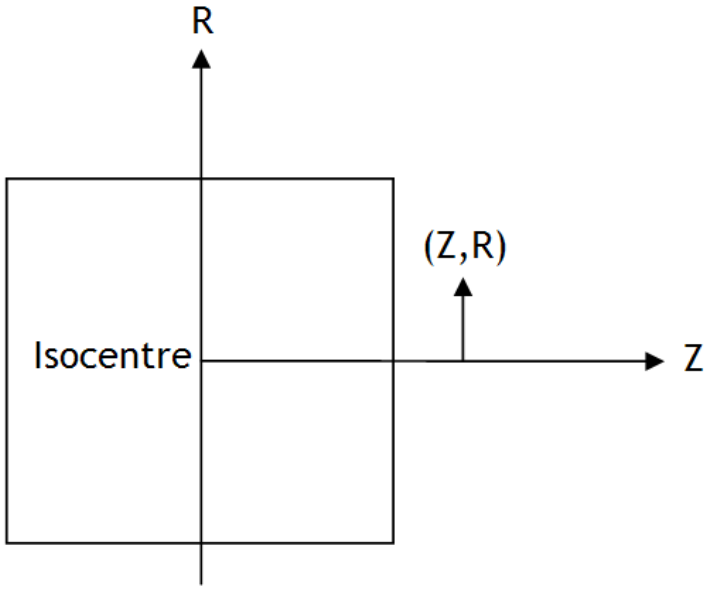

Figure 3.1 Location of fringe field maximum for data of Table 3.1. Reproduced from (General Electric Company 2009).

Gradient non-linearity is the non-ideal nature of the magnetic field produced by a gradient coil. Gradient non-linearity results in spatial distortion of the images. GE (GE Healthcare, WI, USA) supplies the results of gradient linearity response for the Signa HDxt scanner.

The differential linearity (DL) is defined as,

Equation 3.1

$$DL = \left| \frac{(G_{actual} - G_{ideal})_{\max}}{G_{ideal}} \right| \times 100\%$$

where G_{actual} is the calculated actual gradient strength at the spherical field of view (FOV) and G_{ideal} is the calculated ideal gradient strength at the spherical FOV.

The relative linearity (RL) is defined as,

Equation 3.2

$$RL = \left| \frac{(B_{actual} - B_{ideal})_{\max}}{G_{ideal}.R} \right| \times 100\%$$

where B_{actual} is the calculated actual field strength at the spherical FOV due to the gradient coil, B_{ideal} is the calculated ideal field strength at the spherical FOV due to the gradient coil and R is the radius of the spherical FOV.

The gradient non-linearity values are recorded in Table 3.2.

Methods of 3D distortion correction have been published (Breeuwer et al. 2001, Doran et al. 2005, Wang et al. 2004a); however, this requires lengthy measurements, exporting the data for offline manipulation and time consuming computer programming. The manufacturer Siemens provides a 3D distortion correction, although this has only been evaluated in the context of head imaging (Karger et al. 2006).

The two-dimensional (2D) distortion correction algorithm on the MRI scanner at the Beatson West of Scotland Cancer Centre (Beatson) resolves volumes on a slice-by-slice approach and is applied automatically on all GE MRI systems (GE Signa HDx, 1.5T MRI scanner, GE Healthcare, WI, USA). Distortion is amended on each slice and applied independently of other slices. Therefore, with 2D correction there is no through-plane adjustment.

A 3D distortion correction, known as 3D GradWarp, is applied as a post-processing step and operates in the following way. The 2D corrected image dataset is read by the software and the 3D GradWarp corner points are calculated from the 2D image corner points to define the processing volume. Spatial error in the slice direction (through-plane) is determined from a look-up table. This table contains the gradient field maps measured at the design stages

of the system. The software determines the shift in each pixel due to the gradient nonlinearity. It then calculates the correct pixel location from measurements of the gradient field maps and uses a 4-point cubic spline to remap these pixels. Both distortion correction algorithms are gradient coil dependent and are therefore system-related distortion corrections. The correction is the same for all systems with the same gradient coil type.

Table 3.2 Non-linearity results for the GE Signa HDXt MRI scanner, where FOV is the spherical field of view.

	Differential linearity			Relative linearity		
FOV (cm)	X	Y	Z	X	Y	Z
12	2.2%	2.1%	0.3%	0.7%	0.7%	0.1%
14	3.1%	2.9%	0.5%	1.0%	1.0%	0.1%
16	4.1%	3.9%	0.6%	1.3%	1.3%	0.2%
18	5.2%	5.0%	0.9%	1.7%	1.6%	0.3%
20	6.6%	6.3%	1.2%	2.1%	2.0%	0.3%
22	8.1%	7.8%	1.5%	2.6%	2.5%	0.4%
24	9.8%	9.5%	2.0%	3.1%	3.0%	0.5%
26	11.8%	11.4%	2.6%	3.7%	3.6%	0.7%
28	14.0%	13.5%	3.2%	4.4%	4.2%	0.8%
30	16.4%	15.9%	4.1%	5.1%	4.9%	1.0%
32	19.1%	18.6%	5.0%	5.9%	5.7%	1.2%
34	22.1%	21.5%	6.2%	6.8%	6.5%	1.5%
36	25.3%	24.7%	7.5%	7.7%	7.4%	1.8%
38	28.8%	28.2%	9.1%	8.7%	8.4%	2.1%
40	32.7%	32.0%	10.9%	9.8%	9.5%	2.5%
42	36.8%	36.1%	13.0%	11.1%	10.7%	3.0%
44	41.2%	40.5%	15.4%	12.4%	12.0%	3.5%
46	45.9%	45.3%	18.1%	13.8%	13.4%	4.1%
48	50.9%	50.3%	21.2%	15.3%	14.9%	4.7%
50	56.2%	55.6%	24.6%	17.0%	16.6%	5.4%

The purpose of this study was to investigate the accuracy of this inline 3D distortion correction algorithm, provided by the manufacturer (GE Healthcare, WI, USA) and define a safe scanning range for use in RT planning. A range of test objects were used to determine the accuracy of the 3D distortion correction algorithm.

3.2 Methods

3.2.1 MRI test objects

The first phantom used in the experiments of this chapter was the Eurospin TO3 phantom (Diagnostic Sonar Ltd., Livingston, UK). This test object contains 16 pairs of crossed Perspex rods in a solution of copper sulphate ($CuSO_4$). A diagram of the phantom can be seen in Figure 3.2.

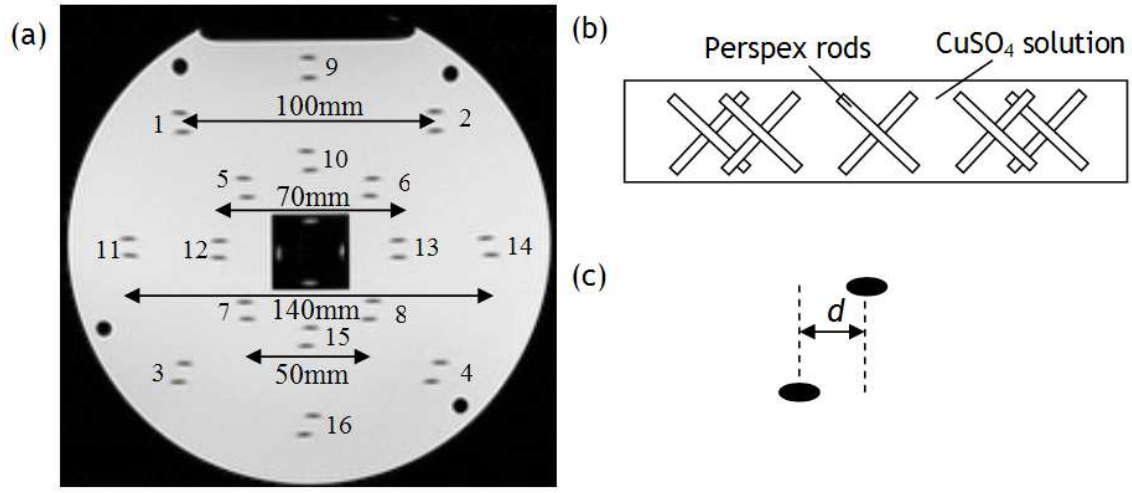

Figure 3.2 The Eurospin TO3 test object in the (a) axial plane, (b) sagittal plane and (c) a close up of the rod separation, *d*.

A slice position test object by MagNET (MagNET, London, UK) was also used in this study. This is a Perspex phantom filled with a paramagnetic solution (0.7 g $CuSO_4$/litre distilled water) with two 90° angled glass rods and four parallel glass rods. A schematic diagram of this phantom is shown in Figure 3.3.

Finally, a bespoke phantom was constructed using LEGO® bricks. LEGO® bricks are made from acrylonitrile butadiene styrene and are injection moulded to a tolerance of less than 20 µm (Hyer et al. 2012). It is an inexpensive phantom material and can be quickly and easily assembled into different shapes and sizes in a modular fashion. Therefore, when LEGO® bricks are immersed in fluid, they make an excellent building material for MRI test objects.

A grid structure was formed by building LEGO® bricks in a simple layered structure on top of base-plates and affixed in position with bricks at the top.

This grid structure was positioned in a water tank. An image of the test object can be seen in Figure 3.4.

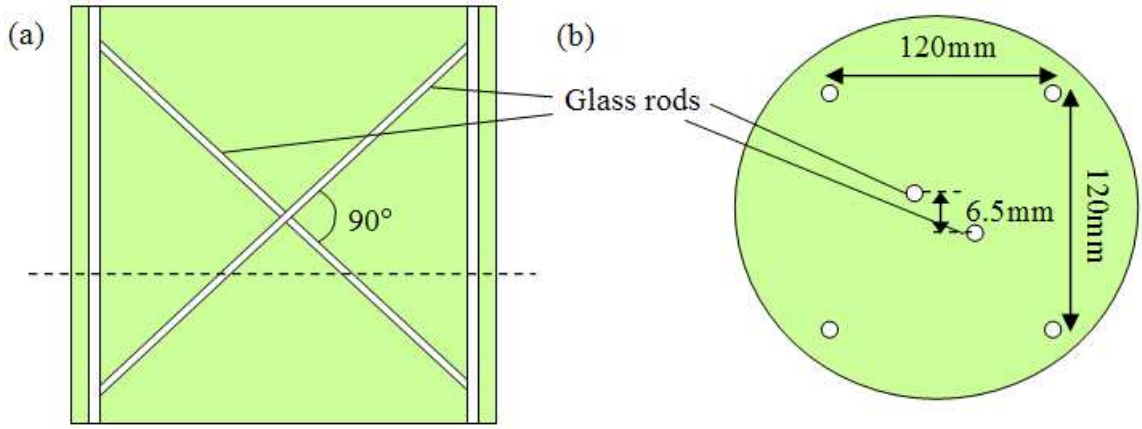

Figure 3.3 Schematic of the MagNET slice position phantom in the coronal (left) and axial (right). The axial plane is shown at the position of the dashed line.

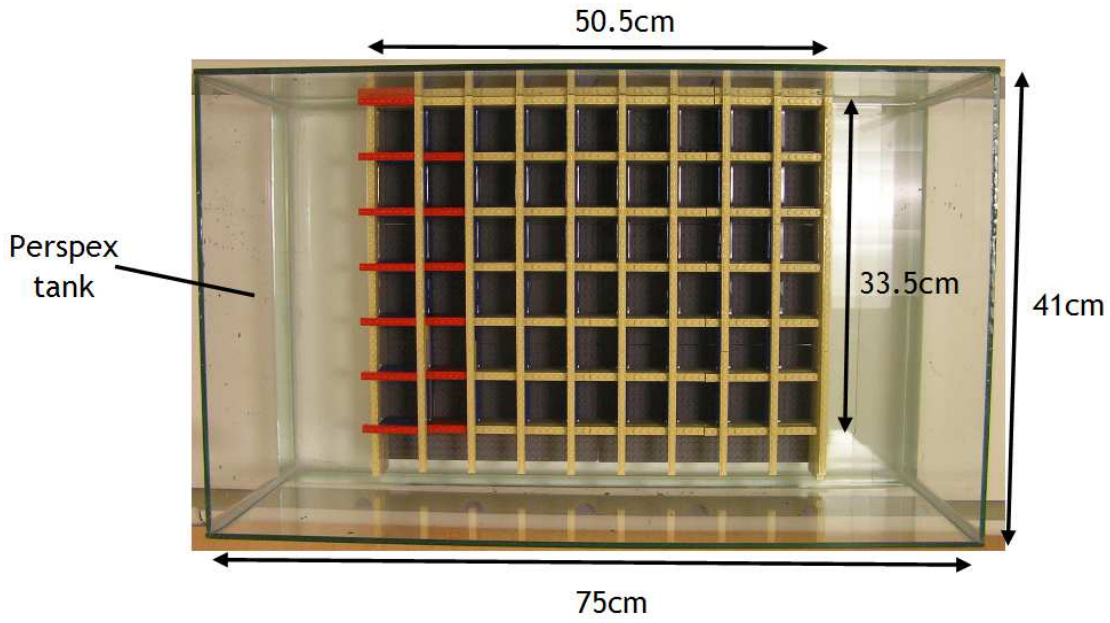

Figure 3.4 Overhead view of LEGO® phantom, with dimensions. Height of phantom is 23 cm.

All MRI measurements in this study were made on a GE Signa HDxt 1.5T scanner (GE Healthcare, WI, USA).

3.2.2 TO3 test object measurements

A measurement of slice position error was performed in accordance with IPEM Report 80 (IPEM 1998) using the Eurospin TO3 phantom (Diagnostic Sonar Ltd., Livingston, UK) as shown in Figure 3.2. Measurements were taken comparing the

2D and 3D distortion correction algorithms. Rod separation was measured as the separation of each of the crossed Perspex rods using the tools on the GE Advantage Windows workstation (GE Healthcare, WI, USA). The slice position error can be calculated by taking the mean of the rod separation measurements and dividing by two. A T1-weighted SE sequence with a repetition time (TR) of 1000 ms, an echo time (TE) of 30 ms, a FOV of 250 $\times$ 250 mm^2 and a bandwidth of $\pm$ 11.9 kHz. with an echo time (TE) of 30 ms and a repetition time (TR) of 1000 ms with a slice thickness of 5 mm and no slice gap over a 250 $\times$ 250 mm^2 FOV, with a matrix size of 256 $\times$ 256 and bandwidth of $\pm$ 11.9 kHz was acquired in the axial plane with the centre of the Eurospin phantom positioned within 4.5 mm of isocentre. This bandwidth was chosen since it is thought this would give a worst case scenario as it is less than the recommended $\pm$ 30 kHz to minimise distortion (Moore et al. 2004). Interleaved 5 mm thick slices with zero spacing between slices were taken with the central slice at the centre of the test object. The couch was moved to position the TO3 phantom 75 mm to 225 mm superior and inferior to the isocentre in increments of 25 mm. A two-tailed t-test was performed to evaluate statistically significant differences between the 2D and 3D distortion correction algorithms in this and other experiments in this chapter. The null hypothesis was rejected when the *p* value was less than 0.05.

3.2.3 Slice position test object measurements

To determine the distortion correction accuracy of 3D GradWarp with multiple slices the MagNET (MagNET, London, UK) slice position phantom was used (Figure 3.3). The test object was positioned at the scanner isocentre and images were acquired using the same imaging parameters as section 3.2.2 except the FOV was 256 x 256 mm^2 in accordance with the MagNET test instructions and IPEM Report 80 (IPEM 1998). The centre of the phantom was found by positioning the object until the rod separation was zero. Interleaved 5 mm thick slices with zero spacing between slices were taken with the central slice at the centre of the test object. The intersection of the two 90° angled rods was checked for coincidence with the scanner isocentre in three planes using the measurement tools on the scanner interface. The phantom was then repositioned as necessary until it was centred in all three planes. This was repeated with the centre of test object positioned at 50 mm increments up to 200 mm superior and inferior

to the scanner isocentre. With the phantom positioned at isocentre, the average distance between the four parallel glass rods was measured at isocentre and at 70 mm inferior and superior to isocentre for the 2D and 3D corrected datasets. Dividing this average value by the true distance of the rod separation gave a correction factor.

The measured slice position, SP_{meas}, was determined using the following expression,

Equation 3.3

$$SP_{meas} = \frac{\sqrt{(d \times c)^2 - s^2}}{2}$$

where d is the measured separation of the angled rods, c is the correction factor and s is the rod separation which is equal to 6.5 mm.

Finally, the magnitude of the slice position error for each slice was calculated by subtracting the actual slice position from the measured slice position.

3.2.4 In-plane distortion measurements using the slice position test object

Using the MagNET (MagNET, London, UK) slice position test object shown in Figure 3.3 the in-plane distortion was measured for the top left parallel rod. This was achieved using the report cursor tool on the GE (GE Healthcare, WI, USA) Advantage Windows workstation which indicates the coordinate location. The top left parallel rod location was measured at the scanner isocentre plane for both the 2D and 3D distortion corrected scans. At isocentre, distortion is at a minimum and so this coordinate location became a reference for all other measurements. Using the slice position datasets (of section 3.2.3) the location of the top left parallel rod was measured for slices with the phantom centred at isocentre and at 200 mm inferior and superior to isocentre. An in-plane error was calculated as the difference between the isocentre reference location and all other slice positions. This difference was measured in both the right-left and anterior-posterior directions. These measurements were possible since the test object was not adjusted between the scans acquired at the scanner isocentre

and those at 200 mm from isocentre. Certain slice positions gave more than one measurement and an average slice position error was calculated.

3.2.5 LEGO® phantom measurements in the coronal plane

To test the 3D GradWarp correction algorithm across a 33.5 $\times$ 48 cm FOV the bespoke LEGO® phantom was used Figure 3.4. The LEGO® dimensions were first measured using a digital calliper with an accuracy of $\pm$ 0.02 mm. These measurements were then confirmed by scanning the phantom in a GE Hi-Speed CT scanner (GE Healthcare, WI, USA). The phantom was aligned in the axial plane and aligned using the laser positioning system. Distances between the bricks were measured using the tools on the RT planning system Eclipse version 8.6.15 (Varian Medical Systems Inc., CA, USA). These results were compared to a coronal T1-weighted MR dataset close to the isocentre plane with a bandwidth at a typical clinical setting of $\pm$ 31.2 kHz using the Eclipse treatment planning system.

Using a T2-weighted short TI (inversion time) recovery (STIR) sequence the water was shown to be bright against the signal void of the bricks. Scans were acquired at a slice thickness of 10 mm with zero spacing, a TE of 37.7 ms, TR of 3660 ms and TI of 145 ms at maximum FOV of 48 $\times$ 48 cm^2, resolution of 384 $\times$ 224 and a bandwidth of $\pm$ 31.2 kHz. This sequence was chosen because it was used clinically for whole body imaging. A clinical sequence was chosen for this phantom, rather than the settings used for the QA phantoms since this was a bespoke phantom and so a clinical sequence could be chosen.

The extent of the warping at the central furthest edge superior and inferior to the isocentre was determined by imaging a catheter filled with saline within a recess of the table. This same catheter was first positioned at the isocentre plane where there is very little image distortion. Taking the difference between the slice positions at which the saline filled catheter was visible gave a measure of the coronal through-plane distortion.

3.3 Results

3.3.1 TO3 test object measurements

Figure 3.5 shows the slice position error values with the TO3 phantom positioned superior and inferior to isocentre. The error bars are given by the standard deviation of the slice position error measurements for the 2D and 3D distortion correction algorithms.

From Figure 3.5 it can be seen that there is a general trend of increased slice position error with distance from isocentre, as expected. Slice position error is greater in the inferior than the superior direction. The reason for this may be due to differences in the gradient performance or shimming accuracy in the superior and inferior directions. A maximum slice position error of 2.3 mm was found at 175 mm inferior to isocentre for both the 2D and 3D correction. The largest slice position error superiorly was at the maximum extent of 225 mm from isocentre with a value of 1.7 mm for the 2D and 3D correction. A two tailed t-test gave a p value = 0.58 confirming that the difference between the 2D and 3D distortion algorithms were not statically significant when imaging with three slices.

Bland Altman plots were also graphed at 25 mm intervals from 75 mm to 225 mm superior and inferior to isocentre. Using this data the mean difference between the 2D and 3D correction algorithms was plotted along with the standard deviation (SD) of the difference between the two correction algorithms shown as the error bars (Figure 3.6). This shows the mean difference value for these graphs is approximately zero for all plots. The size of the SD of the difference between the two correction algorithms is approximately the same for all the plots except for the more extreme positions where the SD increases. This increase in SD is expected furthest from the isocentre since the geometric distortion is greatest at these positions.

Since the mean difference between the 2D and 3D correction measurements is approximately zero from 225 mm inferior to 225 mm superior this is further evidence that the difference between the two correction algorithms is minimal in the axial plane using three slices.

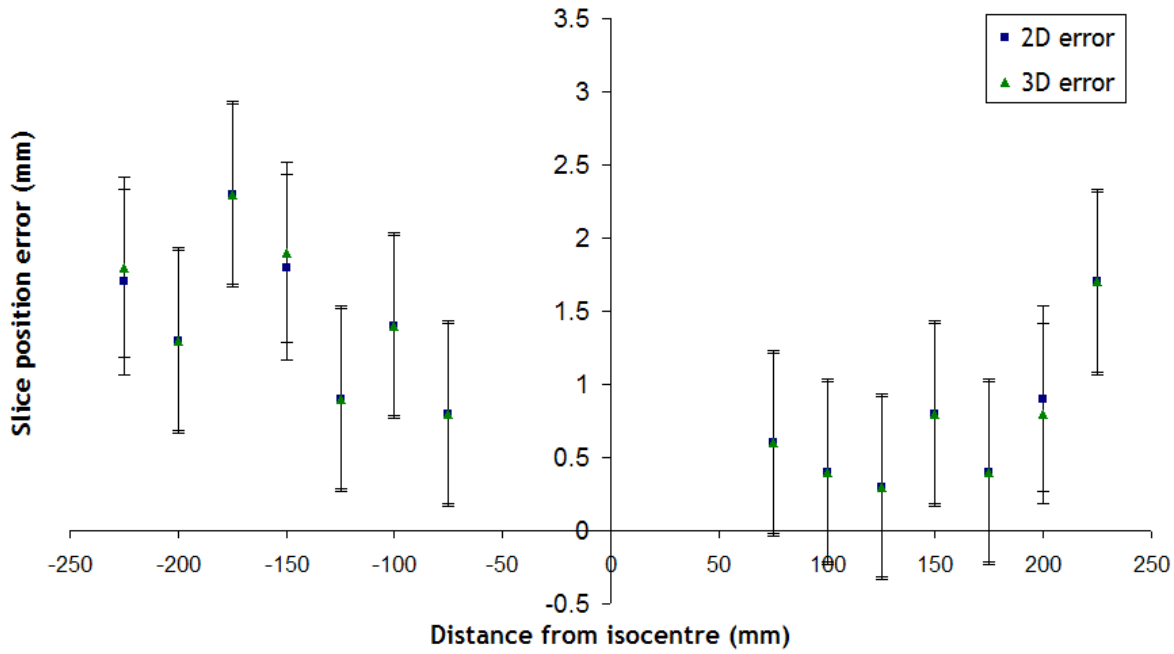

Figure 3.5 Slice position error measurements at 75-225 mm superior and inferior to the isocentre. The error bars are ± 1 standard deviation. Negative and positive values in the x-axis represent inferior and superior distances from isocentre respectively.

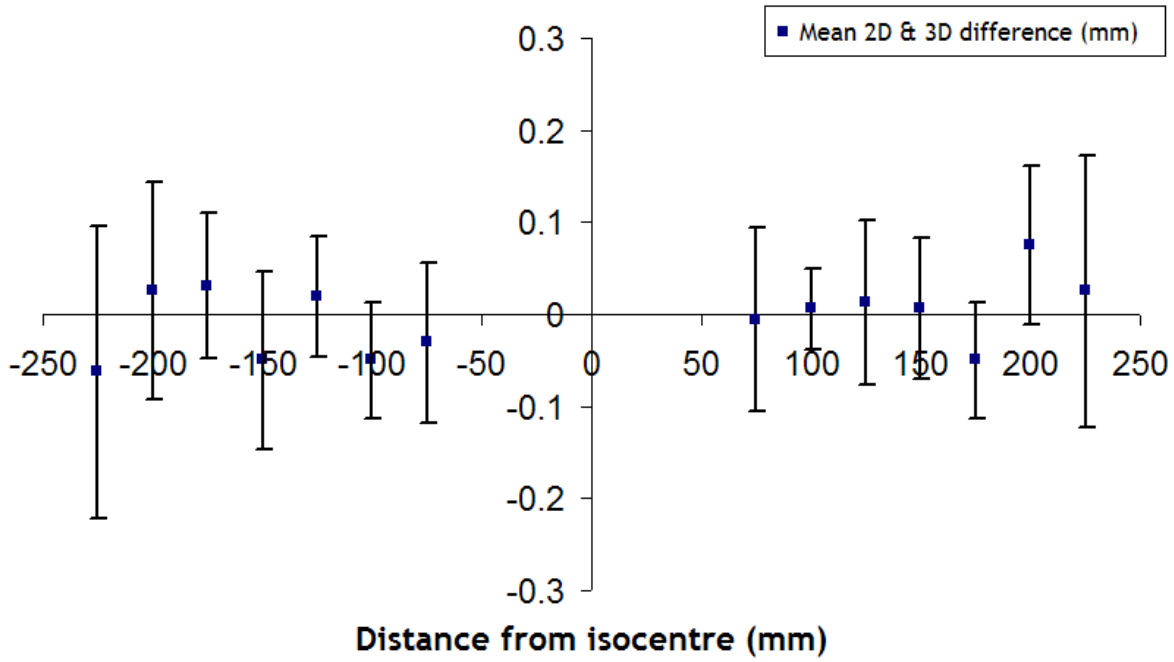

Figure 3.6 Mean difference between the 2D and 3D distortion correction algorithms. The error bars are ± 1 standard deviation. Negative and positive values in the x-axis represent inferior and superior distances from isocentre respectively.

3.3.2 Slice position test object measurements

Since there was statistically no difference shown between the 2D and 3D distortion correction measurements in the axial plane with three slices (*p* value

= 0.58), it was expected that an increase in slice number would give a measurable difference. This is because, unlike the 2D correction algorithm, 3D GradWarp uses information from all the slices to determine the required pixel correction.

The magnitude of the slice position error measurements was averaged over each dataset in 5 mm increments. The phantom was positioned in different locations both superior and inferior to the isocentre which gave more than one measurement at the same location. This resulted in one, two or three slice position error measurements at different slice positions, strengthening the reproducibility of this test, and these measurements were then averaged. In order to demonstrate the region where the data points begin to exceed an average slice position error of 1 mm, Figure 3.7 (b) shows the data of Figure 3.7 (a) within a 5 mm error range.

Typically, a 2 mm tolerance is used for most imaging parameters in RT. A 1 mm error tolerance was chosen to ensure the MRI does not exceed the tolerances required for RT. The average slice position error exceeds 1 mm at 195 mm inferior and superior to isocentre for the 2D correction and 90 mm inferior and 110 mm superior to isocentre for the 3D correction as shown in Figure 3.7 (b).

Images of the 2D and the 3D corrected slice position phantom at 270 mm superior to isocentre can be seen in Figure 3.8. This clearly shows the difference between the two distortion correction algorithms. A two tailed t-test resulted in a p value of < 0.01 confirming there is a statistically significant difference between the 2D and 3D distortion correction results. 3D GradWarp uses error measurements from the gradient field maps to calculate the correct pixel value. This algorithm appears to shift the pixels to an incorrect location based on a difference between the measured gradient field map at the design stage of the scanner and the gradient field map at the superior end of this scanner. To correct this inaccuracy a measurement of the field map for each scanner may be required. Another possibility for this error is that it is testing the 3D distortion correction algorithm beyond a volume that it had been designed to perform a correction. However, this does not explain why 3D Gradwarp is able to correct in the inferior direction. Figure 3.8 also shows that the 3D distortion algorithm

blurs the image of the crossed rods. This blurring altered the rod separation measurements and therefore affected the slice position results of Figure 3.7.

(a)

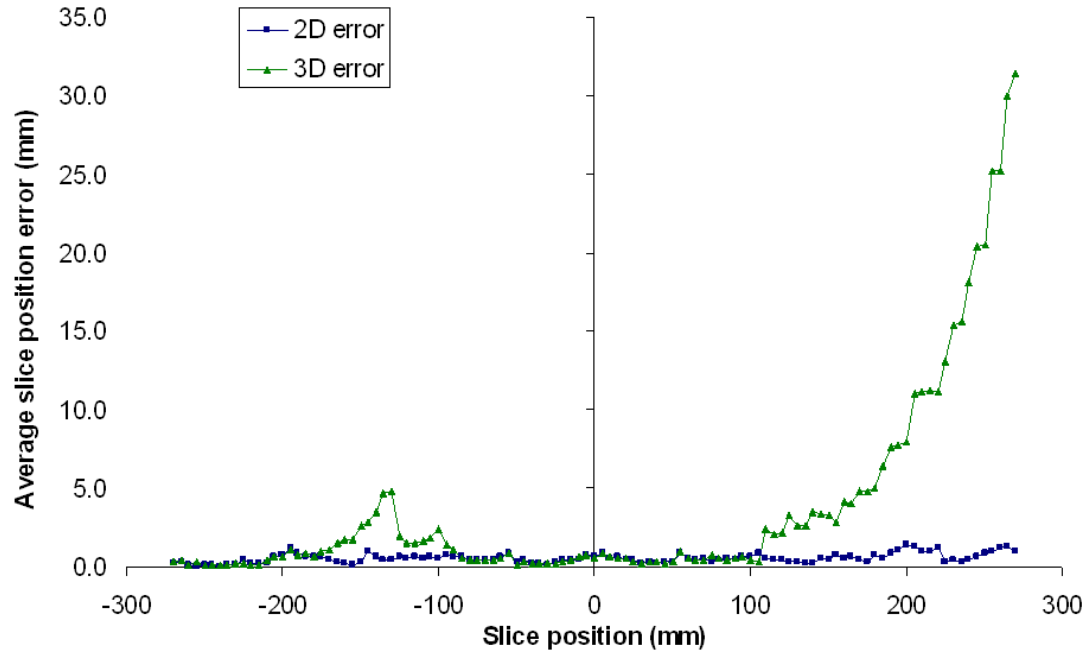

(b)

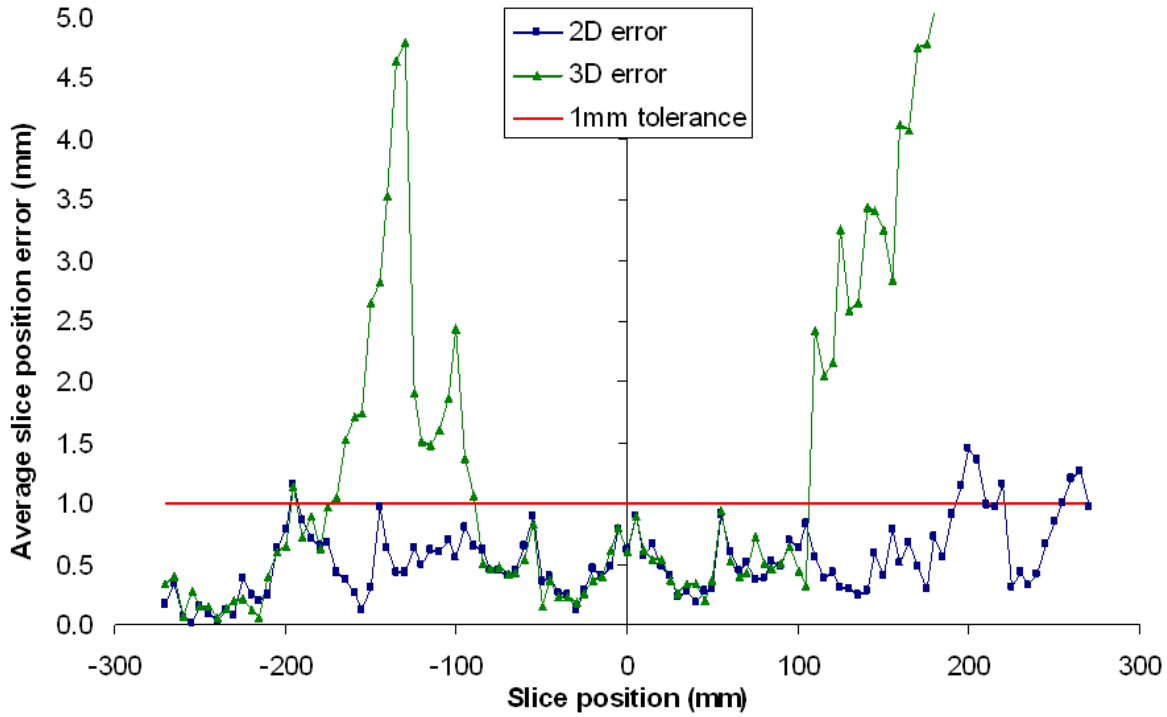

Figure 3.7 (a) The magnitude of the slice position measurements averaged over each dataset in 5 mm increments and (b) the same data scaled with a maximum slice position error of 5 mm. Negative and positive values in the x-axis represent inferior and superior distances from isocentre respectively.

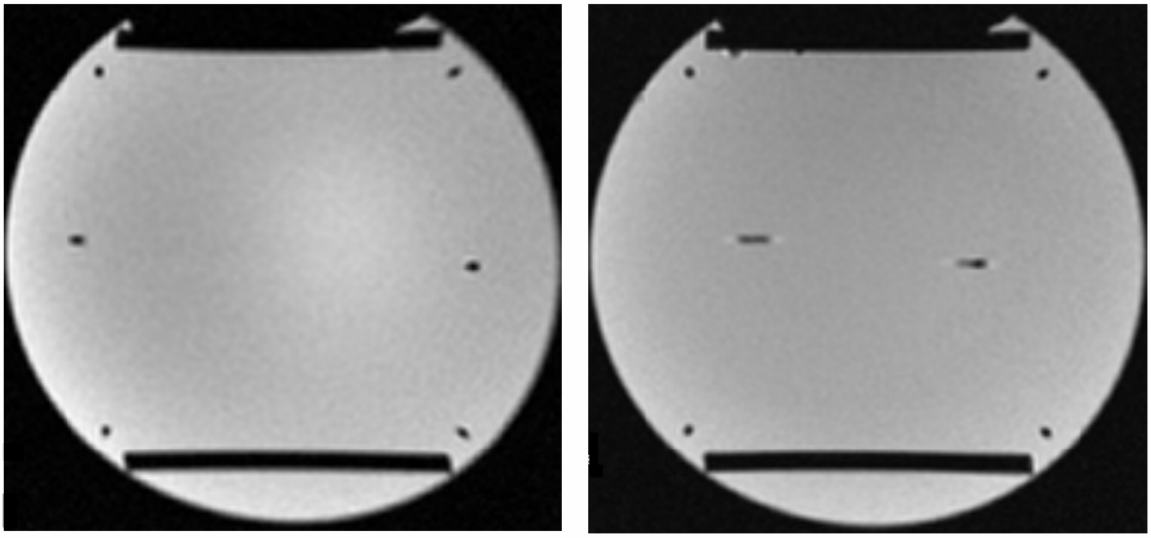

Figure 3.8 Image of slice position phantom at 270 mm superior to isocentre with 2D (left) and 3D (right) distortion correction applied.

3.3.3 In-plane distortion measurements using the slice position test object

The in-plane error measurements in the right-left and anterior-posterior directions are shown in Figure 3.9 as a moving average trendline. These measurements show that 3D GradWarp reduces the in-plane error significantly in the superior direction, but has little effect in the inferior direction. At a slice position of 285 mm superior to isocentre the 2D distortion correction results in an error of 12.9 mm to the right and 2.6 mm anteriorly while 3D GradWarp reduces this error to 0.7 mm to the right and 1.6 mm posteriorly at the same slice position. The results for the slice position test object at 280 mm inferior show the 2D error is 6.4 mm to the right and 3.7 mm anteriorly while the 3D error is 6.5 mm to the right and 3.6 mm anteriorly.

The 2D distortion correction error exceeds a 1 mm tolerance at 110 mm superior (error in posterior direction) and 180 mm inferior to isocentre (error in left direction), while the 3D correction algorithm exceeds the 1 mm tolerance at 120 mm superior (error in posterior direction) and 180 mm inferior to isocentre (error in left direction). This shows that while the 3D GradWarp demonstrates improvements in the in-plane distortion at the edges of the field of view, it offers little benefit over the 2D distortion correction algorithm, in improving a clinically safe range for the use of MRI in RT.

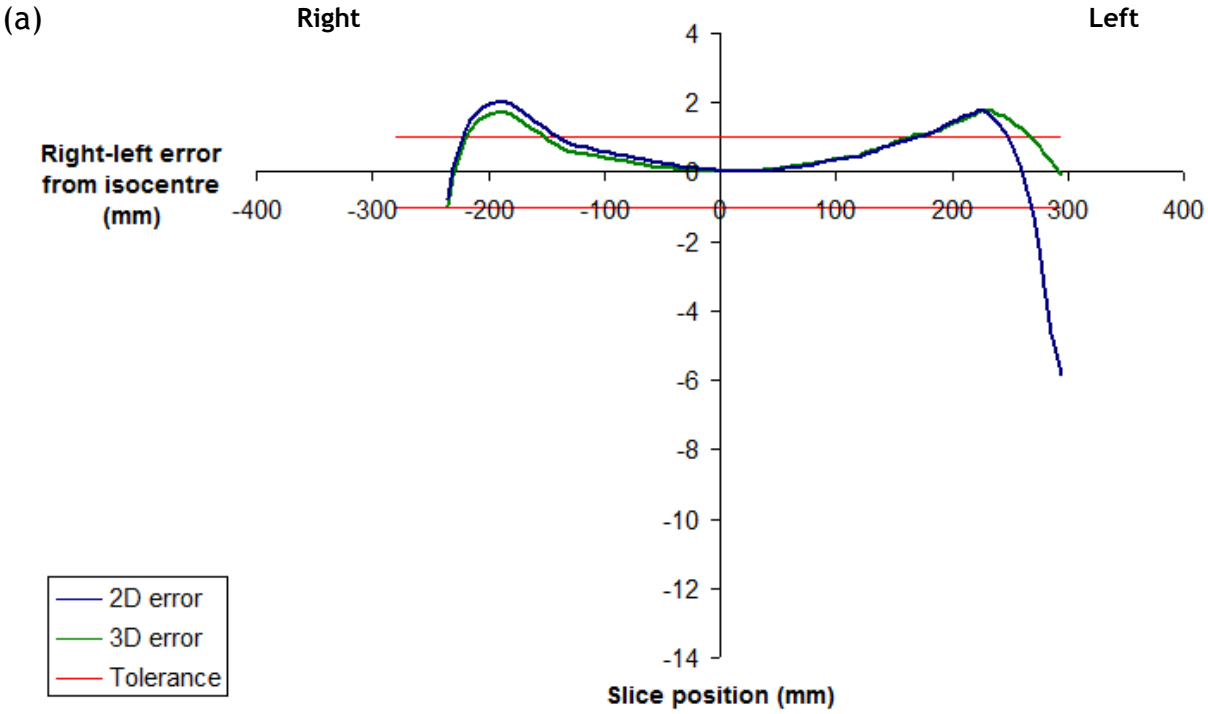

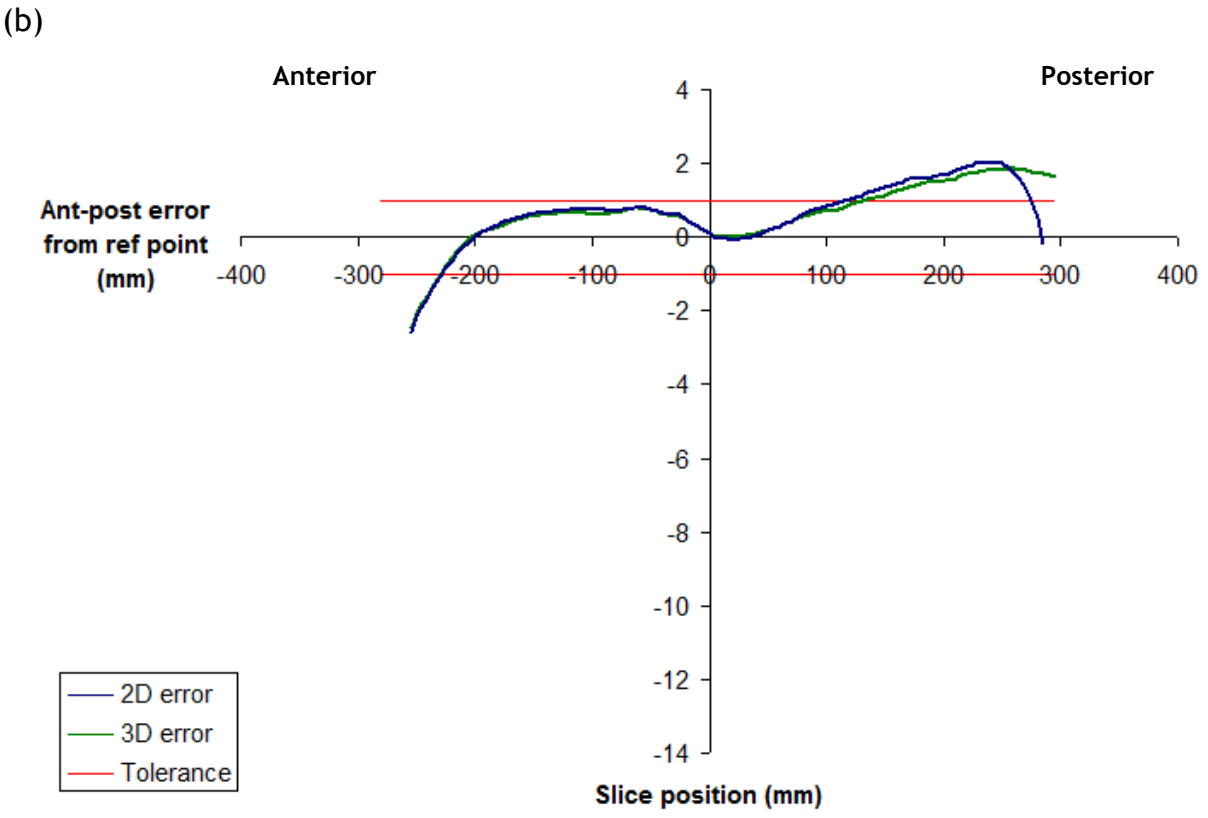

Figure 3.9 In-plane distortion of the top left parallel rod from the isocentre position in the (a) left-right direction, where left is positive and right is negative and (b) posterior-anterior direction, where posterior is positive and anterior is negative. Negative and positive values in the x-axis represent inferior and superior distances from isocentre.

3.3.4 LEGO® phantom measurements in the coronal plane

A total of 18 calliper measurements were made at different distances across different sections of the phantom in the vertical and horizontal directions. This gave an average measurement of 55.86 ± 0.02 mm from the centre-to-centre of two adjacent bricks. The total dimensions of the phantom are therefore (335.15 mm × 502.72) ± 0.02 mm with a height of 23 cm.

A CT scan of the phantom can be seen in Figure 3.10. Using the Eclipse treatment planning system, 30 measurements were made across different lengths of the phantom in both in-plane coordinate axes to give an average measurement from the centre-to-centre of two adjacent bricks 55.9 mm in agreement with the calliper measurements.

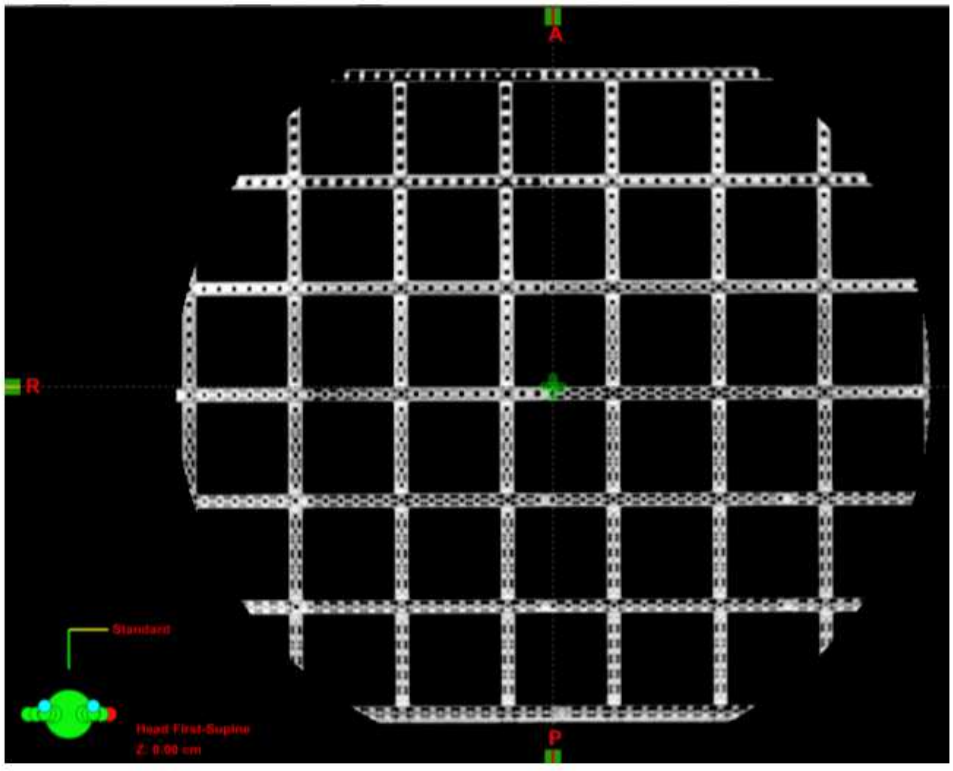

Figure 3.10 CT scan of the LEGO® phantom positioned in the axial plane.

In total, 36 measurements were made of an MRI scan of the phantom near to the isocentre and across different lengths of the phantom using Eclipse, giving an average centre-to-centre brick measurement of 56.1 mm. This agrees closely with the measurements on the CT scan and with the digital calliper. This

suggests that any deviations due to the susceptibility difference of the plastic and water are minimal.

A coronal slice near the base of the LEGO® phantom with 2D and 3D distortion correction applied is shown in Figure 3.11. This was a T1-weighted STIR scan using typical parameters for whole body imaging at the Beatson. From Figure 3.11 it can be seen that the 2D correction fails to correct the through-plane distortion and the image is warped superior and inferior towards the isocentre. This accounts for a loss of 9 cm at the superior and inferior ends of the FOV. The 3D correction is capable of correcting for this and the missing section of the phantom is shown in the post-processed image in Figure 3.11. The 3D corrected image does however demonstrate some in-plane warping. Furthermore, the inhomogeneity of the static magnetic field can again be seen as warping at the edges of the FOV.

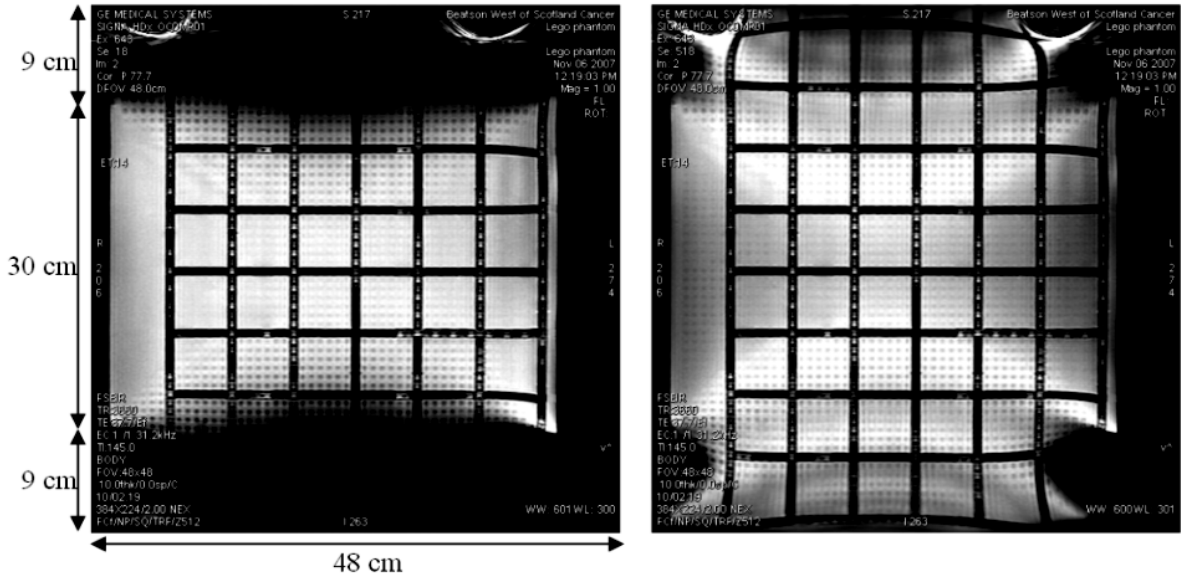

Figure 3.11 Coronal image of the LEGO® phantom with the 2D (left) and 3D (right) distortion correction algorithm applied.

The through-plane distortion at the edges of the FOV was determined using a saline filled catheter. The difference between the slice positions through the catheter gave a distortion error of 4.0 ± 0.5 cm with the 0.5 cm uncertainty due to the slice thickness used. Therefore, 3D GradWarp can be considered to correct by as much as 4.0 ± 0.5 cm in the coronal plane.

3.4 Conclusions

With only three slices 3D GradWarp behaves in the same way as the 2D distortion correction algorithm. Axial plane correction is relevant to the registration of MR images with CT for RT planning. Increasing the number of slices to 39 showed there was a large difference in geometric accuracy between the two distortion correction algorithms, particularly in the superior direction. The large difference between the correction algorithms in the superior direction is due to dissimilarity in the way in which 3D GradWarp corrects. A reason for the error may be due to the blurring shown in Figure 3.8. This blurring is perhaps because the phantom contains discrete points, resulting in inaccuracies in the 3D distortion correction algorithm. In a clinical setting when imaging a patient the algorithm may not suffer from this artefact.

In-plane distortion measurements (Figure 3.9) show that the 3D distortion correction algorithm reduced the error on the left but not the right. The asymmetry of the correction again indicates the distortion correction has not been optimised for this scanner.

The LEGO® phantom gives evidence of through-plane correction in the coronal plane using 3D GradWarp. Limitations with this phantom are the possibility of additional distortion from susceptibility differences between the plastic and water. However, the measurements of the MRI scan of the phantom using the Eclipse treatment planning system compared closely to the same measurements on a CT scan and with a digital calliper showing that any susceptibility deviations are small.

It must be appreciated that the effect of 3DGradWarp is potentially greater for a 3T scanner due to the increase in geometric distortion with the field strength of the main magnetic field. 3D distortion correction is of great importance as MRI becomes more heavily employed in RT. In the same way as the shimming of MRI systems improves the default settings on a scanner-by-scanner basis, there is scope for improvement with 3D GradWarp by enabling scanner specific distortion evaluation and correction. This will increase confidence in MRI-based RT planning in the future when even greater geometric accuracy will be required.

In its current form it would not be recommended that 3D GradWarp be used clinically. Since the completion of this study, GE (GE Healthcare, WI, USA) has released a clinical version of the 3D distortion correction algorithm. This version was not available for use on the MRI scanner at the Beatson and so no testing was possible.

This study has shown that for multiple axial through plane measurements, the 2D correction algorithm does not exceed a 1 mm tolerance for a range of 195 mm superior and inferior from isocentre. For axial in-plane distortion the 2D distortion correction algorithm exceeds the 1 mm tolerance at 110 mm superior and 180 mm inferior to isocentre. While the 1 mm tolerance is exceeded at 110 mm superior to the isocentre it does not exceed 1.1 mm until 180 mm superior to isocentre. In the coronal plane a range of approximately 150 mm superior and inferior to isocentre is achievable before the through-plane distortion becomes unacceptable. The results of this study demonstrate that, provided a small amount of in-plane distortion is acceptable, a clinically safe range to use the 2D distortion correction algorithm in MRI for critical structure delineation in RT is 150 mm superior and inferior from isocentre.

4 Patient immobilisation in MRI

4.1 Introduction

Patient immobilisation is necessary in radiotherapy (RT) planning for certain anatomical sites. Immobilisation devices have three fundamental purposes: firstly to immobilise the patient during treatment, secondly to provide a reliable means of reproducing the patient's position from simulation to treatment and from one treatment to another and finally to ensure accurate beam alignment.

The following chapter describes the problems associated with incorporating immobilisation into the magnetic resonance imaging (MRI) environment as well as the benefits this provides for RT planning. A new technique is developed using surface coils to image brain cancer patients in a beam directional shell (BDS) and the following chapter contains the measurements of this study conducted using a variety of test objects.

This work has been presented at a national and international level and published in a peer reviewed journal:

- **The Dorado laser in MR**, Hanvey S, Glegg M, Foster J, Oral presentation, The 5th Annual Scientific meeting of Advanced Practices in Radiotherapy, Belfast 2008.

- **MR imaging of head and neck cancer patients in the radiotherapy treatment position without loss of image quality**, Hanvey S, Glegg M, Foster J, Poster presentation, 17th Scientific Meeting of the International Society for Magnetic Resonance in Medicine (ISMRM), Honolulu, 2009.

- **Magnetic resonance imaging for radiotherapy planning of brain cancer patients using immobilization and surface coils**, Hanvey S, Glegg M, Foster J, Physics in Medicine and Biology 54, 5381-5394, 2009 (Hanvey et al. 2009).

4.2 The benefits and problems of patient immobilisation in MRI for RT planning

The planning target volume (PTV) defined by International Commission on Radiation Units and Measurements, ICRU, (ICRU 1993; ICRU 1999) consists of a clinical target volume (CTV) with additional margins for movement of internal

organs (Internal Margin) and geometrical variations and inaccuracies in the patient set-up (Set-up Margin).

Since the PTV must take into account the inaccuracies of the patient set-up it is dependent on the precision of tools such as immobilisation devices and lasers. It is therefore desirable to incorporate immobilisation into the RT planning process for all imaging techniques where immobilisation is used.

It is standard practice to immobilise patients with brain cancer, being treated with RT, using a headrest and a thermoplastic BDS. At the Beatson, patients with head and neck cancer are immobilised using a 5-point fixation mask which immobilises the shoulders and cranium. Patients are immobilised during their simulator computed tomography (CT) scan, pre-verification imaging and subsequent RT.

When additional imaging techniques are used for registration with CT, such as MRI or positron emission tomography (PET), it is beneficial to have patients positioned in the treatment position to minimise registration errors and to ensure the orientation of the MR imaging plane through the patient is coplanar with CT. Mismatches in the registration of CT and MRI data can result in changes to the PTV.

While immobilisation in MRI reduces registration error with CT it can also result in reduced image quality. The diagnostic imaging coils used in MRI, such as the Head-Neck-Spine Array imaging coil (GE Healthcare, WI, USA), are not designed to incorporate a BDS and so surface coils must be used instead. The use of surface coils can result in a reduction in image quality due the reduced signal-to-noise ratio (SNR) and contrast-to-noise ratio (CNR) of these coils. If this reduced image quality occurs through the gross tumour volume or organs at risk then this can compromise an oncologist’s confidence in being able to delineate tumour boundaries.

4.3 MRI for radiotherapy planning of brain cancer patients using surface coils and immobilisation: A test object study

4.4 Introduction

Currently, at the Beatson, external beam RT planning for patients with brain cancer relies on CT and MR for target localisation. CT scans are taken with the patient immobilised using a thermoplastic face mask or BDS. All subsequent plans and treatment are performed with the patient held in the same position by the BDS. Contours are delineated around the CTV, which is expanded to a planning target volume to take into account set-up errors and positional errors. Pre-operative MR datasets are registered to the CT images using the Eclipse RT planning system (Varian Medical Systems, Inc. CA, USA). It is beneficial to use pre-operative MR images in the treatment position since it enables the clinician to clearly define the tumour extent at the planning process. If the MR images are able to give a better description of the CTV over the use of CT alone, then despite uncertainties in the MR dataset, there will be an overall improvement in target accuracy. For this reason, it is desirable to incorporate MRI into RT practice.

In normal diagnostic MRI the patient is scanned in a multi-channel head coil. This head coil does not allow space for either a head rest or a thermoplastic face mask. The patient therefore receives their MRI scan in a different position to their CT scan and this can result in errors in the registration process which is evident as a mismatch between the image sets. Therefore, it is beneficial to image the patient in the same position for their MRI scan, CT scan and subsequent radiation treatment. In MRI, a 4-channel cardiac coil can be used with a thermoplastic head mask in-situ ensuring the same patient positioning. This new coil arrangement, ideally, should provide at least as much diagnostic detail as the multi-channel head coil. However, it may be necessary to compromise on image quality for the benefits of imaging in the RT position.

4.5 Method and Materials

Quality assurance MRI phantoms were used to determine the image quality of different available image coils. All phantom studies were conducted using the

MagNET test objects (MagNET, London). Scanning parameters and tolerances were chosen in accordance with the MagNET test instructions and IPEM Report 80 (IPEM 1998). The MagNET test objects were used to assess the image quality of MR scans. These phantoms were positioned within the same thermoplastic face mask immobilisation device used in the treatment of patients and four imaging coils (the integrated body coil, the 8- and 12-channel body array coils and the 4-channel cardiac coil) were tested and compared to the technical evaluation from the National Health Service (NHS) Purchasing and Supply Agency Report 06005 (PASA 2006). This report provides information on image quality of available imaging coils, measured with the MagNET test objects, for a variety of manufacturers, including the GE Signa Excite HD. The GE Signa HDx 1.5T scanner was used for this assessment and can be compared to Report 06005 (PASA 2006) since the HDx is a software upgrade to the HD and does not adversely affect image quality.

Set up of the integrated body coil provides no physical restrictions to positioning patients within the head rest and thermoplastic face mask. The 8-channel and 12-channel body array coils are flexible enabling the lower anterior element to be wrapped around the patient's head, as shown in Figure 4.1. The posterior and upper anterior sections of the coils are redundant and could be positioned on top of the patient's chest and extended beyond the head respectively. To ensure close contact between the active section of the coil and the immobilisation mask, foam blocks were positioned laterally against the coil. Finally, a 4-channel cardiac coil was arranged laterally and again kept in close contact with the immobilisation mask using foam pads.

Figure 4.1 Arrangement of 8- and 12-channel body array coils

For this study, image quality was assessed in terms of normalised signal-to-noise ratio (NSNR), resolution, fractional uniformity, geometric linearity and

distortion, multiple slice position error, slice width and the CNR. The filling factor of the coils was also considered.

Since phased array coils have intrinsically poor uniformity the GE scanner is equipped with a uniformity correction algorithm known as Phased array Uniformity corREction (PURE). This algorithm reduces coil intensity variations by first performing a calibration scan prior to image acquisition.

4.5.1 Normalised signal-to-noise ratio

For all tests the phantoms were positioned at the isocentre of the scanner, using a spin echo (SE) sequence and with the parameters shown in Table 4.1.

Table 4.1 Acceptance testing parameters. TR is the repetition time, TE is the echo time and FOV is the field of view.

TR (ms)	TE (ms)	FOV	Resolution	Slice Thickness
1000	30	250/256 mm	256×256	5 mm

Image analysis was performed on both the GE Advantage Windows workstation (GE Healthcare, Waukesha) and using the Osiris software package (Osiris, Windows Version 4.19, Digital Imaging Unit, University Hospitals of Geneva, Radiology Department)

The NSNR is dependent on a number of factors including the main magnetic field strength, the radiofrequency (RF) receive and transmit design and the choice of sequence and imaging parameters. An oil flood field phantom was positioned with the centre of the test object at the isocentre of the scanner using a foam block. Images were taken using the parameters shown in Table 4.1 with a field of view (FOV) of 250 mm. The signal was measured in five regions of interest (ROIs) of size 20×20 pixels on the flood field image as shown in Figure 4.2 (ROIs 1-5). For each ROI the mean pixel value was measured using the computer analysis software and this value was averaged over the five regions.

A nickel chloride filled phantom could have been used for the NSNR and uniformity tests. However, at 1.5T dielectric resonance effects can perturb uniformity profiles in water-based phantoms. The test object manufacturer

therefore recommends that the oil-filled flood field phantom is used if a comparison is being made with evaluation data as was the case in these experiments.

To measure the noise, five ROIs of size 20×20 pixels were positioned as shown in Figure 4.2 (ROIs 6-10), in regions free from ghosting. The mean of the five standard deviation (SD) values was calculated and the noise, N, was measured using the following expression,

Equation 4.1

$$N = SD/0.655$$

The background noise follows a Rayleigh distribution rather than a Guassian distribution. In a Guassian distribution the mean of the background would be zero, however with MR images all the negative numbers are made positive and the mean is therefore greater than zero. This results in a smaller standard deviation and so a factor of 0.655 is applied as a correction (Kaufman et al. 1989). The NSNR was calculated for the sagittal, coronal and axial views.

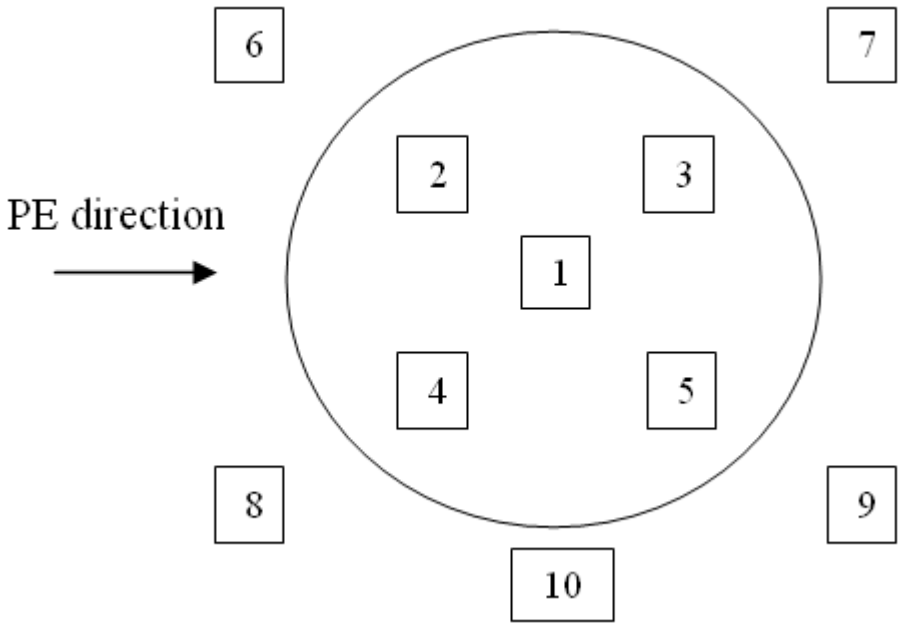

Figure 4.2 NSNR regions of interest in flood field test object, where PE is the phase encoding direction.

Using IPEM Report 80 (IPEM 1998) the NSNR was calculated in the following way. First, the voxel volume was calculated using the expression,

Equation 4.2

$$\text{Voxel}_{vol} = \frac{FOV_R}{N_R} \times \frac{FOV_P}{N_P} \times SW$$

where $FOV_{R,P}$ and $N_{R,P}$ are the FOV (in cm) and the number of pixels in the read and phase encodings respectively and *SW* is the measured slice width in cm.

The scan time, t_{scan}, is calculated as,

Equation 4.3

$$t_{scan} = N_{av} \times N_P \times TR$$

where N_{av} is the number of averages, N_P is the number of phase encoding steps and *TR* is the repetition time.

Finally, the NSNR is calculated using the following formula,

Equation 4.4

$$NSNR = \frac{1}{\sqrt{t_{scan}}} \times \frac{1}{\text{Voxel}_{vol}} \times SNR \times \frac{\sqrt{BW}}{\sqrt{BW_0}}$$

where *SNR* is the signal-to-noise ratio calculated for each view using ROI in the method described above, *BW* is the receiver bandwidth in kHz (11.9 kHz) and BW_0 is arbitrarily chosen as 30 kHz for normalisation.

An increase in the Quality- (Q) factor leads to an improvement in the SNR by a factor of $\sqrt{Q}$ and produces a sharper frequency response. The Q-factor is a measure of the tuned circuit performance of an RF coil and is the ratio of stored energy to dissipated energy. Since this information is not readily accessible in clinical scanners the Q-factor was not considered in the findings.

4.5.2 Resolution

The resolution test object contains a square angled Perspex block and four groups of parallel glass plates. It is filled with a paramagnetic solution (0.7

grams $CuSO_4$/litre of distilled water, pH 2). A diagram of the resolution test object can be seen in Figure 4.3.

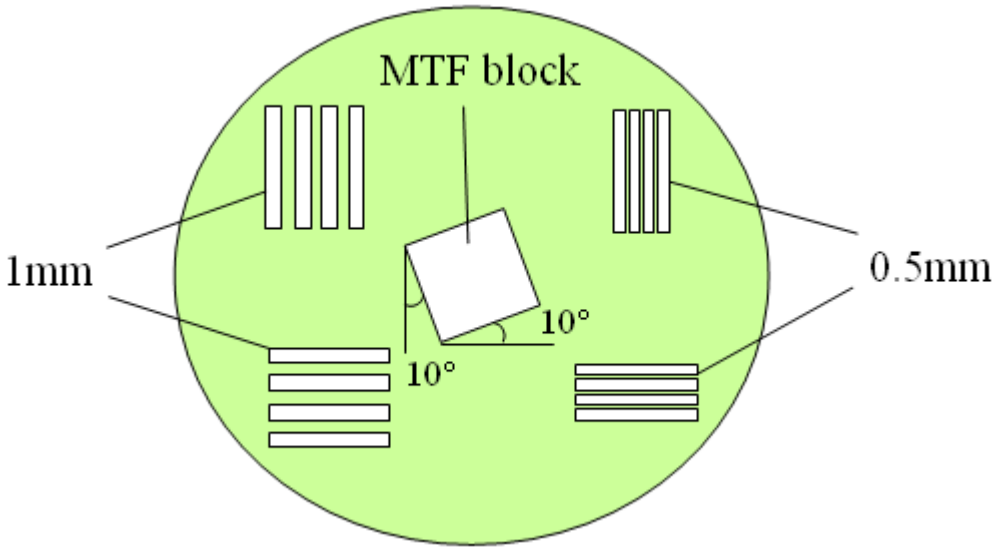

Figure 4.3 Axial plane through the resolution test object

Using localisation pre-scans the resolution test object was positioned with its centre at the scanners isocentre. The scanning parameters were set up in accordance with Table 4.1, with a FOV of 250 mm and an image resolution of both 256 × 256 and 512 × 512 pixels in all planes.

The MagNET resolution test object consists of plates with thickness and separation of 1 mm and 0.5 mm groups. Both the phase encode and the read encode directions were assessed with a single image since the sets of parallel bars were perpendicular to each other. To assess the resolution a line profile was drawn through the bars. The 50 % intensity line was used to determine the degree to which the bars were resolved.

With a FOV of 250 mm and a matrix size of 256 × 256 the pixel resolution is 0.98 mm therefore only the 1mm bars can be resolved. Similarly, a matrix size of 512 × 512 gives a pixel resolution of 0.49 mm so the 0.5 mm bars can be resolved.

4.5.3 Fractional uniformity

Image uniformity is affected by the RF homogeneity which is influenced by resonator design and set up, the magnetic field homogeneity and eddy current correction. The RF resonator is designed by the manufacturer to transmit and receive RF energy. RF noise spikes can be produced from poorly designed resonators and appear as light and dark stripes across the image. The design and orientation of the coil fundamentally determines uniformity.

Uniformity measurements were performed on the NSNR datasets and analysed using the Osiris software package. Line profiles of 160mm were taken in the horizontal and vertical direction for each image set and centred over the centre of the object to avoid ringing at the edges of the phantom.

Fractional uniformity was calculated using the equation,

Equation 4.5

$$\text{Uniformity} = \frac{\text{Pixels}_{\text{R}}}{\text{Pixels}_{\text{T}}} \times 100$$

where $Pixels_R$ is the number of pixels within ± 10 % of the mean value and $Pixels_T$ is the total number of pixels. It was multiplied by 100 to express the value as a percentage.

4.5.4 Geometric linearity and distortion

Distortion in MRI is a result of system induced effects, such as field inhomogeneity, gradient maladjustment or sampling irregularities and patient induced effects, namely chemical shift and magnetic susceptibility effects. Chemical shift has been investigated by previous authors and is not dependent on the imaging coil. Moore *et al* measured a chemical shift of 0.46 pixels at a bandwidth of 62.5 kHz and 3.2 pixels at a bandwidth of 9 kHz. This paper recommends a minimum bandwidth of 30 kHz and taking a linear fit between these two measured points gives a shift of 1.5 pixels at this bandwidth. At our centre we have a standard FOV of 256 mm and a matrix size of 256×256 for our T1-weighted images and 512×512 for our T2-weighted scans. This would result in an approximate shift of 1.5 and 0.8 mm for T1- and T2-weighted images

respectively. It should be noted, however, that this error will be localised to areas such as the subcutaneous fat in the neck and scalp.

Magnetic susceptibility effects have also been rigorously investigated and are not dependent on the imaging coil. A review paper (Fransson et al. 2001) noted that susceptibility effects are likely to be most pronounced at tissue-air interfaces, such as around the nasal cavities and along the patient outline and this is expected to generate field changes of up to ± 9 parts per million and a susceptibility shift of 0.2 pixels at a bandwidth of 30 kHz. This would result in a distortion of 0.15 and 0.08 mm at our centre for T1- and T2-weighted scans respectively. These distortions would be localised to regions of high magnetic susceptibility.

To calculate system related errors in terms of geometric linearity and distortion the distances (centre-to-centre) between the glass rods in the geometric linearity test object were measured. Six distances of a known length of 120 mm were measured in both the horizontal and vertical positions as shown in Figure 4.4.

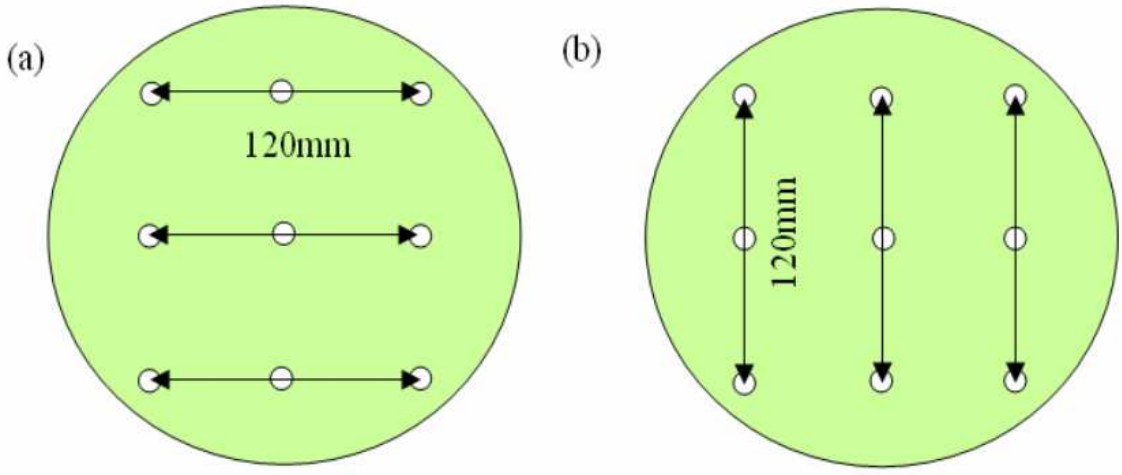

Figure 4.4 Geometric linearity measurements in the (a) horizontal and (b) vertical directions

Geometric linearity is calculated by finding the error between the measured distance and the actual distance. These errors should be < 1 mm in accordance with the IPEM Report 80 (IPEM 1998).

Geometric distortion is the variation in errors between the measured and actual distance. The coefficient of variation, CV, is used to determine the distortion and is defined as,

Equation 4.6

$$CV = \frac{SD}{mean} \times 100\%$$

The distortion is expected to fall within 1 % as an acceptable tolerance in accordance with the IPEM Report 80 (IPEM 1998).

4.5.5 Multiple slice position error

Multiple slice position error was measured using the MagNET slice position test object. This phantom is made of Perspex containing two angled glass rods and four parallel glass rods. It is filled with a paramagnetic solution and a diagram of its construction can be seen in Figure 3.1 of Chapter 3.

The test object was positioned at the isocentre of the scanner and slice widths of 5 mm were acquired with the central slice at the centre of the test object using the scanning parameters of Table 4.1 and a FOV of 256 mm.

A correction factor was determined by comparing the measured distance to the physical distance of the glass rods in the geometric linearity phantom of Figure 4.4. This correction factor was then applied to the measured rod positions to give a true distance. Next, the distance (centre-to-centre) between the angled rods of the slice position object was measured. The measured slice position, SP_{meas}, was determined using the following expression,

Equation 4.7

$$SP_{meas} = \frac{\sqrt{d^2 - s^2}}{2}$$

where d is the measured distance of the angled rods after an appropriate correction factor and s is the rod separation which is equal to 6.5 mm.

The centre of the phantom was determined by positioning the object until the rod separation was zero. A scanning protocol with no spacing between the slices

was delivered and the scans were interleaved to prevent crosstalk between slices. Finally, the magnitude of the slice position error for each slice was calculated by subtracting the actual slice position from the measured slice position.

4.5.6 Slice width

Slice width is affected by the RF pulse shape, the magnetic field homogeneity, the gradient linearity and gain and the eddy current correction. The slice width object contains two angled 1mm thick glass plates in a paramagnetic solution. Using the Osiris software package a profile was created across the plates (as shown by the dashed lines in Figure 4.5). The full width at half maximum (FWHM) was measured from the profiles and the slice width was calculated using the following expression,

Equation 4.8

$$Slice\ width = FWHM / Stretch\ factor$$

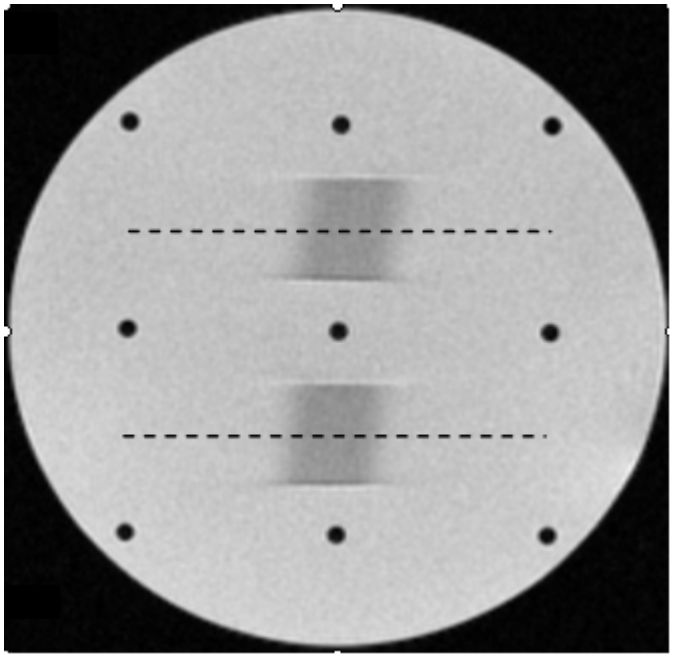

Figure 4.5 Position of profiles through plates in image

For this test object, the angle of the plates is 11.3°, giving a stretch factor of 5. The tolerance for the slice width error is less than or equal to ± 10 % of the

nominal slice width (i.e. for a 5 mm slice width, values should fall in the range 4.5 mm to 5.5 mm).

4.5.7 Contrast-to-noise ratio

CNR measurements were taken using 5 different solutions and the MagNET oil uniformity phantom and were positioned in the same way for each coil. Contrast bottles contained $NiCl_2$, $NiCl_2$ loaded, $CuSO_4$, H_2O and a bottle from the GE Endorectal Phantom. These gave uniform signal measurements enabling the measurement of the CNR defined as,

Equation 4.9

$$CNR = \frac{(Max - Min)}{(Max + Min)}$$

where *Max* and *Min* are the mean maximum and minimum signal intensity measurements in a ROI of 20×20cm.

A T1-weighted spin echo (SE), a T2-weighted SE and a T2-weighted fast spin echo (FSE) scan was performed for each imaging coil and an average CNR was calculated.

4.5.8 Filling factor

The filling factor gives a measure of the geometrical relationship between the imaging coil and the object being imaged. This is related to the SNR since it is the fraction of the flux produced by the coil which passes through the sample. Using the oil phantom from the NSNR measurements it is possible to calculate relative filling factors for the coils by taking the ratio of the volume of the oil phantom to the volume of the active coil elements.

4.6 Results

4.6.1 Normalised signal-to-noise ratio

The NSNR results averaged over the axial, sagittal and coronal planes for the four coils are shown in Figure 4.6. The error bars are the SD of the measurements over the three planes. These results were compared with

measurements made in the NHS Evaluation Report 06005 (PASA 2006) for the multi-channel head coil.

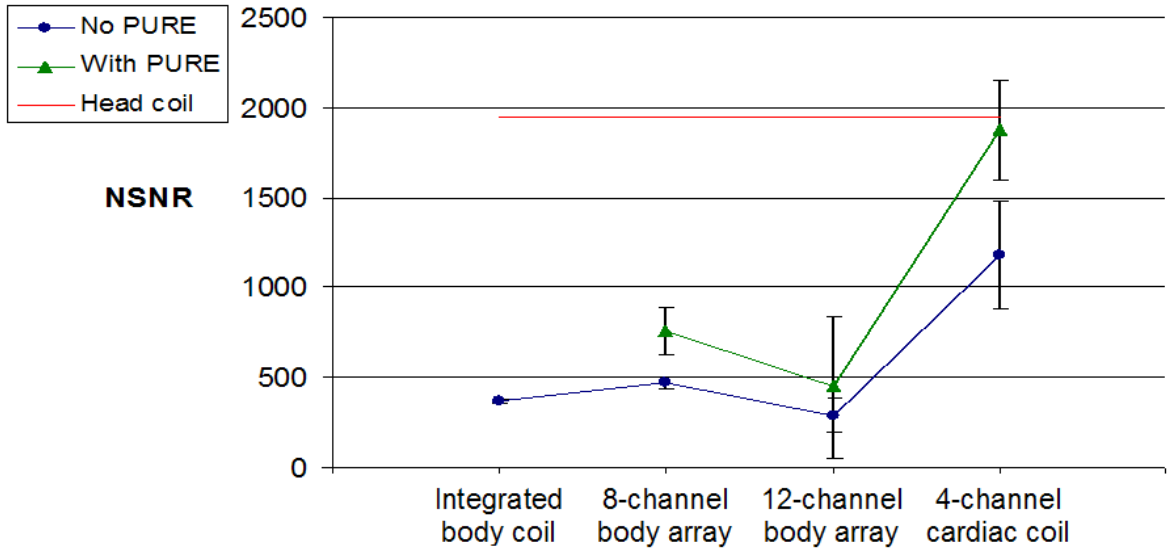

Figure 4.6 NSNR measurements averaged over the axial, sagittal and coronal planes for the four coils and comparison with the multi-channel head coil NSNR measurement from Report 06005, with and without PURE applied

From the results it can be seen that all coils tested fall below the NSNR values measured with the head coil. Although the 4-channel cardiac coil performs best it has a mean of 39.5 % below the mean of the multi-channel head coil.

By applying PURE the NSNR for the 4-channel cardiac coil reaches 96.3 % of the head coil results averaged over the three planes. The 8- and 12-channel body array coils have a NSNR of 38.8 % and 23.0 % of the multi-channel head coil with PURE applied.

4.6.2 Resolution

By inspecting the profiles through the 1 mm and 0.5 mm bars it was found that it was always possible to resolve the 1 mm bars for the 256 × 256 matrix and the 0.5 mm for the 512 × 512 matrix size for each of the four coils tested, so the resolution meets the minimum standard expected for RT planning.

4.6.3 Fractional uniformity

Fractional uniformity measurements gave results shown in Figure 4.7 for the oil flood field phantom when averaged over the x- and y-axes and the axial, sagittal and coronal planes. Error bars represent the SD for the measurements in the two axes and three planes.

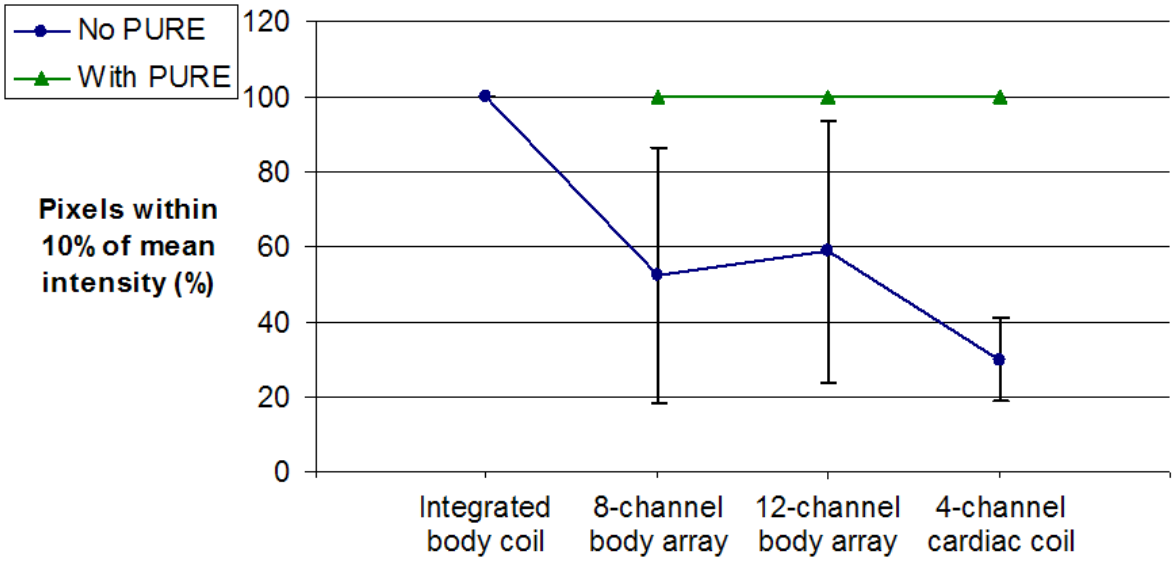

Figure 4.7 Fractional uniformity results for the four coils averaged over the x- and y- axes and the three planes showing the percentage of pixels ± 10% of the mean, with and without PURE applied.

From Figure 4.7 it can be seen that only the integrated body coil has suitable uniformity before correction. Fractional uniformity measurements with the remaining three coils are less than ± 10 % of the mean. The 8-channel and 12-channel body array coils gave the poorest uniformity in the vertical axis. This is because the unconventional arrangement of these coils causes the signal to drop off with distance from the coil surface (Figure 4.1). The difference between the vertical and horizontal measurements accounts for the large SD values for the 8- and 12-channel body array coils.

Figure 4.7 also shows that when PURE is applied all pixels for each of the coils are within the mean ± 10 % tolerance, which is ideal for integration with RT.

4.6.4 Geometric linearity and distortion

The results of the linearity and distortion tests can be seen in Table 4.2. This shows that the linearity and distortion measurements are all within the 1 mm and 1 % tolerance respectively.

Table 4.2 Linearity and distortion measurements for the four coils, where SD is the standard deviation and CV is the coefficient of variation.

Coil	Plane	Average measured distance (mm)	SD	CV	Distortion (%)
Integrated body	Axial	120.2	0.3	0.26	0.3
	Sagittal	120.0	0.2	0.16	0.2
	Coronal	120.9	0.4	0.34	0.3
8-channel body array	Axial	120.3	0.5	0.40	0.4
	Sagittal	120.0	0.3	0.27	0.3
	Coronal	120.4	0.5	0.42	0.4
12-channel body array	Axial	120.0	0.4	0.34	0.3
	Sagittal	120.1	0.3	0.23	0.2
	Coronal	120.1	0.5	0.45	0.4
4-ch cardiac	Axial	120.5	0.4	0.30	0.3
	Sagittal	119.7	0.2	0.20	0.2
	Coronal	120.2	0.6	0.47	0.5

4.6.5 Multiple slice position error

The physical distance between the rods in the geometric linearity phantom is 120 mm, as shown in Figure 4.4. From the measurements shown in Table 4.2, this gave a correction factor of 0.997, 0.998, 0.999 and 0.999 for the integrated body coil, 8- and 12-channel body array coils and the four channel cardiac coil respectively. The corrected measured slice positions in the axial plane for the integrated body coil can be seen in Figure 4.8 and the slice position error measurements for the slice position test object are shown in Figure 4.9. Error bars correspond to the SD of the calculated error measurements.

For diagnostic imaging the mean slice position error is expected to be < 2 mm, but for RT planning a tolerance of 1 mm is the ideal standard. All four coils demonstrated an average slice position error within this tolerance, regardless of whether PURE was applied.

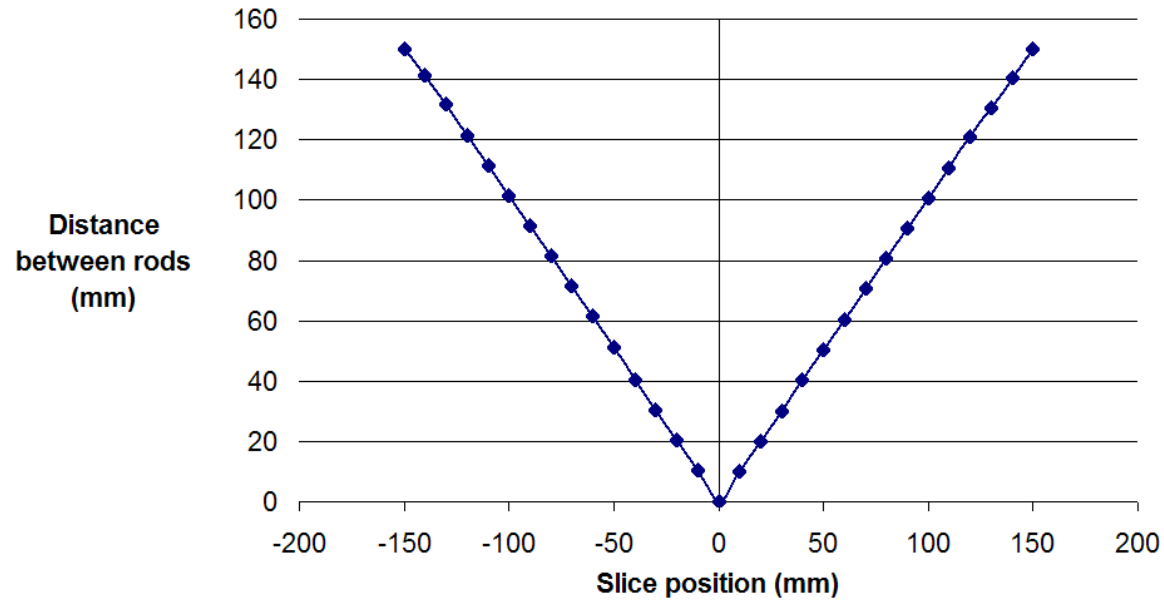

Figure 4.8 Glass rod separation measurements for the integrated body coil

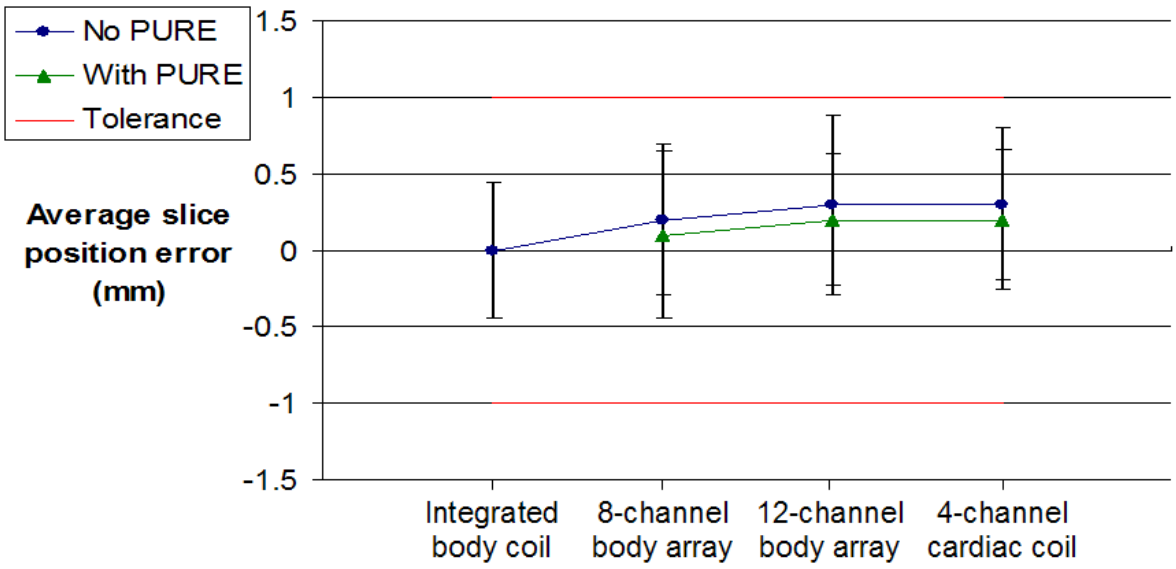

Figure 4.9 Average slice position error measurements for the four coils, with and without PURE applied.

To try and reduce the time required to analyse the multiple slice position error a Matlab code was written and this code can be seen in Appendix 1. There are, however, some limitations with the code in its current form. It is limited to a 256 x 256 matrix size; if the matrix size is changed the image cropping must also be changed. The alignment of the phantom when it is scanned must be perfect. If the phantom is at an angle the code will fail to detect the rod positions. The code is only able to work with the phantom in one position. If the phantom is rotated by 90° a separate code would need to be written.

4.6.6 Slice width

Using a slice thickness of 5 mm and 3 mm, and averaging over the three planes, gave slice width results shown in Figure 4.10 and Figure 4.11 respectively. The error bars are the SD of the slice width measurements over the three planes. These figures show that all the slice width measurements are within a tolerance of ± 10 % the nominal slice width, with and without PURE applied.

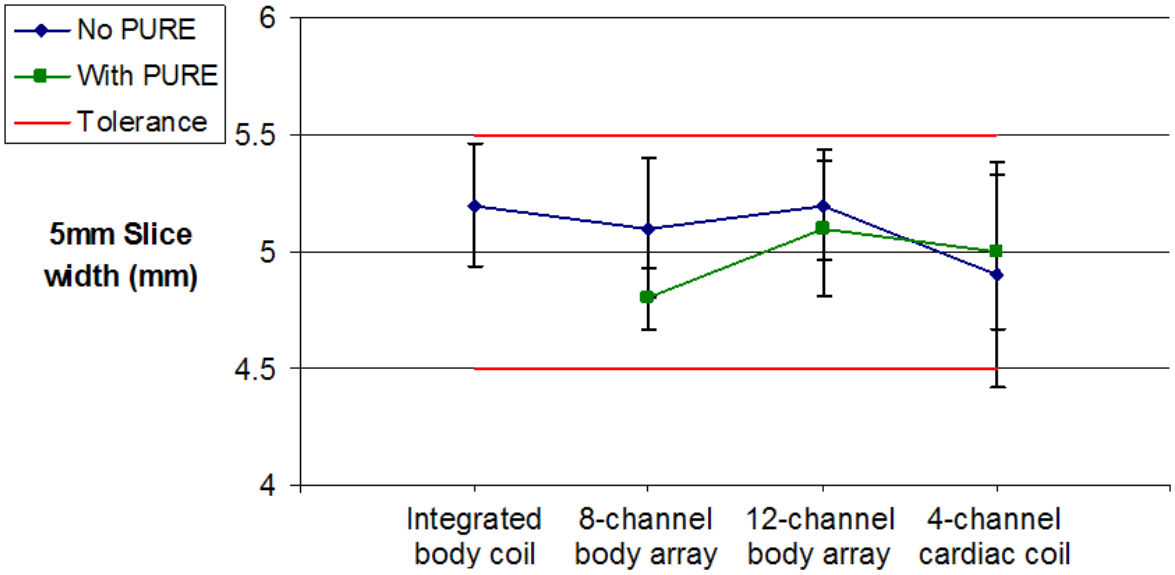

Figure 4.10 Slice width values for 5 mm slices for the four coils averaged for both plates in the three planes with and without PURE applied.

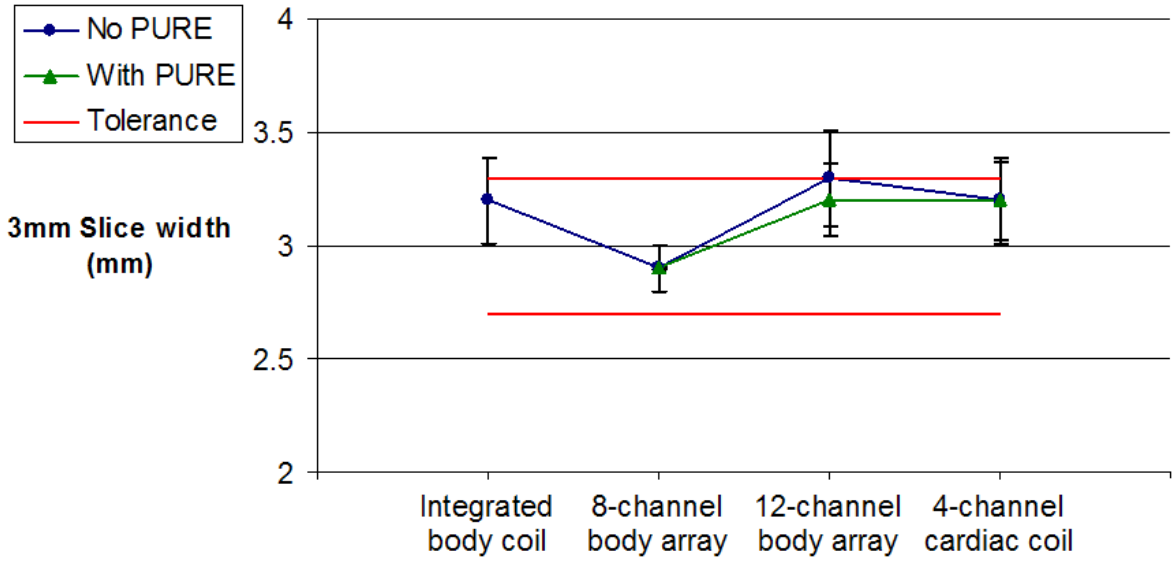

Figure 4.11 Slice width values for 3 mm slices for the four coils averaged for both plates in the three planes with and without PURE applied.

4.6.7 Contrast-to-noise ratio

The CNR results of Figure 4.12 were obtained for a slice through the centre of the containers of solution and the oil phantom. Error bars denote the SD of the CNR measurements using the three scanning parameters recorded above.

From these results it can be seen that there is acceptable CNR from each of the coils. By applying PURE it was found that there was a reduction in the CNR as variations in intensity were reduced. However, the CNR results with PURE applied are still greater than the multi-channel head coil values and therefore satisfactory for use in RT planning.

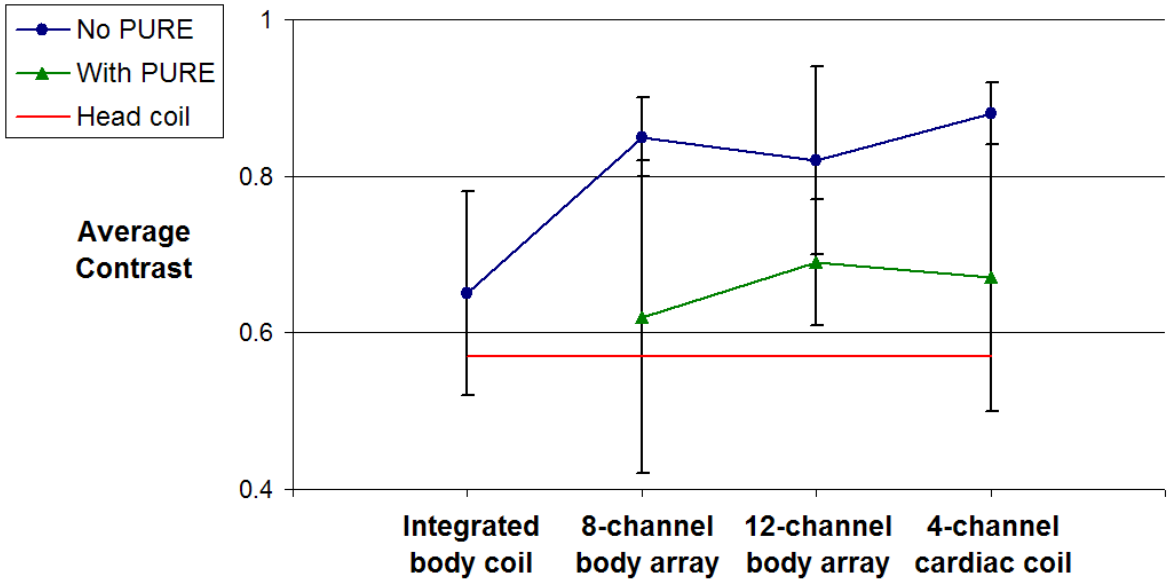

Figure 4.12 Contrast-to-noise ratio results for the four coils averaged over the T1-weighted SE, T2-weighted SE and T2 FSE sequences and comparison with the head coil NSNR measurements from Report 06005, with and without PURE applied.

4.6.8 Filling Factor

The active volume of the integrated body coil is calculated using the bore diameter of 60cm and the length of the phantom of 21cm giving a volume of 59376.1 cm^3. The ratio of the volume of the oil uniformity phantom to the volume of active elements of the integrated body coil gives a filling factor of 0.11. The volume of the 8- and 12-channel body array coils gives filling factors of 0.78 for both coils. The filling factor for the 4-channel cardiac coil is equal to

0.69. The low NSNR of the integrated body coil is in accordance with its low filling factor.

4.7 Discussion

These results show that it is possible to incorporate a RT thermoplastic immobilisation mask into MRI for treatment planning purposes without compromising the image quality. Although the integrated body coil would offer the greatest flexibility and ease of use, it did not provide a high enough NSNR to match the multi-channel head coil which would potentially result in tumours being missed if used clinically. The integrated body coil with a thermoplastic face mask is therefore not the best available choice for RT.

The only coil capable of matching or exceeding the image quality tests was the 4-channel cardiac coil. It is necessary however to use this in conjunction with the uniformity correction algorithm (PURE) to bring the NSNR and the fractional uniformity to an acceptable tolerance. This coil is light-weight and can be easily wrapped around a face mask to give suitable images for registration with CT. It has been suggested that the reduction in SNR by a factor of four, demonstrated by the integrated body coil, is acceptable for the differentiation of anatomical detail since the CNR is comparable to the head coil (Moore et al. 2004). However, the drop in SNR diminishes the quality of MR and negates the diagnostic benefits that MRI provides over CT for discerning the subtle contours of the tumour extent. Furthermore, a drop in the NSNR may be problematic in the use of contrast enhanced imaging where small differences in signal intensity are of greater importance. We have presented a simple method whereby immobilisation may be incorporated in the MR imaging of brain or head and neck patients without losing the image quality which distinguishes MRI from other modalities.

4.8 Conclusion

This method will help to improve image registration of MRI with CT for RT planning. The 4-channel cardiac coil, when used with the uniformity correction algorithm, offers suitable image quality comparable with the multi-channel head coil. It also opens up the exciting possibility of using MRI alone for RT planning.

5 The influence of MRI scan position on patients with prostatic cancer undergoing radiotherapy

5.1 Introduction

This chapter contains a study performed to investigate the effect of magnetic resonance imaging (MRI) scan position when integrated with the radiotherapy (RT) planning process for patients with prostate cancer.

Although, it could be anticipated that imaging the patient in the same orientation as they receive their treatment would result in an improvement in the registration quality, many RT centres neither register the computed tomography (CT) datasets with MRI nor ensure the MRI positioning is consistent with treatment. Furthermore, no publication which tests how this assumption will affect the RT planning process could be found.

The aim of this study was to determine how different patient positions in MRI affected the registration quality with CT. A further goal of this research was to examine the changes in the target volume and how this affects RT planning. It was the overall intention of this study to determine if it was necessary to obtain an MRI scan in the RT position for RT planning or whether a diagnostic MRI scan would suffice.

It is anticipated, that by addressing the problems related to changes in the tumour volume, registration and importantly the subsequent effect on prostatic RT, this will facilitate an adjustment in current practice.

This work has been presented at a national and international level and published in a peer reviewed journal:

- **Does setting up prostate patients in the radiotherapy position when using MRI affect radiotherapy planning?**, Hanvey S, Sadozye A, Glegg M, Foster J, Oral presentation, Advanced Clinical MR in Oncology, Institute of Physics and Engineering in Medicine (IPEM), Leeds, 2011

- **Effects of MRI scan position on image registration accuracy, target delineation and calculated dose in prostatic IMRT**, Hanvey S, McJury M, Sadozye A, Glegg M, Foster J,

Poster presentation, European Society for Radiotherapy and Oncology 31, Barcelona, 2012.

- **The influence of MRI scan position on image registration accuracy, target delineation and calculated dose in prostatic radiotherapy**, Hanvey S, Sadozye A, McJury M, Glegg M, Foster J, The British Journal of Radiology, 85, e1256-e1262 (2012).

5.2 Methods

5.2.1 Patient group and study overview

Twenty patients with prostate cancer (age 56-75) due to undergo radical RT were selected for the study. This investigation was approved by the Local Ethics Committee. Informed consent was obtained from all patients before entering into this study. The patients received a CT planning scan, an MRI scan in the standard diagnostic position (denoted as MRI_D) and an MRI scan in the RT position (denoted as MRI_{RT}) during the same scan session. Both MRI scans were registered separately with CT as shown in Figure 5.1. The gross tumour volume (GTV) was delineated on the CT dataset by a Consultant Clinical Oncologist using a treatment planning system, with the aid of viewing MRI_D on a separate computer console, as is the current practice at our centre. This patient position protocol is denoted as P_C. Delineations of the GTV were then performed on the MRI_D registered to the CT, this is denoted as P_D. The GTV was also delineated on the MRI_{RT} registered to the CT image set, this is denoted as P_{RT}.

5.2.2 CT scanning protocol

Patients were scanned on a GE Light-speed RT 16 CT scanner (GE Medical Systems, WI, USA) using the current clinical scanning protocol. All patients received three gold seed implants to the prostate for positioning adjustment at treatment. Patients were asked to empty their bladder before being given 200ml of water 30 minutes before their scan. To immobilise the patients a knee support and head rest was used. Using a LAP (LAP Laser, Lüneberg, Germany) laser positioning system the patients were aligned with the laser and lateral and anterior markers were placed on the patient. Following the scout scan, tattoos were located 1 cm below the superior border of the symphysis pubis and 1 cm anterior to half of the patient's anterior-posterior separation. A scan extent of

inferior superior-inferior joints to 3 cm below inferior pubic ramus was used. A helical scan was acquired with a detector configuration of 16 × 1.25, pitch 0.938: and speed 18.75 mm/rot with a slice thickness and interval of 2.5 mm.

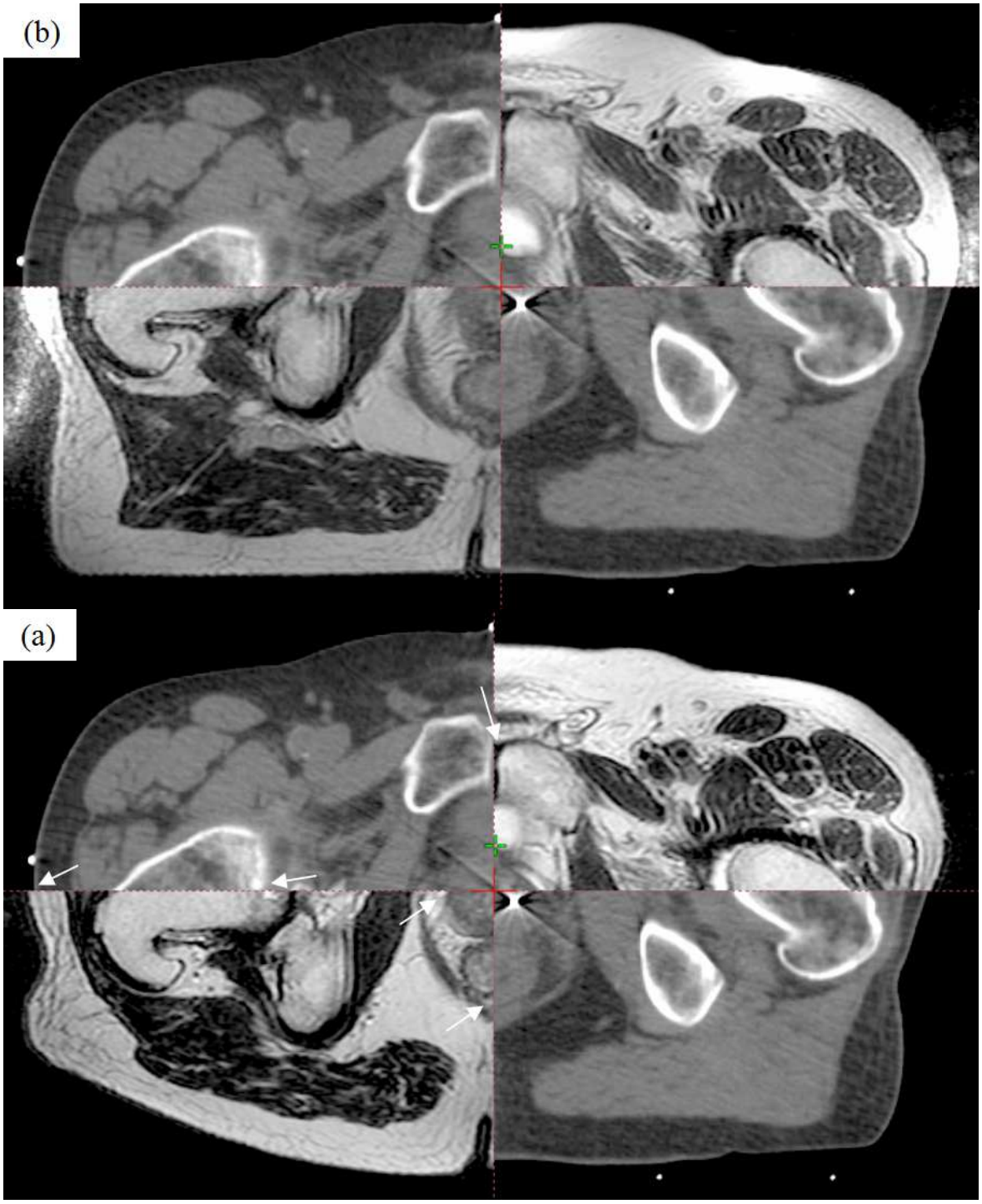

Figure 5.1 Split view showing the registration of (a) the CT and MRI_D and (b) the CT and MRI_{RT} datasets. White arrows on image (a) indicate errors in registration which can be seen to be corrected on (b). MRI_D: diagnostic MRI scan; MRI_{RT}: MRI scan in the radiotherapy position.

5.2.3 MRI scanning protocol

Patients received their MRI scans without contrast, in accordance with our centre's current clinical protocol, on a GE Signa HDxt 1.5T MRI scanner (GE Medical Systems, WI, USA). Weekly geometric linearity and distortion measurements are conducted on this scanner. It was found that the linearity error did not exceed 0.3 mm and the distortion coefficient of variation was no more than 0.3 % over the last 12 months. In addition, monthly uniformity and slice position measurements are performed. The percentage image uniformity measurements were found to be at worst 96.0 % and the largest average slice position error was 0.6 mm for a given month over the previous 12 months. These results were within the tolerances defined in the IPEM report 80 (IPEM 1998) and American Association of Physicists in Medicine (AAPM) report 100 (AAPM 2010).

The patients were scanned in two different positions. For the MRI_{RT} scan, patients were positioned on a customised polymethyl methacrylate (PMMA) sheet, to simulate the treatment couch, with a 4-channel (4-ch) flexible surface cardiac coil beneath the PMMA positioned posterior to the prostate and another positioned on the anterior surface of the patient, as shown in Figure 5.2. The posterior section of the 4-ch cardiac coil was held flat against the underside of the PMMA using high density foam, to maximise the signal-to-noise ratio (SNR). The same knee rest immobilisation and a similar bladder preparation was used as their CT scan, except there was a delay of only 15 minutes after drinking the required volume of water for the MRI scans to take into account the longer scan times. Using the permanent skin markers the patients were firstly positioned with the markers at the centre of the 4-ch imaging coil to maximise the signal at the prostate. Patients were then aligned in the same way as their CT using the markers and a LAP laser positioning device and this became the isocentre plane and central slice. A similar scan extent was used as the CT scan. The imaging parameters for the T1 and T2-weighted scans are shown in Table 5.1. T1 and T2-weighted scans were performed to enable visualisation of the bony anatomy and soft tissue for structure delineation.

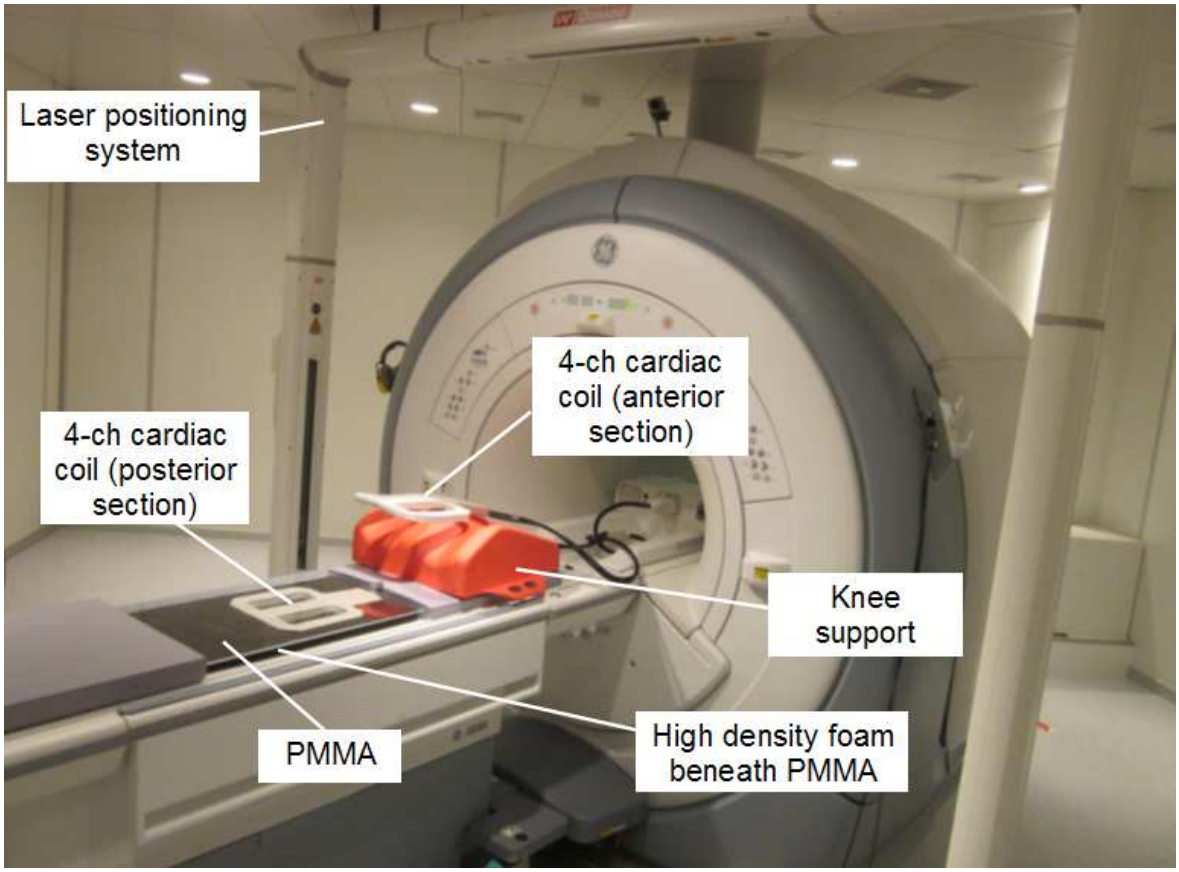

Figure 5.2 MRI_{RT} flat table set up. MRI_{RT}: MRI scan in the radiotherapy position; 4-ch: 4-channel; PMMA: polymethyl methacrylate.

Table 5.1 MRI imaging parameters

Scan type	FOV (mm)	Slice thick (mm)	Spacing (mm)	TE (ms)	TR (ms)	Matrix size
2D driven-equilibrium FSE (T2-weighted)	480	2.5	0	93.9	2520	512×256
3D FSPGR (T1-weighted)	480	2.5	0	2.2	4.5	512×384

FOV: Field of view; TE: echo time; TR: repetition time; FSE: Fast Spin Echo; FSPGR: Fast SPoiled GRadient echo.

The patient was then removed from the table and a standard diagnostic scan was performed using a curved couch and 8-channel cardiac coil during the same scan session. This scan was repeated in the same way as the flat table MRI scan except that the patients were not aligned with the LAP laser positioning device, but were positioned in the magnet as they would be for a typical diagnostic MRI scan of the pelvis. The 8-channel cardiac coil was not used for the MRI_{RT} scan because this coil is curved and rigid and so there would have been a greater distance between the patient and the posterior section of the coil than with the 4-channel cardiac coil. This would have resulted in a reduced SNR of

approximately 14% (McJury et al. 2011) and could potentially have prevented very large patients participating in the study due to the restrictions of the magnet bore size.

5.2.4 Image registration

The CT data set was registered with the MRI_{RT} and MRI_D T1 and T2-weighted scans using the treatment planning system Eclipse (Varian Medical Systems, Inc. CA, USA). This software performed a fully automatic, mutual-information based rigid registration. The entire scanned pelvis was used for the registration to provide as much information for the registration algorithm as possible. A fully automatic registration was used to keep user interaction to a minimum.

An attempt was made to register the CT and MRI datasets using the prostate seeds as registration points to then transform the MRI coordinate system to the CT. The treatment planning system used in this study (Eclipse, Varian Medical Systems, Inc. CA, USA version 8.6.15) could not perform the registration because of the close proximity of the seeds to one another. Changing the volume of interest to include only the prostate so that the registration was performed using the pixel data within the volume of interest resulted in a poor registration. There was also no change to the registration results by prioritising the prostate volume. While deformable registration is available for Eclipse, it does not allow inter-modality registration. Since inter-modality deformable registration is generally not available, nor employed clinically at our centre, this was not subject to further investigation. Fully automated registration was used without manual adjustment since this would introduce subjective errors.

To assess the registration accuracy three rigid volumes were outlined on the CT and MRI T1-weighted data sets. The volumes delineated were the symphysis pubis and three transverse sections of the left and right femoral heads. The transverse sections chosen for the femoral heads were at the most inferior level of the ischial tuberosity, the most inferior aspect of the symphysis pubis and the transverse section above the most proximal slice in which the femoral neck is in continuity with the femoral head. This bony anatomy was delineated firstly using P_C and then repeated on the registered image sets P_D and P_{RT} for each patient.

The quality of registration was assessed in two ways. Firstly, the distance from the centre of bony anatomy drawn in CT to those delineated in MRI was measured using the coordinate location of the centre of the structures determined by the treatment planning system. Since this data was not normally distributed the geometric mean was calculated. Secondly, the spatial overlap of the structures drawn on CT and MRI was measured. The spatial overlap of the volumes contoured in CT and MRI was assessed by calculating the Dice coefficient (spatial overlap) for each volume, which is given by,

Equation 5.1

$$\text{spatial overlap} = \frac{\text{CT} \cap \text{MRI}}{(\text{CT} + \text{MRI})/2}$$

where CT $\cap$ MRI is the volume of intersection between the CT and MRI structures. The value of the spatial overlap ranges from zero, which indicates no spatial overlap between the CT and MRI volumes, to one, which is complete overlap (Zou et al. 2004). As volumes outlined on CT and MRI may differ, even with perfect registration, a spatial overlap of one may not be achieved in practice. However, comparisons of spatial overlap for the MRI volumes with different patient set-up and registration quality will show changes in spatial overlap, which are dependent on these differences.

The assessment of registration quality was applied to the GTVs in the same way as the bony anatomy: by measuring the distance between GTVs and the spatial overlap of the GTVs delineated using P_C, P_D and P_{RT}.

5.2.5 Gross tumour volume, organs at risk and planning target volume delineation

A trained Consultant Clinical Oncologist delineated two volumes for all patients; the prostate and the prostate plus seminal vesicles. The Oncologist delineated the two volumes using P_C, P_D and P_{RT}. When delineating on the registered image sets, the clinician was able to view both the CT and MRI information at the same time. The clinician generally used the T2-weighted MRI datasets for contouring the prostate and seminal vesicles, although the T1-weighted images were also referenced. There was a period of at least a week between delineations of the same patient using a different imaging protocol and the Oncologist was blinded

to previous delineations. The organs at risk (OARs) for patients with prostate cancer are the rectum, bladder and femoral heads. It was known from previous experience that due to the orientation of the beams used in intensity modulated radiotherapy (IMRT) planning the dose to the femoral heads never reached the clinical dose constraint, therefore only the dose to the bladder and rectum was investigated. The OARs were outlined using the three patient position protocols P_C, P_D and P_{RT} for each patient.

Planning target volumes (PTVs) were generated from the Oncologist's delineations of the GTV for the purposes of IMRT planning. PTV1 was the prostate plus the seminal vesicles with a margin of 10 mm isotropically. PTV2 was the prostate plus a 10 mm margin in all directions except in the posterior direction where a margin of 5 mm was given. Finally, PTV3 was the prostate with a margin of 5 mm in all directions except in the posterior direction where there was no expansion from the prostate. PTV3 was not expanded into the rectum. All three PTVs were investigated but since a similar pattern was demonstrated for each PTV only the results of PTV3 are presented. PTV3 delineated with P_C, P_D and P_{RT} will henceforth be denoted PTV_C, PTV_D and PTV_{RT} respectively.

5.2.6 Dose analysis

To determine the effect changes in tumour volumes have on RT planning, IMRT plans were generated for each patient. For each patient three IMRT plans were calculated by optimising for PTV1, PTV2 and PTV3 generated from the prostate volumes delineated using the patient position protocols P_C, P_D and P_{RT}.

The IMRT plans were calculated in accordance with the Conventional or Hypofractionated High Dose Intensity Modulated Radiotherapy for Prostate Cancer (CHHiP) trial (Dearnaley et al. 2012) dose constraints using the pencil beam convolution algorithm in Eclipse (Varian Medical Systems, Inc) version 8.2.23. At the time of the study using the CHHiP dose constraints for IMRT planning of prostatic cancer patients was the current clinical protocol. With this set of PTVs, we have taken each PTV in turn and assumed for analysis it is the volume for clinical planning, and optimised the plan for this volume.

Of particular interest in this study was to investigate the quality of the RT plan for P_C and P_D with reference to P_{RT}, since our working hypothesis postulates that the optimum target volume definition is achieved with P_{RT}. To achieve this IMRT plans were optimised for PTV_C and PTV_D while the dose coverage of PTV_{RT} for these plans was investigated.

To determine the quality of each RT plan a conformation number (CN) was calculated for PTV_C, PTV_D and PTV_{RT}. The CN indicates the extent to which the target volume is being irradiated and healthy tissue is being spared. The CN is defined according to the following equation (Reit et al. 1997),

Equation 5.2

$$CN = \frac{TV_{RI}}{V_{PTV}} \times \frac{TV_{RI}}{V_{RI}}$$

where TV_{RI} = target volume covered by the reference isodose, V_{PTV} = volume of the PTV and V_{RI} = volume of the reference isodose. The reference isodose volume is defined as the volume receiving the therapeutic prescribed dose.

The first fraction of the equation relates to the quality of the target coverage while the second fraction is an indicator of healthy tissue sparing. The CN varies from 0 to 1, where 1 is the ideal value and the target is covered completely with total sparing of the surrounding healthy tissue (Reit et al. 1997). The PTV for which the plan was optimised would be expected to have a high value of CN, whilst the CN for the other two non-optimised PTVs will reflect the impact of registration differences on the planning doses. With the working hypothesis stating that PTV_{RT} is the gold standard, it was possible to determine the extent to which the PTV_C and PTV_D achieve a similar IMRT quality by optimising for PTV_C and PTV_D but investigating the CN of the non-optimised PTV_{RT}.

Two-tailed student t-tests were performed to examine the statistical significance of the differences of the registration quality and dosimetric indices, except for the differences in the geometric mean distances from the centre of the structures in CT and MR where a two-tailed Mann-Whitney test was used. The null hypothesis was rejected when the *p* value was less than 0.05.

5.3 Results

While performing CT-MRI registration, qualitatively it was found that there was improved registration with MRI_{RT} compared to MRI_D. An example of this is shown in Figure 5.1 where discrepancies in the registration can be seen for the CT-MRI_D, as indicated by the arrows, but not with MRI_{RT}.

This is in agreement with the quality of registration measurements which show a reduction in the geometric mean distance from the centre of the CT to the MRI_{RT} bony anatomy to that of the CT to MRI_D volumes (Table 5.2). This data showed a statistically significant improvement in the CT-MRI registration accuracy of each structure for the MRI_{RT} over the MRI_D datasets (left femoral head, *p* value = 0.049; right femoral head, *p* value = 0.003; symphysis pubis, *p* value < 0.001).

The mean spatial overlap for the bony landmarks demonstrated an improvement between CT and MRI_{RT} over MRI_D as shown in Table 5.2. Combining the spatial overlap results for the bony anatomy, by averaging the data for the left and right femoral heads and symphysis pubis gave a mean spatial overlap of 0.67 for the P_D compared to 0.74 for the P_{RT} (*p* value = 0.046).

Table 5.2 Geometric mean error and mean spatial overlap of the bony anatomy. The geometric mean error is the geometric mean of the distance from the centre of the CT structures to the centre of the MRI structures. The error bars represent ± 1 standard deviation.

	CT to MRI_D geometric mean error (mm)	CT to MRI_{RT} geometric mean error (mm)	Mean CT to MRI_D spatial overlap	Mean CT to MRI_{RT} spatial overlap
Left femoral head	2.4 ± 2.2	1.5 ± 1.6	0.77	0.85
Right femoral head	3.0 ± 1.8	1.5 ± 1.2	0.72	0.81
Symphysis pubis	4.2 ± 3.0	1.6 ± 1.1	0.52	0.56

MRI_D: diagnostic MRI scan; MRI_{RT}: MRI scan in the radiotherapy position.

Investigating the registration quality of the GTVs revealed that there was a decrease in the mean distance from the centre of the prostate and prostate plus seminal vesicles volumes delineated on P_C to P_{RT} compared to the volumes drawn on the P_D (Table 5.3). There was a statistically significant difference in the mean error of the prostate and prostate plus seminal vesicles volumes delineated on P_C and P_D to those drawn using P_C and P_{RT} (*p* value = 0.021).

There was also an improvement in the mean spatial overlap of the GTVs delineated using P_C and P_{RT} rather than the P_D (Table 5.3). A significant difference was found in the spatial overlap between the prostate volumes delineated using P_C and P_D and those delineated on P_C and P_{RT} (*p* value = 0.045) but not for the prostate plus seminal vesicles (*p* value = 0.058).

Table 5.3 Mean error and mean spatial overlap of the prostate and prostate plus seminal vesicles. Mean error is the distance from the centre of structures drawn using P_C to those drawn using P_D or P_{RT}.

	P_C and P_D mean error (mm)	P_C and P_{RT} mean error (mm)	Mean P_C and P_D spatial overlap	Mean P_C and P_{RT} spatial overlap
Prostate	5.0 ± 2.5	3.6 ± 2.2	0.70	0.74
Prostate & seminal vesicles	5.2 ± 2.3	4.1 ± 2.6	0.64	0.69

P_C: CT with the diagnostic MRI scan viewed on a separate console; P_D: CT registered with the diagnostic MRI scan; P_{RT}: CT registered with the MRI scan in the radiotherapy position.

In Table 5.2 and Table 5.3 the mean error results are presented with their standard deviations. It can be seen that the bony anatomy and prostate volumes show a reduction in the standard deviation values for the CT dataset registered to the MRI_{RT} rather than the MRI_D. This is due to the use of patient positioning lasers to set-up the patients for their MRI_{RT} scan. The lasers enabled the patients to be positioned for their MRI_{RT} scan more closely to their CT set-up position and thereby resulted in a reduction in the set-up error, whereas for their MRI_D scan, the patients were not aligned with the positioning lasers and so were unlikely to be scanned in the same plane as their CT scan. However, the standard deviation for the prostate and seminal vesicles mean error results was seen to increase using P_{RT} instead of P_D. This is thought to be as a result of the challenges associated with delineating the seminal vesicles using CT.

The mean prostate and prostate plus seminal vesicles volumes were significantly larger when the clinician contoured on P_C rather than on P_D or P_{RT} as shown in Table 5.4. The *p* values in Table 5.4 refer to the differences in the prostate and prostate plus seminal vesicles volumes delineated on the P_C to those drawn using the P_D or P_{RT}.

Conformation number results for PTV_C, PTV_D and PTV_{RT} are presented in Table 5.5. It can be seen from the first three rows of Table 5.5 that an excellent CN of

average 0.98 can be achieved when evaluating the dose coverage of the PTV being optimised.

Table 5.4 Mean volume of the prostate and prostate plus seminal vesicles in the different set-ups. The *p* values refer to the differences in the prostate and prostate plus seminal vesicles volumes delineated on the P_C to those drawn using the P_D or P_{RT}.

Structure	Mean P_C volume (cm^3)	Mean P_D volume in cm^3 (*p* value)	Mean P_{RT} volume in cm^3 (*p* value)
Prostate	36.3 ± 10.8	32.0 ± 11.1 (0.001)	31.4 ± 11.0 (0.001)
Prostate & seminal vesicles	45.9 ± 12.0	41.2 ± 12.9 (0.001)	40.3 ± 12.5 (0.002)

P_C: CT with the diagnostic MRI scan viewed on a separate console; P_D: CT registered with the diagnostic MRI scan; P_{RT}: CT registered with the MRI scan in the radiotherapy position.

Optimising the RT plan for PTV_C but calculating the CN for PTV_{RT} results in a mean CN of 0.80 (row 4 of Table 5.5). This is significantly different to the mean CN of 0.98 found when optimising for PTV_C and calculating the dose coverage of PTV_C (*p* value < 0.001). Similarly, optimising for PTV_D but calculating the CN for PTV_{RT} gives a mean CN of 0.85 (last row of Table 5.5) instead of the expected 0.99 for PTV_D (*p* value < 0.001). Only by optimising for the working hypothesis gold standard PTV, PTV_{RT}, is it possible to achieve a mean CN of 0.98, since the mean CN is significantly lower for both PTV_C and PTV_D. All PTV optimisation combinations were assessed but are not recorded, because they are not clinically relevant.

Table 5.5 Mean CN for PTV_C, PTV_D and PTV_{RT} when optimised for PTV in the three set-ups.

PTV for which the IMRT plan was optimised	PTV under examination	Mean CN
PTV_C	PTV_C	0.98 ± 0.03
PTV_D	PTV_D	0.99 ± 0.01
PTV_{RT}	PTV_{RT}	0.98 ± 0.06
PTV_C	PTV_{RT}	0.80 ± 0.11
PTV_D	PTV_{RT}	0.85 ± 0.13

IMRT: intensity modulated radiotherapy; PTV: planning target volume; PTV_C: PTV drawn on CT with the diagnostic MRI scan viewed on a separate console; PTV_D: PTV drawn on CT registered with the diagnostic MRI scan; PTV_{RT}: PTV drawn on CT registered with the MRI scan in the radiotherapy position; CN: conformation number.

5.4 Discussion

This is the first study to compare CT-MR image registration accuracy and RT plan quality of a diagnostic versus RT positioned MRI scan for patients with prostate cancer. The results of this study have shown that prostatic patients undergoing RT should be positioned in the RT position when registering MR images to CT for RT planning, since this provides optimal registration and target delineation accuracy.

The quality of registration to CT improved using the MRI_{RT} instead of the MRI_D images. This was demonstrated by a statistically significant reduction in the geometric mean error of the rigid bony landmarks from CT to the MRI_{RT} to that drawn on the CT and MRI_D datasets and an improvement in the spatial overlap of these structures (from a mean of 0.67 to a mean of 0.74; p value = 0.046). In this study the relative changes in the spatial overlap were assessed, since, as mentioned previously, a spatial overlap of 1 may not be attained because of the differences in the volumes delineated on MRI and CT.

A reduction in the average distance of the prostate volumes was found when delineated on P_C and P_{RT} (5.0 ± 2.5 mm) rather than P_C and P_D (3.6 ± 2.2 mm). Similarly, for the prostate plus seminal vesicles volumes, there was a reduction in the average distance between P_C and P_{RT} (5.2 ± 2.3 mm) versus the distance between P_C and P_D (4.1 ± 2.6 mm). This improvement was found to be statistically significant when the results of both the prostate and prostate plus seminal vesicles were analysed (*p* value = 0.021).

An improvement in the mean spatial overlap of the prostate was evident between P_C and P_{RT} (0.74) versus P_D (0.70). There was also an improvement in the mean spatial overlap for the prostate plus seminal vesicles volumes between P_C and P_{RT} (0.69) over P_D (0.64). This improvement in mean spatial overlap was significant for the prostate (*p* value = 0.045) but not the prostate plus seminal vesicle volumes (*p* value = 0.058), due to the difficulty in delineating the seminal vesicles, particularly on CT. The quality of registration results for the GTVs is in agreement with the improved registration accuracy demonstrated between CT and MRI_{RT} for the bony anatomy. The reduced error and improved spatial overlap between CT and MRI_{RT} for the prostate and seminal vesicles

offers the clinician greater confidence in the use of MRI for RT planning. Accurate target localisation becomes more important as RT planning moves towards dose escalation and dose painting techniques with high dose gradients.

It was shown that the rigid landmarks and prostate results show a reduction in the standard deviation values for the CT dataset registered to the MRI_{RT} rather than the MRI_D. This strongly implies that patients are positioned more closely to the CT set-up when using the RT positioned MRI rather than the diagnostic MRI. However, unlike the rigid landmarks and the prostate structures, the standard deviation of the prostate plus seminal vesicle volumes slightly increased from P_D to P_{RT}. An increase in the standard deviation of these volumes is due to the challenges associated with delineating the seminal vesicles.

The importance of CT-MRI registration is demonstrated by a statistically significant difference between the prostate volumes when the clinician contoured using P_C rather than the registered datasets, P_D (p value = 0.001) and P_{RT} (p value = 0.001). A significant difference was also found for the prostate plus seminal vesicles volumes between the unregistered imaging protocol, P_C, and the registered set-ups, P_D (p value = 0.001) and P_{RT} (p value = 0.002). This significant difference is because the prostatic capsule cannot be distinguished from surrounding tissue on CT, but with T2-weighted MRI this can be seen as a thin rim of low signal intensity. MRI is also superior to CT in defining the prostatic apex and distinguishing the boundaries of the prostate with the base of bladder and anterior wall of the rectum.

The changes in target volume in this study are in agreement with several other studies (Charnley et al. 2005; Khoo and Joon 2006; Rasch et al. 1999; Sannazzari et al. 2002; Sefrova et al. 2012; Smith et al. 2007), which have demonstrated that outlining prostate and seminal vesicles using MRI results in more accurate treatment volumes. One study (Rasch et al. 1999) has shown that outlining with MRI results in a smaller volume of rectal wall being included, potentially leading to a reduced risk of late toxicity. It may also help to reduce complications to important structures such as the penile bulb.

Dosimetric results showed that it was possible to achieve an average CN of 0.98 when optimising and investigating the dose coverage of PTV_C, PTV_D or PTV_{RT}.

This shows that the planning methodology of this study results in excellent target coverage with minimal dose to the surrounding healthy tissue.

It was the working hypothesis of this study to regard PTV_{RT} as the gold standard. The results have demonstrated that P_{RT} offers improved registration accuracy over P_D. Registering CT with MRI has also been shown to result in significant differences in target delineation due to the improved soft tissue contrast provided by MRI. In light of this evidence, it is reasonable to assume that PTV_{RT} is the gold standard.

In this study we optimised the dose to the PTV_C and PTV_D while calculating the dose received by the gold standard PTV_{RT}. There was a statistically significant difference between the mean CN values when optimising for PTV_C and investigating the dose coverage of PTV_C or PTV_{RT} (p value < 0.001). Similarly, when optimising for PTV_D the dose coverage was found to be significantly different for PTV_D and PTV_{RT} (p value < 0.001). The improvement in the quality of IMRT planning using the PTV_{RT} demonstrates that it would be suboptimal to rely on the PTV_C or PTV_D for prostatic RT planning.

Obtaining a second MRI in the RT position, rather than relying on the diagnostic MRI, clearly places greater financial demands on the healthcare service. This must be balanced with the improved registration and target definition and, as a result, superior dose coverage of the PTV, as demonstrated by this study. It may be possible to reduce the MRI scanning time by obtaining only the T2-weighted MRI scan in the RT position, which was the favoured MRI scan by the Oncologist due to anatomical detail of this sequence. Further research in this area could be to correlate the dosimetric results with clinical outcome data, which could give a clearer indication of the balance between cost and benefits. A study into the use of non-rigid registration to determine the effects on GTV localisation and subsequent RT plans is also warranted.

5.5 Conclusion

A practical methodology for obtaining prostatic MR images in the RT position for registration with CT planning images has been demonstrated. This study has shown that when MRI scans are performed in the RT position, significant

improvements in the quality of CT-MRI registration can be achieved. Significant changes have also been shown in the target definition and dose coverage of RT positioned MRI datasets, which may result in changes to patient outcomes.

6 The influence of MRI scan position on patients with oropharyngeal cancer undergoing radiotherapy

6.1 Introduction

The following chapter describes a study performed to demonstrate how magnetic resonance imaging (MRI) patient position protocols influence registration quality in patients with oropharyngeal cancer undergoing radical radiotherapy (RT). In addition, the consequences for gross tumour volume (GTV) definition and RT planning were examined.

With intensity modulated radiotherapy and volumetric modulated arc therapy (VMAT) it is possible to deliver high doses of radiation to irregular volumes whilst sparing normal tissue, which can result in reduced severity of radiation toxicities in patients with head and neck cancer (Nutting et al. 2011). Increased dose delivery and dose conformity has led to a greater significance on the accurate localisation of the GTV and neighbouring structures.

It has been shown that an approximate image registration uncertainty of 2 mm occurs when registering computed tomography (CT) image sets in the treatment position to a diagnostic MRI for patients with brain cancer (Kenneth et al. 2010). As a result of this small registration error, many RT centres routinely register a planning CT scan with a diagnostic MRI scan for RT planning of patients with brain cancer. Prior to this study, there was no published evidence investigating the errors associated with registering a planning CT scan with a diagnostic MRI scan, for patients with oropharyngeal cancer. Additionally, this experiment analyses the dosimetric consequences of patient positioning during MRI scan acquisition.

The purpose of this study was to compare an MRI acquired with a diagnostic patient position on a standard MRI table to an MRI acquired on a flat table with custom immobilisation and to determine how this affects CT-MRI registration, GTV definition and the resulting VMAT RT plans. The magnitude of the associated geometric and dosimetric errors is discussed. The results obtained would then provide an answer to whether it was necessary to obtain a planning

MRI scan for patients with oropharyngeal cancer in the RT treatment position using an immobilisation mask or whether a diagnostic patient position protocol would provide similar results.

This work has been presented at a national and international level and published in a peer reviewed journal:

- **MRI of head and neck cancer patients for radiotherapy planning**, Hanvey S, Paterson C, Rizwanullah M, Thomson M, Glegg M, Foster J, Poster presentation, 19th International Society for Magnetic Resonance in Medicine (ISMRM), Montreal, 2011.

- **Effects of MRI scan position on CT image registration accuracy and target delineation for oropharyngeal cancer VMAT patients** Hanvey S, McJury M, Paterson C, Rizwanullah M, Thomson M, James A, Tho LM, Grose D, Glegg M, Foster J, Poster discussion, European Society for Radiotherapy and Oncology (ESTRO) 31, Barcelona, 2012.

- **The influence of MRI scan position on patients with oropharyngeal cancer undergoing radical radiotherapy**, Hanvey S, McJury M, Tho LM, Glegg M, Thomson M, Grose D, James A, Rizwanullah M, Paterson C, Foster J. Radiation Oncology, 28;8(1):129 (2013).

6.2 Methods

6.2.1 Patient group and study overview

Twenty two patients with oropharyngeal cancer (age 37-72), being worked up for radical RT, were identified for the study, regardless of tumour or nodal stage. The study protocol was approved by Local Ethics Committee and informed written consent was obtained from all patients. Registration quality assessment was conducted on all patients, however, in three patients a GTV evaluation was not possible, since two patients had undergone primary surgical resection and another had received induction chemotherapy, resulting in complete response.

Patients underwent a CT planning scan, and two MRI scans (patients scanned between February 2010 and January 2012; median time between CT and MRI scans = 5 days, range = 0 to 21 days). The first MRI scan was obtained with the patient in the standard diagnostic position (denoted as MRI_D) and the second with the patient in an immobilisation mask in the RT position (MRI_{RT}). Both MRI scans were registered separately with the CT planning scan as shown in Figure

6.1. The GTV was delineated on the CT images by trained Consultant Radiation Oncologists using the treatment planning system, with the aid of viewing MRI_D on a separate console, as is the current practice at our centre. This patient position protocol is denoted as P_C. For the purposes of this study, the GTV was delineated using two other patient set-ups. Firstly, the GTV was delineated on the MRI_D registered to the CT datasets, this is denoted as P_D. The GTV was also delineated on the MRI_{RT} registered to the CT image sets, this is denoted as P_{RT}.

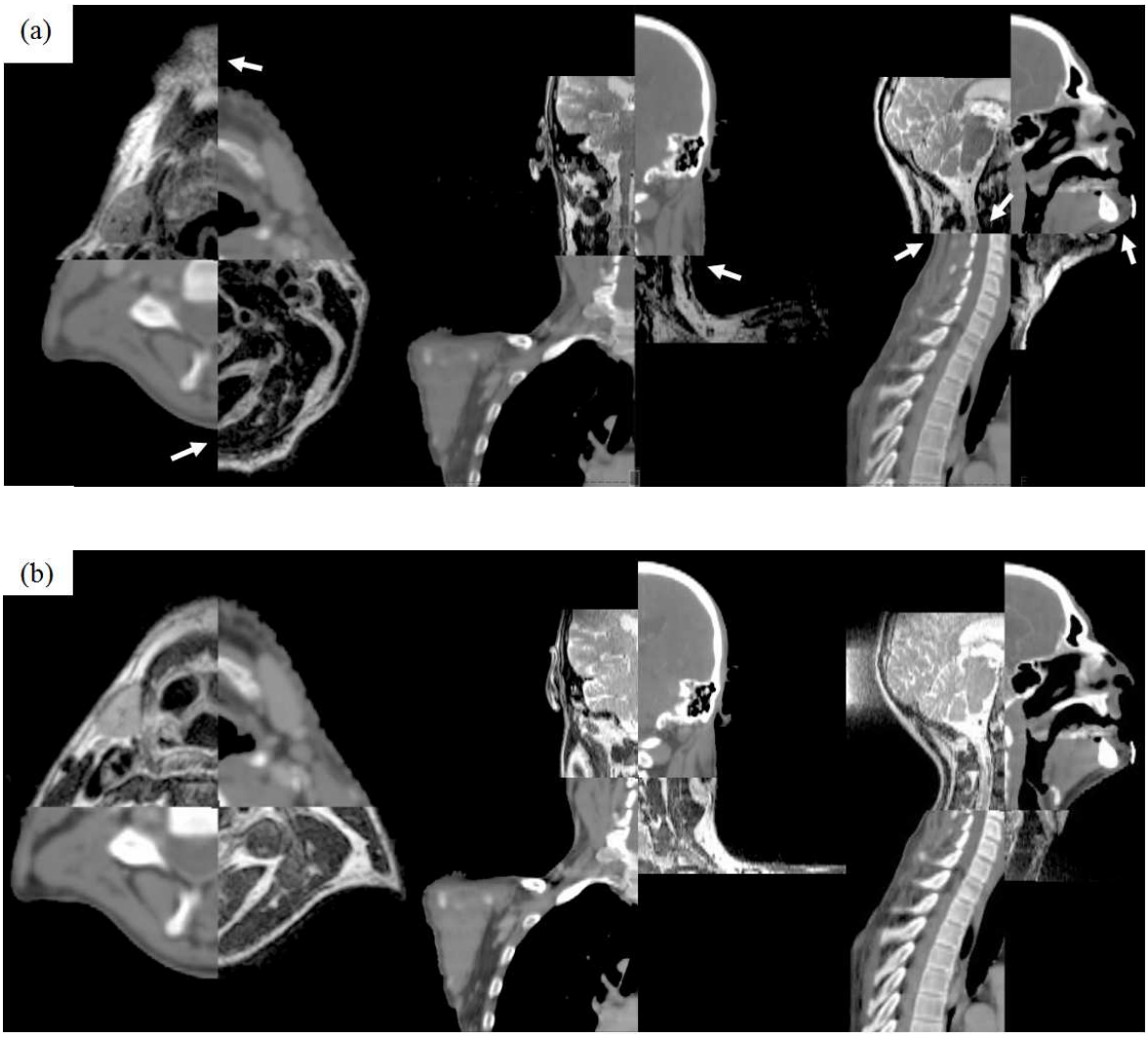

Figure 6.1 Split view showing the registration in the axial, coronal and sagittal planes of (a) the CT and MRI_D and (b) the CT and MRI_{RT} datasets. Arrows indicate regions where there is a registration mismatch between CT and MRI_D. Typically, more discrepancies in registration occurred with MRI_D than MRI_{RT}. MRI_D: diagnostic MRI scan; MRI_{RT}: MRI scan in the radiotherapy position.

6.2.2 CT and MRI scanning protocol

Patients were scanned on a GE Light-speed RT 16 slice CT scanner (GE Healthcare, WI, USA), using the current clinical scanning protocol, and

immobilised within a full face and neck five point fixation thermoplastic beam directional shell (BDS) with appropriate head rest (CIVCO Medical Solutions, IA, USA). The scan extent was from superior orbital ridge to carina. A helical scan was acquired with a detector configuration of 16 $\times$ 1.25, pitch 0.938, matrix 512 $\times$ 512 and speed 18.75 mm/rot with a slice thickness of 2.5 mm.

Patients underwent MRI scans in two different positions during the same scan session. For the MRI_{RT} scan, patients were positioned on a flat MRI Oncology Table (GE Healthcare, WI, USA) within a BDS with a 4-channel flexible surface cardiac coil positioned laterally over the patient's neck (Figure 6.2). The same scan extent as the CT scan was employed and the imaging parameters, chosen in accordance with local protocol, are presented in Table 6.1. Weekly and monthly quality assurance tests (described in Chapter 5, Section 5.2.3) ensured the MRI scanner performed within recommended image quality tolerances.

Figure 6.2 MRI acquired in the radiotherapy position with a 4-channel flexible surface coil positioned laterally

The scan was repeated for the MRI_D on a standard curved diagnostic table without BDS using a 16-channel head, neck and spine coil, with the CT scan extent. The 16-channel head, neck and spine coil was not used for the MRI_{RT} scan since it is not compatible with the BDS. A previous investigation using test objects has shown the image quality obtained using the 4-channel cardiac coil is of diagnostic quality (Hanvey et al. 2009).

Table 6.1 MRI scanning parameters.

Scan type	FOV (mm)	Slice thick (mm)	Spacing (mm)	TE (ms)	TR (ms)	Bandwidth (± kHz)	Matrix size
2D Driven-equilibrium FSE (T2-weighted)	400	2.5	0	94	2620	63	512×256
3D Spoiled gradient echo (T1-weighted post-contrast)	400	2.5	0	2	15	50	256×256

FOV: field of view; TE: echo time; TR: repetition time.

6.2.3 Image registration

The treatment planning system (Eclipse, Varian Medical Systems, Inc. CA, USA version 10.0.39) was used to register the MRI_{RT} and MRI_{D} T1 and T2-weighted scans to the CT data. This software enabled fully automated, mutual-information based rigid registration to be performed. While deformable registration is available for Eclipse, it does not allow inter-modality registration. Since commercial inter-modality deformable image registration is generally not available, nor employed clinically in our centre at present, this was not subject to further investigation. The volume over which the registration was performed was centred over the oropharyngeal region and chosen to include as much information for the registration algorithm as possible (Ahmed et al. 2010). Fully automated registration was used without manual adjustment since, for this site, satisfactory registration for both target and nodes is not always achievable and would introduce subjective errors.

To quantitatively assess the quality of registration the orbits and the odontoid process were outlined on the CT and T1-weighted MR image sets. These three structures were delineated on the CT, for each patient, and then repeated on the MR datasets registered to the CT.

Two metrics determined the quality of registration. Firstly, the distance between the centres of the orbits and odontoid process drawn on the CT and the MRI datasets was calculated using the coordinate location of the centre of the structures determined by the treatment planning software. The geometric mean was calculated to ensure normality of the data. Secondly, the quality of

registration was assessed by measuring the spatial overlap of these structures drawn on CT and MRI. The spatial overlap was assessed by calculating the Dice coefficient (spatial overlap) for each structure, which is given by,

Equation 6.1

$$\text{spatial overlap} = \frac{\text{CT} \cap \text{MRI}}{(\text{CT} + \text{MRI})/2}$$

where CT $\cap$ MRI is the volume of intersection between the CT and MRI structures. The value of the spatial overlap can range from zero, which indicates no spatial overlap between the CT and MRI volumes, to one, which indicates complete overlap (Zou et al. 2004). Since structures outlined on CT and MRI may differ, even with perfect registration, a spatial overlap of one may not be achieved in practice, but will still be dependent on different patient set-up and registration quality.

6.2.4 Gross tumour volume, lower risk clinical target volume and organ at risk delineation

Three Oncologists were assigned five patients each and a fourth was assigned four patients. The Oncologists delineated the GTV on their patients using the three set-ups P_C, P_D and P_{RT}, which in this study are referred to as GTV_C, GTV_D and GTV_{RT} respectively. Anonymised information sheets, containing the patient's clinical history and radiology report, were available to the Oncologists. The clinicians generally utilised the T2-weighted MR datasets while contouring the GTV, although T1-weighted images were also referenced. A period of at least a week was given between delineations of the GTV for the same patient using a different imaging protocol and the Oncologists were blinded to previous delineations. Changes in the magnitude of the GTV were assessed. Contouring was also performed on the lower risk clinical target volume (CTV LR) of the nodal areas at risk of microscopic involvement for a randomly selected cohort of ten patients, in each of the set-ups. Nodal delineation was performed according to international consensus guidelines (Grégoire et al. 2003). For these patients, the organs at risk (OARs), which included the left and right parotids, larynx, spinal cord and the brainstem, were also contoured.

The GTV and CTV LR were expanded to obtain planning target volumes, (PTV) and lower risk planning target volumes (PTV LR) respectively. To create the clinical target volume (CTV) the GTV was expanded by 1 cm isotropically, removing any overlap with bone or air cavities. The CTV was then enlarged by 3 mm isotropically and cropped from the external outline of the body to create the PTV. It is necessary to crop the PTV from the body outline to assist in the VMAT optimisation process. The PTVs were generated from the GTVs using the three set-ups P_C, P_D and P_{RT}, which are denoted as PTV_C, PTV_D and PTV_{RT} respectively. Similarly, to generate the PTV LR the CTV LR was expanded by 3 mm isotropically and cropped by an appropriate margin from the body outline. Target volumes and OARs were generated in accordance with local protocol.

6.2.5 Dose analysis

VMAT plans were calculated for the ten patients for whom the GTV, CTV LR and OARs were contoured, to determine the impact that changes in target volume definition have on RT planning. The VMAT plans were calculated in accordance with our centre's clinical dose constraints using the Anisotropic Analytical Algorithm and Progressive Resolution Optimiser VMAT algorithm in Eclipse (Varian Medical Systems, Inc, CA, USA) version 10.0.28. A VMAT plan was calculated for PTV_C, PTV_D and PTV_{RT}. Dose volume histograms (DVHs) were generated for PTV_C, PTV_D and PTV_{RT}. A mean DVH for all ten patients was then calculated for P_C, P_D and P_{RT}. These results are presented using our centre's dose constraint protocol i.e. $D_{99} > 90\%$, $D_{95} > 95\%$, $D_5 < 105\ \%$ and $D_2 < 107\%$, where $D_{99} > 90\%$ means 99% of the total PTV volume should receive a dose > 90% of the prescribed dose. The other dose constraints are defined similarly.

Of particular interest in this study was to establish the quality of the RT plan for P_C and P_D with reference to P_{RT}, since our working hypothesis postulates that the optimum target volume definition is achieved with P_{RT}. To achieve this we optimised for PTV_C and PTV_D but investigated the dose coverage of PTV_{RT} at $D_{99} > 90\%$, $D_{95} > 95\%$, $D_5 < 105\ \%$ and $D_2 < 107\%$.

To determine the degree to which the RT plans conformed to the target volume a conformation number (CN) was calculated. The CN is a single numerical value

which indicates the extent to which the plan conforms to the target. The CN is defined according to the following equation (Reit et al. 1997),

Equation 6.2

$$CN = \frac{TV_{RI}}{V_{PTV}} \times \frac{TV_{RI}}{V_{RI}}$$

where TV_{RI} = target volume covered by the reference isodose, V_{PTV} = volume of the PTV and V_{RI} = volume of the reference isodose. The reference isodose volume is defined as the volume receiving the therapeutic prescribed dose.

The first fraction of the equation refers to the coverage of the target volume and the second term indicates the volume of healthy tissue receiving a dose equal to or greater than the reference dose. The CN varies from 0 to 1, where 1 represents a reference isodose which covers the target completely without any irradiation of healthy tissue and is therefore the optimal conformation. A value of 0 means no conformation at all, which would arise in the event of a geographical miss. Since the working hypothesis states that PTV_{RT} is the true target volume, the quality of the RT plan for PTV_C and PTV_D was analysed with reference to PTV_{RT}. This was accomplished by optimising for PTV_C and PTV_D while analysing the dose coverage for PTV_{RT}.

A quantitative comparison of the homogeneity of the dose to the PTV was completed using the sigma index. The sigma index was compared individually for PTV_C, PTV_D and PTV_{RT} as well as for PTV_C, PTV_D with reference to PTV_{RT}. The sigma index is equal to the standard deviation of the dose throughout the PTV, calculated on a voxel by voxel basis (Yoon et al. 2007), thus the higher the sigma index, the greater the dose inhomogeneity.

Finally, the dose to the OARs was assessed by evaluating the mean received using P_C, P_D and P_{RT}. The number of patients exceeding the local dose constraints was measured and compared with each patient position protocol.

Two-tailed paired student t-tests were performed to examine the statistical differences of the registration quality and dosimetric indices, except for the geometric mean distance from the centre of structures in CT and MRI where two-tailed Mann-Whitney tests were performed. A Mann-Whitney test was used

to assess the geometric mean distance from the centre of the structures because the data was not normally distributed. The null hypothesis was rejected when the *p* value was less than 0.05.

6.3 Results

There was a reduction in the geometric mean distance from the centre of the orbits and odontoid process delineated on the CT and MRI_{RT} to that delineated on the CT to MRI_D volumes (Figure 6.3) and this was significant (*p* value < 0.001) for each structure. Narrower error bars exist for the CT registered to the MRI_{RT} versus the MRI_D, which strongly implies that the patients are positioned more closely to their CT set-up in the BDS than when using the ordinary diagnostic set-up. No correlation was found between the time from the CT and MRI scan in days and the mean registration error for either MRI_D (R^2 = 0.06) or MRI_{RT} (R^2 = 0.02).

An improvement in the mean spatial overlap for the orbits and odontoid process was observed between CT and the CT-MRI_{RT} over the CT to CT-MRI_D data sets as shown in Table 6.2. Analysing the difference between the spatial overlap of CT to CT-MRI_D versus CT to CT-MRI_{RT} was shown to have a *p* value < 0.001 for both orbits and odontoid process (Table 6.2). The volume of the three structures delineated on CT was larger than those delineated on MRI; however, their mean difference was within one standard deviation. Therefore, the spatial overlap is expected to give a good measure of the quality of registration.

The mean GTV_C was significantly larger than the GTV_D or GTV_{RT} as shown in Table 6.3. The *p* values in Table 6.3 refer to the differences in the magnitude of the GTV_C and the other two GTVs. There was no significant difference between GTV_D and GTV_{RT} (*p* value = 0.14).

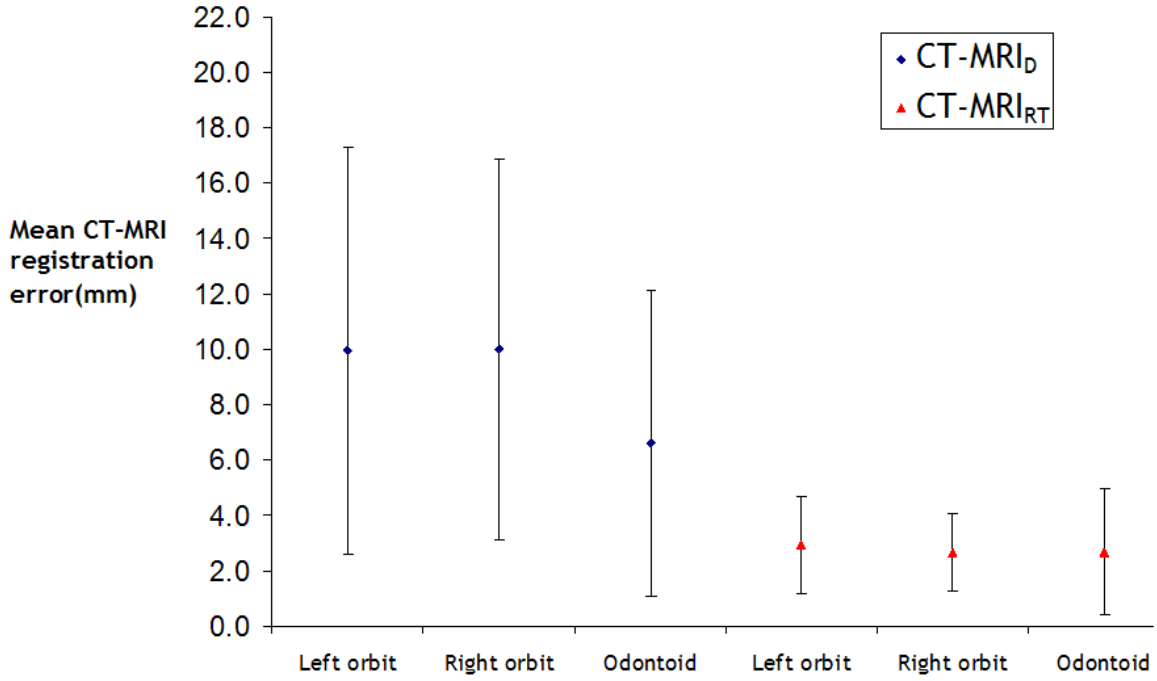

Figure 6.3 Quality of registration results, where the mean error is the distance from the centre of the CT structures to the centre of the MRI structures. Odontoid: odontoid process; CT-MRI$_D$: CT registered with the diagnostic MRI scan; CT-MRI$_{RT}$; CT registered with the MRI scan in the radiotherapy position.

Table 6.2 Mean spatial overlap of the anatomical landmarks for the two registration set-ups.

	CT-MRI$_D$ mean spatial overlap	CT-MRI$_{RT}$ mean spatial overlap	*p* value
Left orbit	0.49	0.81	< 0.001
Right orbit	0.48	0.81	< 0.001
Odontoid process	0.37	0.67	< 0.001

CT-MRI$_D$: CT registered with diagnostic MRI; CT-MRI$_{RT}$ CT registered with the radiotherapy positioned MRI.

Table 6.3 Mean GTV (cm^3) delineated with the different patient position protocols.

Mean GTV$_C$	Mean GTV$_D$ (*p* value)	Mean GTV$_{RT}$ (*p* value)
44.1	33.7 (0.027)	30.5 (0.014)

The *p* value relates to differences in the magnitude of GTV$_C$ and the other two GTVs. GTV: gross tumour volume, GTV$_C$: GTV delineated on CT with diagnostic MRI scan viewed separately; GTV$_D$: GTV delineated using the CT registered with diagnostic MRI; GTV$_{RT}$: GTV delineated using the CT registered with radiotherapy positioned MRI.

Clinical dose constraints were met for the mean DVHs of PTV$_C$, PTV$_D$ and PTV$_{RT}$ (columns 3-5 of Figure 6.4 (b)), which validates the planning methodology in this study. When optimising the RT plan for PTV$_C$, or repeating the optimisation

process for $PTV_{D,}$ the dose to PTV_{RT} shows that neither the D_{99} nor the D_{95} dose constraints are met for the mean DVHs of P_C or P_D (the last 2 columns of Figure 6.4 (a) and (b)). For example, for D_{99} mean dose to the PTV for PTV_D : PTV_{RT} is 14.9 % rather than the 90 % required. Where the PTV left of the colon indicates the PTV for which the VMAT plan was optimised and right of the colon indicates the PTV under examination. Conformity to dose constraints is poorer for PTV_D : PTV_{RT} compared to PTV_C : PTV_{RT} (Figure 6.4 (b)). Only by using P_{RT} can all dose constraints be achieved for PTV_{RT}.

The justification for choosing only ten patients to perform the dose analysis was that none of the ten patients met the 90 % dose constraint for PTV_C : PTV_{RT} and PTV_D : PTV_{RT} and only one of the ten patients met the 95 % dose constraint for both PTV_C : PTV_{RT} and PTV_D : PTV_{RT}. This relates to a 95 % confidence interval of 0.0 % to 30.9 % and 0.3 % to 44.5 % respectively. These confidence intervals demonstrate that no further cases are statistically necessary in the analysis.

The quality of the RT was also analysed using the CN, which gives a measure of the dose conformity to the target volume and the degree of sparing of healthy tissue. The mean CN was calculated for PTV_C, PTV_D and PTV_{RT} optimising for each of these PTVs in turn. Next, the dose conformity for PTV_{RT}, which the working hypothesis postulates is the optimal target, was calculated while optimising the plans for PTV_C and PTV_D. These results are shown in Table 6.4.

It can be seen from Table 6.4 that a mean CN value of at least 0.8 is achievable when optimising for the PTV under examination. This is in agreement with Figure 6.4 which shows that the dose constraints for the PTVs are met for these plans. When investigating the dose coverage of PTV_{RT} while optimising the plans for the PTV_C and PTV_D the mean CN was shown to be significantly lower than when optimising for the same PTV under investigation with values of 0.53 ± 0.14 (p value < 0.001) and 0.54 ± 0.19 (p value = 0.001) respectively.

(a)

Ratio of total PTV volume (%)	Dose constraint (%)	Mean dose to PTV (%)				
		PTV_C : PTV_C	PTV_D : PTV_D	PTV_{RT} : PTV_{RT}	PTV_C : PTV_{RT}	PTV_D : PTV_{RT}
99 %	> 90	90.8	91.4	90.9	58.8	14.9
95 %	> 95	95.3	95.7	95.3	84.7	66.2
5 %	< 105	104	104.4	104	103.8	104.1
2 %	< 107	105.7	105.4	105.1	104.7	105.1

(b)

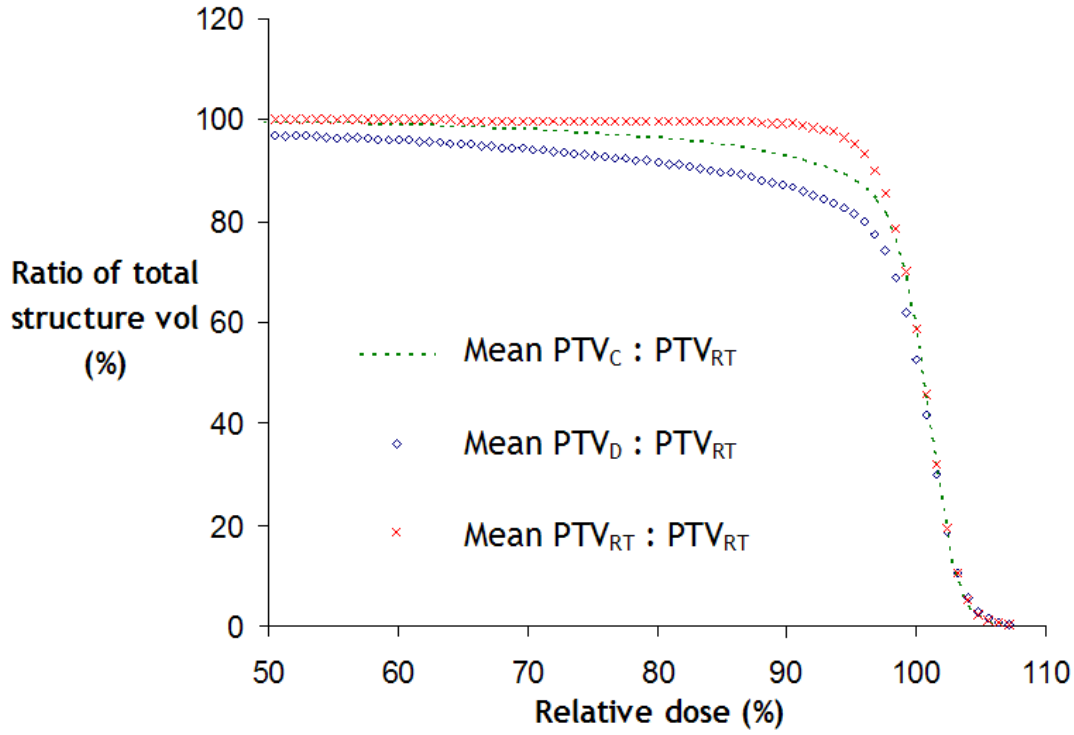

Figure 6.4 (a) Mean dose volume histogram values for each PTV optimised in turn and optimising for PTV_C and PTV_D but investigated the dose coverage of PTV_{RT} and (b) mean dose volume histograms that were achieved optimising for PTV_C, PTV_D and PTV_{RT} but investigated the dose coverage of PTV_{RT}. The PTV left of the colon indicates the PTV for which the VMAT plan was optimised and right of the colon indicates the PTV under examination. PTV_C: PTV delineated using the CT with the diagnostic MRI scan viewed on a separate console; PTV_D: PTV delineated on the CT registered with the diagnostic MRI scan; PTV_{RT}: PTV delineated on the CT registered with the MRI scan in the radiotherapy position.

The mean sigma indices are shown in Table 6.5. In the first three columns of Table 6.5 the sigma indices are within 3.3% again validating the planning methodology in this study. The dose homogeneity becomes considerably poorer for PTV_C : PTV_{RT} and PTV_D : PTV_{RT} at 7.3 % and 9.1 % respectively. A statistically significant difference between the sigma indices was found between PTV_C : PTV_C

and PTV_C : PTV_{RT} (*p* value = 0.004) and between PTV_D : PTV_D and PTV_D : PTV_{RT} (*p* value = 0.008). The mean sigma index for PTV_D : PTV_{RT} is poorer than for PTV_C : PTV_{RT} in agreement with the results of Figure 6.4 (a).

Table 6.4 Mean conformation number (CN) for PTV_C, PTV_D and PTV_{RT} when optimised for PTV in the three set-ups and optimising for PTV_C, PTV_D while analysing the dose to PTV_{RT}.

PTV for which the VMAT plan was optimised	PTV under examination	Mean CN
PTV_C	PTV_C	0.81 ± 0.02
PTV_D	PTV_D	0.85 ± 0.02
PTV_{RT}	PTV_{RT}	0.80 ± 0.03
PTV_C	PTV_{RT}	0.53 ± 0.14
PTV_D	PTV_{RT}	0.54 ± 0.19

Table 6.5 Mean sigma indices for the PTVs.

	PTV_C : PTV_C	PTV_D : PTV_D	PTV_{RT} : PTV_{RT}	PTV_C : PTV_{RT}	PTV_D : PTV_{RT}
Mean sigma index (%)	3.0	3.1	3.3	7.3	9.1

PTV left of the colon indicates the PTV for which the VMAT plan was optimised and right of the colon the PTV under examination.
PTV_C: PTV delineated using the CT with diagnostic MRI viewed separately; PTV_D: PTV delineated on the CT registered with diagnostic MRI; PTV_{RT}: PTV delineated on the CT registered with radiotherapy positioned MRI.

Figure 6.5 demonstrates for a typical patient the PTV_{RT} and the dose distributions optimised for PTV_C (left) and PTV_D (right). This figure shows that the 95 % isodose line does not cover PTV_{RT} entirely with a posterior proportion of the PTV receiving a dose less than 95 % of the prescribed dose. Figure 6.5 is in agreement with the results of Figure 6.4 which shows that when optimising for PTV_C or PTV_D not all the dose constraints are met for PTV_{RT}.

Results for parotid and larynx OAR dose analyses are presented in Table 6.6. In situations where there was overlap between a parotid and PTV, it was considered that dose sparing to that parotid was not possible without compromising PTV dose; hence it was excluded from the analysis. The results demonstrate that in planning PTV_C, PTV_D and PTV_{RT}, in all 10 patients the mean dose to the parotid was < 2400 cGy which met clinical dose constraints.

However, when RT plans were optimised for PTV_C and PTV_D and the dose to the parotid for P_{RT} were analysed (PTV_C : PTV_{RT} and PTV_D : PTV_{RT}) in 5 out of 10 patients the parotid dose exceeded the tolerance. For the larynx, the tolerance of 4000 cGy was exceeded in 4 out of 10 for P_C, 3 out of 10 for P_D and 1 out of 10 patients for P_{RT}. However, as with the parotid, when RT plans were optimised for PTV_C and PTV_D and the dose to the larynx for P_{RT} were analysed there were more instances of unmet dose constraints (5 out of 10 patients for both PTV_C : PTV_{RT} and PTV_D : PTV_{RT}).

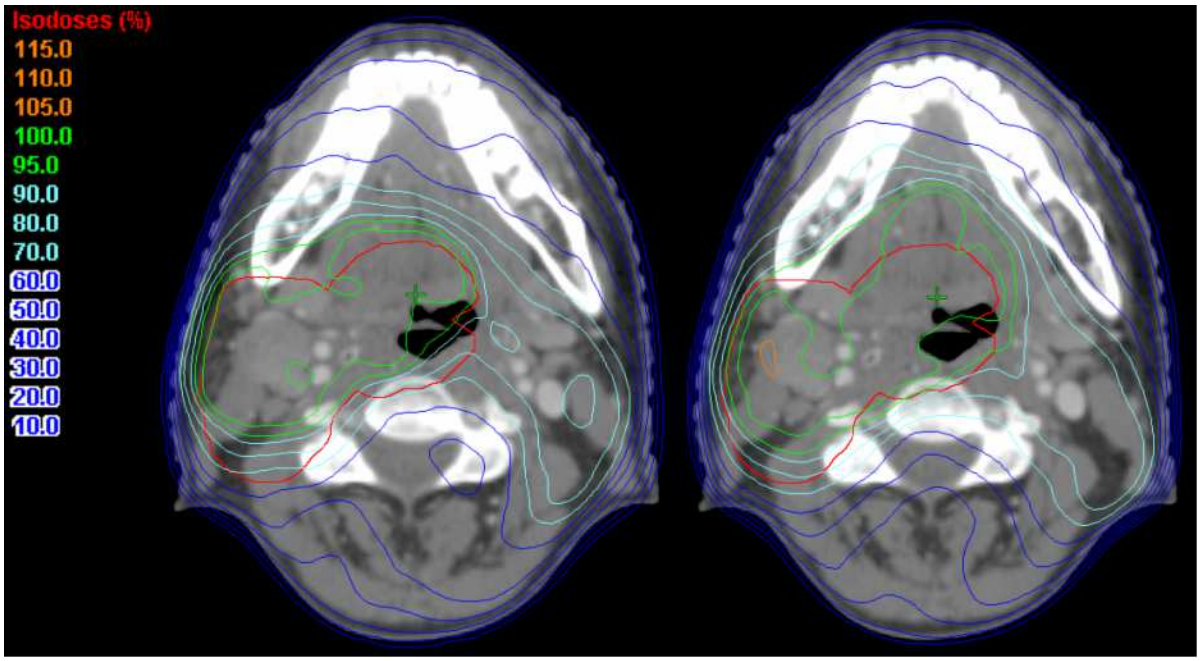

Figure 6.5 PTV_{RT} in red and the dose distributions optimised for PTV_C (left) and optimised for PTV_D (right). PTV_{RT}: PTV delineated on the CT registered with the MRI scan in the radiotherapy position; PTV_C: PTV delineated using the CT with the diagnostic MRI scan viewed on a separate console; PTV_D: PTV delineated on the CT registered with the diagnostic MRI scan.

When the mean dose to the parotid and larynx for all 10 patients was calculated, an incrementally smaller value was seen for PTV_C, PTV_D and PTV_{RT} (first 3 columns of Table 6.6), which can be explained by the decrease in the magnitude of the GTV. Dose to the spinal cord and brainstem were also measured but were not found to exceed clinically relevant tolerances for any of the patient position protocols.

Table 6.6 Mean dose for the (a) parotid and (b) larynx.

(a)

	Parotid mean dose (cGy) Mean dose constraint 2400 cGy				
	$P_C : P_C$	$P_D : P_D$	$P_{RT} : P_{RT}$	$P_C : P_{RT}$	$P_D : P_{RT}$
Mean	2179.6	1965.5	1820.3	2233.8	1992.4
Number of patients which exceed the dose constraint	0	0	0	5	5

(b)

	Larynx mean dose (cGy) Mean dose constraint 4000 cGy				
	$P_C : P_C$	$P_D : P_D$	$P_{RT} : P_{RT}$	$P_C : P_{RT}$	$P_D : P_{RT}$
Mean	3979.6	3892.3	3613.2	4108.8	4020.6
Number of patients which exceed the dose constraint	4	3	1	5	5

Where there was overlap between a parotid and the PTV the parotid dose was not included in the mean contralateral parotid dose. P left of the colon indicates the patient position protocol for which the VMAT plan was optimised and right of the colon indicated the patient position protocol under examination.
P_C: Patient position protocol with CT and diagnostic MRI scan viewed separately; P_D: patient position protocol with CT registered to the diagnostic MRI; P_{RT}: patient position protocol with CT registered to the radiotherapy positioned MRI.

6.4 Discussion

Advanced imaging techniques have been shown to improve tumour and nodal staging (Prestwich et al. 2012) and the benefits of integrating MRI are well known (Ahmed et al. 2010; Chung et al. 2004; Newbold et al. 2006; Prestwich et al. 2012; Rosenman et al. 1998). While the advantages in positioning patients in a similar way to their CT planning scan when acquiring MR images are also known (Ahmed et al. 2010; Hanvey et al. 2012; Prestwich et al. 2012), this is the first study to compare the CT-MRI registration accuracy and dosimetric effects of a diagnostic versus RT positioned MRI scan in patients with oropharyngeal cancer.

During the process of registering CT to MR images, there was improved registration with fewer discrepancies using MRI_{RT} compared to MRI_D, as demonstrated in Figure 6.1. In this example, there are registration discrepancies at the body outline and spinal cord for CT-MRI_D, as indicated by the arrows (Figure 6.1(a)), but not with MRI_{RT} (Figure 6.1 (b)).

A significant improvement in the registration quality of CT to MRI_{RT} versus the MRI_D was demonstrated by a reduction in the geometric mean distance from the centre of the orbits and odontoid process delineated on CT and the MRI_{RT} and an increase in the spatial overlap of these structures. These results show that patient setup significantly influences CT-MRI registration accuracy. With increased interest in the use of dose escalation and dose painting techniques within RT planning the importance of improved image registration becomes ever more relevant.

The significant difference between the magnitude of the GTV_C and GTV_D and between the GTV_C and GTV_{RT} implies that the GTV is significantly smaller when using registered rather than unregistered CT-MR images. This underlines the importance of registering CT to MRI for patients with oropharyngeal cancer, rather than viewing them separately. It also highlights the difficulty in delineating oropharyngeal cancers with CT due to the similarity in Hounsfield Units of tumour and surrounding tissue as well as artefacts caused by dental amalgam. While there was no significant difference between the mean GTV_D and GTV_{RT}, there were important differences in the VMAT plans, as discussed below. To achieve the clinical goal of reduced late toxicities and improved tumour control using dose escalation with tighter PTV margins, uncertainties in GTV delineation need to be minimised and our data suggest P_{RT} offers the optimal of the three set-ups.

The results reveal that there are potentially clinically relevant improvements to the quality of the VMAT plans when using P_{RT} rather than P_C or P_D. This is demonstrated by the PTV dose coverage, PTV dose homogeneity and instances of unmet dose constraints by the OARs. Due to improved registration accuracy and MRI being the recommended imaging modality for soft tissue oropharyngeal cancers (ENT UK 2011), it may be assumed that PTV_{RT} would be the gold standard PTV. To determine the dose received by the presumed gold standard, PTV_{RT}, the plans were optimised for PTV_C and PTV_D while calculating the dose to PTV_{RT}. When investigating the dose coverage of PTV_{RT} it was shown that the mean DVH for PTV_D had poorer dose coverage than PTV_C (Figure 6.4). Despite the magnitude of the mean GTV_{RT} and GTV_D being similar there may be differences in the shape and location of the GTV using these patient set-ups which would

result in the DVHs of Figure 6.4. Neither the P_C nor the P_D VMAT plans were able to meet the clinical dose constraints of D_{99} and D_{95} for gold standard, PTV_{RT}.

This was supported by the results of Table 6.4 which showed that when optimising for PTV_C and PTV_D while analysing the CN for PTV_{RT}, the gold standard PTV, the mean CN was significantly lower than when optimising and analysing the same PTV. These results show that while it may seem that a particular quality of RT plan can be achieved, if the plan is not optimised for the true PTV, the resultant dose coverage will be poorer than expected.

When optimising for PTV_D and investigating the dose to this structure this gave a higher CN (0.85 ± 0.02) than when optimising and analysing the dose to PTV_C (0.81 ± 0.02) and PTV_{RT} (0.80 ± 0.03). It is thought this is because of the low number of patients used for the dose analysis. With a larger number of patients it is expected that these values would be comparable.

The CN for the patients with head and neck cancer can be seen to be lower than for the patients with prostate cancer (Chapter 5) when optimising and analysing the dose coverage of the same PTV. Averaging over the three set-ups the head and neck CN was 0.82 while the average prostate CN was 0.98. The reason for the lower CN for the head and neck group is the volume of the PTV was larger making it more challenging to achieve a conformal dose coverage than with the prostate group. The average volume of the PTV for the three set-ups in the head and neck group was 197.5 cm^3, whereas for the prostate group it was 67.9 cm^3. In addition, while the prostate follows a reasonably spherical shape the PTVs for the head and neck group were more complex. The complicated shape of the head and neck PTVs would also have contributed to a lower CN.

Furthermore, this study shows that there is a significant increase in the mean sigma index when optimising for PTV_C or PTV_D while investigating the dose coverage of PTV_{RT} rather than analysing the dose coverage of the PTV for which the RT plan has been optimised. It has been argued that tumour control probability can be considerably compromised by an inhomogeneous dose to the PTV (Goitein and Niemierko 1996). It is therefore suboptimal to use P_C or P_D rather than P_{RT} for RT planning of patients with oropharyngeal cancer.

Finally, there were greater instances of unmet dose constraints for the parotids and the larynx when optimising for P_C and P_D but examining the dose sparing of P_{RT} than when investigating the dose to the OARs for which the plan was optimised. While the dose to the parotids and larynx were within the dose constraints when averaged over all patients, the effect of exceeding dose constraints for individual patients could lead to unwanted side-effects. This shows that not only is the PTV compromised by using the sub-optimal set-ups of P_C and P_D but the dose to the OARs could also be different from the expected RT plan.

Obtaining a further MRI in the RT position, rather than using the original diagnostic MRI, may place greater demands on increasingly stretched healthcare resources. However, this must be weighed against the potential advantages of improved image registration and, by consequence, superior target volume definition and dose coverage of the PTV, as these results have demonstrated. Our study suggests further research, particularly in correlating dosimetric investigations with clinical outcome data, would be warranted.

6.5 Conclusions

When MRI scans are performed in the RT position, as opposed to using diagnostic MR images not obtained in RT position, there are significant improvements in the quality of CT-MR registration. This study has also shown that RT positioned MRI scans offer improvements in target definition, dose coverage and dose homogeneity, which could have significant implications for tumour control rates. To the author's knowledge, this is the first study in the literature to confirm these advantages.

7 Final Conclusions

7.1 Conclusions from this thesis

The aim of this thesis was to investigate the role of magnetic resonance imaging (MRI) in radiotherapy (RT). This began with a study comparing a two-dimensional (2D) with a three-dimensional (3D) distortion correction algorithm for RT. The results of this study showed that with only three slices there is little difference between the 2D and 3D distortion correction algorithms. However, when more slices are used the differences become apparent. Within a range of around 100 mm superior and inferior from isocentre both algorithms perform with an accuracy of approximately 1 mm with regards the through-plane and in-plane distortion, using multiple slices.

Following this, the image quality obtained using MR while immobilised within a beam directional shell (BDS) in the RT position was investigated using test objects. This work showed that, if the manufacturer-supplied uniformity correction algorithm is applied, surface coils can achieve the same or improved diagnostic image quality results as a standard multi-channel head coil, typically used for imaging brain patients. The parameters investigated were the signal-to-noise ratio (SNR), spatial resolution, uniformity, geometric linearity and distortion, multiple slice position error, slice width and contrast-to-noise. These results were an important step in showing that it is possible to use surface coils to image patients with prostate and head and neck cancer in the RT position for MR imaging without compromising image quality.

The next study investigated three set-ups for imaging patients with prostate cancer: viewing the computed tomography (CT) and MRI datasets on separate computer consoles (the current methodology at the Beatson); viewing the CT registered with a diagnostic MRI and viewing the CT registered with a RT positioned MRI. The benefits of registering MRI with CT were shown for imaging patients with prostate cancer by comparing the viewing of the CT and MRI datasets separately with CT-MRI registration. This was found to have a significant effect on the mean prostate and prostate plus seminal vesicles volumes in agreement with other published studies (Charnley et al. 2005; Khoo and Joon 2006; Rasch et al. 1999; Sannazzari et al. 2002; Sefrova et al. 2012;

Smith et al. 2007). It was also shown that there was a statistically significant improvement in the quality of registration between CT and the RT positioned MRI compared to the diagnostic MRI. This was shown as an improvement in both the geometric error of rigid landmarks and the spatial overlap of these landmarks. Similarly, this improvement in geometric error between CT and MRI was found for the prostate and prostate plus seminal vesicle volumes. Finally, intensity modulated radiotherapy (IMRT) plans were generated for all three set-ups. When investigating the dose received by the planning target volume (PTV) generated using the RT positioned MRI, while optimising the IMRT plan for the PTVs of the other two set-ups, a significant difference in the mean conformation numbers was found. The conformation number is a measure of the dose received by the target volume and a measure of sparing of dose to the healthy tissue. This demonstrates that given there is an improved image registration between CT and MRI when the patients are positioned in the RT position then it is suboptimal to plan IMRT using CT and a diagnostic MRI dataset rather than use the CT registered to the RT positioned MRI.

A similar study investigated patients with head and neck cancer with the same three set-ups except that patients imaged in the RT position were immobilised in a BDS. As with the prostate group, there was found to be an improvement in the CT-MRI registration accuracy of patients with head and neck cancer, when the patients are in the RT position. This was shown as a reduction in the geometric error of three rigid landmarks and as an improvement in the spatial overlap of these structures. The magnitude of the mean gross tumour volume (GTV) was shown to change significantly when the CT was registered with the MRI datasets rather than being viewed separately. Tumour definition has similarly been shown by other groups to be changed by the inclusion of MRI in patients with head and neck cancer (Ahmed et al. 2010; Chung et al. 2004; Emami et al. 2003; Newbold et al. 2006).

Volumetric modulated arc therapy (VMAT) plans were performed on the three set-ups of a randomly selected cohort of the patients with head and neck cancer. It was shown that while investigating the dose coverage of the PTV generated using the RT positioned MRI but optimising for the PTVs of the other two set-ups, not all the clinical dose constraints were achieved. Only by investigating the dose coverage of the RT positioned PTV while optimising for

the RT positioned PTV were all the dose constraints met. A conformation number (CN) was calculated, which demonstrated the degree to which the dose conforms to the target. It was shown that when analysing the dose to the RT positioned PTV while optimising for the PTVs in the other two set-ups the mean CN was significantly lower than when optimising and analysing the CN for these set-ups. Since the working hypothesis states that the RT positioned PTV is the optimal of the three set-ups, this shows that optimising for the PTVs of the other two set-ups will significantly compromise the dose conformity to the true, RT positioned, PTV. The dose homogeneity received by the mean PTV is considerably poorer when analysing the dose to the RT positioned PTV but optimising the plan for the PTVs of the other two set-ups than when optimising and analysing the dose coverage of the same PTV. Tumour control probability is thought to be compromised considerably by an inhomogeneous dose to the PTV (Goitein and Niemierko 1996). For the parotids and larynx, two of the organs at risk (OARs) in the treatment of head and neck cancer, there were greater instances of unmet dose constraints when analysing the dose to the RT positioned set-up, while optimising for either of the other two set-ups. As with the patients with prostate cancer, these results show that it is suboptimal to use the CT or the diagnostic MRI instead of the RT positioned MRI when planning VMAT of patients with head and neck cancer.

7.2 Study limitations

7.2.1 Three-dimensional distortion correction algorithm

One of the limitations of the study comparing the 2D and 3D distortion correction algorithms is that the 3D algorithm was a prototype version made available as part of a research agreement with the manufacturer. This software has potentially been improved since it was tested; however, it is only available on newer MRI systems as a final product version.

A high degree of asymmetry was demonstrated by the 3D distortion correction algorithm in the superior direction (Chapter 3, Figure 3.7). It was thought that the reason for this was because the prototype version had not been optimised for the MRI scanner used in the experiment. Blurring of the 3D corrected images made it challenging to identify the position of the error. It would have been

beneficial to have repeated the scanning with the polarity of the gradients reversed to determine whether the direction of the asymmetry reversed.

It would also have been of benefit to compare the prototype distortion correction algorithm from GE (GE Healthcare, WI, USA) with an independent 3D distortion correction algorithm. This may have been challenging to accomplish since the GE distortion correction was based on gradient maps of the MRI system, while an independent distortion correction would not have this information available.

7.2.2 Imaging coil

The 4-channel surface coil used for the imaging of patients for the test object study and for the RT positioning of patients with prostate and head and neck cancer had a relatively small size. Although the image quality was not compromised close to the isocentre, the small size of the imaging coil, originally intended for cardiac imaging, resulted in a drop off in signal outwith the footprint of the coil. This coil was chosen because it is light and flexible and so could easily be positioned along the contour of the patient. In newer MRI systems, large flexible multi-channel coils, which can operate in conjunction with posterior elements, embedded in the table are now available and would potentially be better suited to these patient groups.

7.2.3 Deformable Registration

One of the limitations of the studies involving patients with prostate and head and neck cancer is the use of rigid registration. While intra-modality deformable registration is not generally available commercially and was not available clinically at the Beatson this may improve the registration accuracy between CT and MRI. This may make the positioning of the MRI less important if the deformable registration was able to accurately map the diagnostic MRI to the RT positioned CT. This would prevent the need to perform another MRI scan at the RT planning stage helping to reduce healthcare costs. This may also be useful for movable organs such as the prostate which can be affected by the bladder or rectum volumes. Deformable registration could be used in adaptive RT, where patients may experience weight loss. Adaptive RT is commonly used in the

treatment of head and neck cancer patients and deformable registration may allow the diagnostic MRI at the start of the treatment to be registered to a CT taken during treatment following weight loss.

7.2.4 Patient numbers and treatment outcomes

The patient numbers used in Chapters 5 and 6 are relatively small and could potentially be repeated with a larger patient group for the prostate and head neck studies. In the clinical studies of this thesis the quality of registration, gross tumour volume and dosimetric effects were examined for different patient position protocols. While a statistically significant effect was demonstrated in the dose analysis sections of these chapters, it is not yet known whether this would have a clinical effect. A randomised controlled trial examining changes in patient survival, toxicity and patient's quality of life would possibly reveal the true clinical benefits of MRI patient positioning for RT.

7.3 Future Work

7.3.1 Imaging coil

The imaging coil used for the prostate and head and neck studies was limited in size causing a drop off in the SNR outside the coil footprint. To improve the SNR for the patients with head and neck cancer it may be possible to incorporate the imaging coil with the BDS. This would enable the contact between the patient and the imaging coil to be maximised.

It is also feasible that additional imaging coils could be positioned posterior to the patient head beneath the head rest, again improving the SNR. As a result of the studies conducted at the Beatson, GE (GE Healthcare, WI, USA) has designed new coils for RT planning which are available on newer MRI models, as shown in Figure 7.1. These large, flexible coils, known as the GEM suite imaging coils, can be positioned around the patient's immobilisation mask or body. Additionally, there are imaging coils integrated into the table to boost the signal posteriorly. There is also a removable flat table which can be used for imaging in the RT position. Using a GEM coil with the imaging coil integrated into the table enables good image quality for prostate patients in the treatment position. The

GEM coils can also be combined with other coils for head and neck imaging in the treatment position.

Figure 7.1 GE Healthcare GEM suite coil, with immobilisation and a flat table for radiotherapy positioned planning (used with permission, GE Healthcare, WI, USA).

7.3.2 Deformable Registration

It would be beneficial to determine the limitations of a deformable registration algorithm for registering a planning CT with a diagnostic MRI scan. This could involve investigating how deformable registration affects the magnitude and position of the GTV and OARs after registration. It is known to be difficult to verify the accuracy of a deformable registration algorithm, but this could potentially be achieved by using the rigid landmarks of the previous studies to determine the quality of registration. It may be possible to use images of patients in the diagnostic position to achieve similar registration errors as when registering the RT positioned MRI to the treatment positioned CT. This could potentially reduce resource demands and costs by removing the requirement of a second RT positioned MRI.

Deformable registration could also potentially be used to reduce errors between the RT positioned MRI and CT. This may lead to improved accuracy in the tumour and OAR definition. Furthermore, it may be possible to reduce the geometric distortion errors found in MRI using deformable registration. If the MRI is registered to the geometrically accurate CT this may negate the requirement for distortion correction.

7.3.3 Functional MRI

Functional MRI techniques such as spectroscopy, diffusion weighted imaging and dynamic contrast enhanced imaging could be used to aid in tumour delineation for RT. These techniques have been shown to assist in the detection of tumours (Jackson et al. 2009; Kim et al. 2009; Westphalen et al. 2012). The addition of functional MRI in the RT planning process may lead to significant changes in the tumour volume over conventional MR imaging alone and may enable those patients who will not respond to treatment to be identified.

It is possible that the reduced SNR from the imaging coil used for the RT positioned MRI scans would result in inaccuracies in any functional MRI results. This would particularly affect the head and neck group where the target volume often extended far from the isocentre where the SNR was reduced. Using the new coils available (see Section 7.3.1) it may be possible to achieve the image quality required to obtain useful functional MRI data.

Functional MRI has also been shown to be useful in predicting the response of tumours to therapy both before treatment has been administered (DeVries et al. 2003; Dzik-Jurasz et al. 2002) and in response to therapy (de Lussanet et al. 2005; Kim et al. 2009; Liu et al. 2009). The purpose of this is to provide a patient specific treatment by determining the tumour response before or at an early stage of treatment to try and improve tumour control. The results of tumour response to therapy could be used in a randomised controlled trial to give an early indication of whether there is a difference in the tumour response of patients with a RT positioned MRI for tumour definition compared to using a diagnostic MRI scan.

7.3.4 Auto segmentation

Developments in auto segmentation software for tumour volumes are underway. This may assist in a more objective comparison of different patient set-up protocols by removing the intra or inter clinician variability in the delineation of GTVs. It may also enable a quantitative measure of changes in GTV using deformable registration. Developments in tumour auto segmentation are expected to reduce clinician workload helping to reduce healthcare costs.

Auto-segmentation would also have a role in outlining structures for MRI RT planning. One of the disadvantages of MRI only planning is that it can often require the time consuming delineation of structures to apply Hounsfield Units for dose calculation. If these structures could be delineated using auto-segmentation then it would enable a quicker, more objective solution.

7.3.5 Adaptive radiotherapy

Adaptive RT is increasingly being employed by cancer centres as tools, such as functional MRI, enable the response of tumours to treatment to be assessed. Adaptive RT could also be used in instances where patients have lost weight throughout the course of their treatment, resulting in a change to the dose distribution. One of the key considerations before implementing adaptive RT in a busy centre is prioritising the patients that would benefit most from this form of treatment. At the Beatson, patients receiving RT to the head and neck are rescanned with CT at the sixteenth fraction. The dose distribution is reassessed on the new CT scan set and it is determined whether a new plan is required based on the dose to sensitive organs. This avoids the additional work of creating new plans for patients that do not require it.

7.3.6 Radiotherapy planning using MRI alone

The interest in MRI alone in RT planning is likely to increase in use over the coming years. However, there are a number of challenges which must be addressed for it to become a practical solution.

With the availability of new 3D distortion correction algorithms by MRI manufacturers, geometric distortion is no longer an insurmountable obstacle in the use of MRI alone for RT planning.

Digitally reconstructed radiographs (DRRs) are a requirement for accurate RT planning, but this can be overcome by outlining bony anatomy in MRI to give beams eye view images similar to DRRs. Delineating bone on MRI can be time consuming but auto segmentation techniques along with special MRI sequences such as ultra short echo times should help to reduce this time. Similarly, the time taken to outline structures to assign electron density values should be considered. It is also possible to generate pseudo CT data from MRI by converting the MRI intensity values to Hounsfield Units by way of a conversion factor (Kapanen and Tenhunen 2012). This technique allows MRI datasets to be used for dose calculation and to generate DRRs.

Finally, the cost of an MRI scan is much higher than CT and MRI scanners are generally more scarcely available, therefore, despite the advantages being offered from MRI alone RT planning, MRI scans will need to become less costly if they are to compete with CT in the near future. While MRI alone RT planning is not likely to be the mainstay procedure, this technique will possibly be used for specific sites where the advantages of MRI outweigh the challenges. The advantage of localised metal artefacts in MRI is likely to make it an attractive solution for RT planning, for example, in patients with abdominal cancer and bilateral hip replacements. Another example would be in patients with head and neck cancer where dental amalgam or metal from surgery would make delineation of tumour volumes less accurate using CT. Performing MR imaging of patients in the RT position at the diagnostic stage may prevent the requirement for a subsequent repeat scan and reduce costs. If the patients do not require RT it would still be possible to obtain diagnostic information of the required image quality using new manufacturer provided imaging coils.

7.4 Recommended MRI protocol for radiotherapy

On the basis of the work of this thesis this final section outlines a recommended MRI protocol for patients undergoing or likely to undergo radiotherapy. When MR images are used in RT planning, patients should be positioned in the RT position,

to ensure registration errors are kept to a minimum. However, there is evidence to suggest that patients with brain cancer may not require to be imaged in the RT position because of the small associated registration error (Kenneth et al 2010). With the advent of improved imaging coils it may be possible to image patients at the diagnostic stage in the RT position which would help to reduce costs and resource demands. This would be easier to achieve in patients that do not require customised immobilisation, since it may not be feasible to immobilise all patients undergoing a diagnostic scan. Furthermore, the type of headrest used is dependent on the tumour extent, and this is unlikely to be fully known prior to imaging. Therefore, a second MRI in the RT position is a likely requirement for patients with head and neck cancer.

The data from chapter 3 shows that in a range of 15 cm from isocentre, distortion errors can be kept to approximately 1 mm, using 2D distortion correction. This gives a range within which the MRI scan be used with confidence, for the purposes of target and OAR delineation. Careful consideration must be given when using data beyond this range and it may be necessary to extend PTV margins to compensate for this uncertainty. The availability of 3D distortion correction algorithms may extend the volume of tissue which can be used for delineation in RT planning, but this should be confirmed by local physicists.

A receiver bandwidth greater than or equal to ± 30 kHz has been recommended to minimise distortion and chemical shift artefacts in MR images (Moore et al. 2004). Using a slice width of the same thickness or thinner than the planning CT would also be considered best practice. T2-weighted MR images were found to be the most popular scan type with radiation oncologists in the studies of this thesis, but the exact sequence required may differ with oncologist, tumour type and anatomical site. The most appropriate set of MRI sequences should also be discussed with a radiologist.

A uniformity correction algorithm was shown to be a requirement, when scanning with surface coils, to ensure the signal-to-noise and uniformity were within acceptable tolerances. It is likely that uniformity correction will continue to be a necessity, while surface coils remain popular for RT positioned MR imaging.

Rigid registration should minimise errors to an acceptable level for most sites, but once a registration has been performed it should be checked prior to use. A manual adjustment may be necessary in some cases. Deformable registration may provide further improvements in registration quality, but such algorithms should be tested to ensure that they give clinically acceptable results.

This thesis has shown the advantages and limitations of incorporating MRI in the RT process. It has also demonstrated the benefits of imaging patients in the RT position. This has shown to offer improvements in the registration quality, target definition, dose coverage and dose homogeneity while minimising the dose to organs at risk.

Appendix 1

```
% First it is necessary to rename files to add .dcm
% Put files in separate folder from code
% In command prompt, when in correct file path type:
% ren * *.dcm

% 3D Distortion Correction Analysis

clear
sequenceStartNo =7 ;
sequenceEndNo =33;
basename = ('IM');
fileExtension = ('.dcm');
Slice_No=(sequenceStartNo:sequenceEndNo);
z=0;
   for q=sequenceStartNo:sequenceEndNo
        % convert a number to a character
        sequenceNo = num2str(q);
        % Concatenating information to generate image file information
        filename=strcat(basename,sequenceNo,fileExtension);
        % Reading the DICOM image
        Im = dicomread(filename);
        % Convert the DICOM image into an arithmetic matrix
        Im = double(Im);

        % Crop the image
        Im = Im(85:174,54:204);
        % SPlit image into left and right
        Im_Lt=Im(1:42,1:151);
        Im_Rt=Im(43:90,1:151);

        % Filter image to give zero at the rod position and one elsewhere
        Im_Lt=imextendedmax(Im_Lt,850);
        Im_Rt=imextendedmax(Im_Rt,850);
```

```
        % Looks for zeros in image
        [a, b]=find(Im_Lt==0);
        tb = [ a(:) b(:)];
        T_Lt(q) = mean(b);
        [A, B]=find(Im_Rt==0);
        TB = [ A(:) B(:)];
        T_Rt(q) = mean(B);
        % Calculates rod separation
        dist(q)= abs(T_Lt(q)-T_Rt(q));
        % Stores value of rod separation as separate numbers
        z=z+1;
        dist2(z)=dist(q);
    end

% Values for calculating SP_meas
CF=1;
Rod_Sep=6.5;
% Loop to compute SP_meas for each rod separation
    for i=1:length(dist2)
        SP_meas(i)=sqrt((dist2(i)*CF).^2-Rod_Sep^2)/2;
    end
%SP_meas;

% Error calculation
SP_meas=real(SP_meas);
r=0:5:130;
SP_cal=abs(65-r);
Error= SP_meas-SP_cal; save SC1 Error

% Output the table of values
fprintf( '\n\n   Slice No   Distance(mm)   SP_meas (mm)      Error \n');
fprintf( '\n %5.0f          %5.2f          %5.2f          %5.2f          ',[Slice_No; dist2;
SP_meas; Error])
```

References

AAPM 2010, *Acceptance testing and quality assurance procedures for magnetic resonance imaging facilities*, American Association of Physicists in Medicine, Maryland.

Aboagye, E. & Bhujwalla, Z. 1999. Malignant transformation alters membrane choline phospholipid metabolism of human mammary epithelial cells. *Cancer Research*, 59, (1) 80-84

Ahmed, M., Schmidt, M., Sohaib, A., Kong, C., Burke, K., Richardson, C., Usher, M., Brennan, S., Riddell, A., Davies, M., Newbold, K., Harrington, K., & Nutting, C. 2010. The value of magnetic resonance imaging in target volume delineation of base of tongue tumours - a study using flexible surface coils. *Radiotherapy and Oncology*, 94, (2) 161-167

Altas, S. 1995. *Magnetic resonance imaging of the brain and spine*, 4th ed. Lippincott, Williams and Wilkins.

Bakker, C., de Leeuw, H., van de Maat, G., van Gorp, J., Bouwman, J., & Seevinck, P. 2012. On the utility of spectroscopic imaging as a tool for generating geometrically accurate MR images and parameter maps in the presence of field inhomogeneities and chemical shift effects. *Magnetic Resonance Imaging* -article in press

Balter, J. & Kessler, M. 2007. Imaging and alignment for image-guided radiation therapy. *Journal of Clinical Oncology*, 25, (8) 931-937

Bammer, R., Markl, M., Barnett, A., Acar, B., Alley, M., Pelc, N., Glover, G., & Moseley, M. 2003. Analysis and generalized correction of the effect of spatial gradient field distortions in diffusion-weighted imaging. *Magnetic Resonance in Medicine*, 50, (3) 560-569

Beavis, A., Gibbs, P., Dealey, R., & Whitton, V. 1998. Radiotherapy treatment planning of brain tumours using MRI alone. *The British Journal of Radiology*, 71, 544-548

Brahme, A. 1988. Optimization of stationary and moving beam radiation therapy techniques. *Radiotherapy and Oncology*, 12, (2) 129-140

Breeuwer, M., Holden, M., & Zylka, W. 2001. Detection and correction of geometric distortion in 3D MR images. *SPIE Medical Imaging Proceedings*, 4322, 1110-1120

Brock, K. 2010. Deformable Registration Accuracy Consortium. Results of a multi-institution deformable registration accuracy study (MIDRAS). *International Journal of Radiation Oncology Biology Physics*, 76, (2) 583-596

Brunt, J. 2010. Computed Tomography-Magnetic Resonance image registration in radiotherapy treatment planning. *Clincal Oncology*, 22, 688-697

Burke, B., Ghila, A., Fallone, B., & Rathee, S. 2012. Radiation induced current in the RF coils of integrated linac-MR systems: The effect of buildup and magnetic field. *Medical Physics*, 39, (8) 5004-5014

Chang, H. & Fitzpatrick, J. 1990. Geometrical image transformation to compensate for MRI distortions. *SPIE Medical Imaging Proceedings*, 1233, 116-127

Chang, H. & Fitzpatrick, J. 1992. A technique for accurate magnetic resonance imaging in the presence of field inhomogeneities. *IEEE Transaction on Medical Imaging*, 11, (3) 319-329

Charnley, N., Morgan, A., Thomas, E., Wislon, S., Bacon, S., Wilson, D., & Bottomley, D. 2005. The use of CT-MR image registration to define target volumes in pelvic radiotherapy in the presence of bilateral hip replacements. *British Journal of Radiology*, 78, (931) 634-636

Cherry, P. & Duxbury, A. 2009. *Practical radiotherapy physics and equipment*, 2nd ed. West Sussex, Wiley-Blackwell.

Chen, L., Nguyen, T.-B., Jones, E., Chen, Z., Luo, W., Wang, L., Price, R., Pollack, A., & Ma, C.-M. 2007. Magnetic resonance-based treatment planning for prostate intensity-modulated radiotherapy: creation of digitally reconstructed radiographs. *International Journal of Radiation Oncology Biology Physics*, 68, (3) 903-911

Chen, L., Price, R., Wang, L., Jinsheng, L., Qin, L., McNeeley, S., Ma, C.-M., Freedman, G., & Pollack, A. 2004. MRI-based treatment planning for radiotherapy: dosimetric verification for prostate IMRT. *International Journal of Radiation Oncology Biology Physics*, 60, (2) 636-647

Cho, P. & Marks, R. 2000. Hardware-sensitive optimization for intensity modulated radiotherapy. *Physics in Medicine and Biology*, 45, 429-440

Chui, C.-S. & Spirou, S. 2001. Inverse planning algorithms for external beam radiation therapy. *Medical Dosimetry*, 26, (2) 189-197

Chung, N., Ting, L., Hsu, W., Lui, L., & Wang, P. 2004. Impact of magnetic resonance imaging versus CT on nasopharyngeal carcinoma: primary tumor target delineation for radiotherapy. *Head and Neck*, 26, 241-246

Clivio, A., Fogliata, A., Franzetti-Pellanda, A., Nicolini, G., Vanetti, E., Wytenbach, R., & Cozzi, L. 2009. Volumetric-modulated arc radiotherapy for carcinomas of the anal canal: A treatment planning comparison with fixed field IMRT. *Radiotherapy and Oncology*, 92, (1) 118-124

Crijns, S., Kok, J., Lagendijk, J., & Raaymakers, B. 2011. Towards MRI-guided linear accelerator control: gating on an MRI accelerator. *Physics in Medicine and Biology*, 56, 4815-4825

Crum, W., Hartkens, T., & Hill, D. 2004. Non-rigid image registration: theory and practice. *The British Journal of Radiology*, 77, 140-153

Dearnaley, D., Syndikus, I., Sumo, G., Bidmead, M., Bloomfield, D., Clark, C., Gao, A., Hassan, S., Horwich, A., Huddart, R., Khoo, V., Kirkbride, P., Mayles,

H., Mayles, P., Naismith, O., Parker, C., Patterson, H., Russell, M., Scrase, C., South, C., Staffurth, J., & Hall, E. 2012. Conventional versus hypofractionated high-dose intensity-modulated radiotherapy for prostate cancer: preliminary safety results from the CHHiP randomised controlled trial. *The Lancet Oncology*, 13, (1) 43-54

de Lussanet, Q., Backes, W., Griffioen, A., Padhani, A., Baeten, C., van Baardwijk, A., Lambin, P., Beets, G., van Engelshoven, J., & Beets-Tan, R. 2005. Dynamic contrast-enhanced magnetic resonance imaging of radiation therapy-induced microcirculation changes in rectal cancer. *International Journal of Radiation Oncology Biology Physics*, 63, (5) 1309-1315

DeVries, A., Kremser, C., Hein, P., Griebel, J., Krezcy, A. Ofner, D., Pfeiffer, K., Lukas, P., & Judmaier, W. 2003. Tumor microcirculation and diffusion predict therapy outcome for primary rectal carcinoma. *International Journal of Radiation Oncology Biology Physics*, 56, (4) 958-965

Doran, S., Charles-Edwards, L., Reinsberg, S., & Leach, M. 2005. A complete distortion correction for MR images: I. Gradient warp correction. *Physics in Medicine and Biology*, 50, 1343-1361

Dzik-Jurasz, A., Domenig, C., George, M., Wolber, J., Padhani, A., Brown, G., & Doran, S. 2002. Diffusion MRI for prediction of response of rectal cancer to chemoradiation. *Lancet*, 360, (9329) 307-308

Emami, B., Sethi, A., & Petruzzelli, G. 2003. Influence of MRI on target volume delineation and IMRT planning in nasopharyngeal carcinoma. *International Journal of Radiation Oncology Biology Physics*, 57, (2) 481-488

ENT UK 2011, *Head and neck cancer: multidisciplinary management guidelines.*, ENT UK, London.

Ezzell, G., Galvin, J., Low, D., Palta, J., Rosen, I., Sharpe, M., Xia, P., Xiao, Y., Xing, L., & Yu, C. 2003. Guidance document on delivery, treatment planning, and clinical implementation of IMRT: Report of the IMRT subcommittee of the AAPM radiation therapy committee. *Medical Physics*, 30, (8) 2089-2115

Fallone, B., Murray, B., & Rathee, S. 2009. First MR images obtained during megavoltage photon irradiation from a prototype integrated linac-MR system. *Medical Physics*, 36, (6) 2084-2088

Firbank, M., Harrison, R., Williams, E., & Coulthard, A. 2000. Quality assurance for MRI: practical experience. *The British Journal of Radiology*, 73, 376-383

Fitzpatrick, J., Hill, D., Shyr, Y., West, J., Studholme, C., & Maurer, C. 1998. Visual assessment of the accuracy of retrospective registration of MR and CT images of the brain. *IEEE Transactions on Medical Imaging*, 17, (4) 571-585

Fitzpatrick, J. & West, J. 2001. The distribution of target registration error in rigid-body point-based registration. *IEEE Transactions on Medical Imaging*, 20, (9) 917-927

Fransson, A., Andreo, P., & Pötter, R. 2001. Aspects of MR Image Distortions in Radiotherapy Treatment Planning. *Strahlentherapie und Onkologie*, 177, 59-73

General Electric Company 2009, *MRI safety guide - Appendix D.*, GE Heathcare, 2381696-100.

Goitein, M. & Niemierko, A. 1996. Intensity-modulated therapy and inhomogeneous dose to the tumor: A note of caution. *International Journal of Radiation Oncology Biology Physics*, 36, (2) 519-522

Grégoire, V., Levendag, P., Ang, K., Bernier, J., Braaksma, M., Budach, V., Chao, C., Coche, E., Cooper, J., Cosnard, G., Eisbruch, A., El-Sayed, S., Emami, B., Grau, C., Hamoir, M., Lee, N., Maingon, P., Muller, K., & Reychler, H. 2003. CT-based delineation of lymph node levels and related CTVs in the node-negative neck: DAHANCA, EORTC, GORTEC, NCIC, RTOG consensus guidelines. *Radiotherapy and Oncology*, 69, 227-236

Hall, E. 2006. Intensity-modulated radiation therapy, protons, and the risk of second cancers. *International Journal of Radiation Oncology Biology Physics*, 65, (1) 1-7

Hall, E. & Wuu, C.-S. 2003. Radiation-induced second cancers: the impact of 3D-CRT and IMRT. *International Journal of Radiation Oncology Biology Physics*, 56, (1) 83-88

Hanvey, S., Glegg, M., & Foster, J. 2009. Magnetic resonance imaging for radiotherapy planning of brain cancer patients using immobilization and surface coils. *Physics in Medicine and Biology*, 54, 5381-5394

Hanvey, S., McJury, M., Tho, L., Glegg, M., Thomson, M., Grose, D., James, A., Rizwanullah, M., Paterson, C., & Foster, J. 2013. The influence of MRI scan position on patients with oropharyngeal cancer undergoing radical radiotherapy. *Radiation Oncology*, 8, (1) 129

Hanvey, S., Sadozye, A., McJury, M., Glegg, M., & Foster, J. 2012. The influence of MRI scan position on image registration accuracy, target delineation and calculated dose in prostatic radiotherapy. *The British Journal of Radiology*, 85, e1256-e1262

Hargreaves, B., Worters, P., Pauly, K., Pauly, J., Koch, K., & Gold, G. 2011. Metal-Induced artifacts in MRI. *American Journal of Roentgenology*, 197, (3) 547-555

Hendee, W., Ibbott, G., & Hendee, E. 2005. *Radiation therapy physics*, 3rd ed. Madison, Wisconson, Wiley.

Hill, D., Batchelor, P., Holden, M., & Hawkes, D. 2001. Medical image registration. *Physics in Medicine and Biology*, 46, (3) 1-45

Hill, D., Hawkes, D., Gleeson, M., Cox, T., Strong, A., Wong, W., Ruff, C., Kitchen, N., Thomas, D., Sogat, A., Crossman, J., Studholme, C., Gandhe, A., Green, S., & Robinson, G. 1994. Accurate frameless registration of MR and CT images of the head: applications in planning surgery and radiation therapy. *Radiology*, 191, 447-454

Hornack, J. 2000, "The basics of MRI," Rochester Institute of Technology.

Hyer, D., Mart, C., & Nixon, E. 2012. Development and implementation of an EPID-based method for localizing isocenter. *Journal of Applied Clinical Medical Physics*, 13, (6) 72-81

ICRU 1993, *Report 50 Prescribing, recording, and reporting photon beam therapy*, International Commission on Radiation Units and Measurements, Washington, DC.

ICRU 1999, *Report 62 Prescribing, recording, and reporting photon beam therapy*, International Commission on Radiation Units and Measurements, Washington, DC.

IPEM 1998, *Report 80 Quality control in Magnetic Resonance Imaging*, The Institute of Physics in Engineering and Medicine, York, 80.

IPEM 1999, *Report 81 Physics aspects of quality control in radiotherapy*, The Institute of Physics and Engineering in Medicine, York, 81.

Irarrazabal, P., Meyer, C., Nishimura, D., & Macovski, A. 1996. Inhomogeneity correction using an estimated linear field map. *Magnetic Resonance in Medicine*, 35, (2) 278-282

Jackson, A., Reinsberg, S., Sohaib, S., Charles-Edwards, E., Jhavar, S., Christmas, T., Thompson, A., Bailey, M., Corbishley, C., Fisher, C., Leach, M., & Dearnaley, D. 2009. Dynamic contrast-enhanced MRI for prostate cancer localization. *The British Journal of Radiology*, 82, 148-156

Jansen, J., Schöder, H., Lee, N., Stambuk, H., Wang, Y., Fury, M., Patel, S., Pfister, D., Shah, J., Koutcher, J., & Shukla-Dave, A. 2012. Tumor metabolism and perfusion in head and neck squamous cell carcinoma: pretreatment multimodality imaging with ^{1}H magnetic resonance spectroscopy, dynamic contrast-enhanced MRI, and [^{18}F]FDG-PET. *International Journal of Radiation Oncology Biology Physics*, 82, (1) 299-307

Jonsson, J., Brynolfsson, P., Garpebring, A., Karlsson, M., Söderström, K., & Nyholm, T. 2011. Registration accuracy for MR images of the prostate using a subvolume based registration protocol. *Radiation Oncology*, 6, (73) 1-5

Jonsson, J., Karlsson, M., Karlsson, M., & Nyholm, T. 2010. Treatment planning using MRI data: an analysis of the dose calculation accuracy for different treatment regions. *Radiation Oncology*, 5, (62)

Kapanen, M. & Tenhunen, M. 2012. T1/T2*-weighted MRI provides clinically relevant pseudo-CT density data for the pelvic bones in MRI-only based radiotherapy treatment planning. *Acta Oncologica* 1-7

Karger, C., Höss, A., Bendl, R., Canda, V., & Schad, L. 2006. Accuracy of device-specific 2D and 3D image distortion correction algorithms for magnetic resonance imaging of the head provided by a manufacturer. *Physics in Medicine and Biology*, 51, N253-N261

Kashani, R., Hub, M., Balter, J., Kessler, M., Dong, L., Zhang, L., Xing, L., Xie, Y., Hawkes, D., Schnabel, J., McClelland, J., Joshi, S., Chen, Q., & Lu, W. 2008.

Objective assessment of deformable image registration in radiotherapy: a multi-institution study. *Medical Physics*, 35, (12) 5944-5953

Kashani, R., Hub, M., Kessler, M., & Balter, J. 2007. Technical note: A physical phantom for assessment of accuracy of deformable alignment algorithms. *Medical Physics*, 34, (7) 2785-2788

Kaufman, L., Kramer, D., Crooks, L., & Ortendahl, D. 1989. Measuring signal-to-noise ratios in MR imaging. *Radiology*, 173, (1) 265-267

Kaus, M., Brock, K., Pekar, V., Dawson, L., Nichol, A., & Jaffray, D. 2007. Assessment of a model-based deformable image registration approach for radiation therapy planning. *International Journal of Radiation Oncology Biology Physics*, 68, (2) 572-580

Kenneth, U., Urie, M., & Cherlow, J. 2010. Results of a multi-institutional benchmark test for cranial CT/MR image registration. *International Journal of Radiation Oncology Biology Physics*, 77, 1584-1589

Kessler, M. 2006. Image registration and data fusion in radiation therapy. *The British Journal of Radiology*, 79, S99-S108

Khoo, V. 2000. MRI - "magic radiotherapy imaging" for treatment. *The British Journal of Radiology*, 73, (867) 229-233

Khoo, V., Adams, E., Saran, F., Bedford, J., Perks, J., Warrington, A., & Brada, M. 2000. A comparison of clinical target volumes determined by CT and MRI for the radiotherapy planning of base of skull meningiomas. *International Journal of Radiation Oncology Biology Physics*, 46, (5) 1309-1317

Khoo, V. & Joon, D. 2006. New developments in MRI for target volume delineation in radiotherapy. *British Journal of Radiology*, 79, 2-15

Kim, S., Loevner, L., Quon, H., Sherman, E., Weinstein, G., Kilger, A., & Poptani, H. 2009. Diffusion-weigted magnetic resonance imaging for predicting and detecting early response to chemoradiation therapy of squamous cell carcinomas of the head and neck. *Clinical Cancer Research*, 15, (3) 986-994

Koch, K., Lorbiecki, J., Hinks, R., & King, K. 2009. A multispectral three-dimensional acquisition technique for imaging near metal implants. *Magnetic Resonance in Medicine*, 61, (2) 381-390

Koch, M. 2008. Automatic coregistration of volumetric images based on implanted fiducial markers. *Medical Physics*, 35, (10) 4513-4523

Kremser, C., Plangger, C., Bösecke, R., Pallua, A., Aichner, F., & Felber, S. 1997. Image registration of MR and CT images using a frameless fiducial marker system. *Magnetic Resonance Imaging*, 15, (5) 579-585

Kristensen, B., Laursen, F., Løgager, V., Geertsen, P., & Krarup-Hansen, A. 2008. Dosimetric and geometric evaluation of an open low-field magnetic resonance simulator for radiotherapy treatment planning of brain tumours. *Radiotherapy and Oncology*, 87, 100-109

Kry, S., Salehpour, M., Followil, D., Stovall, M., Kuban, D., White, R., & Rosen, I. 2005. The calculated risk of fatal secondart malignancies from intensity-modulated radiation therapy. *International Journal of Radiation Oncology Biology Physics*, 62, (4) 1195-1203

Lagendijk, J., Raaymakers, B., Raaijmakers, A., Overweg, J., Brown, K., Kerkhof, E., van der Put, R., Hårdemark, B., van Vulpen, M., & van der Heide, U. 2008. MRI/linac integration. *Radiotherapy and Oncology*, 86, 25-29

Lambert, J., Greer, P., Menk, F., Patterson, J., Parker, J., Dahl, K., Gupta, S., Capp, A., Wratten, C., Tang, C., Kumar, M., Dowling, J., Hauville, S., Hughes, C., Fisher, K., Lau, P., Denham, J., & Salvado, O. 2011. MRI-guided prostate radiation therapy planning: Investigation of dosimetric accuracy of MRI-based dose planning. *Radiotherapy and Oncology*, 98, 330-334

Lamey, M., Yun, J., Burke, B., Rathee, S., & Fallone, B. 2010. Radio frequency noise from an MLC: a feasibility study of the use of an MLC for linac-MR systems. *Physics in Medicine and Biology*, 55, (4) 981-994

Lee, Y., Bollet, M., Charles-Edwards, G., Flower, M., Leach, M., McNair, H., Moore, E., Rowbottom, C., & Webb, S. 2003. Radiotherapy treatment planning of prostate cancer using magnetic resonance imaging alone. *Radiotherapy and Oncology*, 66, 203-216

Leibel, S., Fuks, Z., Zelefsky, M., Wolden, S., Rosenzweig, K., Alektiar, K., Hunt, M., Yorke, E., Hong, L., Amols, H., Burman, C., Jackson, A., Mageras, G., LoSasso, T., Happersett, L., Spirou, S., Chui, C.-S., & Ling, C. 2002. Intensity-modulated radiotherapy. *The Cancer Journal*, 8, (2) 164-176

Levitt, S., Purdy, J., Perez, C., & Vijayakumar, S. Technical basis of radiation therapy. 4th. 2008. Berlin, Springer.
Ref Type: Edited Book

Li, B., Christensen, G., Hoffman, E., McLennan, G., & Reinhardt, J. 2003. Establishing a normative atlas of the human lung : intersubject warping and registration of volumetric CT Images. *Academic Radiology*, 10, (3) 255-265

Li, G., Xie, H., Ning, H., Capala, J., Arora, B., Coleman, N., Camphausen, K., & Miller, R. 2005. A novel 3D volumetric voxel registration technique for volume-view-guided image registration of multiple imaging modalities. *International Journal of Radiation Oncology Biology Physics*, 63, (1) 261-273

Li, G., Xie, H., Ning, H., Citrin, D., Capala, J., Maass-Moreno, R., Guion, P., Arora, B., Coleman, N., Camphausen, K., & Miller, R. 2008. Accuracy of 3D volumetric image registration based on CT, MR and PET/CT phantom experiments. *Journal of Applied Clinical Medical Physics*, 9, (4) 17-36

Li, S. & Padhani, A. 2012. Tumor response assessments with diffusion and perfusion MRI. *Journal of Magnetic Resonance Imaging*, 35, 745-763

Litzenberg, D., Balter, J., Hadley, S., Hamstra, D., Willoughby, T., Kupelian, P., Djemil, T., Mahadevan, A., Jani, S., Weinstein, G., Solberg, T., Enke, C., Levine, L., & Sandler, H. 2011. Prostate Intrafraction Translation Margins for Real-Time Monitoring and Correction Strategies. *Prostate Cancer* -130579

Liu, Y., Bai, R., Sun, H., Liu, H., Zhao, X., & Li, Y. 2009. Diffusion-weighted imaging in predicting and monitoring the response of uterine cervical cancer to combined chemoradiation. *Clinical Radiology*, 64, (11) 1067-1074

Maintz, J. & Viergever, M. 1998. A survey of medical image registration. *Physics in Medicine and Biology*, 2, (1) 1-36

Manning, M., Wu, Q., Cardinale, R., Mohan, R., Lauve, A., Kavanagh, B., Morris, M., & Schmidt-Ullrich, R. 2001. The effect of setup uncertainty on normal tissue sparing with IMRT for head-and-neck cancer. *International Journal of Radiation Oncology Biology Physics*, 51, (5) 1400-1409

Markl, M., Bammer, R., Alley, M., Elkins, C., Draney, M., Barnett, A., Moseley, M., Glover, G., & Pelc, N. 2003. Generalized reconstruction of phase contrast MRI: analysis and correction of the effect of gradient field distortions. *Magnetic Resonance in Medicine*, 50, (4) 791-801

McJury, M., O'Neill, A., Lawson, M., McGrath, C., Grey, A., Page, W., & O'Sullivan, J. 2011. Assessing the image quality of pelvic MR images acquired with a flat couch for radiotherapy treatment planning. *The British Journal of Radiology*, 84, (1004) 750-755

McRobbie, D., Moore, E., Graves, M., & Prince, M. 2003. *MRI from picture to proton*. Cambridge, Cambridge University Press.

MHRA 2007, *Safety guidelines for magnetic resonance imaging equipment in clinical use.*, Department of Health, DB2007(03).

Moerland, M., Boersma, R., Bhagwandien, R., Wijrdeman, H., & Bakker, C. 1995. Analysis and correction of geometric distortions in 1.5-T magnetic-resonance images for use in radiotherapy treatment planning. *Physics in Medicine and Biology*, 40, 1651-1664

Moore, C., Liney, G., & Beavis, A. 2004. Quality assurance of registration of CT and MRI data sets for treatment planning of radiotherapy for head and neck cancers. *Journal of Applied Clinical Medical Physics*, 5, 25-35

Mutic, S., Dempsey, J., Bosch, W., Low, D., Drzymala, R., Chao, K., Goddu, S., Cutler, P., & Purdy, J. 2001. Multimodality image registration quality assurance for conformal three-dimensional treatment planning. *International Journal of Radiation Oncology Biology Physics*, 51, (1) 255-260

Newbold, K., Partridge, M., Cook, G., Sohaib, S., Charles-Edwards, E., Rhys-Evans, P., Harrington, K., & Nutting, C. 2006. Advanced imaging applied to radiotherapy planning in head and neck cancer: a clinical review. *The British Journal of Radiology*, 79, (943) 554-561

Nutting, C., Marden, J., Harrington, K., Urbano, T., Bhide, S., Clark, C., Miles, E., Miah, A., Newbold, K., Tanay, M., Adab, F., Jeffries, S., Scrase, C., Yap, B., A'Hern, R., Sydenham, M., Emson, M., & Hall, E. 2011. Parotid-sparing intensity modulated versus conventional radiotherapy in head and neck cancer (PARSPORT): a phase 3 multicentre randomised controlled trial. *The Lancet Oncology*, 12, 127-136

Nyholm, T., Jonsson, J., Söderström, K., Bergström, P., Carlberg, A., Frykholm, G., Behrens, C., Geertsen, P., Trepiakas, R., Hanvey, S., Sadozye, A., Ansari, J., McCallum, H., Frew, J., McMenemin, R., & Zackrisson, B. 2013. Variability in prostate and seminal vesicle delineations defined on magnetic resonance images, a multi-observer, -center and -sequence study. *Radiation Oncology*, 8, (1) 126

Nyholm, T., Nyberg, M., Karlsson, M., & Karlsson, M. 2009. Systematisation of spatial uncertainties for comparison between a MR and a CT-based radiotherapy workflow for prostate treatments. *Radiation Oncology*, 4, (54)

OSL. Advanced tools for complex QA, ImSimQA TriFold brochure. Revision 1. 2012. Shrewsbury, Oncology Systems Limited. 12-11-2012. www.osl.uk.com
Ref Type: Online Source

Otto, K. 2008. Volumetric modulated arc therapy: IMRT in a single gantry arc. *Medical Physics*, 35, (1) 310-317

Palma, D., Vollans, E., James, K., Nakano, S., Moiseenko, V., Shaffer, R., McKenzie, M., Morris, J., & Otto, K. 2008. Volumetric modulated arc therapy for delivery of prostate radiotherapy: comparison with intensity-modulated radiotherapy and three-dimensional conformal radiotherapy. *International Journal of Radiation Oncology Biology Physics*, 72, (4) 996-1001

Palma, D., Verbakel, W., Otto, K., & Senan, S. 2010. New developments in arc radiation therapy: A review. *Cancer Treatment Reviews*, 36, 393-399

Park, S., Kim, C., Park, B., Park, W., Park, H., Han, D., & Kim, B. 2011. Early changes in Apparent Diffusion Coefficient from diffusion-weighted MR imaging during radiotherapy for prostate cancer. *International Journal of Radiation Oncology Biology Physics*, 83, (2) 749-755

PASA 2006, *Evaluation Report 06005, 1.5T MRI Systems, Issue 6*, NHS Purchasing and Supply Agency.

Philips, M., Singer, K., & Hounsell, A. 1999. A macropencil beam model: clinical implementation for conformal and intensity modulated radiation therapy. *Physics in Medicine and Biology*, 44, 1067-1088

Prabhakara, R., Haresh, K., Ganesh, T., Joshi, R., Julka, P., & Rath, G. 2007. Comparison of computed tomography and magnetic resonance based target volume in brain tumors. *Journal of Cancer Research and Therapeutics*, 3, (2) 121-123

Prestwich, R., Sykes, J., Carey, B., Sen, M., Dyker, K., & Scarsbrook, A. 2012. Improving target definition for head and neck radiotherapy: a place for magnetic resonance imaging and 18-fluoride fluorodeoxyglucose positron emission tomography? *Clincal Oncology*, 24, (8) 577-589

Price, D., de Wilde, J., Papdaki, A., Curran, J., & Kitney, R. 2001. Investigation of acoustic noise on 15 MRI scanners from 0.2 T to 3 T. *Journal of Magnetic Resonance Imaging*, 13, 288-293

Raaijmakers, A., Raaymakers, B., & Lagendijk, J. 2005. Integrating a MRI scanner with a 6 MV radiotherapy accelerator: dose increase at tissue-air interfaces in a lateral magnetic field due to returning electrons. *Physics in Medicine and Biology*, 50, 1363-1376

Raaymakers, B., Lagendijk, J., Overweg, J., Kok, J., Raaijmakers, A., Kerkhof, E., van der Put, R., Meijsing, I., Crijns, S., Benedosso, F., van Vulpen, M., de Graaff, C., Allen, J., & Brown, K. 2009. Integrating a 1.5 T MRI scanner with a 6 MV accelerator: proof of concept. *Physics in Medicine and Biology*, 54, N229-N237

Raaymakers, B., Raaijmakers, A., Kotte, A., Jette, D., & Lagendijk, J. 2004. Integrating a MRI scanner with a 6 MV radiotherapy accelerator: dose deposition in a transverse magnetic field. *Physics in Medicine and Biology*, 49, 4109-4118

Rasch, C., Barillot, I., Remeijer, P., Touw, A., van Herk, M., & Lebesque, J. 1999. Definition of the prostate in CT and MRI: A multi-observer study. *International Journal of Radiation Oncology Biology Physics*, 43, (1) 57-66

RCR 2008, *Toward Safer Radiotherapy*, The Royal College of Radiologists, London.

Reimer, P., Parizel, P., Meaney, J., & Stichnoth, F. 2010. *Clinical MR imaging*, 3rd ed. Springer.

Reinsberg, S., Doran, S., Charles-Edwards, E., & Leach, M. 2005. A complete distortion correction for MR images: II. Rectification of static-field inhomogeneities by similarity-based profile mapping. *Physics in Medicine and Biology*, 50, 2651-2661

Reit, A., Mak, A., Moerland, M., Elders, L., & Zee, W. 1997. A conformation number to quantify the degree of conformality in brachytherapy and external beam irradiation: application to the prostate. *International Journal of Radiation Oncology Biology Physics*, 37, 731-736

Rosenman, J., Miller, E., Tracton, G., & Cullip, T. 1998. Image registration: an essential part of radiation therapy planning. *International Journal of Radiation Oncology Biology Physics*, 36, 519-522

Ruan, D., Fessler, J., Roberson, M., Balter, J., & Kessler, M. 2006. Nonrigid registration using regularization that accommodates local tissue rigidity. *SPIE Medical Imaging Proceedings*, 6144

Ruben, J., Davis, S., Evans, C., Jones, P., Gagliardi, F., Haynes, M., & Hunter, A. 2008. The effect of intensity-modulated radiotherapy on radiation-induced second malignancies. *International Journal of Radiation Oncology Biology Physics*, 70, (5) 1530-1536

Sannazzari, G., Ragona, R., Ruo Redda, M., Giglioli, F., Isolato, G., & Guarneri, A. 2002. CT–MRI image fusion for delineation of volumes in three-dimensional conformal radiation therapy in the treatment of localized prostate cancer. *British Journal of Radiology*, 75, (895) 603-607

Sarkar, A., Santiago, R., Smith, R., & Kassaee, A. 2005. Comparison of manual vs. automated multimodality (CT-MRI) image registration for brain tumors. *Medical Dosimetry*, 30, (1) 20-24

Sarrut, D. 2006. Deformable registration for image-guided radiation therapy. *Zeitschrift fur Medizinische Physik*, 16, (4) 285-297

Schad, L., Ehricke, H., Wowra, B., Layer, G., Engenhart, R., Kauczor, H., Zabel, H., Brix, G., & Lorenz, W. 1992. Correction of spatial distortion in magnetic-resonance angiography for radiosurgical treatment planning of cerebral arteriovenous-malformations. *Magnetic Resonance Imaging*, 10, (4) 609-621

Schaly, B., Kempe, J., Bauman, G., Battista, J., & Van Dyk, J. 2004. Tracking the dose distribution in radiation therapy by accounting for variable anatomy. *Physics in Medicine and Biology*, 49, (5) 791-805

Schenck, J. 1996. The role of magnetic susceptibility in magnetic resonance imaging: MRI magnetic compatibility of the first and second kinds. *Medical Physics*, 23, 815-850

Sefrova, J., Odrazka, K., Paluska, P., Belobradek, Z., Brodak, M., Dolezel, M., Prosvic, P., Macingova, Z., Vosmik, M., Hoffmann, P., Louda, M., & Nejedla, A. 2012. Magnetic Resonance Imaging in Postprostatectomy Radiotherapy Planning. *International Journal of Radiation Oncology Biology Physics*, 82, (2) 911-918

Shaffer, R., Nichol, A., Vollans, E., Fong, M., Nakano, S., Moiseenko, V., Schmuland, M., Ma, R., McKenzie, M., & Otto, K. 2010. A Comparison of Volumetric Modulated Arc Therapy and Conventional Intensity-Modulated Radiotherapy for Frontal and Temporal High-Grade Gliomas. *International Journal of Radiation Oncology Biology Physics*, 76, (4) 1177-1184

Sharpe, M. & Brock, K. 2008. Quality assurance of serial 3D image registration, fusion, and segmentation. *International Journal of Radiation Oncology Biology Physics*, 71, (1) 33-37

Sherouse, G., Novins, K., & Chaney, E. 1990. Computation of digitally reconstructed radiographs for use in radiotherapy treatment design. *International Journal of Radiation Oncology Biology Physics*, 18, (3) 651-658

Shmueli, K., Thomas, D., & Ordidge, R. 2007. Design, construction and evaluation of an anthropomorphic head phantom with realistic susceptibility artifacts. *Journal of Magnetic Resonance Imaging*, 26, 202-207

Shukla-Dave, A., Lee, N., Jansen, J., Thaler, H., Stambuk, H., Fury, M., Patel, S., Moreira, A., Sherman, E., Karimi, S., Wang, Y., Kraus, D., Shah, J., Pfister, D., & Koutcher, J. 2012. Dyanamic contrast-enhanced magnetic resonance imaging as a predictor of outcome in head-and-neck squamous cell carcinoma patients with nodal metastes. *International Journal of Radiation Oncology Biology Physics*, 82, (5) 1837-1844

Smith, W., Lewis, C., Bauman, G., Rodrigues, G., D'Souza, D., Ash, R., Ho, D., Venkatesan, V., Downey, D., & Fenster, A. 2007. Prostate volume contouring: A 3D analysis of segmentation using 3DTRUS, CT, and MR. *International Journal of Radiation Oncology Biology Physics*, 67, (4) 1238-1247

Spirou, S. & Chui, C.-S. 1994. Generation of arbitrary intensity profiles by dynamic jaws or multileaf collimators. *Medical Physics*, 21, (7) 1031-1041

Staffurth, J. 2010. A review of the clinical evidence for intensity-modulated radiotherapy. *Clincal Oncology*, 22, 643-657

Sumanaweera, T., Glover, G., Song, S., Adler, J., & Napel, S. 1994. Quantifying MRI geometric distortion in tissue. *Magnetic Resonance in Medicine*, 31, 40-47

Sundar, S. & Symonds, R. 2002. Diagnostic Radiology for Radiotherapist: the Case for Structured Training in Cross-Sectional Imaging (CT and MRI). *Clincal Oncology*, 14, (5) 413-414

Symonds, P., Deehan, C., Mills, J., & Meredith, C. 2012. *Walter and Miller's textbook of radiotherapy*, 7th ed. Elsevier.

Tanaka, H., Hayashi, S., Ohtakara, K., Hoshi, H., & Iida, T. 2011. Usefulness of CT-MRI fusion in radiotherapy planning for localized prostate cancer. *Journal of Radiation Research*, 52, (6) 782-788

Teoh, M., Clark, C., Wood, K., Whitaker, S., & Nisbet, A. 2011. Volumetric modulated arc therapy: a review of current literature and clinical use in practice. *The British Journal of Radiology*, 84, 967-996

Ulin, K., Urie, M., & Cherlow, J. 2010. Results of a multi-institutional benchmark test for cranial CT/MR image registration. *International Journal of Radiation Oncology Biology Physics*, 77, (5) 1584-1589

Vanetti, E., Clivio, A., Nicolini, G., Fogliata, A., Ghosh-Laskar, S., Agarwal, J., Upreti, R., Budrukkar, A., Murthy, V., Deshpande, D., Shrivastava, S., Dinshaw, K., & Cozzi, L. 2009. Volumetric modulated arc radiotherapy for carcinomas of the oro-pharynx, hypo-pharynx and larynx: A treatment planning comparison with fixed field IMRT. *Radiotherapy and Oncology*, 92, 111-117

Varadhan, R., Karangelis, G., Krishnan, K., & Hui, S. 2013. A framework for deformable image registration validation in radiotherapy clinical applications. *Journal of Applied Clinical Medical Physics*, 14, (1) 1-22

Varian Medical Systems 2008, *Eclipse algorithms reference guide*. Palo Alto, CA, USA.

Veninga, T., Huisman, H., Maazen, R., & Huizenga, H. 2004. Clinical validation of the normalized mutual information method for registration of CT and MR images in radiotherapy of brain tumors. *Journal of Applied Clinical Medical Physics*, 5, (3) 66-79

Verbakel, W., Cuijpers, J., Hoffmans, D., Bieker, M., Slotman, B., & Senan, S. 2009a. Volumetric intensity-modulated arc therapy vs. conventional IMRT in head-and-neck cancer: a comparitive planning and dosimetric study. *International Journal of Radiation Oncology Biology Physics*, 74, (1) 252-259

Verbakel, W., Senan, S., Cuijpers, J., Slotman, B., & Lagerwaard, F. 2009b. Rapid delivery of stereotactic radiotherapy for peripheral lung tumors using

volumetric intensity-modulated arcs. *Radiotherapy and Oncology*, 93, (1) 122-124

Wachowicz, K., Stanescu, T., Thomas, S., & Fallone, B. 2010. Implications of tissue magnetic susceptibility-related distortion on the rotating magnet in an MR-linac design. *Medical Physics*, 37, (4) 1714-1721

Wang, D., Doddrell, D., & Cowin, G. 2004a. A novel phantom and method for comprehensive 3-dimensional measurement and correction of geometric distortion in magnetic resonance imaging. *Magnetic Resonance Imaging*, 22, 529-542

Wang, D., Strugnell, W., Cowin, G., Doddrell, D., & Slaughter, R. 2004b. Geometric distortion in clinical MRI systems Part I: evaluation using a 3D phantom. *Magnetic Resonance Imaging*, 22, 1211-1221

Wang, D., Strugnell, W., Cowin, G., Doddrell, D., & Slaughter, R. 2004c. Geometric distortion in clinical MRI systems Part II: correction using a 3D phantom. *Magnetic Resonance Imaging*, 22, 1223-1232

Wang, J., Li, X., D'Souza, W., & Stewart, R. 2003. Impact of prolonged fraction delivery times on tumor control: a note of caution for intensity-modulated radiation therapy (IMRT). *International Journal of Radiation Oncology Biology Physics*, 57, (2) 543-552

Wang, X., Xiaodong, Z., Dong, L., Liu, H., Wu, Q., & Mohan, R. 2004. Development of methods for beam angle optimization for IMRT using an accelerated exhaustive search strategy. *International Journal of Radiation Oncology Biology Physics*, 60, (4) 1325-1337

Webb, S. 2003. The physical basis of IMRT and inverse planning. *The British Journal of Radiology*, 76, 678-689

Webb, S. & McQuaid, D. 2009. Some considerations concerning volume-modulated arc therapy: a stepping stone towards a general theory. *Physics in Medicine and Biology*, 54, 4345-4360

Webster, G., Kilgallon, J., Ho, K., Rowbottom, C., Slevin, N., & Mackay, R. 2009. A novel imaging technique for fusion of high-quality immobilised MR images of the head and neck with CT scans for radiotherapy target delineation. *The British Journal of Radiology*, 82, 497-503

Weis, J., Ericsson, A., Silander, H., & Hemingsson, A. 1998. Magnetic resonance spectroscopic imaging for visualization and correction of distortions in MRI: high precision applications in neurosurgery. *Magnetic Resonance Imaging*, 16, (10) 1265-1272

Westphalen, A., Reed, G., Vinh, P., Sotto, C., Vigneron, D., & Kurhanewicz, J. 2012. Multiparametric 3T endorectal MRI after external beam radiation therapy for prostate cancer. *Journal of Magnetic Resonance Imaging*, 36, 430-437

Williams, J. & Thwaites, D. Radiotherapy physics in practice. 2nd edition. 2000. Oxford University Press.
Ref Type: Edited Book

Wu, Q., Yoo, S., Kirkpatrick, J., Thongphiew, D., & Yin, F-F. 2009. Volumetric arc intensity-modulated therapy for spine body radiotherapy: comparison with static intensity-modulated treatment. *International Journal of Radiation Oncology Biology Physics*, 75, (5) 1596-1604

Yoon, M., Park, S., Shin, D., Lee, S., Pyo, H., Kim, D., & Cho, K. 2007. A new homogeneity index based on statistical analysis of the dose–volume histogram. *Journal of Applied Clinical Medical Physics*, 8, 9-17

Yu, C. 1995. Intensity-modulated arc therapy with dynamic multileaf collimation: an alternative to tomotherapy. *Physics in Medicine and Biology*, 40, 1435-1449

Zaorsky, N., Studenski, M., Dicker, A., Gomella, L., & Den, R. 2013. Stereotactic body radiation therapy for prostate cancer: Is the technology ready to be the standard of care? *Cancer Treatment Reviews*, 39, 212-218

Zhong, H., Kim, J., & Chetty, I. 2010. Analysis of deformable image registration accuracy using computational modeling. *Medical Physics*, 37, (3) 970-979

Zou, K., Warfield, S., Bharatha, A., Tempany, C., Kaus, M., Haker, S., Wells, W., Jolesz, F., & Kikinis, R. 2004. Statistical validation of image segmentation quality based on a spatial overlap index. *Academic Radiology*, 11, 178-189